

Geometry and Kinematics of Breaking Waves

Pål Furset Lader

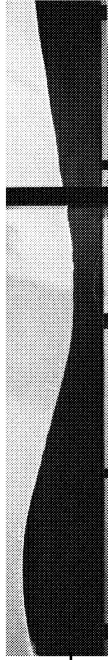
Summary

The objective of this thesis is to experimentally study different breaking wave cases. This is done by measuring in detail the free surface geometry and the internal kinematics of the waves as they approach breaking. Three principal wave cases were chosen for the study: A plunging breaker, a spilling breaker, and an intermediate breaker.

A major part of this work is the design, construction and building of a wave laboratory. The laboratory contains a glass wall wave-flume which is 13.5m long, 1m deep and 0.6m wide, as well as equipment for measuring both the wave kinematics and geometry optically. The wave kinematics is measured using the Particle Image Velocimetry (PIV) method, while the wave profile geometry is measured using image analysis (space domain geometry), as well as standard wave gauges (time domain geometry).

The analysis of both the wave kinematics and geometry is done using parameters describing quantitatively important features in the wave evolution. The surface geometry is described using the commonly known zero-downcross parameters, and in addition, new parameters are suggested and used in the study. The kinematics are described by a set of four parameters suggested for the first time in this work. These parameters are: Velocity at the surface, velocity at the still water line ($z = 0$), mean velocity direction, and local wave number. The purpose of these parameters is to give a better understanding of the space and time domain development of the kinematics, and they appear to be a reasonable compromise between simplicity and accuracy.

Summary



The results presented here represent a thorough and detailed mapping of the breaking process. Much data is gathered and analysed, and throughout this thesis it is sought to present the data in the most intuitive way, so that other investigators may benefit from it.

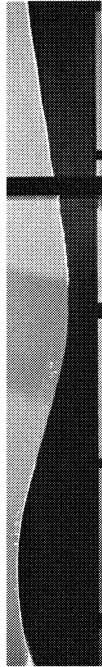
On the left side of each even number page is a wave image. These images are the same as used in the wave geometry measurements (Figs. 13 to 15). They are in chronological sequence starting from page ii, with $1/32s$ between each image. The plunging breaker case is found on page ii to 56, the intermediate breaker case on page 58 to 126 and the spilling breaker case on page 128 to 202. The purpose of these side-page images is to create an animation of the wave cases studied in this thesis. The animation is viewed by browsing fast through the pages.

Preface

Working on this thesis has been a lot of fun. I have had the opportunity to build from scratch a wave laboratory, which I then used to study the intriguing hydrodynamic phenomenon of breaking waves - a poorly understood and almost enigmatic phenomenon. This provided me with a diverse set of tasks to address, from metal work, drilling and soldering to darkroom film development, software programming and digital image analysis. It allowed me to do a lot of practical stuff, but also to spend time in front of the computer doing coding. This diversity is probably one of the reasons why I enjoyed almost every minute working on this thesis, and why there has been only a minimal amount of frustrations.

The lack of frustrations and wealth of enjoyment are also caused by several people who have helped me in the course of my work. Some of them I will name here:

My family; wife Helen, children Hanna, Matilde and Ada, my mother and my late father. Because of them I have been aware of the fact that there are more important things than finishing the thesis, and I have not allowed myself to work evenings and weekends. This has forced me to use my regular hours effectively, making it unnecessary to work long hours, spoiling evening and weekends for others than just myself. I have always looked forward to going to work, and I have always looked forward to coming home. Very important factors on the overall happiness.



During the process of designing, constructing and building the wave laboratory I have received invaluable help from several people. My good friend and colleague, engineer Tormod Leer has been a key person during the construction and building process of the laboratory, and I can not imagine how it would have been without his help and support. The detailed design of the flume was skilfully done by engineer Arvid Skagen.

The Department of Marine Hydrodynamics had no prior experience with the Particle Image Velocimetry (PIV) measurements method, and I had to seek help elsewhere. The Department of Physics and Astronomy at The University of Edinburgh is one of the world leading institutions in the development of PIV, and they run several narrow wave flumes in which they use this method. I had the privilege to visit them on two occasions, using their laboratories, their equipment, their time, asking all sorts of silly questions, and the kind hospitality and high scientific competence of, especially, Professor Clive Greated and Dr. Tim Dewhurst are highly appreciated. The experience I got from these visits was essential for the PIV implementation in the laboratory.

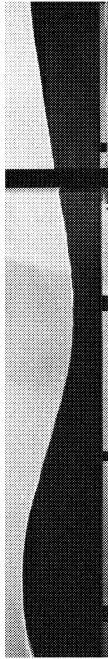
Guttorm Grytøyr first introduced me to b-spline theory, and from this I came up with the idea to use b-spline in the analysis of the free surface geometry. Guttorm wrote the first version of the computer program for the b-spline analysis, and he also co-authored one of my papers on breaking wave geometry analysis. In the period 1996 to 1999, Guttorm together with my other colleagues at the Departments of Marine Hydrodynamics and Marine Constructions formed an exceptional stimulating environment both for social and scientific development, which it was great fun to be a part of.

Needless to say, my supervisor Professor Bjørnar Pettersen, and co-supervisor Professor Dag Myrhaug have been of paramount importance. Both in the process of building the laboratory, and in the phase of experimental work and thesis writing. Their help, support, advice and critical scrutiny of my work have been extremely important to me, and can not be too highly valued. I am especially grateful for the high degree of freedom I have had to choose the course of my work. They seldom gave me detailed instructions, but have allowed me to find my own path and just guided me away from the worst pit-

Preface

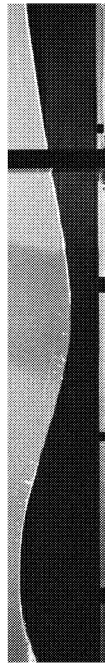
falls. It has been a schoolbook example of good thesis supervising, for which I am truly grateful.

The financial support from The Norwegian Research Council and the Anders Jahres Foundation for the Advancement of Sciences made this work possible. Their support is highly appreciated.



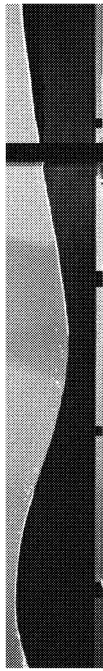
Contents

Summary	i
Preface	iii
Contents	vii
Nomenclature	xi
1 Introduction	1
1.1 What is a Breaking Wave?	2
1.1.1 Definition of Breaking	3
1.1.2 Proposed Breaking Criteria	4
1.2 Importance of Breaking Waves	8
1.3 Description of Breaking Waves	10
1.3.1 Plunging Breakers	11
1.3.2 Spilling Breakers	15
1.4 About this Thesis	18
1.4.1 Case Description	19
1.5 Chapter Summary	23
2 Measuring Wave Kinematics: Particle Image Velocimetry (PIV)	25
2.1 Laboratory Facility	26



2.1.1 Assessment of the Wave Flume Repeatability	29
2.2 Principle of PIV	31
2.3 Seeding	34
2.4 Illumination	35
2.5 Image Acquisition	37
2.5.1 Image Resolution	38
2.6 Image Processing	41
2.6.1 Auto-correlation	42
2.6.2 Peak Detection	47
2.6.3 Velocity Range	49
2.6.4 Resolving Physical Coordinates	52
2.6.5 Correction for Refraction	53
2.6.6 Vector Validation	56
2.7 Errors in PIV	57
2.7.1 Measurement Principle Errors	57
2.7.2 Recording Errors	58
2.7.3 Analysis Errors	60
2.8 PIV Analysis Error Simulation	62
2.8.1 Interrogation Area Generation	62
2.8.2 Results	69
2.9 Description of Wave Kinematics	71
2.9.1 Wave Kinematic Parameters	72
2.9.2 Normalization and Reference Frame	75
2.10 Chapter Summary	79
3 Wave Geometry Measurements	81
3.1 Space Domain Wave Geometry	82
3.1.1 Laboratory Setup	83
3.1.2 Digital Image Processing	88
3.2 Time Domain Wave Geometry	90
3.3 B-spline Curve Fit	92
3.3.1 B-spline Basics	92
3.3.2 B-Spline Parameters	95
3.3.3 Accuracy	98
3.4 Wave Geometry Parameters	100
3.4.1 Zero-Downcross Parameters	100
3.4.2 Inflection Point Parameters	103
3.5 Chapter Summary	107

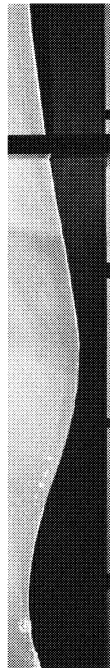
4	Results and Discussion	109
4.1	Wave Geometry	109
4.1.1	Space Domain Wave Geometry	109
4.1.2	Time Domain Wave Geometry	118
4.1.3	Geometry Parameters	126
4.2	Wave Kinematics	140
4.2.1	Velocity	141
4.2.2	Local Wave Number	145
4.2.3	Mean Velocity Direction	148
4.2.4	Principal Development of the Kinematics	149
4.2.5	Comparison with Stokes 5th Order Theory	150
4.3	Chapter Summary	153
5	Conclusions and Suggestions for Further Work	155
5.1	Summary and Conclusions	155
5.2	Suggestions for Further Work	157
	References	161
A	Vector Field Plots of the Wave Kinematics Measurements	167
B	Additional Wave Kinematic Parameter Measurements	189
C	Additional Wave Geometry Parameter Measurements	203
D	Images of the Wave Laboratory	207



Nomenclature

α_1, α_2	transformation angles
$\alpha_a, \alpha_g, \alpha_w$	path of light angles for air, glass and water, maximum
γ, β	spatial frequency in x and z direction, respectively
δ	crest rear steepness
ε	crest front steepness
η	surface elevation
η', η_c	crest elevation
η'', η_{tf}	front trough depth
η_{tr}	rear trough depth
θ	velocity direction $\theta = \tan(u/w)$
$\bar{\theta}$	mean velocity direction
λ	vertical asymmetry factor
μ	horizontal asymmetry factor
σ_{mean}	mean standard deviation
σ_{max}	maximum standard deviation
ω	wave frequency $\omega = \frac{2\pi}{T}$
a_h	wave height asymmetry factor

Nomenclature

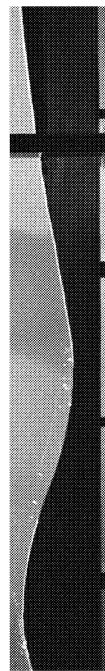


a_l	wave length asymmetry factor
a_s	wave steepness asymmetry factor
C	crest point
c_{fs}	front steepness coefficient
C_{mc}	maximum crest curvature point
C_{mcf}	maximum curvature point front
C_{mcr}	maximum curvature point rear
c_{max}	maximum crest curvature
c_{rs}	rear steepness coefficient
C_w	phase velocity
C_x, C_z	transformation constants
d_p	particle diameter
d_{pi}	particle image diameter
$E[\]$	expected value
F, F^{-1}	Fourier transform and inverse Fourier transform
f	focal length of camera optics
$f(x_m, z_n)$	discrete function representing the grayscale values in an image
f_{peak}	peak frequency of spectrum
g	acceleration of gravity
H, H_f	wave height; vertical length between the crest and the preceding trough
H_{max}	maximum wave height in a time serie
H_r	wave height; vertical length between the crest and the following trough
I	intensity
i, j	pixel coordinates
I_0	particle image intensity
I_f, I_r	front and rear inflection point

Nomenclature

k	order of the basis function in b-spline fit
k	wave number
k'	local wave number made nondimensional with respect to the mean wave number
L	wave length; horizontal length between two zero-crossings with negative gradient
L'	length from zero-upcross point to wave crest
L''	length from wave crest to zero-downcross point
l_a, l_g, l_w	thickness of air, glass and water area, respectively
L_{crest}	length of the wave crest measured from zero-upcross to zero-downcross
L_f	front wave half length; horizontal length from crest point to front trough
l_i	distance between image and focal point
l_{ia}	interrogation area (IA) size
L_{jet}	length of the jet measured horizontally from the tip to the vertical tangent beneath the overturning crest at the moment when the underside of the horizontal crest first becomes horizontal
l_o	distance between focal point and object
L_r	rear wave half length; horizontal length from crest point to rear trough
L_t	wave length; horizontal length between two trough points
l_x, l_z	interrogation area size
MWL	mean water line
M	magnification [-]
\hat{M}	magnification [pix/mm]
m_0	zero order momentum of spectral density
n_a, n_g, n_w	index of refraction for air, glass and water, respectively
N_d	number of measurements points in b-spline fit

Nomenclature

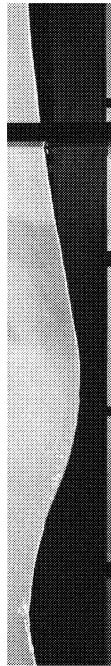


$N_{i,k}$	basis function in b-spline fit
N_{vp}	number of vertices in b-spline fit
R	error/bias
$R(\delta x, \delta z)$	2D autocorrelation function
$R'(\delta x', \delta z')$	scaled 2D autocorrelation function
R_U^{RMS}	RMS value of the error in U
R_θ^{RMS}	RMS value of the error in θ
S	power spectral density
$S(\gamma, \beta)$	2D power spectral density
ΔS	relative change in power spectral density
Δs	particle displacement $\Delta s = \sqrt{\Delta s_x^2 + \Delta s_z^2}$
Δs_a	apparent particle displacement
Δs_r	real particle displacement
$\Delta s_x, \Delta s_z$	particle displacement in x and z direction, respectively
s	total wave steepness
s_f	front wave steepness
s_{if}	front inflection point steepness
s_{ir}	rear inflection point steepness
S_{jet}	relative jet size
s_r	rear wave steepness
SWL	still water line
δt_{cs}	camera shutter time
δt_p	laser pulse separation
T	wave period, time between two zero-crossings with negative gradient
t	time
Δt	time interval
T'	time from zero-upcross point to wave crest

Nomenclature

T''	time from wave crest to zero-downcross point
t'	time made dimensionless with respect to wave period $t' = 0$ at breaking point
$t_{breaking}$	time instance of breaking
T_f	front wave half period; time between the passing of the front trough point and the crest point
T_i	knot vector in b-spline fit
T_r	rear wave half period; time between the passing of the crest point and the rear trough point
Tr_f, Tr_r	front and rear trough points
T_t	wave period; time between two subsequent wave troughs
U	velocity magnitude $U = \sqrt{u^2 + w^2}$
u	horizontal particle velocity
U_η	particle velocity at the surface
U'_η	particle velocity at the surface made nondimensional with respect to the phase velocity
U_{max}	maximum velocity in PIV measurements
U_{min}	minimum velocity in PIV measurements
U_0	particle velocity at $z = 0$
\hat{U}_0	particle velocity at $z = 0$ (taken from the e^{kz} extrapolation)
U'_0	particle velocity at $z = 0$ made nondimensional with respect to the phase velocity (taken from the e^{kz} extrapolation)
\hat{U}'_0	particle velocity at $z = 0$ made nondimensional with respect to the phase velocity (directly from measurements)
w	vertical particle velocity
x	earth bound horizontal coordinate

Nomenclature



x'	earth bound horizontal coordinate with $x' = 0$ at the point of breaking and made nondimensional with respect to the wave length
\hat{x}	wave bound horizontal coordinate with $\hat{x} = 0$ where the particle velocity is horizontal and made nondimensional with respect to the wave length
x	wave bound horizontal coordinate with $x = 0$ at the crest point and made nondimensional with respect to the wave length
$\delta x, \delta z$	displacement
$x_{\theta=0}$	position where the velocity is horizontal
X_a	apparent particle position
$x_{breaking}$	position of breaking
x_{centre}, z_{centre}	particle image centre
x_{crest}	vertical position of the crest point
X_i, Z_i	vertices in b-spline fit
x_m, z_n	pixel position
X_r	real particle position
z	earthbound vertical coordinate
z', \hat{z}, z	vertical coordinate made nondimensional with respect to the wavelength
Z_1, Z_2, Z_3	zero-crossing points

Chapter 1

Introduction

The breaking of waves is a phenomenon that influences life at sea, in the sea and by the sea, as well as the global environment. This makes it important to establish as much knowledge of the phenomenon as possible. Despite this, wave breaking remains one of the fields in hydrodynamics which is poorly understood. Most important, it has not yet been established a criterion for when a wave is going to break, and it is therefore not possible to predict or forecast wave breaking accurately.

The goal of this work is not necessarily to establish such a criterion, but to study the phenomenon of breaking waves in detail. This is done by experimentally studying the behaviour of the waves as they evolve into breaking, and the results presented here may help other investigators in their work towards a breaking criteria.

1.1 What is a Breaking Wave?

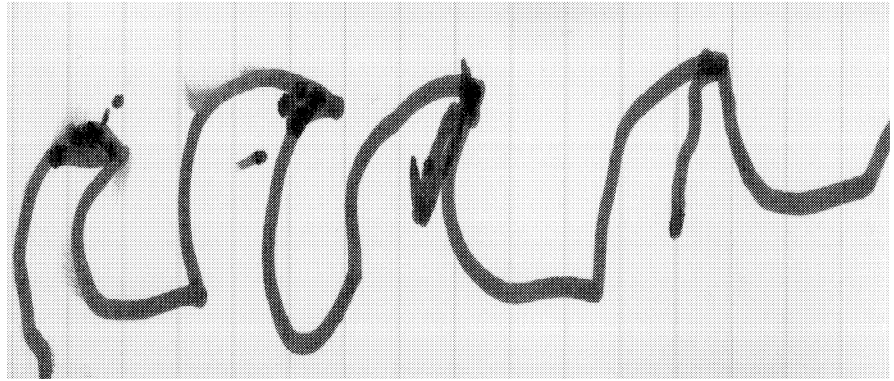
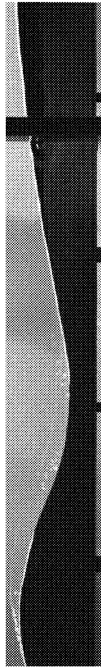


FIGURE 1. Waves as Hanna 3.5 years sees it. Typically plunging breakers.

Breaking is probably the wave phenomenon most people have a relationship to. Everyone has seen a breaking wave, and know how they generally look like. When small children draw waves, they are most likely to appear as plunging breakers (Fig. 1). The phenomenon is an event that nature displays for us at sea, on a beach, in a glass of water, in a river, in a liquid propellant tank on a rocket, and almost everywhere there is liquid moving with a free surface. The breaking event is easily detectable; viewing the sea on a windy day, or watching the waves breaking on a beach, the creation of foam and noise (some might even say music) is obvious (Fig. 2).



FIGURE 2. Breaking waves at sea on the Norwegian coast, near Kristiansund. A heavy breaker (plunging) appears in front, and several light breakers (spilling) can be seen in the background.

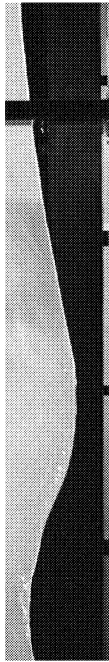
Breaking is initiated when the wave becomes too energetic and unstable. A wave can contain a limited amount of energy. When this limit is exceeded the wave has to release some of its energy, and this is done through the breaking process. The wave energy is due to the motion and displacement of fluid particles. In deep water the particles move in approximately circular orbits, and this gives rise to kinetic energy because of the particle velocity, and potential energy because the particles are forced out of equilibrium. This motion is harmonic, laminar, and to a certain extent predictable. When a wave breaks this motion is transformed into a highly turbulent and unpredictable flow, and the fluid velocities increase. In this flow viscous forces dominate, and energy is dissipated into heat. This causes much of the original wave motion to vanish, and the wave contains less energy after breaking than it did before. The energy from a breaking wave can also be transferred into momentum as a surface current (Mei, 1989), or into waves with lower frequency (Smith, 1973). The breaking transfers energy between different forms in a sea state: from wave to heat, from wave to current, or from wave to another wave. Breaking can also transfer energy from the sea to its environment. Boats hit by a breaking wave increase their kinetic energy. Rocks, sand and segments on a beach are moved as energy is transferred to them from a breaking wave.

1.1.1 Definition of Breaking

How do we define breaking? What characterise a breaking wave? Upon deciding when breaking occurs we must ask: Why do we study breaking waves? The answer to this question may vary from one researcher to another. A marine biologist studying the aquatic life in the upper ocean layers has different interest in breaking waves than an engineer designing an offshore platform.

A general definition of breaking is that a breaking wave loses energy due to generation of turbulence and viscous heat dissipation. To detect breaking by this definition it will be necessary to measure the wave energy before and after the breaking. This is difficult in most cases, and a simplified definition would in most cases be used.

As stated earlier, breaking is visually connected with the occurrence of foam. Would it be sufficient to define breaking waves as waves that create foam, or where air is entrained? Such a wave will certainly lose energy, and will thus be comprised by the general definition. But could waves that not generate foam also lose energy in the same way foam generating waves do? Is there other ways of defining a breaking wave?



Banner and Phillips (1974) suggested a definition of breaking waves: “A breaking wave can be defined as one in which certain fluid elements at the free surface (near the wave crest) are moving forward at a speed greater than the propagation speed of the wave profile as a whole”.

This definition uses the local flow kinematics of the crest compared with the velocity of the wave profile, and is therefore more directly connected to the wave energy. This definition demands neither foam generation nor energy dissipation. However, this will most likely be the consequence when the fluid speed exceeds the crest speed. In the Stokes limiting wave case, the particle velocity at the crest equals the phase velocity (Lamb, 1932). A wave where the particle velocities exceed the phase velocity thus becomes unstable, and will most likely result in the wave turning over, or the wave crest being transformed into foam.

Would this definition of breaking also comprise all cases where there is air entrainment and foam generation, or is it possible for a wave to dissipate its energy without generating foam? Would it be possible that a wave starts generating foam without the fluid velocity at the crest exceeds the wave velocity?

The scope of this thesis is the process of wave breaking, and not applied to any specific field. As this study is using purely deterministic experimental techniques it is not crucial what detection definition is used. For simplicity, breakers are defined as waves that generate foam, or where air is entrained.

When analysing breaking waves it is convenient to have a reference point in space and time called the breaking point. Bonmarin (1989) gave a definition of the breaking point, which will be used here. For typical plunging breakers, the breaking point is the point where the free surface is vertical (see Fig. 6). For typical spilling breakers the breaking point is where the first occurrence of foam appears (see Fig. 10).

1.1.2 Proposed Breaking Criteria

To forecast breaking waves a criterion for when a wave breaks should be connected to a statistical model that predicts the properties of the wave upon which the breaking criterion is based. It is convenient if the breaking criterion is based on a property of the wave that is easily detectable, as this eases the application of the criterion in statistical models. The statistical models used in such forecasts should be based on measurements at sea, because measurements of breaking waves at sea differ from measurements in the laboratory (Tulin and Li, 1992).

Several models for calculating the probability of occurrence of specific wave properties exist, e.g. Myrhaug and Kjeldsen (1984) presented a model for the joint probability density distributions for steepness and asymmetry in deep water waves. Because of the lack of breaking criteria this model is not able to forecast breaking waves, but has been used to predict the probability of occurrence of steep and high waves relevant for capsizing of smaller vessels (Myrhaug and Kjeldsen, 1987; Dahle and Myrhaug, 1996). There is, however, a connection between steepness, asymmetry and the breaking, but no breaking criterion based on these parameters exists.

Tulin and Li (1992) and Ochi (1998) have reviewed the progress towards a breaking criterion, and their findings are summarized in the following.

Stokes limiting wave (regular waves). This criterion applies to regular waves, and is based on analytical work done by Stokes (1849) and Mitchell (1893). The limiting wave is the theoretical steepest wave, and has the following properties: The steepness is $H/gT^2 = 0.027$, the crest has an angle of 120° , and the fluid velocity in the crest is equal to the phase velocity of the wave. It has not been possible to generate a limiting wave in the laboratory, and breaking always occurs for waves less steep than the Stokes limiting wave. Thus this criterion will give to small probability for breaking if it is used in a statistical model.

Limiting steepness less than Stokes limiting wave (irregular waves). Experimental work over the last 25 years has shown that breaking occurs for waves smaller than the Stokes limiting wave. A new breaking criterion based on wave steepness has been derived from laboratory measurements of irregular waves (Van Dorn and Pazan, 1975; Ochi and Tsai, 1983; Ramberg and Griffin, 1987; Bonmarin, 1989): $H/gT^2 = 0.021$. This result has not been confirmed by measurements at sea. Holthuijsen and Herbers (1986) measured the steepness of breaking waves in the North Sea and found a mean value of $H/gT^2 = 0.0067$. From these measurements it was also found that there were small differences in steepness of the waves that break and of those that do not. The wind-speed was in the range 8-12 m/s, and the mean wave height was 1 m during these measurements. Tulin and Li (1992) concluded that steepness can not be used as a breaking criterion due to this. The discrepancies between laboratory and sea measurements have not been explained, but it can be due to several reasons, such as: i) the wind influences the waves at sea so they break earlier; ii) the scale-effects on wave breaking have not been investigated, and this might play an important role; iii) laboratory generated waves will differ from sea waves, although they have identical spec-

tra. This is because sea spectra will be time-varying, while laboratory spectra is stationary.

Figure 3 shows the Stokes limiting wave ($H/gT^2 = 0.027$) together with the findings of Ochi and Tsai (1983) as well as Ramberg and Griffin (1987).

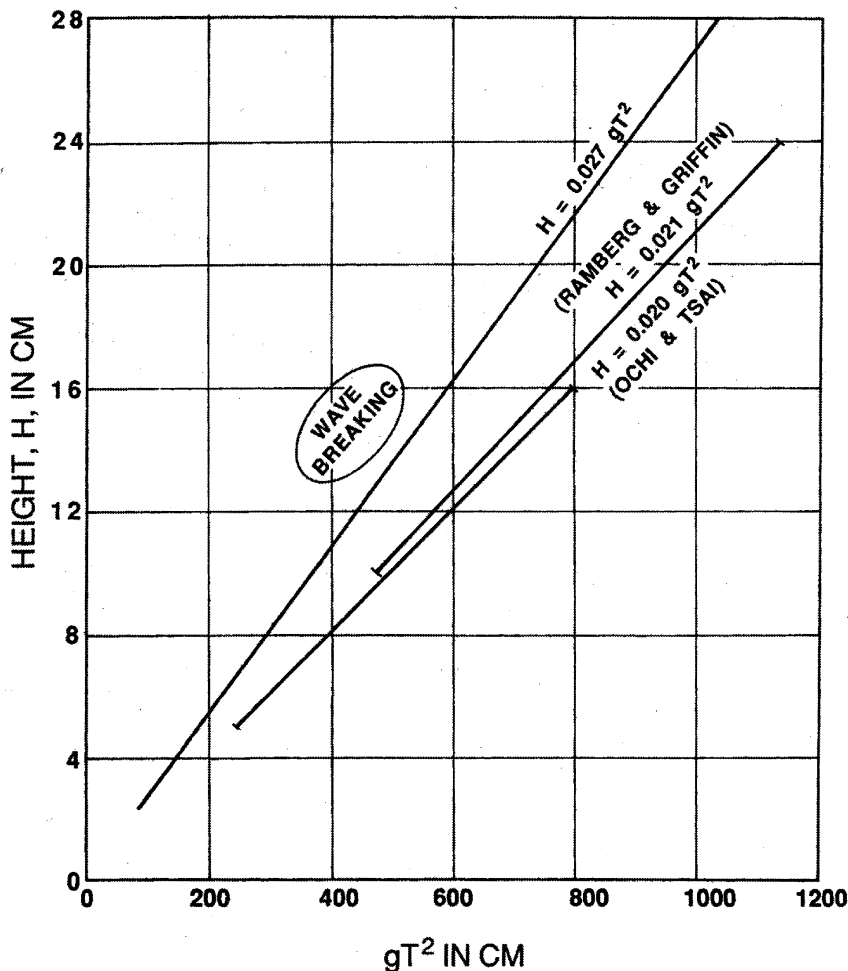
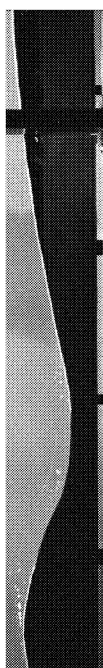


FIGURE 3. Relationship between wave height and periods for breaking irregular waves (adopted from Ochi, 1998).

Limiting crest acceleration. Longuet-Higgins (1969, 1978a, 1978b, 1985) proposed to use the acceleration in the crest as a criterion for breaking. The limit was derived by asymptotic analysis of the flow of a Stokes-like wave. He proposed the value $-0.388g$. This has not been validated by detailed experimental investigations.

1.1 What is a Breaking Wave?

Local steepness and asymmetry. Kjeldsen and Myrhaug (1978) defined parameters that described the local steepness and asymmetry of waves (see *Chapter 3.4.1*). They suggested to use parameters that describe the local mean steepness in the crest and the horizontal and vertical asymmetry of the wave. It has not been possible to find a criterion based on these parameters.

Tulin and Landrini (2000) found from numerical simulation of modulating waves that a well defined criterion for the onset of the initial wave deformation exists: $u_c = c_g$, where u_c is the horizontal particle velocity at the wave crest, and $c_g = d\omega/dk$ is the estimated group velocity of the wave. When a wave crest passes through the peak of a modulation group, and the particle velocity in the crest, u_c , exceeds the group velocity, c_g , the wave will evolve into breaking. Tulin and Landrini also verified this criterion experimentally in the laboratory.

1.2 Importance of Breaking Waves

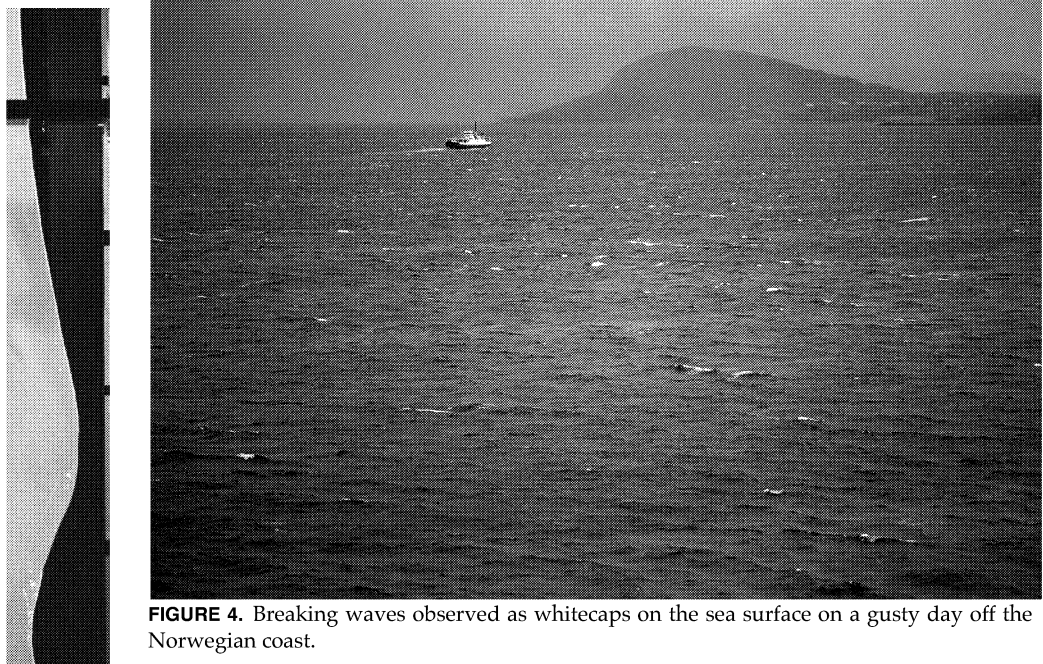


FIGURE 4. Breaking waves observed as whitecaps on the sea surface on a gusty day off the Norwegian coast.

Breaking waves are almost always present at sea. In Figure 4 the breaking waves are identified by the white foam they generate, and such breaking waves are often referred to as *whitecaps*. Whitecaps are very common at sea and play an important role in the sea environment. They have significant influence on the air-sea interaction, by introducing droplets in the air and bubbles in the sea (Thorpe and Humphries, 1980). The bubbles play, among other things, a significant role in the productions of marine aerosol (Resch, 1986) and also affects the gas transfer across the air-sea interface (Memery and Merlivat, 1984). The mixing of the upper sea layer is also influenced by the turbulence created by wave breaking. This mixing is crucial to the transfer of heat and mass and is vital to aquatic life and water quality. On global scale this plays an important role for the Earth's climate, and in the debate on global warming, the CO_2 transfer to the oceans is one factor to consider (Banner and Peregrine, 1993).

Breaking waves also influence the physical process in the oceans, as it is the primary mechanism of wave energy dissipation. The equilibrium in a wind generated sea-state is controlled by wave breaking. It is also the cause of frequency downshift (Tulin, 1996), and is thus important to consider when determining the shape of the sea wave spectra (Phillips, 1985). The dissipation leads to energy being

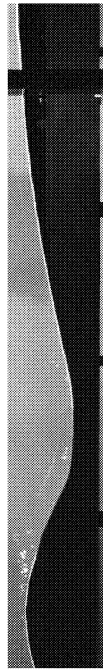
transferred from the waves to current and turbulence (Phillips, 1966). Breaking waves also cause transport of sand and sediments on beaches and erosion near breakwaters (Longuet-Higgins, 1980).

In a given sea-state in deep water, waves break as a result of interaction between waves, current and wind. Breaking is therefore a stochastic process, and some may even argue that it is a chaotic process. Accurate prediction of wave breaking at sea has been impossible. What is easy to predict, however, is that the wave will release much energy when it breaks, and this might have consequences for bodies which are exposed to these events. Many smaller fishing vessel accidents, with no survivors and no wreck, have been explained to be caused by capsizing due to breaking waves. It has been concluded that for ships lost in the Norwegian coastal waters breaking waves are frequently responsible for capsizing (Myrhaug and Kjeldsen, 1984). In capsizing accidents with survivors, the crew has reported a breaker hitting the side of the boat, causing sudden large roll angles and trapping the crew inside the vessel (Myrhaug and Dahle, 1994; Dahle and Kjærland, 1980). The only possible evacuation is directly into the sea, with few chances to use life-saving devices.

Whole communities can also be destroyed by this powerful natural phenomenon. For the people living on Japan's Sanriku coast that was the case on the evening of Friday June 26, 1896 (Mooney, 1993). A tsunami wave came from the Pacific Ocean. The tsunami waves are potentially the most catastrophic of all ocean waves, and are caused by seismic activity on the sea bottom. Very long waves are generated with a wave length as large as 200 km, travelling with a speed of 720 km/h (200 m/s) (Garrison, 1993). The origin of these waves is usually very far off at sea. In deep water the height of a tsunami is usually less than 1m, and from a boat it may even be difficult to discover. As the wave approaches the coast, it transforms due to the influence by the bottom. When reaching the shore the wave height may be as large as 35m, and as the wave breaks it releases its energy with devastating consequences. The villages on the Sanriku coast were washed away when the 30 m high wall of water hit the coast. 27.000 people lost their lives, and more than 10.000 houses were destroyed. The fishermen who had set out in their boats early in the evening had not even noticed the tsunami when it passed under their boats, and when returning the next morning they found their villages destroyed.

The motivation for studying breaking waves is to increase the knowledge of the phenomenon. Thereby we are in better position to establish safety for life and structure at and by the sea. Furthermore, knowledge of breaking waves are also important for oceanographers, marine biologists, environmental scientists and seafarers. They use

information on breaking waves in their work on climate, aquatic life, water quality, pollution spreading or navigation.



1.3 Description of Breaking Waves

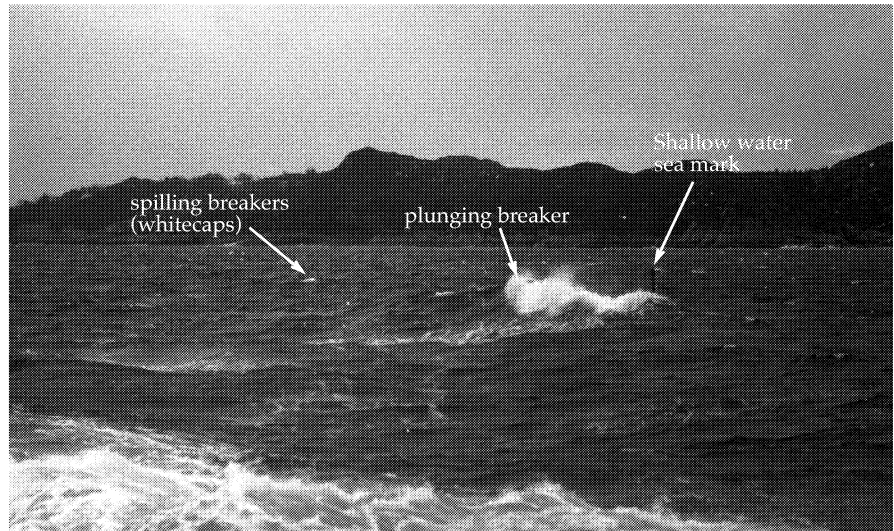


FIGURE 5. A gusty day on the west coast of Norway, near Kristiansund. In the foreground a plunging breaker overturns and break due to a submerged shoal (the shallow water sea mark). In the background several spilling breakers (whitecaps) can be observed. See also Figure 2.

There exists several different types of breaking waves; spilling, plunging, bore, surging, pyramidal etc. In this thesis breaking waves in deep water is considered, and the most common breaker in deep water is the spilling breaker. The plunging breaker occurs also in deep water, but less frequent than the spilling breaker. A brief review of these two types of breaking waves will be given in the forthcoming.

1.3.1 Plunging Breakers

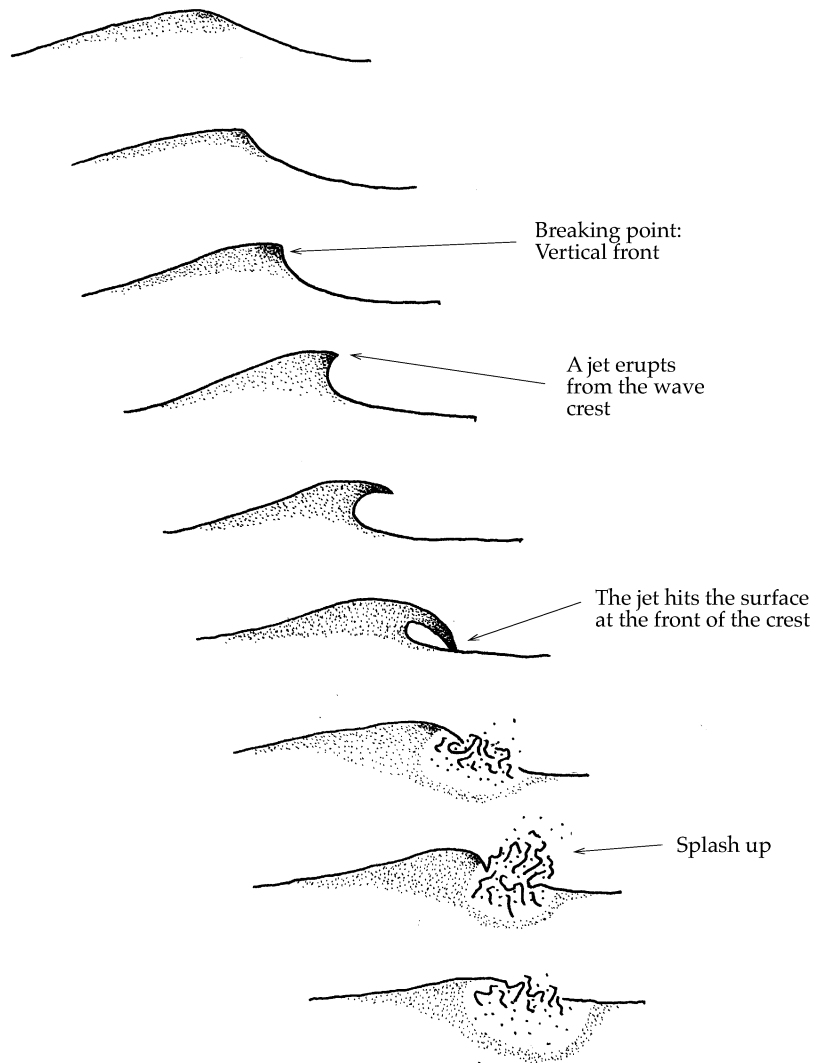


FIGURE 6. The evolution of a plunging breaker.

Although plunging breakers appear on deep water they are mostly associated with beaches. Plunging breakers are energetic breakers, characterized by a jet erupting from the wave crest at break-

ing onset. In the pre-breaking phase¹, before the jet erupts, the wave steepens and the crest moves forward, making the wave asymmetric as the front becomes steeper than the rear (see the first frame in Fig. 6). The velocity in the crest increases until it exceeds the phase velocity, and the jet erupts from the crest front. Air may be entrained when the jet leaves the crest, or when it hits the front face of the wave approximately at the mean water line position (see Fig. 7). This creates turbulence that dissipates much of the wave energy, and most of the wave motion vanishes. At this stage a considerable amount of air is entrained in the water.

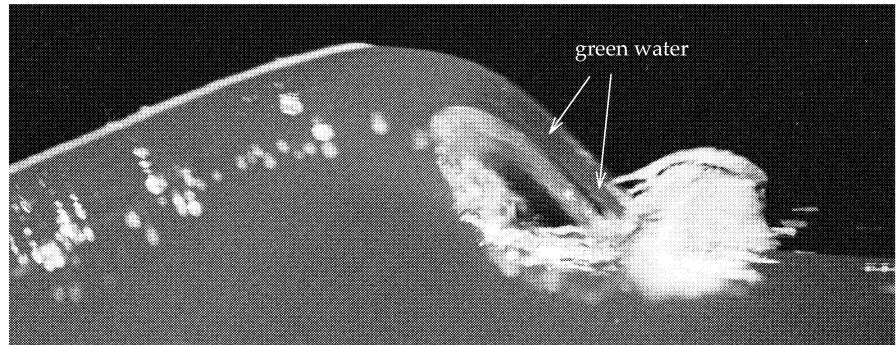
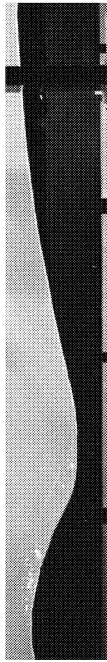


FIGURE 7. The jet from a plunging breaker is seen as it hits the front face of the wave, generating the splash-up of water. As observed the jet consists of green water, and the air is entrained as the jet hits the surface.

Bonmarin (1989) studied experimentally the geometry of a plunging breaker in detail, and gave a qualitative description of the *post-breaking* phase. He also measured the time evolution of several parameters describing geometric features of the wave towards, at and after breaking. Figures 8 and 9 show some of his results.

-
1. The breaking process is usually divided into three phases, and the characteristics of the breakers in each phase are discussed. This way to quantify the breaking process has been used by several authors, e.g. Kjeldsen and Myrhaug (1978), and is convenient as similarities and differences between breakers are easier identified considering part of the process instead of the whole. The phases are as follows
 - i) *pre-breaking*; deformation of the wave up to the start of breaking
 - ii) *breaking onset*; transition from the unbroken wave to a breaking wave.
 - iii) *post-breaking*; deformation of the wave after the breaking has started.

1.3 Description of Breaking Waves

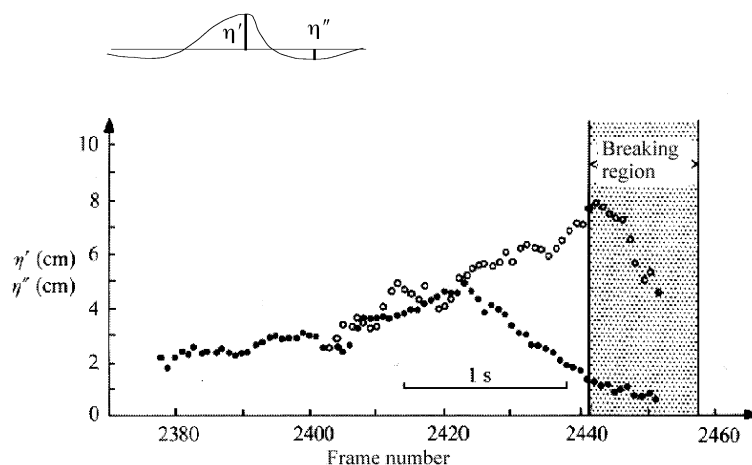


FIGURE 8. Time evolution of the crest elevation, η' (°), and the trough depth η'' (•); frame frequency, 24 f/s (from Bonmarin, 1989).

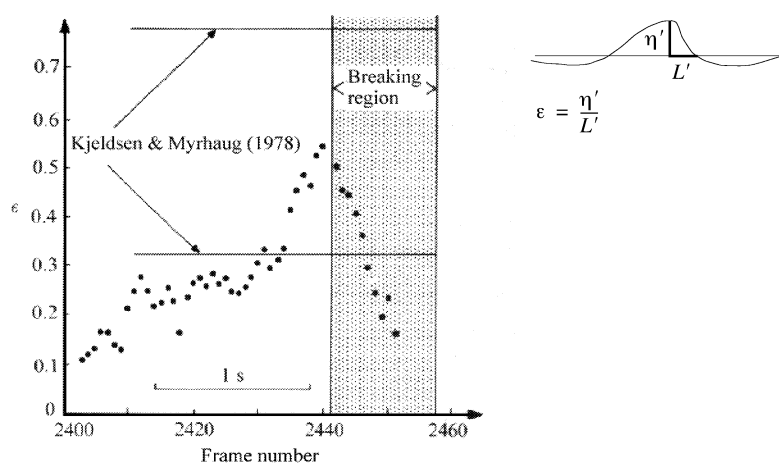
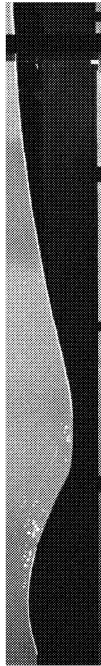


FIGURE 9. Time evolution of the crest front steepness; frame frequency, 24 f/s. See *Chapter 3.4.1* for a more detailed description of the parameter (from Bonmarin, 1989).

From Figure 9 one can see that the crest height increases, and the trough depth decreases as the wave approaches breaking, and thus the wave becomes horizontally asymmetric. This is similar to what happens to a Stokes wave as it steepens, and indicates that the wave becomes more and more non-linear. It can also be interpreted as a set-up of the local wave geometry relative to the still water line. Figure 9 shows that the steepness of the crest front suddenly increases just before breaking. This is connected to the increase in vertical asymmetry, i.e., the shifting of the water in the crest towards the front.

The shape and size of the jet for waves with a wavelength shorter than 2 m are influenced by the surface tension effects (Tulin and Landrini, 2000). The jet is considerably rounded and weakened for waves with a length of 1m, and for waves between 25 and 75 cm the jet does not appear at all. For these short waves (microbreakers), the jet is replaced by a bulge growing out of the wave crest.



The internal kinematics of plunging breakers have been investigated both experimentally and numerically by different authors. Skyner (1992) measured the kinematics of a plunging breaker with the means of PIV, and compared those results with numerical calculations done with a boundary integral method (Dold and Peregrine, 1986). He concluded that the agreement between the numerical method and the measurements is good, and thus that the internal kinematics can be predicted by a numerical model (at least until air is entrained). Skyner (1992) also presented measurements of velocities under the crest when the wave starts to become asymmetric, through the breaking onset, and well into the post-breaking phase. Numerical calculations of the velocity field have also been conducted by Longuet-Higgins and Cokelet (1976), Cokelet (1978) and Vinje and Brevig (1980).

1.3.2 Spilling Breakers

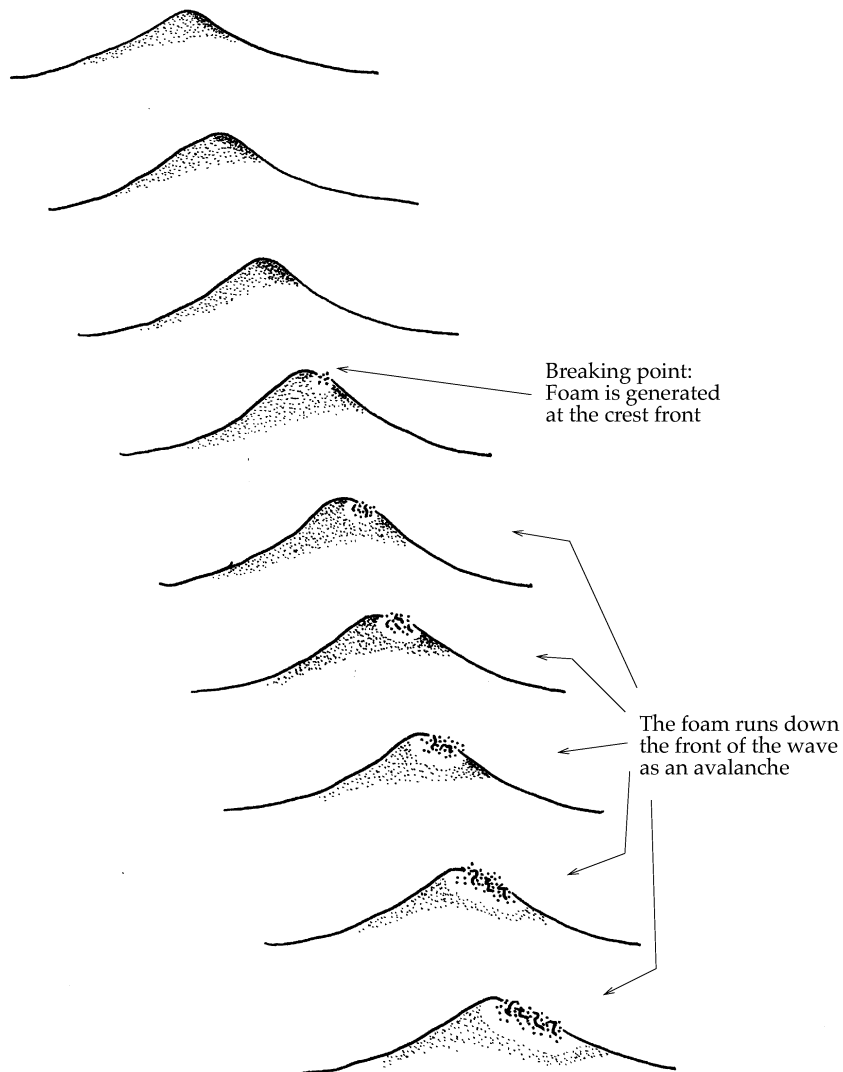


FIGURE 10. The evolution of a spilling breaker.

In deep water the most common type of breaking waves is the spilling breaker, or *whitecaps*. Spilling breakers are characterized by the occurrence of foam on the front face of the wave in the vicinity of the crest. This foam “rolls” down the front of the wave, strikingly similar to a *snow avalanche on a mountain side* (Duncan et al., 1994), as the wave travels forward (Fig. 10). The spilling breaker is more enig-

matic than plungers regarding the foam generation; it just appears on the crest front, and runs down the front face of the wave.

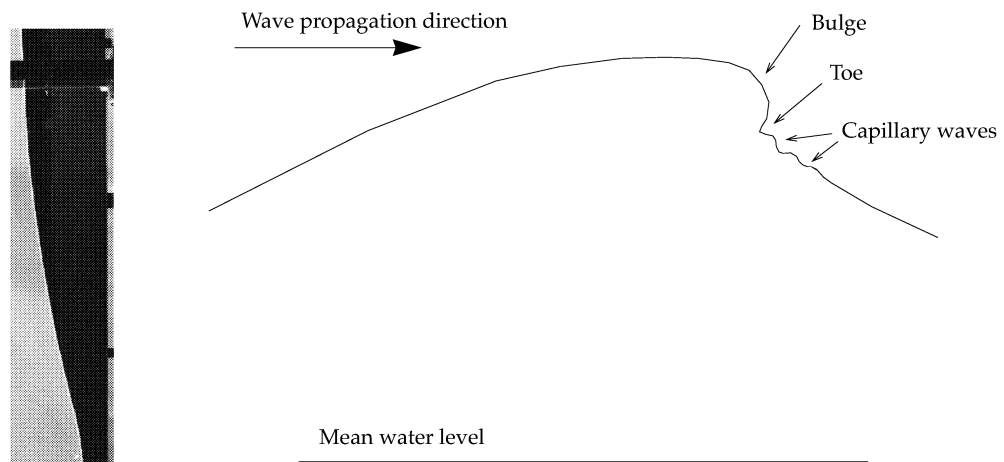


FIGURE 11. Wave shape and nomenclature of a spilling breaker (Reproduced from Qiao and Duncan (2001)).

New et al. (1985) studied the overturning phenomenon numerically, and calculated the development of the crest. After having examined several waves with different size of the overturning jet relative to the wave length, they found that the geometry of the jet was similar for all the waves studied. They concluded that this might indicate that the spilling breaker is initiated by a small scale turnover, that in turn initiates the foam generation. Longuet-Higgins et al. (Longuet-Higgins, 1994; Longuet-Higgins and Cleaver, 1994; Longuet-Higgins et al., 1994) found that the crest of a steep irrotational gravity wave is unstable. Due to this instability water near the crest is shifted towards the forward face of the wave. A bulge is then formed on this location (see Fig. 11). Duncan et al. (1994) found experimentally that on the toe of this bulge capillary waves were formed, which in turn creates foam. Qiao and Duncan (2001) made detailed measurements of the flow field in this bulge in the crest of a spilling breaker. They found that there were no vorticity, or no evidence of a recirculating region under the bulge during the initial phase of the breaking process. A short time after the bulge first appeared, it started to move down the front of the wave. In this phase large particle velocities (1.4 times the crest speed) was measured in the area.

Spilling breakers can thus be initiated without the presence of a micro-scale turnover. This leads to the conclusion that the breakers initiated by capillary waves, and those initiated by a microscale turn-

1.3 Description of Breaking Waves

over are distinctly different types of breaking waves. Should capillary breakers be classified as spilling, and overturning breakers as plunging? This would be the result if classification of breakers purely was based on what happens on breaking onset. However, when classifying waves it has been more usual to classify them from what happens in the post-breaking (and pre-breaking), than the breaking onset. The size of the overturning relative to the wave highly influences the post-breaking scenario, i.e. small overturning yields post-breaking similar to a breaker that is initiated by capillary waves. These waves are usually called spilling breakers, and the breakers that create a significant splash-up in the post-breaking phase are called plungers.

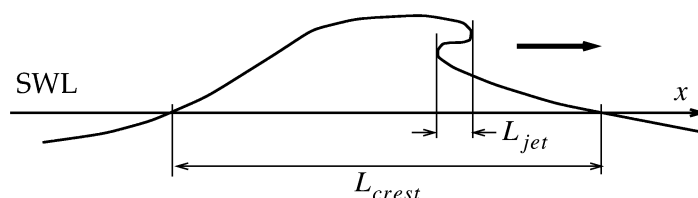


FIGURE 12. Dimensions used to assess the size of the turnover.

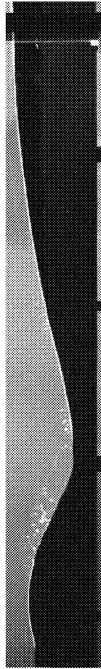
To assess what is a small turnover yielding a spilling breaker, and what is a big one resulting in a plunging breaker, the parameter $S_{jet} = L_{jet}/L_{crest}$ can be used. L_{jet} and L_{crest} are shown in Figure 12. The measurements are done when the underside of the overturning crest becomes horizontal. New et al. (1985) classified several overturners based on the overall asymmetry of the wave into plunging breakers and spilling breakers. From their work the following is derived:

$$\begin{aligned} \text{Plunging breaker:} & \quad S_{jet} > 1/10 \\ \text{Spilling breaker:} & \quad S_{jet} < 3/100 \end{aligned}$$

In the pre-breaking phase a spilling breaker resembles a steep Stokes wave with a higher crest and a shallower trough. The wave is also slightly vertically asymmetric. The particle velocity at the crest increases up towards breaking, being equal to, or larger than the phase velocity at the inception of breaking.

The post-breaking phase of a spilling breaker is different from a plunging breaker in the sense that the breaking happens over a period of time resembling an avalanche, whereas for the plunger the breaking is more similar to an explosion, leaving the pre-breaking turbulent zone as a debris. The original wave motion survives to a much larger extent the spilling than the plunging event. Tulin and Coite (1986) investigated the spilling breaker and made a model

where the breaker was envisaged as an essentially stagnant eddy kept in position by the turbulent shear stresses acting on the streamline which divides the breaker and the underlying flow. Apart from this, not much work has been done on the internal kinematics of the spilling breaker. The spilling breaker problem can not be solved using potential theory, as the initiation of the foam generation in a spilling breaker is due to viscous and capillary forces.



1.4 About this Thesis

This thesis is an experimental investigation of 2D¹ deep water² breaking waves. Three different cases of breaking waves are studied; a plunging breaker, a spilling breaker, and an intermediate breaker, and the geometry and kinematics of the waves are measured.

The motivation for doing this is to get better knowledge of the coupling between the geometry and the kinematics of steep and breaking waves. This is useful when loads from breaking waves are estimated from wave geometry measurements, or in the pursue of a breaking criterion. If we want to be able to predict wave breaking, we need firstly a criterion for when the wave will break, and secondly a statistical model for when the event leading to breaking will occur. The statistical model must be based on field measurements done in the area where breaking is to be predicted. The field measurements that are easiest to conduct are time domain measurements of the wave geometry, carried out with wave buoy, laser or radar. The breaking criterion should therefore be based on the time domain geometry of the wave. In order to find such a breaking criterion it is useful to know as much as possible of the coupling between the geometry, and kinematics of the wave.

In *Chapter 2* the experimental setup for measuring the wave kinematics is described. The method of *Particle Image Velocimetry* (PIV) is applied for this purpose. In the end of *Chapter 2* an alternative way of

-
1. In a real seastate most breaking waves have three-dimensional features. This may be due to interaction between waves, current and/or wind of different directions. However, in this thesis these effects are not considered, and only waves that are two-dimensional are studied.
 2. *Deep water* breaking waves are often used to characterize wave breaking where the breaking is not a consequence of interaction with the bottom, but rather is a consequence of wave, current and wind interaction. A breaking wave can, however, be influenced by the bottom, as long as this is not what generates the breaking, and still be characterized as a *deep water* breaking wave. For the three wave cases studied in this thesis both the plunging and intermediate breakers are affected by the bottom. Both are still considered to be deep water breaking waves as the breaking events are due to wave-wave interaction.

presenting kinematics measurements through a set of parameters are presented, and this method is used in the later analysis.

Chapter 3 describes the methods used to measure the geometry of the wave. This comprises both space and time domain geometry. Parameters describing the geometry of steep and asymmetric waves are described in the end of *Chapter 3*, and both existing and new parameters are used in the analysis.

Both the kinematics and geometry measurements are presented and discussed in *Chapter 4*, and possibilities for further work on the subject are presented in *Chapter 5*.

1.4.1 Case Description

The three cases examined in this thesis are: A typical plunging breaker, a typical spilling breaker and an intermediate breaker. The intermediate breaker is a breaker that is initiated by a microscale plunging event, but has a post-breaking phase similar to the spilling breaker. The three cases are shown in Figures 13 to 15, and the method used to generate the breakers are as follows.

- **Case 1: a plunging breaker** (Fig. 13). The plunging breaker was generated from a Pierson-Moskowitz wave spectrum with peak frequency of 0.6Hz. The energy in the wave spectrum was focused using the method of phase focusing (see e.g. Longuet-Higgins, 1974; Kjeldsen and Myrhaug, 1979) to generate a breaking event 6.75m from the wave generator.
- **Case 2: an intermediate breaker** (Fig. 14). The intermediate breaker was generated using the same method as for the plunging breaker, but with peak frequency 0.9Hz.
- **Case 3: a spilling breaker** (Fig. 15). The spilling breaker was generated due to the increase in wave height when the individual wave crests reaches the front of a wave group (Longuet-Higgins, 1974). The wave group was single harmonic, with frequency 1Hz, and an initial wave height 14.3cm. The initial steepness of the waves was $H/L \approx 1/11$.

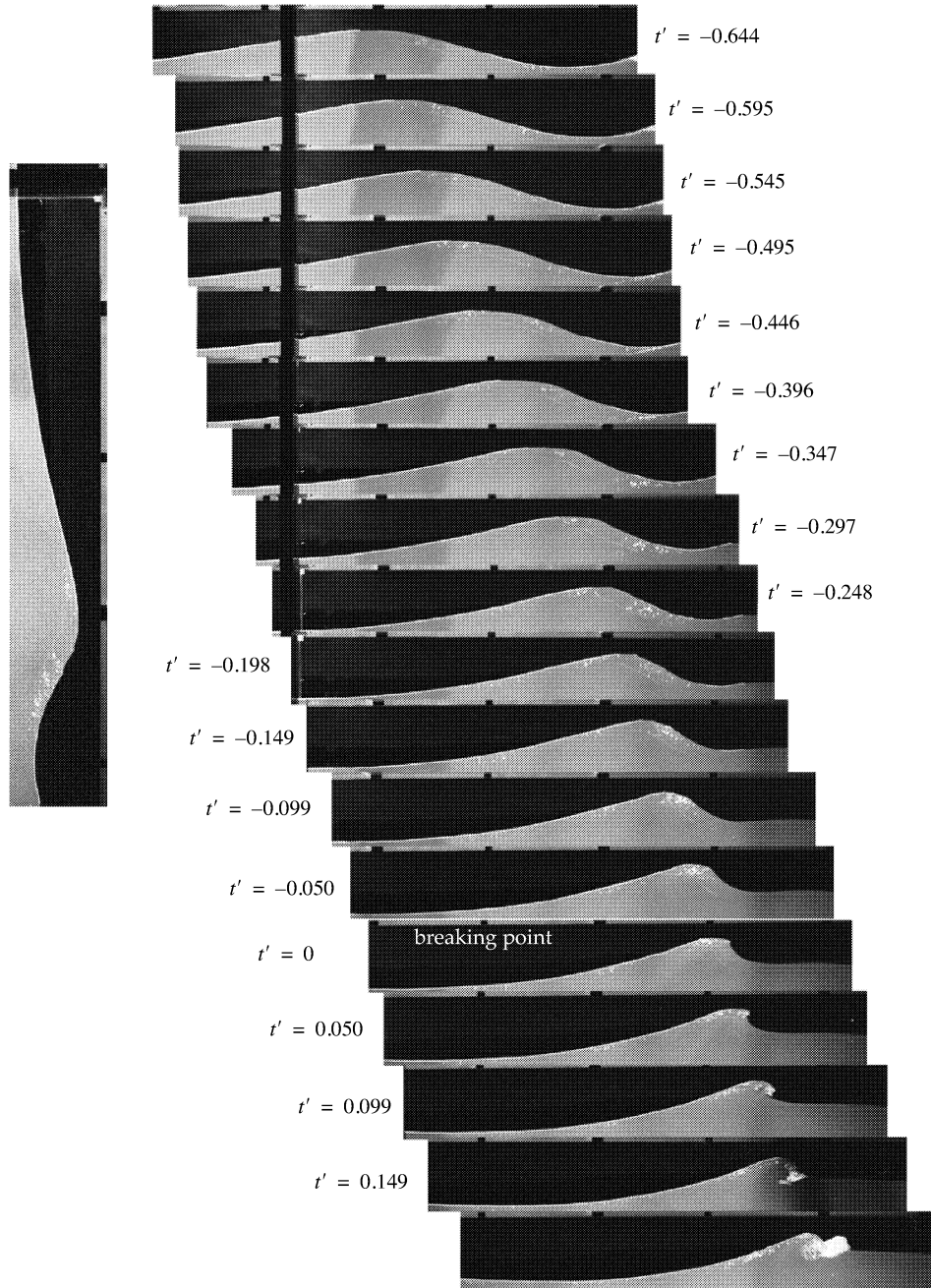


FIGURE 13. The plunging breaker (case 1). Time between each exposure is $1/16s$. The normalized time t' is explained in *Chapter 2.9.2*.

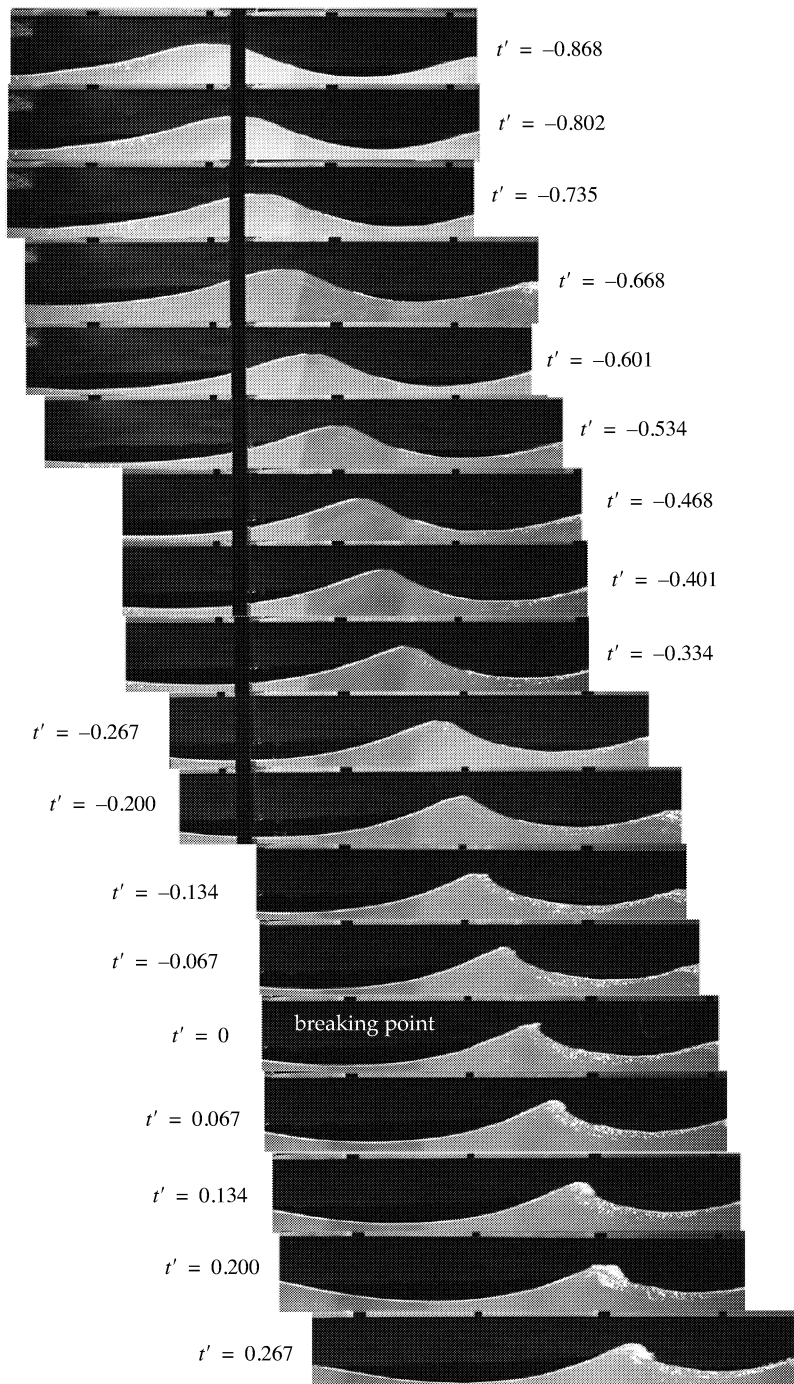


FIGURE 14. The intermediate breaker (case 2). Time between each exposure is $1/16$ s. The normalized time t' is explained in *Chapter 2.9.2*.

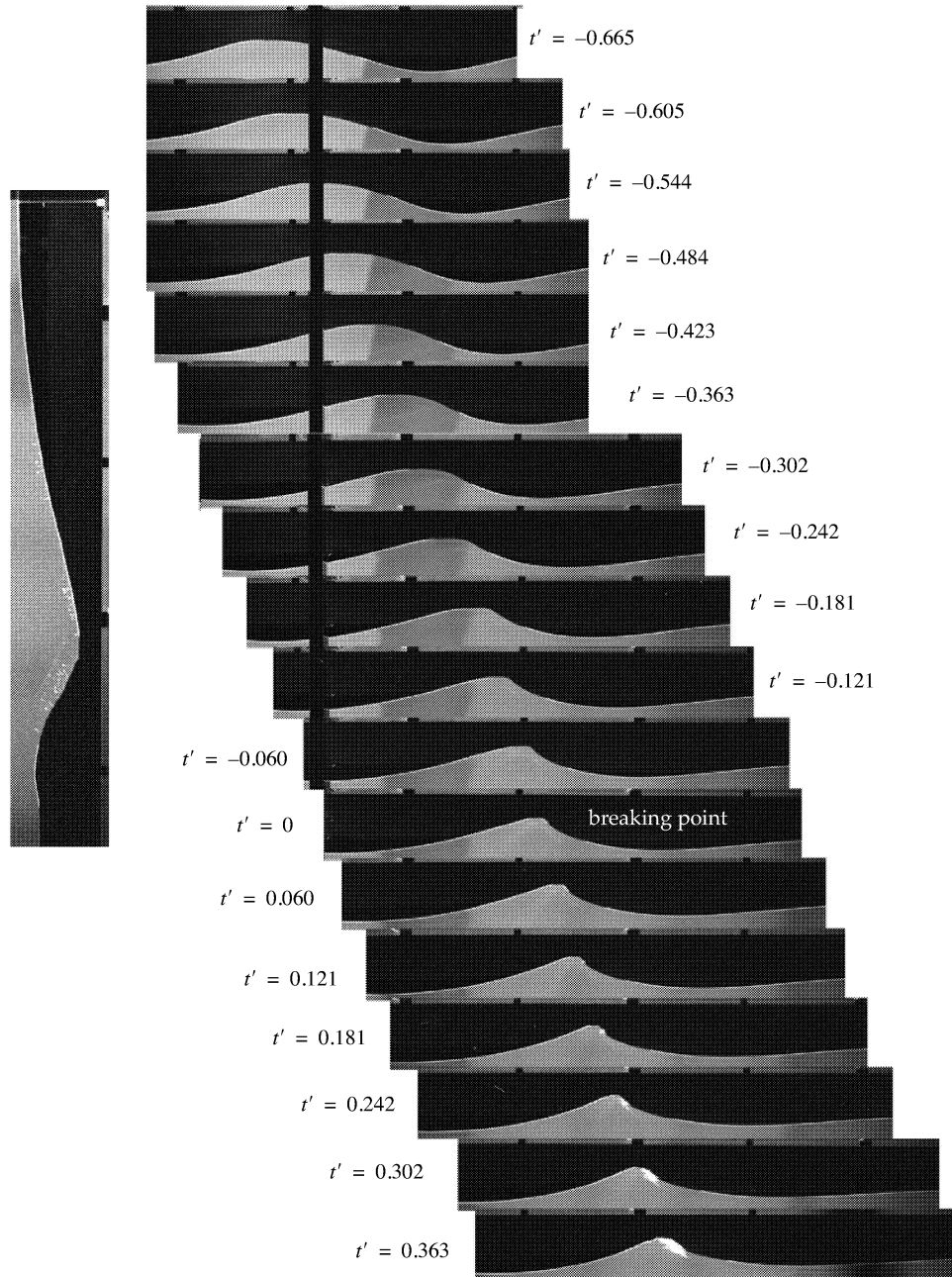


FIGURE 15. The spilling breaker (case 3). Time between each exposure is 1/16s. The normalized time t' is explained in *Chapter 2.9.2*.

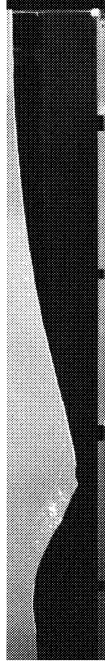
1.5 Chapter Summary

In this chapter it has been discussed what a breaking wave is, and the definition of breaking has been adopted saying that a breaking wave is a wave that generates foam, or where air is entrained.

Breaking criteria proposed by other authors have been reviewed, and none of these criteria give a unique quantification for when a wave will break. Further, the importance of breaking waves in biological, environmental, oceanographic and ocean engineering applications have been summarized. The major part of the earth is covered with water where breaking waves may occur. In this context the impact and significance of breaking waves emphasize the importance of establishing knowledge of the phenomenon.

Relevant selected work done by other authors describing and analysing the breaking phenomenon has been reviewed.

Finally in this chapter the three wave cases that are investigated in this thesis are presented, and the methods used to generate these waves are described.



Chapter 2 **Measuring Wave Kinematics: Particle Image Velocimetry (PIV)**

The fluid velocity is desirable to measure for several aspects of hydrodynamics and fluid dynamics. For instance, basic experiments on measurements of flow velocities can be essential to obtain full understanding of the physics of a fluid process. Measurements of the fluid velocity is also important when e.g. evaluating computer algorithms developed to simulate fluid dynamic processes. For a complete verification of the code the flow velocity is often required.

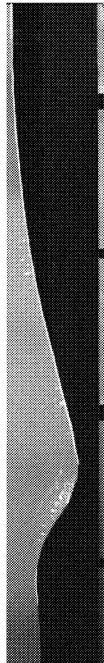
Several methods for measuring fluid velocity have been developed. Among these are hot-wire and hot-film anemometers making use of the fact that heat transfer rate between the hot-wire/film and the fluid is dependent on the velocity (Holman, 1994). These methods have a drawback as the probes are disturbing the flow, causing the measurements to be inaccurate. The same is the case for sonic measurement techniques as they also require a probe in the fluid. The development of Laser Doppler Anemometry (LDA) in 1966 made it possible to measure the velocity without affecting the flow, and this method has been used extensively in many fields of flow research. LDA uses tracer particles in the fluid, and measures the velocity of these particles. The velocity is measured from the Doppler shift in the light scattered from the particles. The particles are assumed to follow the flow, and the type of particles has to be carefully selected to accomplish this. The hot-wire/film and the LDA methods have in common that they measure the velocity at a given geometrical point as a function of time, but are incapable of measuring whole flow fields instantaneously. In many cases it is useful to measure and visualize the complete velocity field when e.g. studying the vortex shedding behind a cylinder or the internal kinematics of a breaking wave. To do this with LDA, the probe has to be moved, and multiple meas-

urements taken. This is very time consuming, and can only be done where total repeatability is possible.

Measuring the whole flow field involves recording large amount of data at the same instance. The best way to do this is by using image analysis. With an ordinary camera it is possible to record as much as several hundred Mbytes¹ of data at a fraction of a second, and it is possible to capture enough information to record a complete flow field. There exists several slightly different methods that use image analysis to measure velocities. Common to all of them is that small particles are introduced in the flow, and that a camera capture images of the tracer particles as they follow the flow. The velocity field is then computed from analysis of the images. These methods are called Particle Image Techniques, and are described by Adrian (1991). The Particle Image Velocimetry (PIV) is a branch of these methods, and has been widely used in fluid dynamic research applications over the last two decades.

In this chapter the general principle of PIV will be explained, and the particular PIV system used in this work will be described. There exists PIV systems that can measure three component velocities in a three-dimensional field, but here only 2D velocity fields are considered, and therefore 3D PIV systems will not be discussed². The system implemented as a part of this work is very similar to the one developed at the University of Edinburgh, and a description of that system is given by Greated et al. (1992) and Quinn et al. (1994).

First, however, we start with a description of the laboratory facility.



2.1 Laboratory Facility

The experiments were conducted in the wave laboratory at the *Department of Marine Hydrodynamics, NTNU*. The laboratory was built as a part of this work, and the design and construction process, as well as development of measurements and analysis routines have been a major part of the work. The department had no prior experience with quantitative optical measurement techniques, and new routines had to be established and developed for the laboratory. Contact was early established with *The Fluid Dynamics Group at The University of Edinburgh*, where they operate a similar experimental facility. The

1. One A4 sheet of paper filled with text contains approx. 32 Kbytes of data.

2. For references on 3D PIV see: Brücker (1996), Royer and Stanislas (1996) among others.

2.1 Laboratory Facility

design and construction of the flume as well as the establishment of the PIV system were done after taking into account their experiences on the subject. This has been of great help. However, their setup was not duplicated without critically considering possible improvements.

For all empirical/experimental work the cost is an issue. Experimental facilities and equipment are expensive, and it is always possible to improve the measurements by purchasing better (and more expensive) equipment, or by spending more time developing better equipment. However, time and money are limited, and a trade-off must be made between the desire to increase the accuracy of the results and the resources available. When considering some of the experiments in retrospect, several improvements are obvious, but due to the limiting resources it was not possible to redo the experiments. When describing the experimental environment comments will be made to where these improvements could be done.

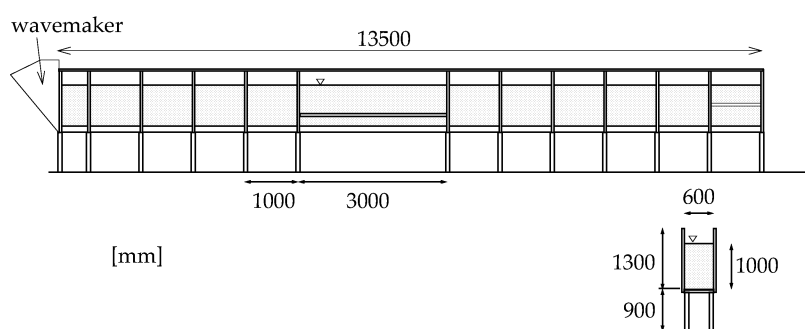


FIGURE 16. The narrow wave flume at the wave laboratory, the *Department of Marine Hydrodynamics, NTNU*.

Figure 16 shows the wave flume where the experiments were conducted. The wave flume is 13.5m long, 1m deep and 0.6m wide.

The flume was built mainly with the use of optical measurements techniques in mind. 19mm glass was therefore used in both sides and in the bottom to give good viewing access and good conditions for optical measurements and visualisation. Glass is a good material to use in wave flumes, as it demands only minor maintenance. The glass was supported by a steel structure designed to be strong enough to withstand the static pressure of fluid when the flume was filled, and also stiff enough to prevent vibrations due to the dynamic pressure.

It was desirable that the flume was flexible with respect to possible experimental setups. The flume should therefore be as deep as possible. When the depth increases, the possible length of unsupported glass sections decreases. One meter water depth allowed us to

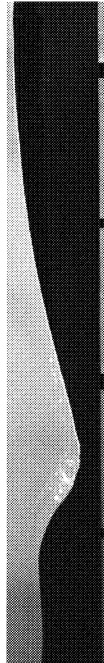
have one meter glass sections, without extra support. This was found sufficient. One meter sections were used, with a three meter long glass section in the middle of the flume to allow possible observation of a full wave length. In this section an extra supporting beam had to be placed 40cm above the bottom due to the limitation in the glass strength.

The length was basically a question of price, and we built it as long as could be afforded. The flume is located in a space where it is possible to lengthen it, as this was considered as a possibility in the future. The location of the flume also makes it possible to, in the future, add current and wind generation.

The decision on the width was made based on a compromise between the desire to make it as wide as possible, and the cost of the wavemaker. In a wider flume it would also be more likely get unwanted 3D effects. On the other hand, a wider flume would give better conditions for 3D experiments, e.g. with physical models. With a width larger than one meter standing waves across the flume would be more likely to occur, as their natural frequency lies in the frequency range mostly used in the experiments (around 1 Hz). This would call for a multi-flap wavemaker capable of removing these waves, and the price would be more than doubled.

The flume is elevated 90cm above the floor level making it possible to position measurement equipment, and viewing aids underneath the flume. This was especially made with the installation of a PIV system in mind, which requires the positioning of the illumination source¹ underneath the flume. A platform on rails was designed for this purpose so that the illumination source could be placed at any position under the mid section of the flume. High power lamps were also installed under the flume as a light source for photographing the wave geometry².

At the end of the flume, occupying the last two meters, a wave absorption device was made from vertical wedge shaped foam rubber. This configuration proved not to be optimal. However, as the wave events examined in this thesis is so limited in time that reflections do not reach the measurement area until after the measurements are finished, no time was spent on optimising the wave absorber. The main reason why the wave absorption device does not perform satisfactorily is believed to be the use of foam rubber for the wedges. The same geometrical configuration, but with different material has been applied elsewhere³ with good result.



1. See *Chapter 2.4*.

2. See *Chapter 3*.

3. *Fluid Dynamics Group, The University of Edinburgh*.

The wavemaker installed in the flume is an electronically operated, computer controlled, single flap. The flap is hinged 10 cm above the bottom, and has a water line depth of 90cm. The wavemaker was made by *Edinburgh Design Ltd.*, and especially fitted to this flume.

Some images showing the wave laboratory can be found in *Appendix D*.

2.1.1 Assessment of the Wave Flume Repeatability

The camera system used here was unable to take pictures with as short intervals as required (30 ms). The picture series of the wave events were for this reason produced by running the wave multiple times, and then shifting the camera trigger time the desired interval between each subsequent run. Time domain measurements at different locations were conducted in the same way as only two wave gauges were available. This demands a high degree of repeatability, and to assure that this was the case, a repeatability test was conducted. Fifteen subsequent runs were done with the same wave case (CASE 2¹). Measurements were taken with wave gauges at two different positions in the flume ($x = 4\text{m}$ and $x = 8.5\text{m}$). The sampling frequency was 16hz. Due to zero level drift all the time series had non-zero mean, and this was adjusted by subtracting the mean value, producing zero-mean time series.

The mean and standard deviation of the wave elevation and the spectral density are shown in Figure 17, and the repeatability can be assessed from the figure. The wave elevation standard deviation has an average of 0.06cm at $x=4\text{m}$, and 0.13cm at $x=8.5$ without considering the zero start phase. This corresponds to approximately 0.3% of maximum wave height for $x=4\text{m}$, and 0.8% for $x=8.5\text{m}$. The maximum standard deviation is 1% (for $x=4\text{m}$) and 2% (for $x=8.5\text{m}$) of the maximum wave height. From the spectral density it can be seen that the inaccuracy is distributed equally over the frequency interval.

1. See *Chapter 1.4.1*. CASE 2 was chosen on random.

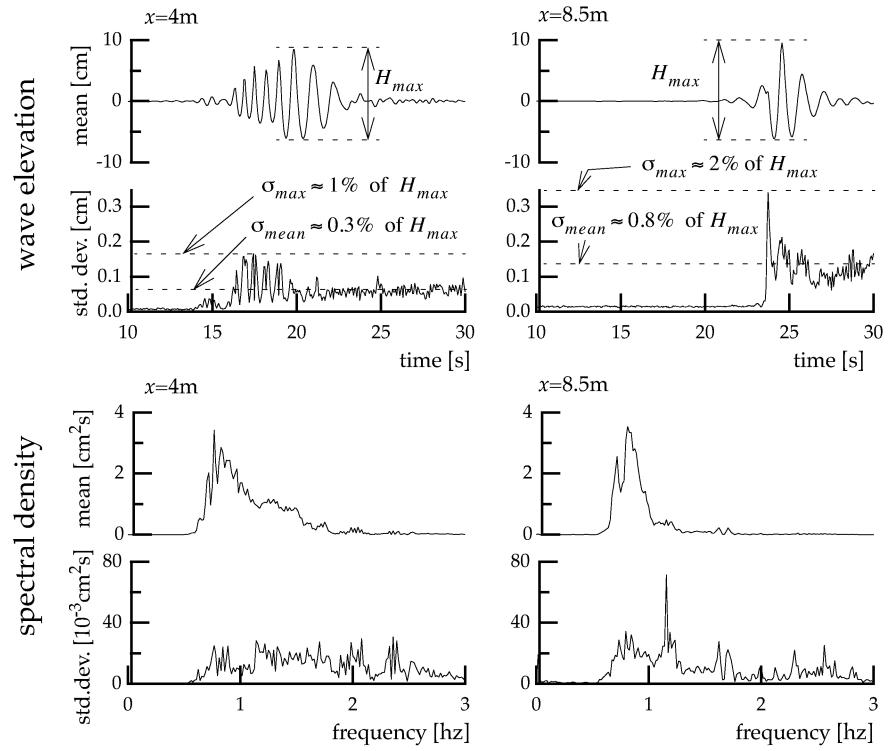


FIGURE 17. Wave elevation measurements at $x=4\text{m}$ and $x=8.5\text{m}$ in the wave flume used for assessment of the repeatability. Fifteen subsequent runs were done in each position, and the mean and standard deviation were found (the two top figures). The spectral density was also found from each of the runs, and the mean and standard deviation computed (the two bottom figures).

2.2 Principle of PIV

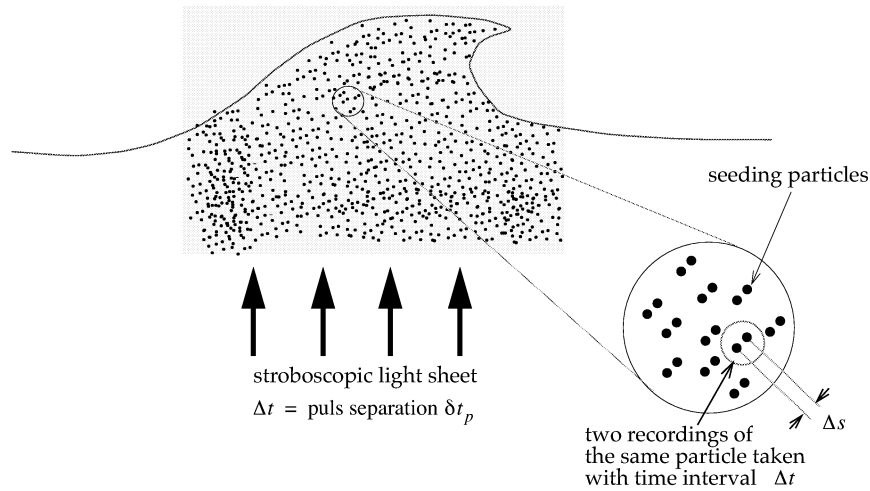


FIGURE 18. PIV principle.

The principle of PIV is to measure the distance, Δs , seeding particles in the fluid move during a time interval, Δt . The velocity, U , is then calculated from:

$$U = \frac{\Delta s}{\Delta t} \quad (1)$$

It is assumed that the seeding particles follow the flow, and that the velocity of the particles is equal to the velocity of the fluid (the validity of this assumption will be addressed in *Chapter 2.3*). The particles are illuminated by a stroboscopic light source, and a camera is used to capture images of the fluid with the illuminated particles. Δt is equal to the time between each light pulse, δt_p . The camera records the position of the particles for each light pulse, and at least two pulses must be recorded. Δs is the distance between the two recordings (see Fig. 18).

There are two different modes of recording/analysing the images. The camera can record several pulses (multiple exposures) on the same image, or it can record two images with one exposure on each. The two modes are called auto-correlation mode and cross-correlation mode, respectively, and are explained in Figure 19. In this work only the auto-correlation mode is used.

Even though PIV in principle is a very simple method, the implementation and usage are not that simple. A wide variety of parameters such as shutter speed, aperture, particle diameter, scan-

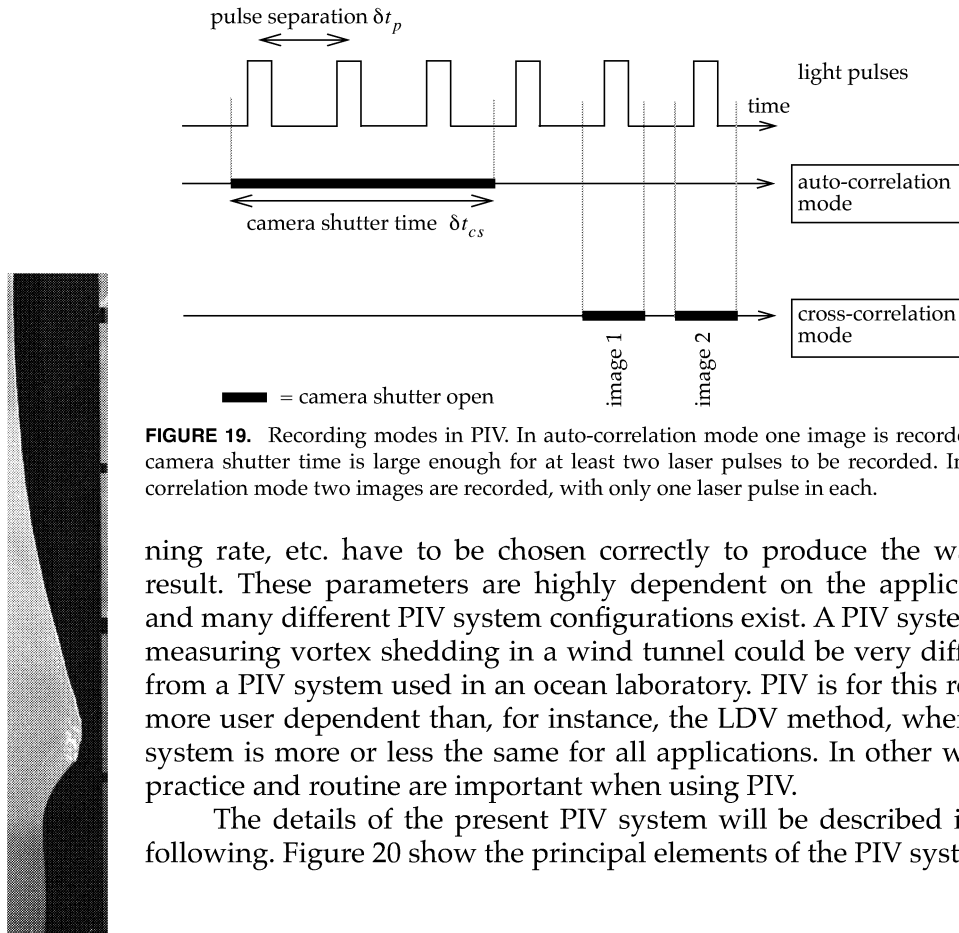


FIGURE 19. Recording modes in PIV. In auto-correlation mode one image is recorded. The camera shutter time is large enough for at least two laser pulses to be recorded. In cross-correlation mode two images are recorded, with only one laser pulse in each.

ning rate, etc. have to be chosen correctly to produce the wanted result. These parameters are highly dependent on the application, and many different PIV system configurations exist. A PIV system for measuring vortex shedding in a wind tunnel could be very different from a PIV system used in an ocean laboratory. PIV is for this reason more user dependent than, for instance, the LDV method, where the system is more or less the same for all applications. In other words, practice and routine are important when using PIV.

The details of the present PIV system will be described in the following. Figure 20 show the principal elements of the PIV system.

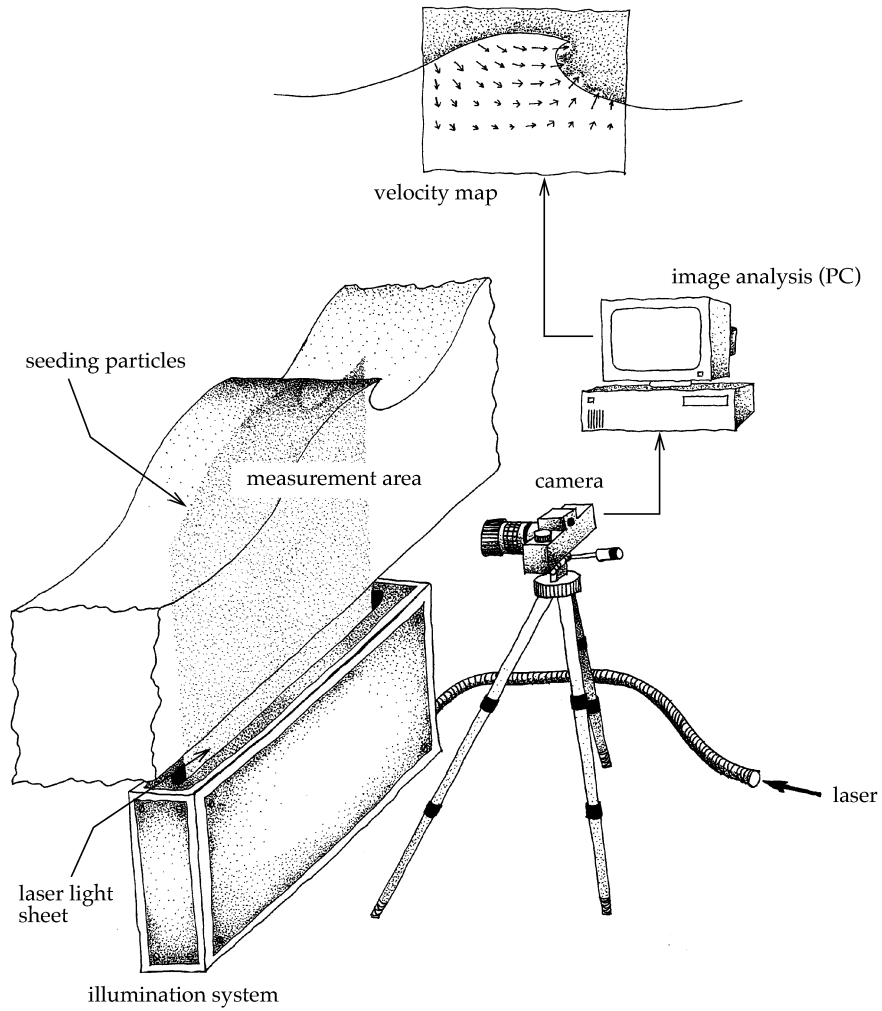
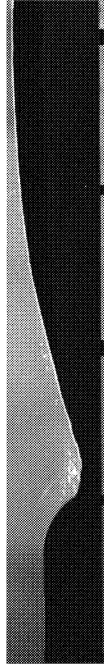


FIGURE 20. Schematic description of the PIV system.

2.3 Seeding

The velocity measured with PIV is thus the velocity of the tracer particles, as it is assumed that the particles follow the flow, and that the velocity of the particles are the same as the flow velocity. The particles ability to perform like this is depends on the particle diameter, as well as the particles density and weight. In high speed flows and in flows with large velocity gradients, the problem with particle lag can be a problem if the particle diameter is to large. For high speed flows (>50 m/s) it has been suggested that the particle diameter should not be larger than $0.5 \mu\text{m}$ (Lourenco, 1996). For PIV measurements in waves the velocities are typically in the order of 1 m/s. The velocity gradients are also relatively small, and larger particles can be used. Quinn et al. (1994) and Skyner (1992) used particles with a diameter of 50-70 μm and reported good results.



In addition to the ability to move with the fluid, the particles must also scatter enough light to be recorded by the camera. For all recording media there is a minimum threshold for what is possible to detect, and the light scattered from each particle must exceed this threshold to be recorded. The surface of the particles should reflect as much incoming light as possible, as the area (i.e. the particle size) is small.

In addition, the price is an issue. Small, uniform particles tend to be expensive, and if large quantities are needed the price must be considered. For the application of PIV the size and shape of the particles do not need to be quite as uniform as in other applications, and the cost of manufacturing these particles reduces if the requirements for uniformity are lowered.

The choice of particles was based on all the preceding considerations, and silver-coated hollow glass spheres were used. The spheres were manufactured by *Potters Industries Inc.*, and had an average particle diameter of $41.6 \mu\text{m}$ ¹. The particles are buoyant with a true density of 480 kg/m^3 . This causes the particles to float, and they tend to rise to the surface. The upward speed of the particles due to their buoyancy is measured to be approximately 0.01 m/s. As the velocity measured here is in the order of 1 m/s, the inaccuracy caused by the buoyancy is about 1%. This is considered to be acceptable.

1. The distribution of the particle size is as follows: 90th percentile: $60.0 \mu\text{m}$, 50th percentile: $41.9 \mu\text{m}$, 10th percentile: $21.5 \mu\text{m}$.

2.4 Illumination

The choice of illumination source is critical, as it plays an important role in the overall performance of the PIV system. It is crucial that there is sufficient light to make the particles detectable for the camera, or else nothing will be measured.

As the object of the measurements is a 2D velocity field it is natural to use a source that illuminate a sheet in the flow parallel to the 2D flow plane. There are several requirements that the light sheet must meet:

- The sheet must be pulsed with prescribed frequency. The pulse frequency must be determined with high accuracy, and it has to be stable. Any inaccuracies will cause errors in the velocity measurements. The error in the velocity measurements is proportional to the frequency inaccuracy for small inaccuracy values.
- The light intensity must be sufficiently high. The particles are rather small, and only a fraction of the light that each particle receives will be scattered in the direction of the camera. The light that the camera receives must be sufficient for the camera to record it.
- The sheet must be thin. The camera has only a limited depth of focus, and most of the particles in the flow will be out of focus. If all particles in the flow are illuminated, the particles that are out of focus will disturb the recordings of those in focus. Therefore it is necessary to limit the illumination to the particles that are in focus. A thin sheet will also “filter out” unwanted 3D flow. A particle that moves at an angle to the 2D plane will only be recorded once if the sheet is sufficiently thin, and will not contribute to the velocity measurements.

The best way to produce such a light sheet is by using a laser. The laser has the ability to concentrate light in a narrow beam, making the laser perfect for PIV applications.

There exists several possibilities to generate an oscillating light sheet from the narrow laser beam. The two most used configurations are the expanded beam illumination and the scanning beam illumination. With the expanded beam method a cylindrical lens is used to spread the beam as a fan. The sheet is pulsed by using a pulse laser, or by using a CW laser and mechanical or electro-optic beam chopper^{1(see next page)}. Due to the Gaussian profile of a laser beam the laser sheet provided by a cylindrical lens will have significant intensity variation. This can be a problem when a large area is to be illuminated. Another problem with this method is that the full power of the

laser is not utilized; by expanding the beam, the intensity that is received by one particle will only be a slight fraction of the total output from the laser (Gray et al., 1991). The expanded beam system is probably the best solution when investigating a small area with high speed flow, but is not the best choice when applying PIV to study breaking waves where the measurement area is 0.5m to 1m wide, and the velocity is below 2m/s.

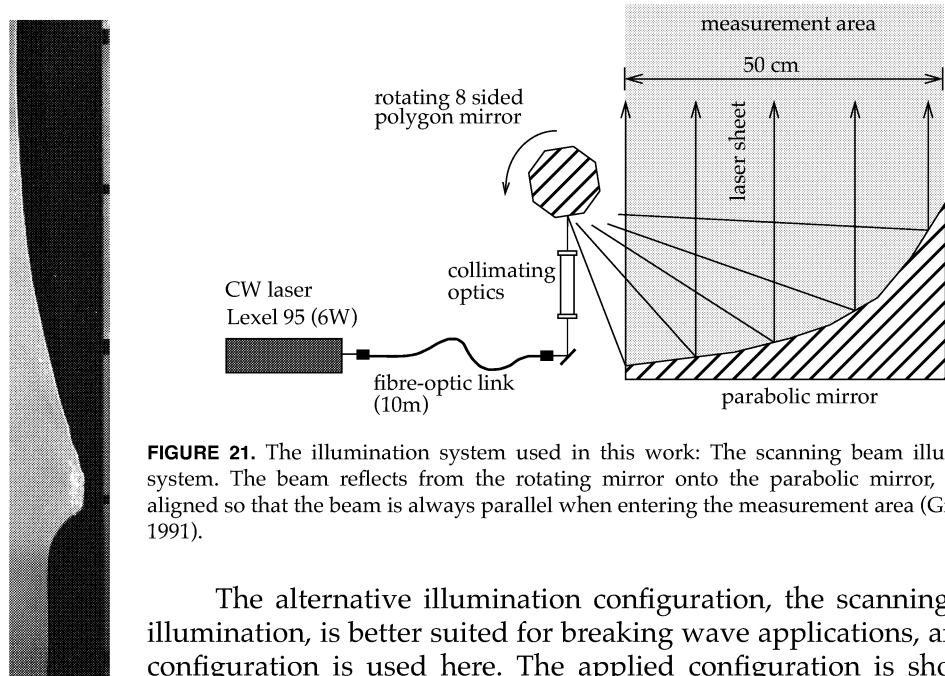


FIGURE 21. The illumination system used in this work: The scanning beam illumination system. The beam reflects from the rotating mirror onto the parabolic mirror, which is aligned so that the beam is always parallel when entering the measurement area (Gray et al., 1991).

The alternative illumination configuration, the scanning beam illumination, is better suited for breaking wave applications, and this configuration is used here. The applied configuration is shown in Figure 21.

The scanning beam illumination system uses a CW laser, and a rotating mirror to scan the beam, creating a light sheet. In the present setup the rotating mirror scans the beam onto a parabolic mirror, which reflects the beam into the measurement area. The parabolic mirror collimates the beam so that it is always parallel when entering the measurement area. This makes the sheet as uniform as possible. Without the parabolic mirror, the laser sheet intensity would decrease

1. A pulse laser is a laser that has a stroboscopic beam. The beam pulses with a given interval, and these lasers are used mostly in high speed flows (Lourenco, 1996). The Nd:Yag lasers are a class of such lasers, and can provide a pulse separation time of 0.1-200 μ sek., with a pulse energy of 100-200 mJ. Continuous Wave (CW) lasers are lasers with continuous beam, unlike the pulse lasers. Argon Ion lasers are CW lasers.

A beam chopper pulses the beam by shutting of the beam in given intervals.

with distance from the rotating mirror. The method is discussed in detail by Gray et al. (1991).

The system is manufactured by *Optical Flow Systems Ltd.* of Edinburgh, and can produce pulsed sheets 50cm wide. The pulse period in the interval 2-12ms, accurate to 0.1%. A Lexel 95 6W Argon-Ion CW laser is used as a light source. As there is no demands on the wavelength of the light, the laser is operated in multi-line mode, maximizing the output intensity. The laser has a maximum output of 8W in this configuration. The beam diameter is approximately 1.5mm.

An 8W laser beam can be harmful for the eye, and can cause sudden and permanent blindness. Great care is taken to assure that this does not happen, and the laser is connected to the SBI system through a 10m fibre-optic link. The link introduces a intensity loss of approximately 10%.

The sheet is approximately 3mm thick with a Gaussian profile. Due to minor defects in the parabolic mirror the sheet is not a totally flat plane. Maximum inaccuracies in the light sheet is ± 3 mm, with respect to a perfectly flat plane.

2.5 Image Acquisition

Image acquisition is the process involving capturing the light scattered from the particles, recording it in a camera and then digitizing the film, making it ready for computer analysis.

A Nikon F-501, 35mm SLR camera was used to capture the images. This was chosen because it had an electronically controlled shutter with electronically triggering, and it was inexpensive. The main requirement to the camera was that the shutter could be triggered with an electronic signal with high accuracy. Most electronically controlled shutters have this ability. The accuracy of the triggering was assessed by measuring the time between sending the electronic trigger signal to the camera, and the opening of the shutter (this time is called the trigger delay). Twelve measurements were made with a resolution of 1ms, and the mean trigger delay was found to be 160.75ms, with a standard deviation of 0.45ms. The standard deviation is 1.8% of the image sampling interval ($1/32s=31.25ms$).

Cameras that capture the image on film have a mechanical shutter. This is a source for trigger inaccuracy. The best choice of camera when trigger accuracy is the only issue, is a CCD¹ based camera. The

1. Charged Coupled Device: A digital camera.

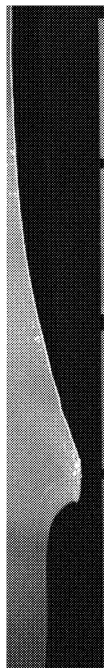
reason for not using CCD camera in this work is financial, as the demands for high resolution on the images are only met by very expensive CCD cameras. It would have been a far superior solution regarding the amount of work involved in the acquisition and processing of the images. The accuracy would, however, been only marginally improved, as the accuracy of the triggering is sufficient.

More important than the camera is the optics, as this is what transfers the light emitted/diffracted from the object to the film, producing the image. Inaccuracies in the optics result in measurement errors. A Micro-Nikkor 55mm/f2.8 lens was chosen based on its optical quality. This lens has very little distortion and a plane field of focus, which is important as the "object" has the form of a 2D field, and should not be out of focus in the corners.

The camera capture the image on 35mm film, which has an image surface of 36mm x 24mm. Kodak T-max 3200 ASA film was used, as it is sensitive enough to record the limited amount of light scattered from the particles, in combination with satisfactory resolution (approx. 100 lines/mm). The scanner¹ used to digitize the images had a resolution of 106 lines/mm, and it was not necessary to use a film with higher resolution than the scanner could take.

The sampling interval (interval between each image) was 1/32s. The camera was not capable of taking subsequent images with as short interval as 1/32s, and to achieve this sampling interval, several runs were made, and the trigger time was shifted 1/32s each time. Each time sampling is thus different runs. The camera and laser sheet are also repositioned for each run, always keeping the wave crest in the field of view. Good repeatability is required for this method, and the repeatability is assessed in *Chapter 2.1.1*.

The light sheet is 50cm wide in the PIV measurements. The camera is positioned so that the distance between the film plane and the laser sheet is 1174mm. This makes the field of view 70cm wide, and allows the whole light sheet (50cm wide) to be captured. When the camera is repositioned along the flume, it slides along a rail parallel to the flume, always keeping the camera at equal distance from the flume.



2.5.1 Image Resolution

The resolution of the image acquisition process is of great importance in PIV. The resolution must be sufficient to resolve the position of each of the particles in the image. For an image, there are

1. Nikon Coolscan II 35mm, 2592x3888 pixels, 8 bit colour.

2.5 Image Acquisition

two aspects of the resolution: The spatial resolution¹, and the gray-scale resolution². The accuracy of the particle position determination increases with increasing resolution, and both spatial and grayscale resolution must be sufficient if the particle positions are to be resolved.

The light is first captured on a photographic film, and then digitized in a scanner. The resolution of the photographic film is superior to the scanner resolution, making the scanner resolution limiting. The scanner has a spatial resolution of 2592x3888 pixels (106 pixels/mm), and a gray-scale depth of 8 bit (256 levels).

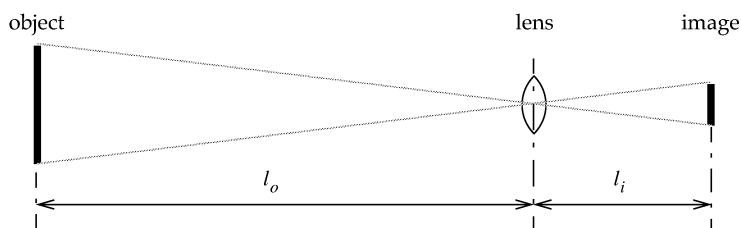


FIGURE 22. The imaging process. l_o is the length between the object plane, and the focal point of the lens, and l_i is the length between the focal point, and the image plane (film plane)

Figure 22 shows the principle of what happens when an object is captured on film (Klein and Furtak, 1986). The magnification³ M is given by

$$M = \frac{l_i}{l_o} \quad (2)$$

The focal length⁴ f is given by:

$$\frac{1}{f} = \frac{1}{l_o} + \frac{1}{l_i} \quad (3)$$

The magnification is then a function of the distance between the object and the camera, and the focal length of the lens. The focal length of the lens is 55mm, and the distance between the laser sheet (object) and the camera film plane is 1175mm ($l_o + l_i = 1175$ mm). From Equations 2 and 3 the magnification is found to be $M = 0.052$.

1. Spatial resolution: The number of pixels in the image.
2. Gray-scale resolution: Each pixel records a gray-scale value. The gray-scale resolution is the number of levels each pixel is capable of resolving.
3. Magnification is the relationship between the object size and the image size.
4. Focal length is associated with the lens, and is defined to be the length between the lens, and the focal point when the incoming light is parallel (coming from a light source at infinite distance from the lens).

This means that 1mm in physical scale is 0.052mm on the film. The scanner has a resolution of 106 pixels/mm, and the resulting image has a resolution of $\hat{M} = 5.52$ pix/mm (0.181 mm/pix) when the film is digitized. This means that each pixel in the image is 0.181 mm² in physical scale.

To adequately resolve the position of the particles there must be at least 4-5 pixels per diameter (TSL, 1994). The seeding particles have a diameter of $d_p = 40\mu\text{m}$, and this should yield a particle diameter in the image of $d_{pi} = 0.22$ pix. This is not sufficient to resolve the particles. However, due to diffraction effects in the lens, the diameter of the recorded particle is larger than this (Adrian, 1991; Raffel and Kopenhans, 1996). For small particles, the size of the particle image is much more affected by lens effects than by the actual size of the particle and the magnification. If for instance the particle is slightly out of focus, the diameter of the image will increase considerably.

Figure 23 shows the digitized image of one particle, and the particle diameter is approximately 6 pixel, and not 0.22 pixel as would be assumed based on the particle size and magnification. This increase is due to lens effects. A particle image diameter of 6 pixel is sufficient to resolve the position of the particle.

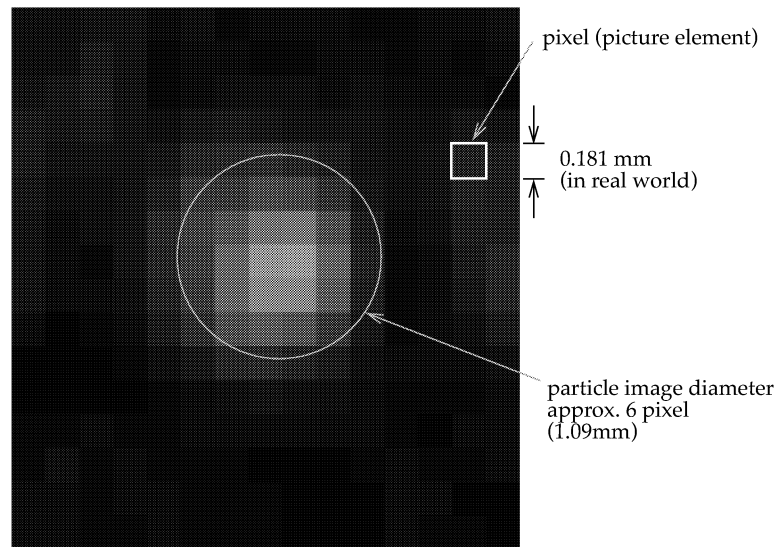
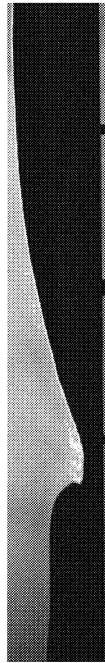


FIGURE 23. The digitized image of one particle

2.6 Image Processing

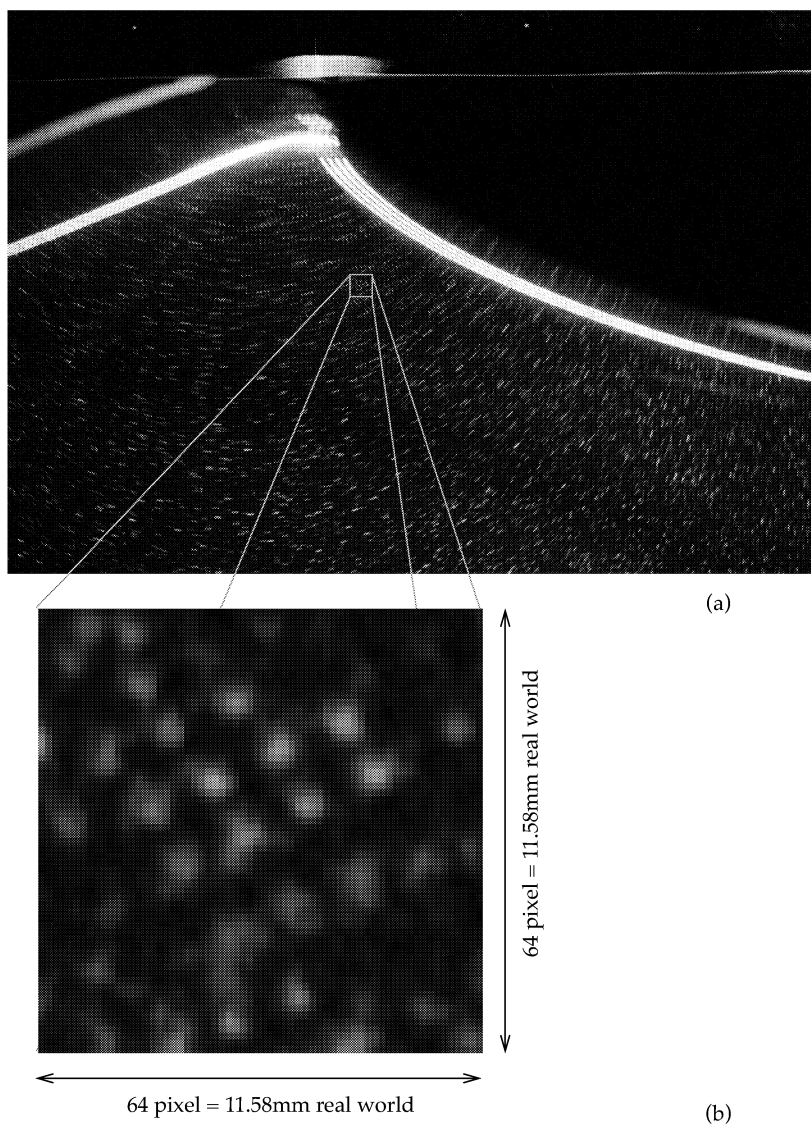
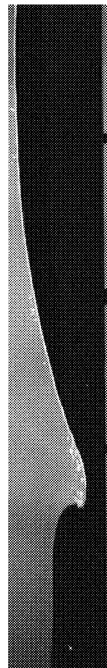


FIGURE 24. (a): Image recorded with auto-correlation mode. The shutter was open for 8ms, and the pulse separation was 2.5ms, allowing four pulses to be recorded on the image. (b): Example of interrogation area.

Figure 24a shows an image recorded with auto-correlation mode. Each particle is exposed several times, with 2.5ms interval. To compute the velocities $U(x, z)$ from this image, the particle displacement $\Delta s(x, z)$ must be found first. The image is divided into small

parts, called interrogation areas (IA) (Fig. 24b). The velocity is assumed to be constant in the IA. Δs is then found in each IA by computing the most probable Δs . There are several strategies of doing this; i) matching methods, ii) Fourier methods and iii) statistical methods (Lourenco, 1996). The most common, and the one used here, is the matching method. This method applies the auto-correlation function (or cross-correlation function¹) of the IA to compute the most probable Δs . This process will be described in the following.

All image processing was done using the commercial PIV software *VidPiv* from *Optical Flow Ltd.*, which used algorithms based on the procedure to be described.



2.6.1 Auto-correlation

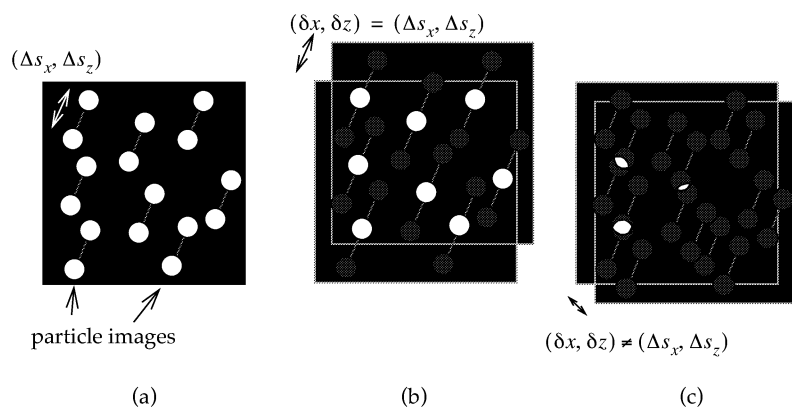


FIGURE 25. An example of an interrogation area (IA) correlated with itself. (a) The original IA, with a particle displacement $(\Delta s_x, \Delta s_z)$ (b) A duplicate IA is placed over the original one, and displaced $(\delta x, \delta z) = (\Delta s_x, \Delta s_z)$. (c) The duplicate IA is given an arbitrary displacement $(\delta x, \delta z) \neq (\Delta s_x, \Delta s_z)$. The white particle images indicates where the first particle image in the original IA coincide with the second particle image in the displaced IA.

The correlation between two functions or data sets is a measure of how well they match each other. The auto-correlation function $R(\delta x, \delta z)$ is a measure of how well a function is correlated with itself if it is displaced a distance $(\delta x, \delta z)$ relative to the original position. This can be used to find the most probable Δs in an interrogation area (IA). Figure 25 illustrates this. When the IA is displaced equal to the particle displacement, the positions of the first particle image in one

1. The auto-correlation function is used when the image is exposed using the auto-correlation mode, and the cross-correlation function when cross-correlation mode is used (see Fig. 19)

IA coincide with the second in the other IA (Fig. 25b). Thus the correlation between the two IA is high for $(\delta x, \delta z) = (\Delta s_x, \Delta s_z)$, and the auto-correlation function will have a peak here. For an arbitrary displacement $(\delta x, \delta z) \neq (\Delta s_x, \Delta s_z)$ (Fig. 25c) only a few particle images coincide, and the correlation is low. Δs can therefore be found by locating the peaks in the auto-correlation function. The positions of these peaks gives Δs directly.

How is the auto-correlation function of an IA calculated? The IA in Figure 24(b) can be described by the discrete function $f(x_m, z_n)$, which contains the gray-scale values¹ in each pixel, with the corresponding pixel positions x_m and z_n . The theory on correlation, and auto-correlation can be found in Newland (1993), and only a brief summary will be given here.

The 2D auto-correlation function $R(\delta x, \delta z)$ is defined by:

$$R(\delta x, \delta z) = E[f(x, z)f(x + \delta x, z + \delta z)] \quad (4)$$

where E denotes the expected value, or ensemble average, and δx and δz is the displacement the function is shifted relative to itself. The auto-correlation function is related to the spectral density $S(\gamma, \beta)$ through an inverse Fourier transform:

$$\begin{aligned} R(\delta x, \delta z) &= F^{-1}[S(\gamma, \beta)] \\ &= \int_{-\infty}^{\infty} \int_{-\infty}^{\infty} S(\gamma, \beta) e^{i(\gamma \delta x + \beta \delta z)} d\gamma d\beta \end{aligned} \quad (5)$$

The spectral density of a two-dimensional discrete function can be estimated by:

$$\begin{aligned} S(\gamma, \beta) &= \frac{(2\pi)^2}{l_x l_z} |F[f(x, z)]|^2 \\ &= \frac{(2\pi)^2}{l_x l_z} \left| \frac{1}{(2\pi)^2} \iint_{l_x l_z} f(x, z) e^{-i(\gamma x + \beta z)} dx dz \right|^2 \end{aligned} \quad (6)$$

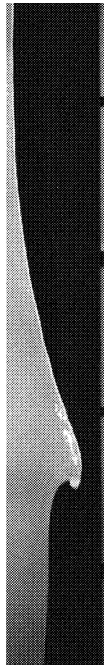
F and F^{-1} denotes the Fourier and inverse Fourier transform, respectively, and $l_x l_z$ is the size of the area where $f(x, z)$ is defined. The auto-correlation function is now given by:

1. The gray-scale values ranges from 0 to 1, representing zero density (black), and full density (white), respectively. With a gray-scale resolution of 8 bit there is $2^8 = 256$ levels between 0 and 1.

$$R(\delta x, \delta z) = F^{-1} \left[\frac{(2\pi)^2}{l_x l_z} |F[f(x, z)]|^2 \right]$$

$$= \int_{-\infty}^{\infty} \int_{-\infty}^{\infty} \frac{(2\pi)^2}{l_x l_z} \left| \frac{1}{(2\pi)^2} \iint_{l_x l_z} f(x, z) e^{-i(\gamma \delta x + \beta \delta z)} dx dz \right|^2 e^{i(\gamma \delta x + \beta \delta z)} d\gamma d\beta \quad (7)$$

Figure 26 shows a MATLAB script that computes the auto-correlation function according to Equation 7. The factor $(2\pi)^2/l_x l_z$ is omitted as it has no influence on the position of the peaks.



```
function R=autocorrelation(f)

    spectral_density=abs(fft2(f)).^2;

    R=fftshift(iff2(spectral_density));

end
```

FIGURE 26. A Matlab script that computes the auto-correlation function as given in Equation 7. The script uses the predefined Matlab functions `fft2`, `iff2` and `fftshift`. `fft2` and `iff2` are the two-dimensional Fast Fourier Transform and the inverse respectively. `fftshift` rearranges the frequency components so that the zero frequency is moved to the centre of the spectrum.

This script can now be used to compute the auto-correlation function of the IA in Figure 24b, and the result is shown in Figure 27. One significant feature of auto-correlation functions is that they are symmetric about the point of no displacement. This introduces a 180 degree direction duality in the measurements that is difficult to resolve. In the case of wave kinematics the velocity direction is rather intuitive and causes no problems. For measurements where the direction is not intuitive the direction must be resolved from the measurements. This can be done by either using cross-correlation mode in the recordings (Fig. 19), or the image shifting method. Since none of these techniques are used here, they will not be described further.

The point of no displacement is represented by the self correlation peak, which will yield the highest possible correlation as this is analogous to correlating two identical functions. The signal peak is the second largest peak, and this represents the correlation when the displacement is equal to the particle displacement Δs . The position of this peak relative to the self correlation peak is then equal to Δs . This is shown in the contour plot of the same auto-correlation function in Figure 28. The displacement $(\Delta s_x, \Delta s_z)$ is indicated, which is equal to the position of the signal peak relative to the self correlation peak.

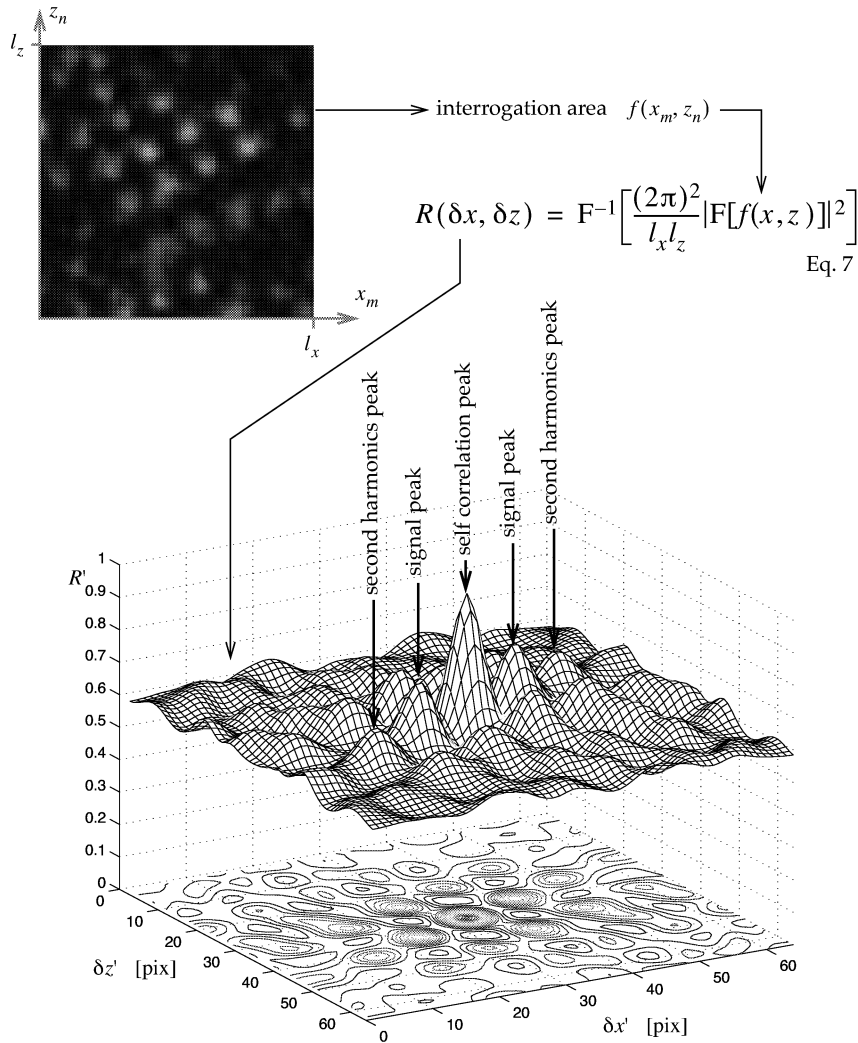


FIGURE 27. The auto-correlation function of the interrogation area in Figure 24b, computed using the script in Figure 26. R' is the auto-correlation scaled so that the self correlation peak has a value of 1. The $(\delta x', \delta z')$ axis is scaled by the fftshift routine (Fig. 26) so that the point of zero displacement is located in the centre. Point of zero displacement is thus equal to $(\delta x', \delta z') = (32, 32)$.

Because the interrogation area contains four images of each particle there will be higher harmonic peaks. The second harmonic peak therefore represents the displacement equal to $2\Delta s$ if the assumption of constant velocity in the IA holds.

In the earlier days of PIV the auto-correlation function was found using optical methods, as the capacity and speed of state-of-the-art computers were not good enough to be used for analysing the

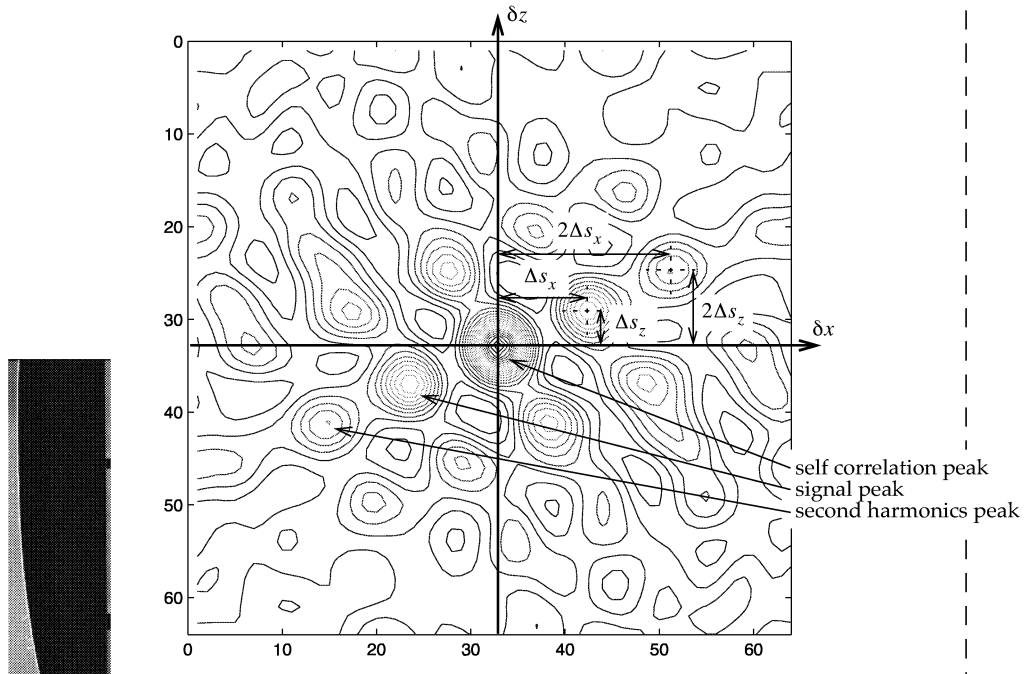
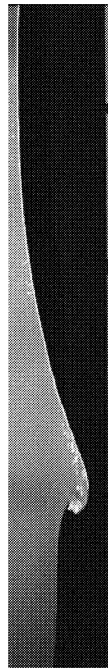


FIGURE 28. A contour plot of the auto-correlation function from Figure 27. The locations of the different peaks are indicated.



images digitally. The method is called Youngs fringes method, and has been described by many authors (e.g. Lourenco, 1996; Adrian, 1991), and will not be discussed in detail here. However, the principle of the method is to find the auto-correlation function of the IA by shining a laser beam through the photographic film with the recording of the particle positions. The size of the IA is now equal to the beam diameter. The resulting diffraction pattern is called Youngs fringes, and is analogous to the Fourier transform of the IA. By doing a subsequent Fourier transform of the diffraction pattern (optically or digitally) the auto-correlation function emerges. Even though the fastest possible way to do a Fourier transform is optically, full digital processing of the images has grown to be a far superior method as the speed and capacity of computer resources have increased. This is because the optical methods involve positioning the film very accurately in front of the laser beam. The film must be accurately repositioned for each IA, and this causes the optical method to be time consuming even though the Fourier transform itself is fast.

2.6.2 Peak Detection

Once the auto-correlation function is computed the next step is to locate the position of the signal peak. To assure best possible accuracy the peak point must be located with sub-pixel accuracy. There exists several methods for doing this (Lourenco, 1996):

i) *Centroid method*: The peak position is assumed to be located at the volume centre of the peak. The limit of integration in finding the volume centre is set to be where the sign of the derivative of the auto-correlation changes. This method should only be used in cases where the signal peak and the self correlation peak are clearly separated.

ii) *Curve fitting*: The maximum point of the signal peak is first located. An analytic function is fitted to the peak through this point in both x and z directions. The peak position is found to be the maximum of the analytic function. The analytic function can be either a parabola, or a Gaussian function. The Gaussian is assumed to be best, as the peak will have a Gaussian shape due to the Gaussian shape of the particle images.

iii) *Padding the FFT's*: To increase better resolution of the auto-correlation function zeros can be added to the image function. This yields good results, but is rather costly in respect to computer resources as it increases the length of the FFT.

iv) *Whittakers reconstruction*: The area in the vicinity of the maximum of the peak is interpolated to give better resolution, and the interpolation is done until the peak is found with wanted accuracy.

The method used in this work is the curve fitting method. This method is described in Figure 29. A three point parabola is fitted to the three highest points in the x and z direction, and the peak point is set to be the maximum of the parabolic functions.

This parabola curve fit method was chosen purely because it was the method implemented in the commercial computer software¹ available.

1. *VidPIV* from Optical flow systems Ltd., Edinburgh.

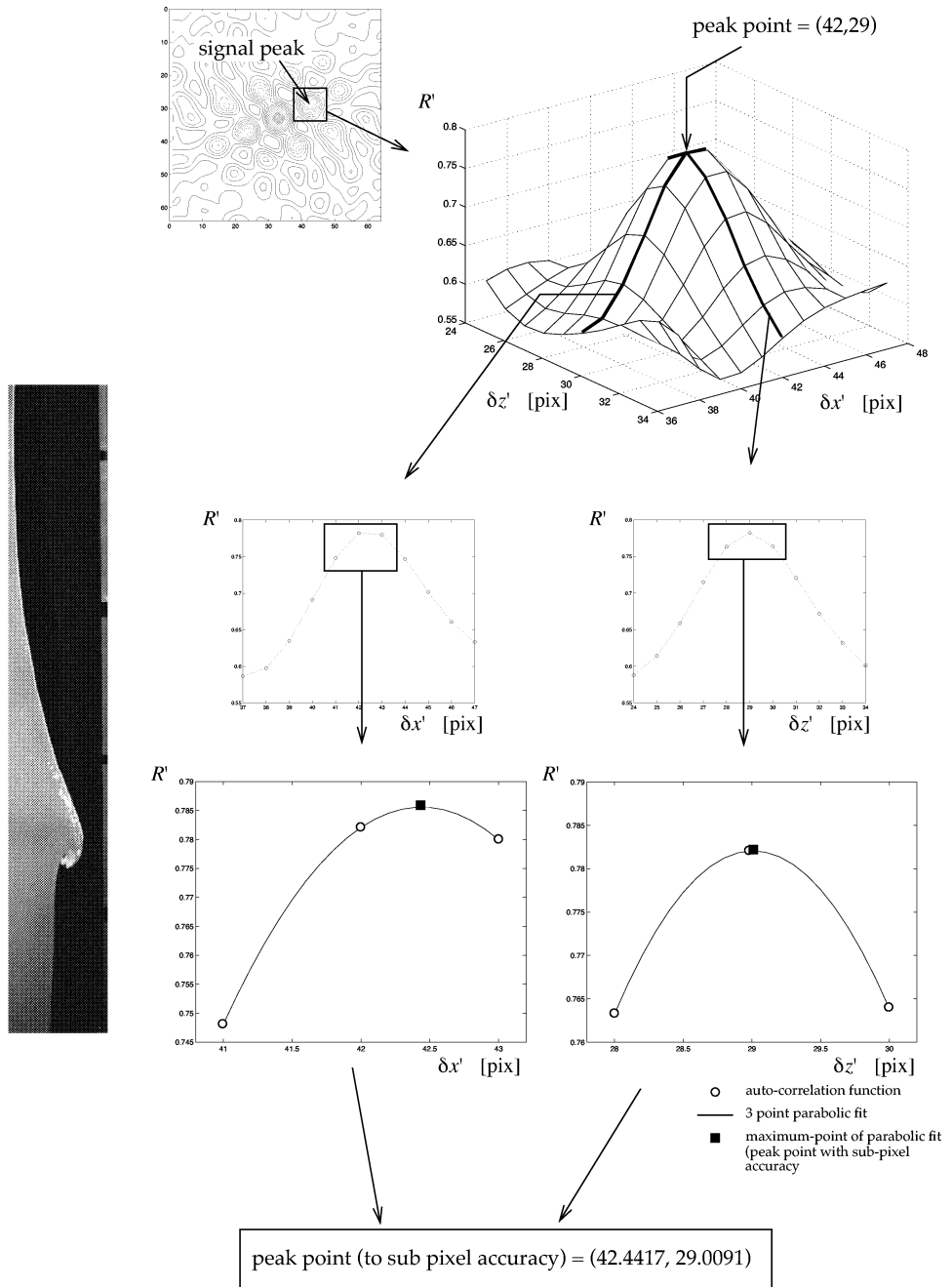


FIGURE 29. Peak detection to sub-pixel accuracy.

2.6.3 Velocity Range

An important limitation of the PIV / auto-correlation mode is the velocity range that the system is capable of measuring. The velocity range is determined by the parameters given in Table 1.

TABLE 1. The PIV parameters that influences the velocity range possible to measure. The typical values are values typically used here.

Parameter		Typical value	
δt_{cs}	camera shutter time	8, 17 ^a	[ms]
δt_p	pulse separation	2.5-4	[ms]
\hat{M}	magnification	5.52	[pixels/mm]
d_{pi}	particle image size	5-6	[pixels]
l_{ia}	interrogation area size	64	[pixels]

a. 8.00ms=1/125s, 16.67ms=1/60s.

Minimum Velocity

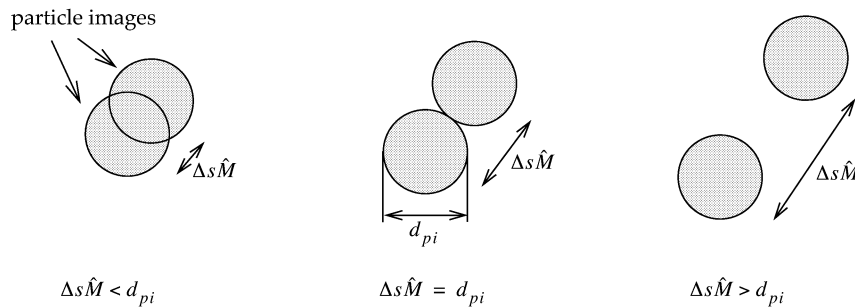


FIGURE 30. Particle separation - minimum velocity.

The minimum velocity possible to measure is governed by the particle image diameter d_{pi} , and the pulse separation δt_p . It is essential that it is possible to distinguish between the two (or multiple) exposures of the same particle. If not, it is impossible to find Δs . This is illustrated in Figure 30; if $\Delta s \hat{M} < d_p$ it is difficult to distinguish between the two exposures. If, however, $\Delta s \hat{M} > d_p$ there will be no problem separating the positions of the two particle images. Since Δs is given by the velocity of the particle and the pulse separation, the minimum velocity is given by:

$$U_{min} = \frac{d_{pi}}{\delta t_p \hat{M}} \quad (8)$$

Once the particle image diameter d_{pi} and the magnification \hat{M} are established, the pulse separation δt_p must be set according to the desired minimum velocity.

Maximum Velocity

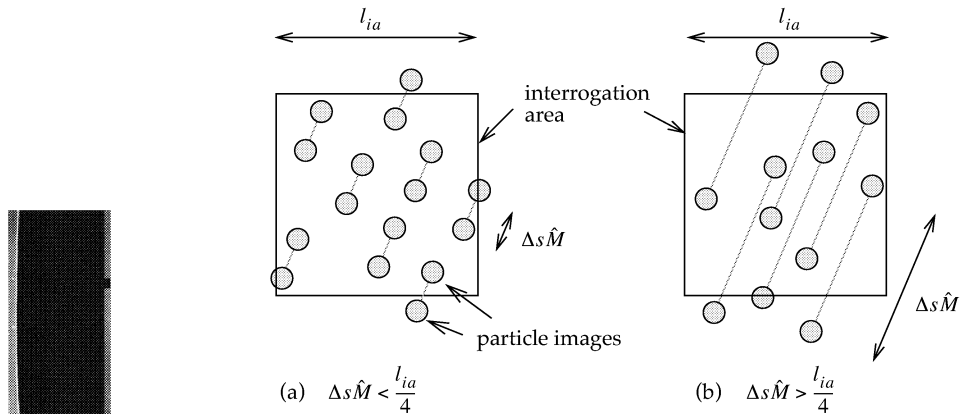


FIGURE 31. Particle separation - maximum velocity.

The size of the interrogation area (IA) puts limitations on the maximum velocity possible to detect. This is illustrated in Figure 31. As previously noted, the velocity is assumed to be constant in each IA, and the velocity is computed by finding Δs in each IA. If Δs is to be found there must be a sufficient number of image pairs of particles in the IA. In Figure 31(a) four particle image pairs are entirely inside the IA, and Δs can be found. In addition to the image pairs there are also several single particle images in the IA. This is because the particle has left the IA during the pulse separation, or the particle was not in the IA at the first pulse, but had moved inside when the next pulse came. This single images represent noise in the measurements, and if there are too many single particle images in the IA, it will be impossible to find Δs . This is shown in Figure 31b, where only one particle image pair is completely contained in the IA. Several single images introduce so much noise that it is impossible to find Δs . The maximum velocity is given by (Lourenco, 1996):

$$U_{max} = \frac{l_{ia}}{4\delta t_p \hat{M}} \tag{9}$$

The velocity range can be computed from the values in Table 1, and this is shown in Figure 32 as a function of the pulse separation, δt_p .

2.6 Image Processing

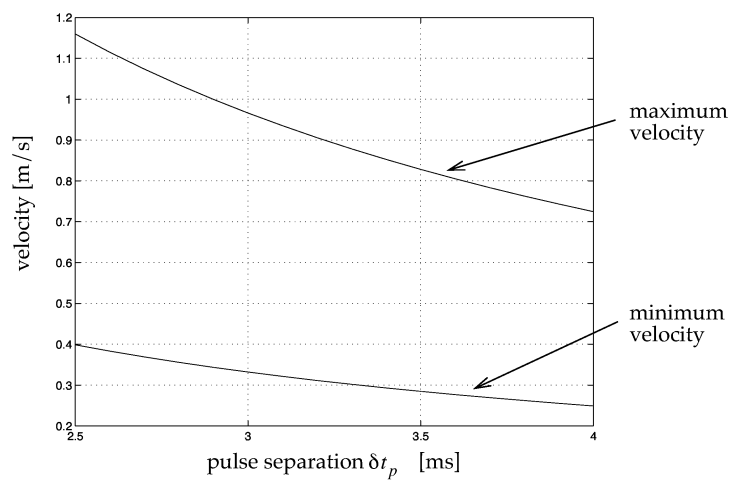


FIGURE 32. Velocity range for the PIV system.

2.6.4 Resolving Physical Coordinates

The size and position of the velocity vectors are first found in the image reference frame. This reference frame has the origin in the upper left corner, and the axis unity is in picture elements [pixels]. The results must then be transformed into the physical reference frame where the velocity vectors are given in [m/s], and the position in [m]. The transformation between the image reference frame and the physical reference frame relies on reference points in the image. Reference points are geometrical points in the measurements plane where both the physical coordinates and the image coordinates are known. All points in the image reference frame can be transformed to the physical reference frame if at least two such points in an image are known. This applies only to points that is located in a plane parallel to the image plane, and the reference points must be located in the same plane.

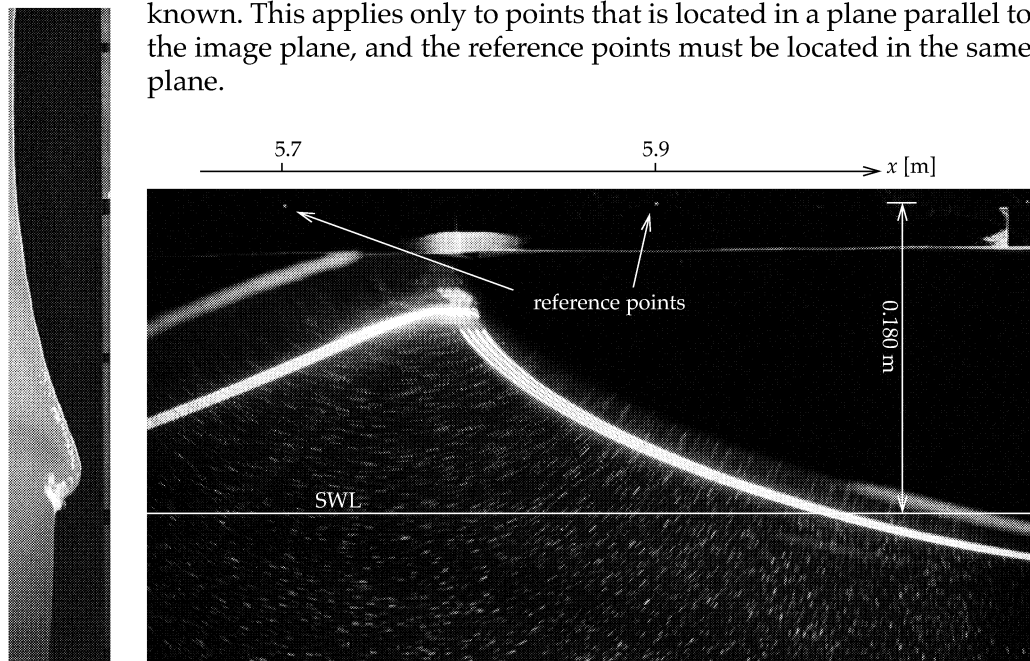


FIGURE 33. Image reference points.

The reference points are shown in Figure 33. These points are produced by green light emitting diodes. The diodes are accurately placed 18 cm above SWL, 20 cm apart over the entire measurements area, allowing two diodes to be in the image at all time. They are placed in the same vertical plane as the light sheet. Great care was taken to assure that the physical position of the diodes was known with a high degree of accuracy. It was especially important that the spacing and relative position between the diodes were correct, and a

digital drilling machine was used to assure this¹. The diodes were shielded, and the light was emitted through a 2 mm hole.

The image coordinates (i, j) of the reference points are found manually by inspecting the digitized image.

Equations of Transformation

Let (x_1, z_1) and (x_2, z_2) be the coordinates of the reference points in the physical reference frame, and (i_1, j_1) and (i_2, j_2) be the coordinates in the image reference frame. The physical coordinates (x, z) of any point (i, j) in the image reference frame can be found by:

$$\begin{bmatrix} x \\ z \end{bmatrix} = \begin{bmatrix} M \cos(\alpha_1 - \alpha_2) & M \sin(\alpha_1 - \alpha_2) \\ -M \sin(\alpha_1 - \alpha_2) & M \cos(\alpha_1 - \alpha_2) \end{bmatrix} \begin{bmatrix} i \\ j \end{bmatrix} + \begin{bmatrix} C_x \\ C_z \end{bmatrix} \quad (10)$$

Here the magnification M is given by:

$$M = \frac{\sqrt{(x_2 - x_1)^2 + (z_2 - z_1)^2}}{\sqrt{(i_2 - i_1)^2 + (j_2 - j_1)^2}} \quad (11)$$

and the transformation angles α_1 and α_2 are given by:

$$\alpha_1 = \text{atan}\left(\frac{x_2 - x_1}{z_2 - z_1}\right) \in (0, 2\pi) \quad (12)$$

$$\alpha_2 = \text{atan}\left(\frac{i_2 - i_1}{j_2 - j_1}\right) \in (0, 2\pi)$$

The transformation constants C_x and C_z are found by substituting the coordinates of one of the reference points in Equation 10:

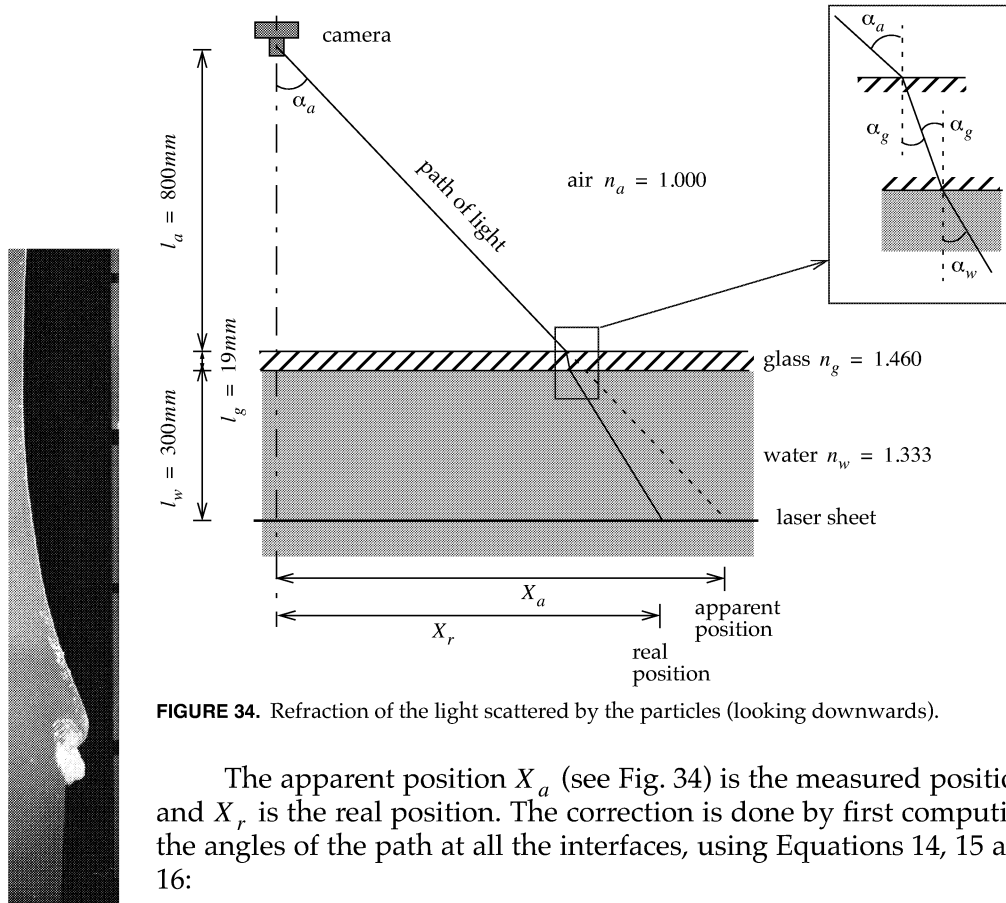
$$\begin{bmatrix} C_x \\ C_z \end{bmatrix} = \begin{bmatrix} x_{1,2} \\ z_{1,2} \end{bmatrix} - \begin{bmatrix} M \cos(\alpha_1 - \alpha_2) & M \sin(\alpha_1 - \alpha_2) \\ -M \sin(\alpha_1 - \alpha_2) & M \cos(\alpha_1 - \alpha_2) \end{bmatrix} \begin{bmatrix} i_{1,2} \\ j_{1,2} \end{bmatrix} \quad (13)$$

2.6.5 Correction for Refraction

The light sheet is positioned in the centre plane of the tank, and the light that is scattered from the particles first passes through 30 cm of water, then 1.9 cm glass, and finally 80cm of air until it goes through the lens, reaches the film, and is recorded. The light captured by the camera does not at all time pass perpendicular through the

1. If the spacing and relative position between the diodes were not accurate, the result would be that the conversion from [pixels/s] to [m/s] could be different from one image to another. As long as this spacing is correct, any errors in the physical coordinates of the reference points would only result in the vector positions being biased by a distance equal in every image, without errors in the velocities.

interfaces between the water, glass and air. The light rays will thus not be straight lines, but will be refracted according to Snell's law¹ each time it passes through an interface. All physical positions measured (velocity vector positions and surface geometry) must be corrected for this refraction.



The apparent position X_a (see Fig. 34) is the measured position, and X_r is the real position. The correction is done by first computing the angles of the path at all the interfaces, using Equations 14, 15 and 16:

$$\alpha_a = \text{atan}\left(\frac{X_a}{l_a + l_g + l_w}\right) \quad (14)$$

$$\alpha_g = \text{asin}\left(\frac{n_a \sin \alpha_a}{n_g}\right) \quad (15)$$

1. Snell's law states the relationship between the path taken by a ray of light moving from one material to another. The relationship is given by: $n_1 \sin \alpha_1 = n_2 \sin \alpha_2$, where α_1 and α_2 are the angles of the incoming and outgoing ray, and n_1 and n_2 are the indexes of refraction of the media.

$$\alpha_w = \text{asin}\left(\frac{n_g \sin \alpha_g}{n_w}\right) \quad (16)$$

$l_a, l_g, l_w, \alpha_a, \alpha_g$ and α_w are explained in Figure 34. n_a, n_g and n_w are the indexes of refraction of air, glass and water, respectively, with the values given in Figure 34. When the angles are known, the correct position can be found from:

$$X_r(X_a) = l_a \tan \alpha_a + l_g \tan \alpha_g + l_w \tan \alpha_w \quad (17)$$

This calculation requires that the physical coordinates of the image centre is known. The image centre coordinates are retrieved from the position of the camera as the camera is directed perpendicular to the flume walls at all time.

This refraction also affected the velocity measurements, and must also be corrected for. Let Δs_a be the apparent distance between two particle images, and Δs_r be the real distance. By using Equation 17, Δs_r can be computed as a function of Δs_a and X_a :

$$\Delta s_r = X_r(X_a + \Delta s_a) - X_r(X_a) \quad (18)$$

The relative bias or error R is given by:

$$R = \frac{\Delta s_a - \Delta s_r}{\Delta s_r} \quad (19)$$

R is a function of Δs_a and X_a . The apparent distance Δs_a can theoretically vary between the particle image diameter (ca. 1mm) and the interrogation area size (ca. 11mm). The apparent position X_a is the distance between the image centre and the particle image pair. This can vary between zero and approximately 0.25m (half the width of the sheet). In Figure 35, R for $\Delta s_a = 1\text{mm}$ and $\Delta s_a = 11\text{mm}$ are shown as a function of X_a .

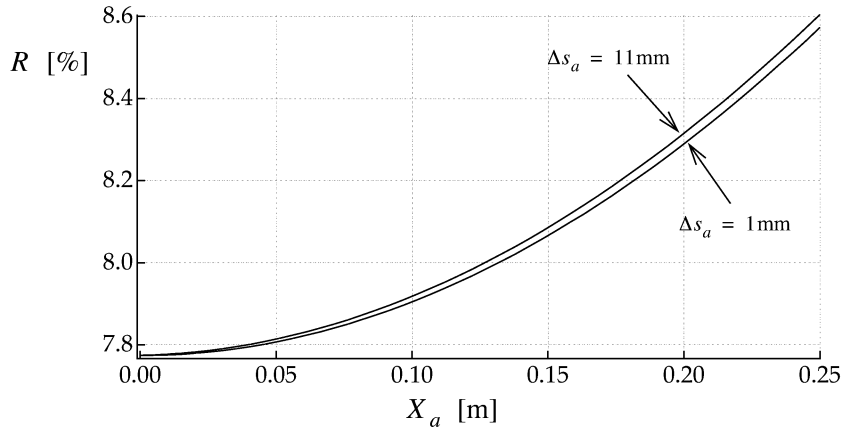
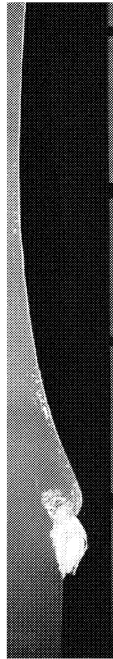


FIGURE 35. Refraction error R in the velocity measurements for $\Delta s_a = 1\text{mm}$ and $\Delta s_a = 11\text{mm}$ as a function of X_a



The bias is also depending on the orientation of the velocity vector. The above calculation assumes that the velocity vector is parallel to the line between the image centre and the vector position. If the vector is perpendicular to this line, the bias is equal to the bias for $X_a = 0$. The change in the bias as a function of X_a is from 7.8% to 8.6%. Because an absolute correction of the bias would be very complicated, and could easily introduce new errors, an estimate of the bias which is independent of both X_a and Δs_a is calculated. This estimate is found as a mean value of $R(X_a, s_a)$:

$$R_{mean} = \frac{1}{0.25(0.11 - 0.1)} \int_{0.1}^{0.11} \int_0^{0.25} R(X_a, s_a) dX_a ds_a \quad (20)$$

The integration is done using the trapezoid method with 100 intervals, and the mean error is estimated to be $R_{mean} = 8.049\%$. This estimate is used to correct all velocity measurements.

2.6.6 Vector Validation

The final step in the analysis procedure is to validate the resulting vectors, and reject obvious wrong vectors. This was to a great extent done manually by examining the vector field, and rejecting vectors that obviously did not correspond well to the neighbouring vectors. Before the manual inspection was done, a velocity filter was applied filtering out the most obvious wrong vectors. Maximum and minimum velocities were set in both x and z direction, and the velocity filter removed vectors that exceeded these limits.

2.7 Errors in PIV

In PIV, as in all other measurements techniques, errors are introduced. The errors make the resulting measurements deviate from what is real, and it is important to make any effort to keep the errors at a minimum. Even more important is to estimate how large the errors are, so that the quality of the measurements can be assessed.

In most measurements there exist several different sources of errors. PIV measurements are no exception, and the errors can be divided into three main parts:

- Errors inherited in the physics of the measurements principle
- Recording errors
- Analysis errors

Each of these will be dealt with in more detail later.

The PIV setup used in this work is similar to the setup applied by other investigators on similar problems. Quinn et al. (1994) did a thorough error analysis of a system similar to the one used here. In this section the recording and analysis errors will be pointed out and discussed. *Chapter 2.8* presents a Monte Carlo simulation of the errors introduced in the analysis of the PIV images due to recording characteristics.

2.7.1 Measurement Principle Errors

Measurements principle errors are inherited in the physics of the measurements method. The origin of these errors are due to the measurements principle, and not to how the measurements are carried out. The errors will be present in the measurements even if the recording and analysis are carried out completely without mistakes or faults.

This kind of errors include the behaviour of the seeding particles in the fluid; do the particles really follow the flow without any lag? The measurement principle in PIV is to measure the velocity of the seeding particles, assuming that this is the same as the fluid velocity. If the seeding particles move relative to the fluid, the velocity of the seeding particles will deviate from the fluid velocity, and errors are introduced.

Since other authors have reported that particles similar to those used here have good ability to follow the fluid (Skyner, 1992; Quinn, 1995), these errors are assumed to be small.

The other kind of measurements principle errors are caused by the assumption that the velocity in each interrogation area is constant



in space and time. The velocity found from each interrogation area is actually the mean velocity in the area during the recording time. If the derivatives of the velocity are large, the assumption will not be valid, and the actual velocity in the centre of the interrogation area (where the measurements are assumed to be) can differ from the mean velocity in the area (what is actually measured). The extent of the errors due to this effect is controlled by the balance between the interrogation area size, the laser pulse duration, the camera shutter time and the velocity derivatives.

2.7.2 Recording Errors

Recording an image of the tracer particles is the first step in a PIV measurement. The purpose of the recording is to register the positions of the tracer particles as accurately as possible. However, the registrations can for various reasons be biased, and errors may be introduced, making the particle positions inaccurate. The recordings can also be contaminated by noise, which can make the detection of the particle positions difficult. The quality of the subsequent analysis of the recorded images is highly dependent of the quality of the recordings. Low quality recordings make the analysis difficult, and introduce errors in the resulting velocity.

The errors and noise introduced in the recording can be divided into two categories, depending on which of the two main system components cause the error: The illumination system or the recording system (camera and lens).

Illumination System Errors

An analysis of the current illumination method is done by Gray et al. (1991). The purpose of the illumination system is to produce a flat light sheet in the flow which is parallel to the film plane, and oscillating with a constant pulse period. This is not a trivial task; the light sheet can sometimes deviate from what is optimal both in pulse period accuracy and in sheet characteristics, producing unwanted effects and errors.

If the sheet is not parallel to the film plane, or not completely flat, the magnification will be different for different regions in the image, and this will directly lead to errors in the velocity measurements. Typical inaccuracies in the light sheet is $\pm 3\text{mm}$, leading to an error of approximately 0.3% if the camera is positioned 1m from the measurement area (Quinn et al., 1994). A random error due to the thickness of the sheet is 0.1%.

The flow is parallel to the flume walls, and the laser sheet should therefore be parallel to the flume walls. If the sheet is not parallel to the 2D flow, particles will move in and out of the sheet. This creates noise, as unpaired particle images appear in the interrogation area.

Inaccuracy in the pulse period directly leads to measurement errors, as the period is used to calculate the velocity. The accuracy of the scanning rate is specified by the manufactures to be 0.1%. In addition the particles are at different horizontal positions when it is illuminated by the beam the first and second time. Due to this the period between each time a particle is illuminated is dependent on how far the particle have moved horizontally. For a horizontal fluid velocity of 1.5m/s and a pulse period of 2.5ms, the error in pulse period will be approximately 0.8%.

The laser sheet is not uniform over its thickness, but has the Gaussian profile of the laser beam. Therefore the particles lying in the sheet will be unequally illuminated depending on their position relative to the centre of the sheet. The diameter of the particle image depends on the intensity of the light scattered by the particles, and thus the diameter of the recorded particles will vary. This introduces noise in the measurements, and influences the accuracy of the analysis. The minimum velocity that is possible to measure depends on the particle diameter (*Chapter 2.6.3*). For small velocities the particle images with small diameter could give good measurements, while the larger diameter particle images are interpreted as noise since their diameter is larger than the particle displacement, and will thus be impossible to resolve as two images.

Recording System Errors

The ideal recording system (camera and lens) records an image that is identical to the reality. However, such a system has yet to be developed, and any camera/lens configuration will in one way or another bias the recording.

The light scattered from the particles passes through water, glass and air before it reaches the lens. Due to the different refraction indexes in water, glass and air the path of the light depends on the angle of attack. This causes bias in both the velocity vector and the position of the velocity vector. The bias is compensated for as described in *Chapter 2.6.5*. This correction was done assuming that the glass wall is completely flat. This is not the case, however, as the pressure from the water causes the wall to bend outward. The angle of attack of the light ray is influenced by this, and errors are introduced in the corrections of the particle position. The RMS value of the position error is estimated to be 3.4mm, with an increasing value depend-



ing on the distance from the image centre. The error in the velocity vector is also due to the curved glass interface, but this has minor effect. The correction for the refraction is done by assuming the bias to be constant. However, the bias depends on the vector orientation, and of the distance to the image centre as given in Figure 35. Thus, assuming a constant bias an error is introduced. This error can be estimated to be less than 0.5% based on the results in Figure 35.

The light passes through the lens before it reaches the film and is recorded. Both distortion, perspective and aberration can give errors in the recordings. No measurements of these errors have been made. Quinn (1995) estimated the lens distortion to be 0.0-0.3% on a 80mm Carl Zeiss lens. The 55mm Micro-Nikkor lens used here is known for its flat field of focus and low distortion. It would probably have slightly larger distortion than the Carl Zeiss lens.

The diameter of each particle image is highly dependent on whether the particle is in focus or not. If the particle is slightly out of focus, the diameter increases considerably. An increase in diameter may cause noise in the recording, and the lens should therefore be able to keep the whole light sheet in focus. The lens has a flat plane of focus, enabling it to do so.

2.7.3 Analysis Errors

Once the recording is done, the analysis is performed. The errors due to the analysis are divided in three categories based on where in the analysis process they originate: Digitization/calibration errors, errors related to the auto-correlation and errors due to the peak detection process.

Generally the analysis errors consist of both errors caused by effects inherited in the recordings (recording errors, noise) and pure analysis errors. The pure analysis errors would be present even with a perfect recording. The analysis errors will be estimated in a Monte Carlo simulation in *Chapter 2.8*.

Digitization/Calibration Errors

Part of the analysis is to determine the physical coordinates from the digitized image (*Chapter 2.6.4*). The reference points are found by manual inspection of the digitized image. Errors in the position of the reference points will result in an error in the magnification, M (see Eq. 11), yielding errors in the velocity. To evaluate this error the magnification found in each time step is used: The relative standard deviation of the magnification factors of all time steps in CASE 1

is 0.3%, and this is an estimate of the error inherited in the digitization/calibration process.

Auto-correlation Errors

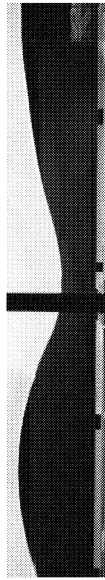
It is important that the signal peaks in the auto-correlation function are easily detectable. This means that they must be high relative to the noise, or in other words; the signal-to-noise ratio (SNR) must be sufficiently high. Noise in the measurements can have various sources. The optimal SNR is achieved when only one image pair is located in the interrogation area (IA) (Lourenco, 1996). The more typical IA holds four to ten particle image pairs. This usually results in several single particle images, where the corresponding particle image lies outside of the IA. These “independent” particle images introduce noise in the IA and contribute to lowering the SNR. Lower SNR will result in lower accuracy.

If the space and time domain derivatives of the flow are large relative to the size of the IA, the SNR will decrease. Large velocity derivatives will result in a lowering and widening of the signal peaks in the auto-correlation function because the uniformity of the particle displacement in the IA will decrease. The determination of the signal peak position is less accurate with a low wide peak, than with a high narrow peak.

The SNR is influenced by the choice of PIV parameters, such as interrogation area size and pulse separation relative to the velocity derivatives. Poor choice of parameters will yield low SNR and difficulties in analysing the image, and corresponding increased uncertainties in the measurements.

Peak Finding Errors

To estimate the error involved in the peak finding algorithm a simulation was conducted. As described in *Chapter 2.6.2* the peak is located with sub-pixel accuracy by fitting a three point parabola to the signal peak. The signal peak was simulated by a three-dimensional Gaussian function, as the particle images have a Gaussian shape, and consequently the signal peak has a Gaussian shape (Lourenco, 1996). The Gaussian function was discretized to resemble the discrete signal peak in the auto-correlation function. The error in the peak finding algorithm depends on the signal peak location in the discrete grid. If the top of the signal peak coincides with a node in the grid, and the peak has a perfect Gaussian shape, the peak position will be accurately located. If the signal peak lies somewhere between nodes (which is most probable), then the peak detection may be inaccurate. If the signal peak does not have a perfect Gaussian shape, this will also affect the accuracy.



In the simulation the signal peak is moved relative to the discrete grid with 0.01 pixel steps in both x and y direction. Totally 2500 positions were investigated. The three point parabola was fitted to the three highest points in both x and y direction. The maxima of the parabolas were compared with the known position of the Gaussian maxima, and the error was computed. The RMS value of the error is 0.015 pixel, which is acceptable.

2.8 PIV Analysis Error Simulation

As shown in the previous subsections, the variety of errors involved in PIV measurements are extensive, and it can be difficult to get a complete understanding of all the errors involved. The characteristics of the recordings affect the analysis, i.e., seeding density, three-dimensional effects, focus, sheet quality and choice of parameters. To assess these effects a Monte Carlo simulation of the PIV analysis procedure was made, where the recording characteristics were taken into account. Artificial interrogation areas with known particle displacement and characteristics equal to the real interrogation areas were generated by a computer, and analysed using a similar routine as in the PIV measurements. Estimates of the errors in the analysis procedure are found by comparing the known velocity with the velocity found from the analysis.

2.8.1 Interrogation Area Generation

The input parameters to the interrogation area generation are velocity, spatial derivatives of the velocity and laser pulse separation. In addition the number of particle pairs in the interrogation area, particle diameter and number of exposures are specified. The interrogation areas are then generated by distributing particle images in the interrogation area according to the given input parameters.

Each particle image is assumed to have a three-dimensional Gaussian intensity profile as given in Equation 21, and this is used to produce the particle images in the interrogation areas.

$$I(x, z) = I_0 \exp \left(- \frac{(x - x_{centre})^2 + (z - z_{centre})^2}{\left(\frac{d_{pi}}{2}\right)^2} \right) \quad (21)$$

Here (x_{centre}, z_{centre}) are the coordinates of the image centre, d_{pi} is the particle image diameter, and I_0 is the intensity in the image centre. The particle image modelling with Equation 21 is illustrated in Figure 36.

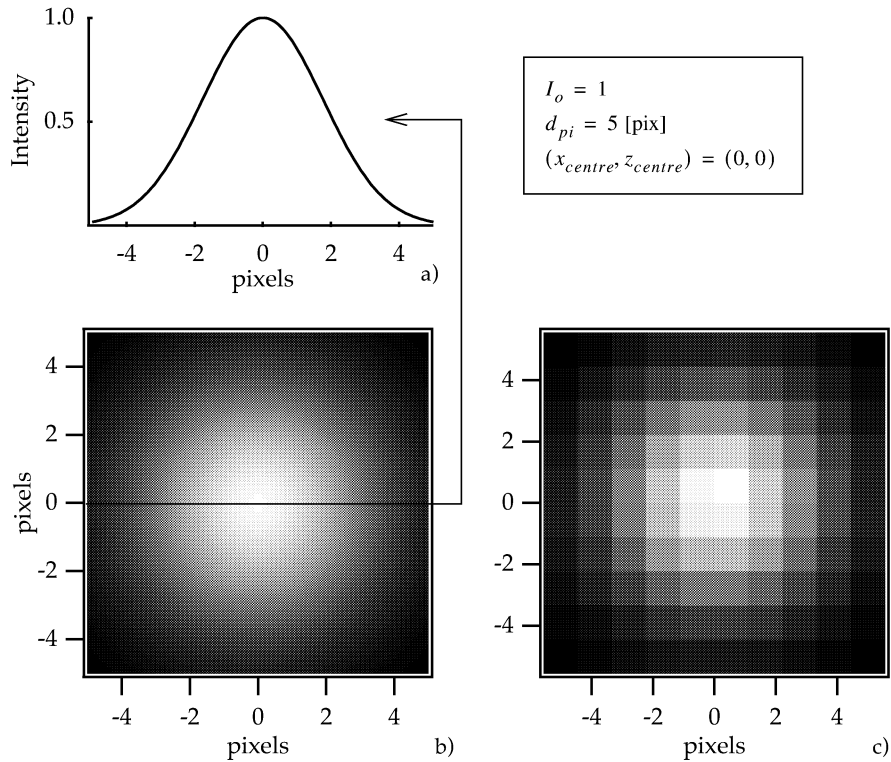


FIGURE 36. Particle image modelling. The particle images are assumed to have a Gaussian intensity distribution as given in Equation 21. This results in an image of a particle as shown in b). Black is zero intensity, and white is full intensity which equals 1. a) shows the two-dimensional Gaussian distribution, which is equal to the intensity in a cut through the centre in b). c) is the digitized version of b) (compare with Fig. 23).

The interrogation areas are generated as follows: First, the position of each particle image pair in the interrogation area is randomly generated by the computer (Fig. 37a). Second, the displacement is computed using Equations 22 and 23.

$$\vec{\Delta s}_n = (\Delta s_{x,n}, \Delta s_{z,n}) = \left(\frac{u_n}{\delta t_p}, \frac{w_n}{\delta t_p} \right) \quad (22)$$



$$u_n = u_0 + \frac{\partial u}{\partial x} x_n + \frac{\partial u}{\partial z} z_n \quad (23)$$

$$w_n = w_0 + \frac{\partial w}{\partial x} x_n + \frac{\partial w}{\partial z} z_n$$

$\vec{\Delta s}_n$ is the displacement vector of particle image pair n , δt_p is the pulse separation, (u_0, w_0) are the velocities in the centre of the interrogation area (the input velocity), and (x_n, z_n) are the coordinates of the particle image pair n . The coordinate system has its origin in the centre of the interrogation area.

Finally, the position of each individual particle image is found (Fig. 37b), and the particle image is generated as in Figure 40.

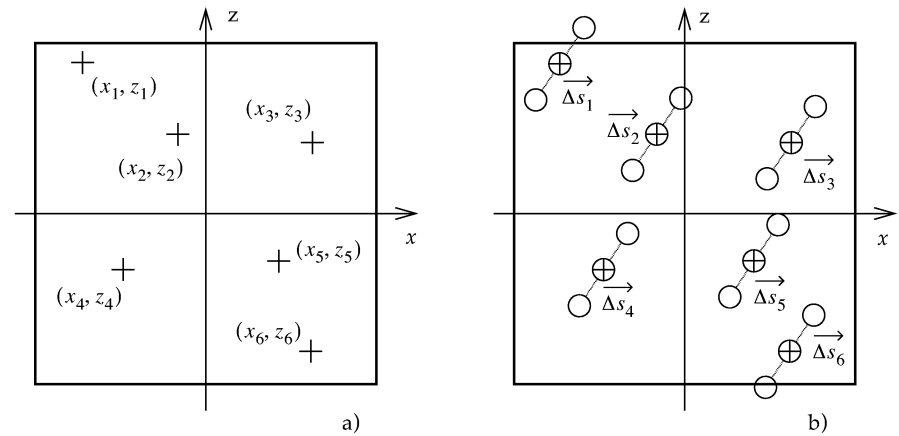


FIGURE 37. Generating artificial interrogation areas. (a) First, the positions (x_n, z_n) of each particle image pair are found using a random generator. (b) Second, the positions of the individual particle images are computed relative to (x_n, z_n) using the particle displacement Δs_n . The particle displacement are found from the particle velocities (Eq. 22), and the particle velocities are found from the defined velocity in the interrogation area centre, and the spatial derivatives of the velocity (Eq. 23).

Figure 38 shows several examples of real interrogation areas taken randomly from the measurements. It is important that the characteristics that can bias the real recordings are present in the artificial interrogation areas. To model these characteristics the particle image

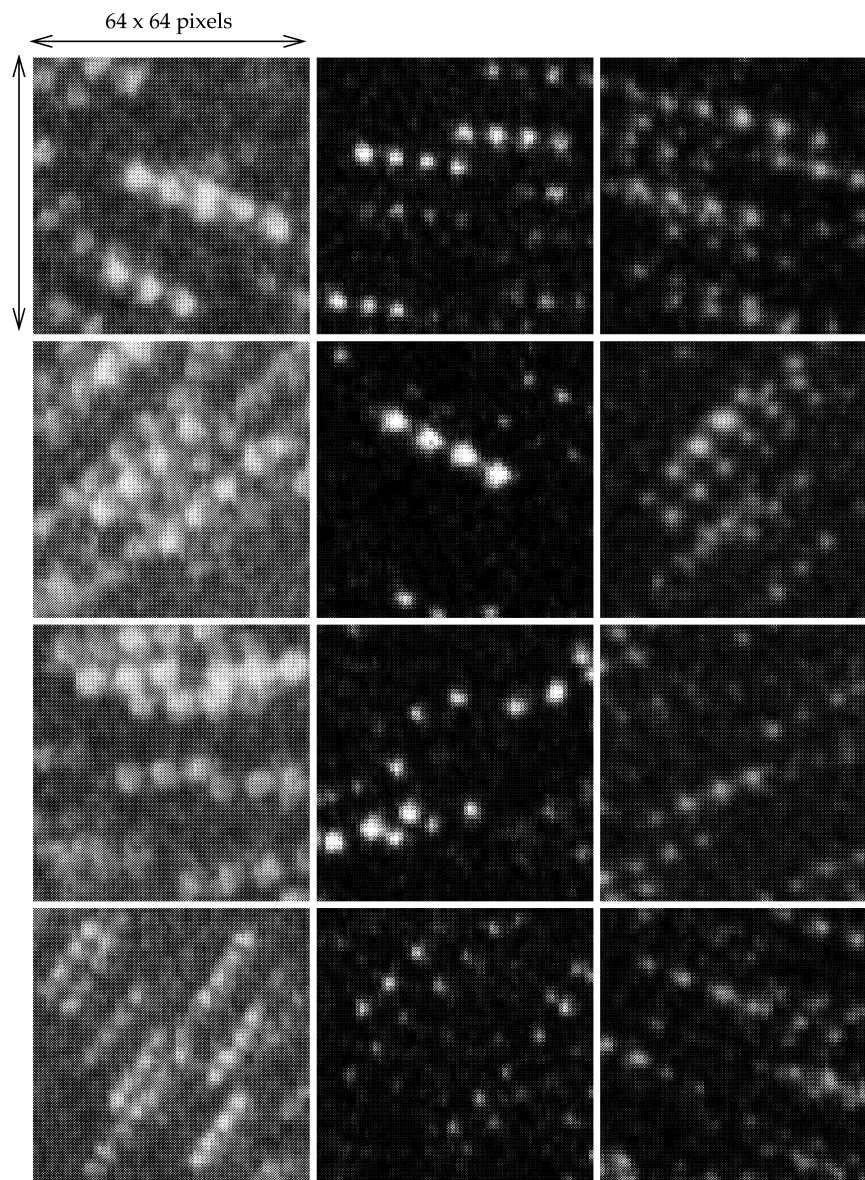


FIGURE 38. Examples of interrogation areas from the real measurements.

size, the number of particles in the interrogation area and the number of exposures of each particle are assumed to be Gaussian distributed with specified mean value and standard deviation (Tab. 2). In addi-

2 Measuring Wave Kinematics: Particle Image Velocimetry (PIV)

TABLE 2. Characteristics of the interrogation areas.



	Particle diameter	Number of particles in IA	Number of exposures of each particle
Mean value	5 [pixels]	8	3
Relative standard deviation	0.2	0.4	0.1
Probability density distribution			

tion white noise is added. The background pixels have value zero, and the centre of the particle images have value $I_0 = 1$. White noise is generated by adding a random number between 0 and 0.15 to each pixel value.

Examples of artificial interrogation areas are shown in Figure 39.

2.8 PIV Analysis Error Simulation

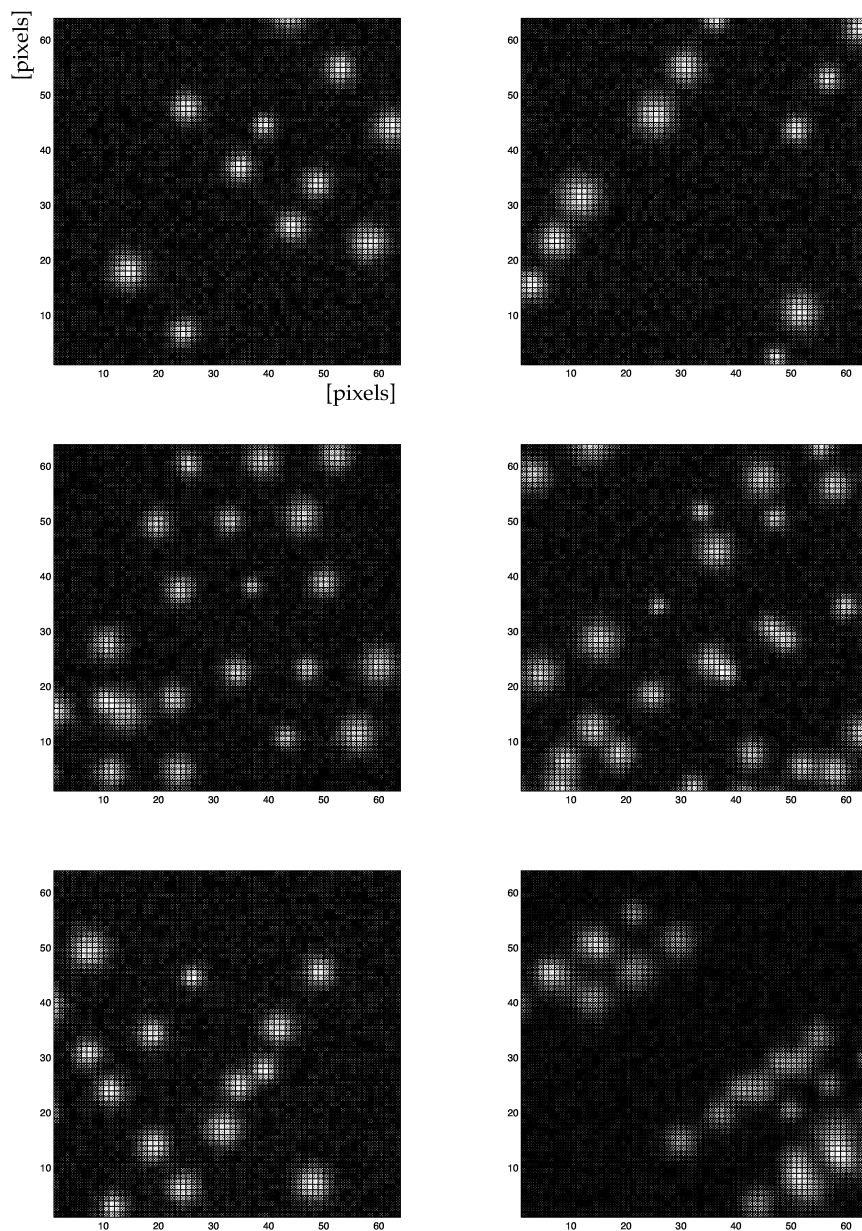


FIGURE 39. Examples of artificial interrogation areas.

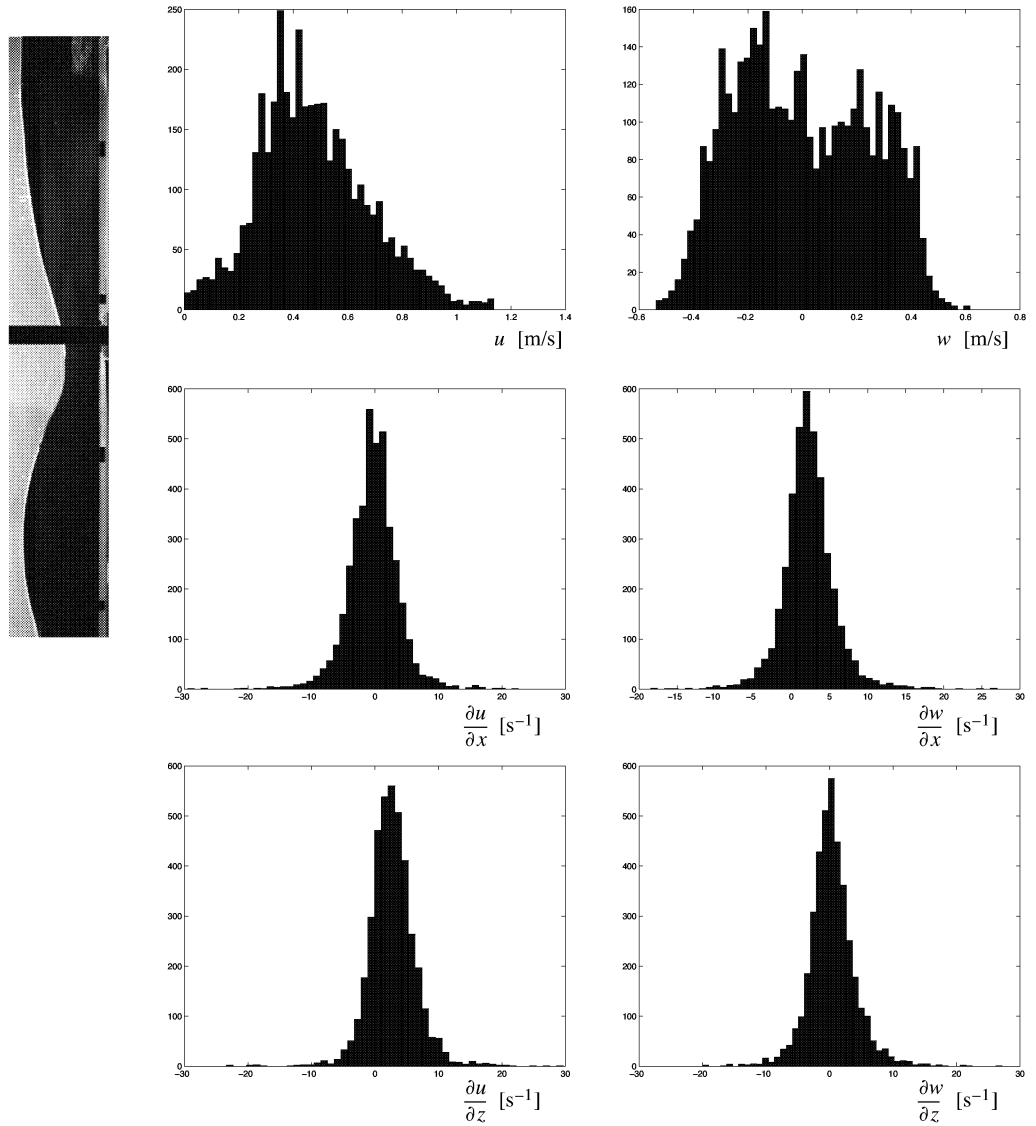


FIGURE 40. Distribution of velocities with first spatial derivatives at breaking point for all three cases. The abscissa has 50 intervals, and the ordinate values are number of measurements in each of the intervals.

2.8.2 Results

To get a good estimate of the error many artificial interrogation areas must be examined. The RMS values of all the errors in the individual interrogation areas can then be used as an error estimate.

The velocity and velocity derivatives used to produce the artificial interrogation areas must be representative of the real cases. The measurements at the breaking instant in each of the three cases are used to compose characteristic pairs of the velocity and its derivatives. The distribution of velocities and its derivatives taken from the breaking point measurement in all three cases are shown in Figure 40. Each pair of velocity/derivatives are used to construct an artificial interrogation area, which is then analysed. The result is compared with the input velocities, and the error is computed. A total number of 2540 artificial interrogation areas were investigated. The resulting error distributions for the absolute velocity, and the velocity direction are shown in Figure 41, together with the RMS values. Errors larger than 10% were ignored as it is assumed that vectors with such large errors are rejected during the manual vector validation.

The RMS values are now the estimates of the error inherited in the analysis as a result of different effects in the recording. Thus the mean velocity error from the analysis is 3.88%. However, the velocity is more likely to be underestimated than to be overestimated. The velocity direction has a mean error of 1.69[deg], and is evenly distributed around zero.

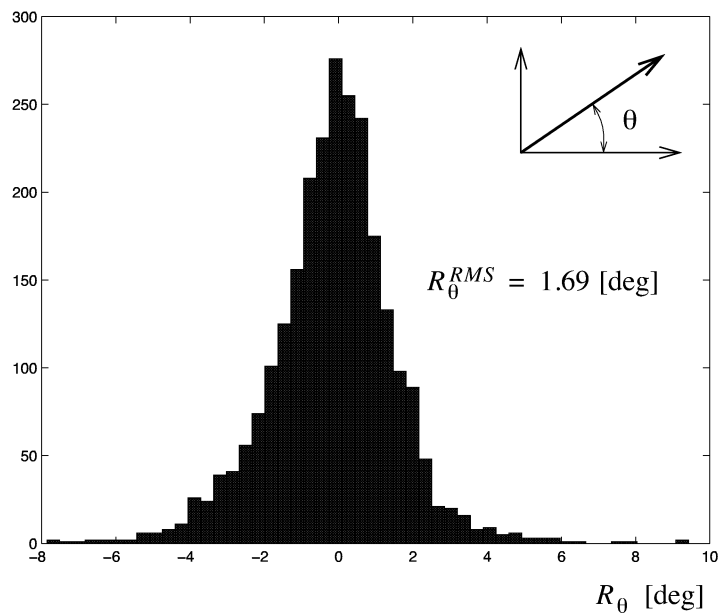
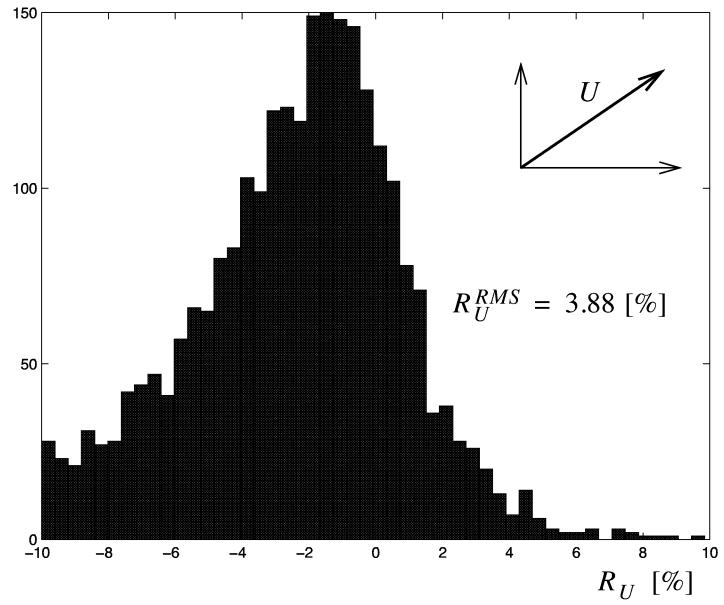
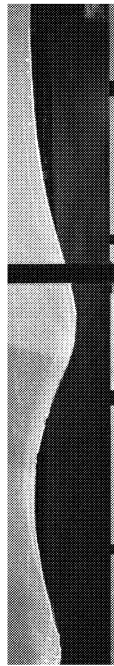


FIGURE 41. Distribution of errors in velocity magnitude (top) and velocity direction (bottom). The abscissa has 50 intervals, and the ordinate values are number of measurements in each of the intervals.

2.9 Description of Wave Kinematics

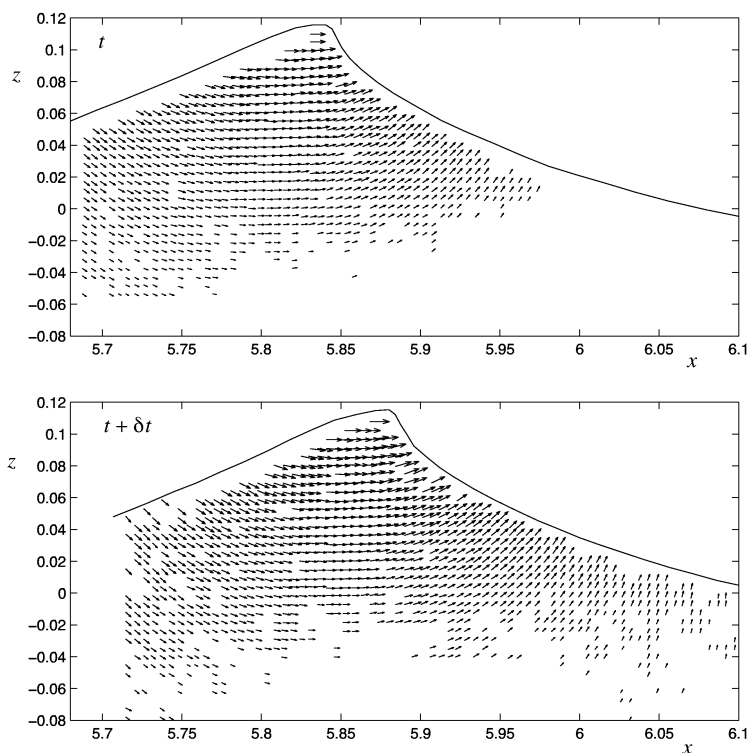


FIGURE 42. Example of wave kinematics measurements.

Is a velocity vector field (Fig. 42) the best way to describe the kinematics of a wave? The vector field gives an overall qualitative understanding of the nature of the flow, i.e. that the velocity is horizontal at the wave crest, it is directed downwards at the rear and upwards at the front of the wave. The decay in magnitude with depth is also apparent, and thus all the common features of the wave kinematics are detected by studying the velocity vector field.

Breaking waves are transient waves, i.e. both the geometry and the kinematics change as they approach breaking. Therefore it is important to reveal these changes to obtain a full understanding of the breaking process. The two velocity fields in Figure 42 are taken with a time interval δt . It is difficult to see the changes just by looking at the two velocity fields, and alternative ways to describe and present the kinematics measurements where the changes are easier to detect should be used. Description of the kinematics by a set of parameters is therefore applied here.

2.9.1 Wave Kinematic Parameters

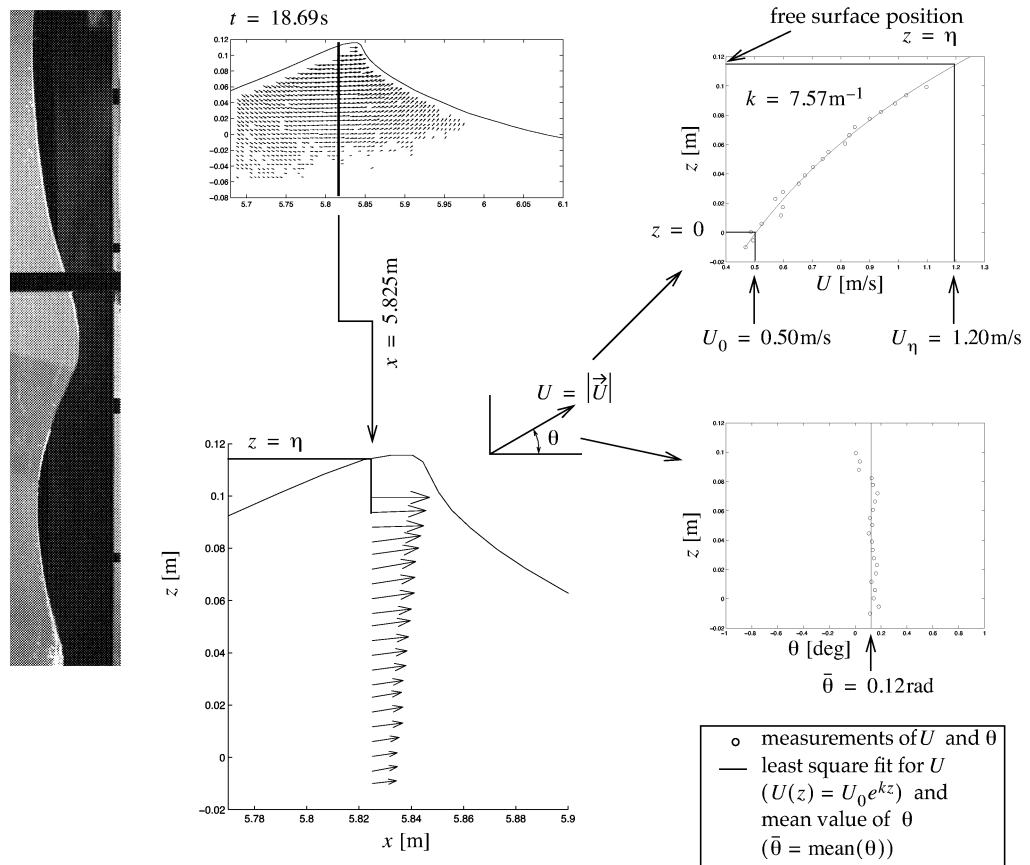


FIGURE 43. Example of how the wave kinematics parameters are found at a given time and for a given x value.

Four parameters are used to describe the kinematics:

- Velocity at the surface $z = \eta$: $U_\eta(x, t)$
- Velocity at $z = 0$: $U_0(x, t)$
- Mean velocity direction: $\bar{\theta}(x, t)$
- Local wave number: $k(x, t)$

The parameters are all functions of x and t as they are calculated at different horizontal x positions for each time step.

It is important that the parameters contain as much information as possible from the original data. The above parameters were chosen so that it is possible to reconstruct almost entirely the original velocity

field data. This means that the parameters nearly represent the original data, and only minimal information is lost in the data analysis.

The parameters are computed by considering individual columns of vectors. For each vector column a set of parameters are calculated. Figure 43 illustrates this. From the measurements at one time instant (upper left corner) a vector column are obtained (below). The magnitude U and the direction θ of the velocity vectors are considered separately (right).

The PIV technique has problems measuring the velocity close to the free surface, as particles tend to gather at the surface, making it difficult to resolve each individual particle image. Velocity measurements at the surface are thus seldom available, and the velocity at the surface $U_\eta(x, t)$ is therefore found by extrapolation.

According to linear theory of deep water waves the velocity U depends exponentially on the vertical coordinate z , i.e. $U \sim e^{kz}$, where k is the wave number. Thus the velocity is taken as:

$$U(z) = U_0 e^{kz} \quad (24)$$

Equation 24 is fitted to the data using the least square method. From this fit the wave number, k , and velocity at $z = 0$, U_0 , is found directly, while the surface velocity U_η is obtained by setting $z = \eta$.

Figure 44 shows examples of the curve fitting at six different x positions of the velocity field from Figure 42 (top). For each position U vs z is plotted with both linear and log scales along the horizontal axis. In log scale Equation 24 represents a straight line, and the quality of the fit can more easily be assessed. Overall, and as demonstrated in the examples shown in Figure 44, Equation 24 appears to represent the data reasonably well.

The velocity at $z = 0$ can also be found directly from the measurements by using the measurements at each side of $z = 0$, and then interpolate to find the velocity at $z = 0$. This parameter is denoted \hat{U}_0 , and the reason for using two estimates for this parameter is that the difference can be used to assess how good the curve fit is.

The mean velocity direction $\bar{\theta}$ is the mean value of the velocity direction at each x position.

2 Measuring Wave Kinematics: Particle Image Velocimetry (PIV)

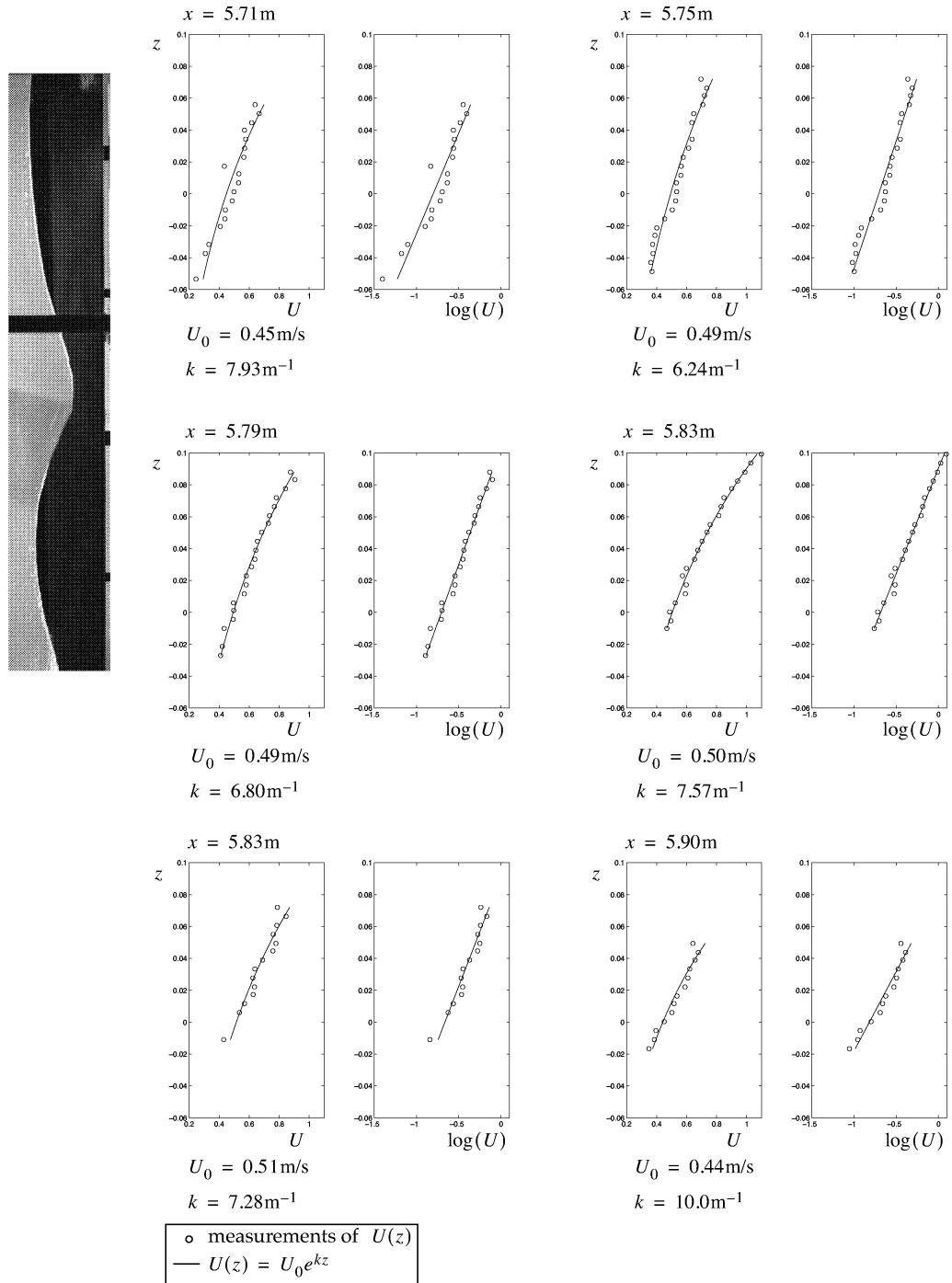


FIGURE 44. Examples of curve fitting for six different x positions in the velocity profile in Figure 42 (top).

2.9.2 Normalization and Reference Frame

The kinematics parameters except the mean velocity direction are normalized before presentation. Wave length, wave period and phase velocity are used for this purpose. The phase velocity is estimated from the velocity of the wave crest point by a linear fit to the time history of the crest point position (Fig. 45). The wave length and wave period are derived from the phase velocity by using linear wave theory, and are given in Table 3. The normalized kinematics parameters are described in Table 4.

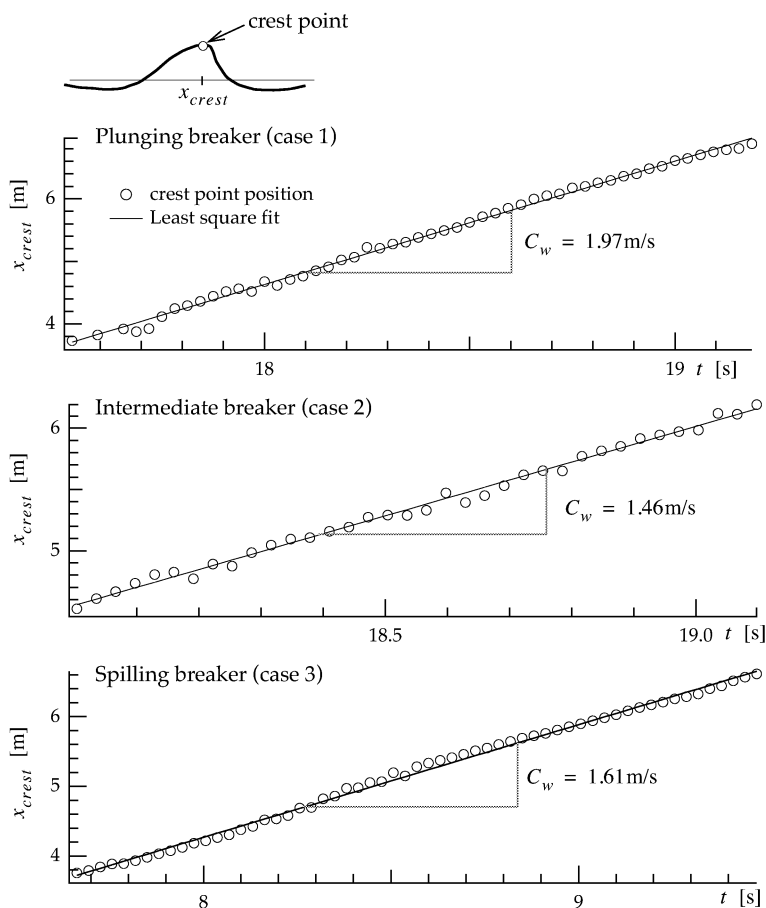


FIGURE 45. The phase velocity of the wave is taken to be the velocity of the crest point. A linear function is fitted to the time history of the crest point position by using the method of least square. The phase velocity is estimated by the derivative of this linear function.

In the kinematics measurements, as well as in the geometry measurements, the coordinates x and z are normalized with the

2 Measuring Wave Kinematics: Particle Image Velocimetry (PIV)

TABLE 3. Phase velocity, wave length and wave period used to normalize the parameters. The wave length and period is derived from the phase velocity using deep water linear wave theory. See Figure 45 for how the phase velocity is determined.

Case	Phase velocity C_w [m/s]	Wave length $L = 2\pi \frac{C_w^2}{g}$ [m]	Wave period $T = 2\pi \frac{C_w}{g}$ [s]
Plunging breaker (case 1)	1.97	2.48	1.26
Intermediate breaker (case 2)	1.46	1.37	0.94
Spilling breaker (case 3)	1.61	1.67	1.03

TABLE 4. Normalized parameters.

Parameter	Normalized
Velocity at the surface U_η	$U'_\eta = \frac{U_\eta}{C_w}$
Velocity at $z = 0$, U_0	$U'_0 = \frac{U_0}{C_w}$
Wave number k	$k' = k \frac{L}{2\pi}$

wave length L , and t is normalized with the wave period T . x and z are earth bound coordinates, but in the analysis both earth bound and a wave bound reference frames are used. In the earth bound frame of reference the horizontal origin is located at the breaking point. The time reference frame also uses the breaking point¹ as reference, with the time of breaking as origin. In the wave bound frame of reference the horizontal origin is located where the velocity is horizontal for the wave kinematics measurements, and at the crest point for the wave geometry measurements. In the vertical direction origin is always located at the still water level (SWL). Normalized coordinates and time are given in Table 5.

1. The breaking point is defined in *Chapter 1.1.1*.

2.9 Description of Wave Kinematics

TABLE 5. Normalized coordinates and time.

Coordinate	Normalized
Time t	$t' = \frac{t - t_{breaking}}{T}$ ^{a)}
Horizontal coordinate x	$x' = \frac{x - x_{breaking}}{L}$ ^{b)} (Earth bound reference frame)
	$\hat{x} = \frac{x - x_{\theta=0}}{L}$ ^{c)} (Wave bound reference frame)
	$\tilde{x} = \frac{x - x_{crest}}{L}$ ^{d)} (Wave bound reference frame)
Vertical coordinate z	$z' = \hat{z} = \tilde{z} = \frac{z}{L}$

- a. $t_{breaking}$ is the time of breaking.
- b. $x_{breaking}$ is the x position of the breaking point.
- c. $x_{\theta=0}$ is the x position where the velocity is horizontal.
- d. x_{crest} is the x position of the crest point.

As described earlier, the geometry of the wave was measured at the interface between the free surface and the glass wall of the flume, while the kinematics were measured in the centre of the flume. This caused a problem as the breaking point detected in the kinematics and the geometry measurements were different for both the intermediate and the spilling breaker. For the intermediate breaker, breaking was initiated 2/32 s earlier at the wall than in the centre of the flume. For the spilling breaker the difference was 4/32 s. The geometry of the wave also had some other differences at the two measurements positions, as the surface was smoother at the wall than in the centre. Figure 46 shows the position of the crest as a function of time measured in the centre of the flume (kinematics measurements) and at the flume wall (geometry measurements). At the centre of the flume the crest is shifted forward relative to the crest at the wall. Figure 46 also shows the position of the point where the velocity is horizontal.

This difference is partly caused by three-dimensional effects in the flume. For the intermediate and the spilling breaker it was observed that foam generation began earlier at the wall than in the centre. It is also possible that the difference is caused by inaccuracies in the wave generation equipment, but it has not been possible to confirm this.

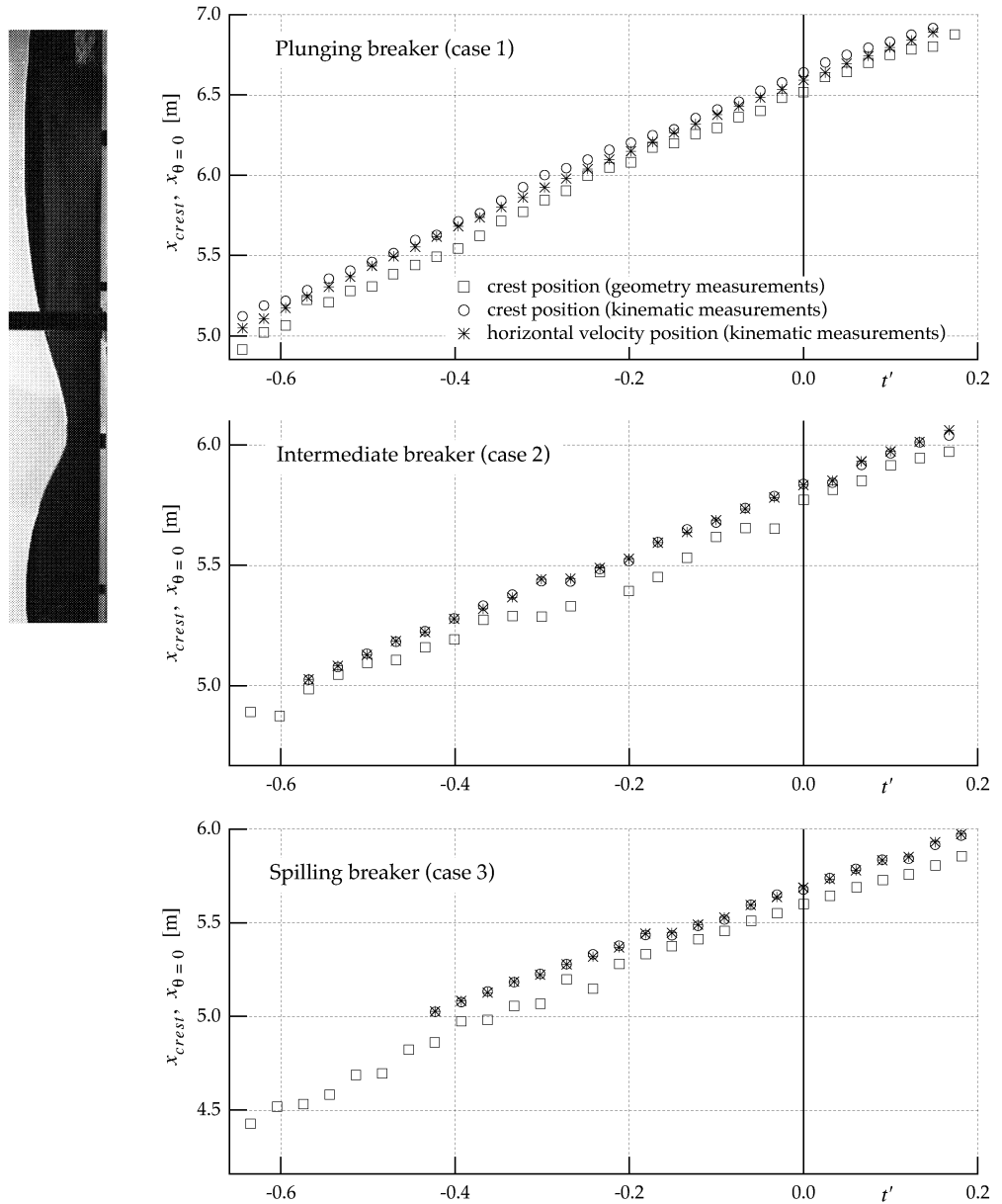


FIGURE 46. Position of the crest point x_{crest} (from the kinematics and the geometry measurements) and the position of the point with horizontal velocity (from the kinematics measurements) as a function of time t' . x_{crest} is measured relative to the wavemaker position. t' is normalized with respect to wave length, and has origin at the breaking point.

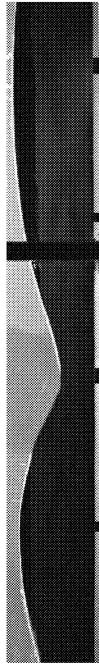
2.10 Chapter Summary

In this chapter the laboratory setup that was used to measure the wave kinematics has been described and analysed.

A wave flume was constructed and built as a part of this work. The flume is 13.5m long, 1m deep and 0.6m wide, and its walls and bottom are made of glass, enabling optical measurements techniques. The repeatability of the flume and wavemaker was assessed, and found to be good.

For the measurements of the kinematics the Particle Image Velocimetry (PIV) method was used, and the PIV hardware and software were described. An estimate of the error involved in the PIV measurements was given by a Monte Carlo simulation of the PIV image analysis algorithm. From this analysis the RMS value of the error was found to be 3.9 percent of the velocity magnitude, and 1.7 degrees of the velocity direction. In addition to this analysis error, which is a software error, errors in the hardware also occurred. The accumulated errors from the hardware were approximately 2-3 percent, and this gives an estimate of the total error of approximately 6 percent.

At the end of the chapter a set of four parameters that describes the wave kinematics was suggested. These parameters were: Velocity at the surface, local wave number, velocity at still water line ($z = 0$), and velocity direction. The purpose of the parameters is to give a better understanding of the space and time domain development of the kinematics.



Chapter 3 Wave Geometry Measurements

The elevation of the free surface is referred to as the wave geometry. Unlike the wave kinematics, the geometry is highly visible, and can be observed. It is in fact the free surface geometry most people think of when talking about water waves. Water waves move both in space and time, and we often refer to the space and time domain geometry of the wave. This is not two different geometries, but two different ways of observing or measuring the wave geometry. The space domain geometry is the geometry of the wave as observed if we take a photograph of the wave, i.e., the wave geometry in space at a time instance. If we, on the other hand, use a wave gauge, the result is a measurement of the time domain geometry, i.e. the wave geometry at one point in space as a function of time. Both the space and time domain geometry are measured in this study.

The time domain geometry is easily measured, e.g. by wave buoys at sea, or by wave gauges in the laboratory. The space domain geometry is more difficult to measure. The easiest way is to use image analysis, i.e. taking photographs of the wave, and analyse them to get the geometry. Both techniques will be described in this chapter.

The results from the wave geometry measurements do not reveal all the “secrets” of the wave at once; they need to be thoroughly analysed. As part of the analysis, parameters describing different wave features are calculated from the geometry. Such parameters are important when analysing transient waves (such as breaking waves), where the evolution process is important to understand. Parameters used by other authors in previous studies along with new parameters will be presented at the end of this chapter. These parameters are used in the analysis of the wave geometry which will be presented in *Chapter 4*.

3.1 Space Domain Wave Geometry

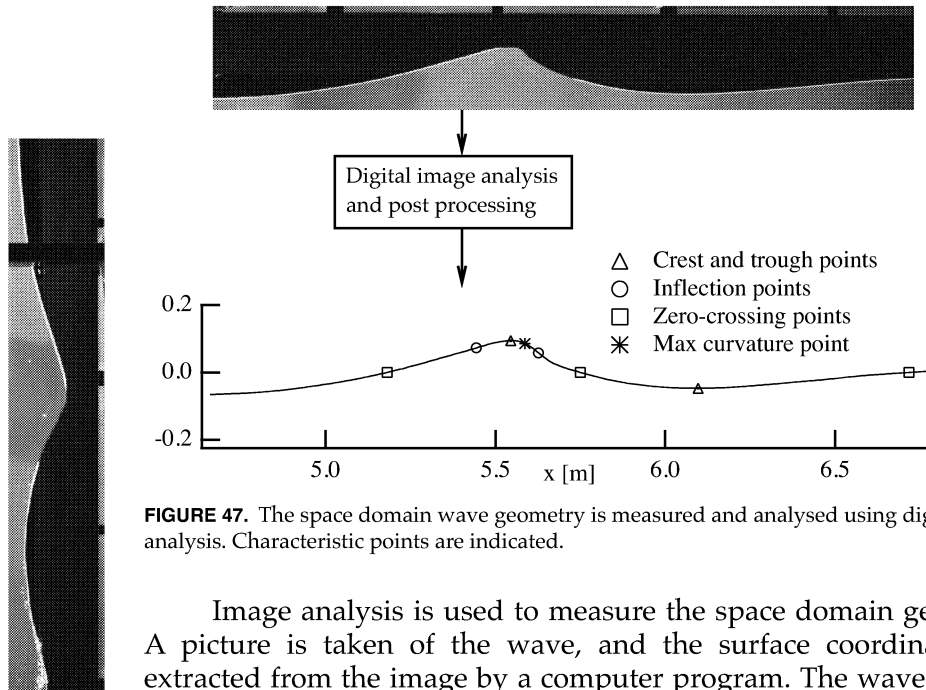


FIGURE 47. The space domain wave geometry is measured and analysed using digital image analysis. Characteristic points are indicated.

Image analysis is used to measure the space domain geometry. A picture is taken of the wave, and the surface coordinates are extracted from the image by a computer program. The wave geometry analysis uses several parameters (see *Chapter 3.4*). These parameters are calculated from the position of the crest and trough points, zero-crossing points, together with the steepness (first spatial derivative) and the curvature (second spatial derivative). To find these from the surface measurements, a b-spline curve is fitted to the coordinates. The b-spline was chosen because it is semi-analytical, and makes computing of the derivatives easy and straight forward. Also characteristic points, such as maximum, minimum and zero-crossing points, can be determined with high accuracy.

The process from image to parameters is indicated in Figure 47. This process is almost fully computerized, and the reason for doing this is to get an analysis routine that gives objective results, not biased by human factors.

3.1.1 Laboratory Setup

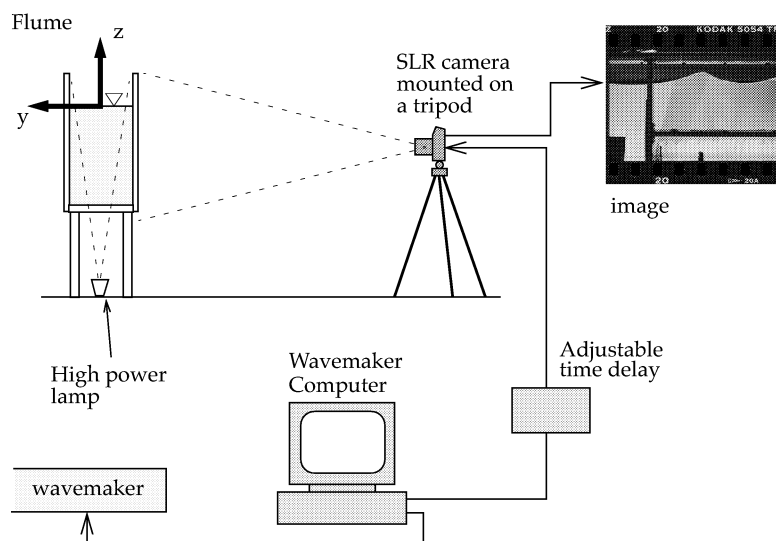


FIGURE 48. Laboratory setup for the space domain geometry measurements.

The laboratory setup for the space domain measurements (Fig. 48) consists of several high power lamps under the flume, and a SLR (single lens reflex) camera mounted on a tripod on the side of the flume taking pictures perpendicular to the flume walls. The camera is triggered by the computer that controls the wavemaker, and the trigger time can be adjusted accurately relative to the wave motion. The wavemaker computer runs with a clock frequency of 16 Hz, and can trigger the camera with a resolution of 1/16s. To allow higher resolution of the timing, an adjustable time delay was built. Pictures are taken of the wave as it approaches breaking, through the breaking event and into the post-breaking phase. Several runs were made with the same wave, shifting the camera trigger time 1/32s for each run, giving a sampling frequency of 32 Hz. This is the same method as used in the kinematics measurements, and the necessary repeatability in the flume has been assessed earlier in *Chapter 2.1.1*.

As the images are to be processed digitally, special care has to be taken to assure that it is possible to obtain the required information from the image. It is important to assure that there is high contrast between air and water, making it easy to resolve the free surface. This is accomplished by introducing fluorescent dye into the water, and painting the background above the water level black. Then the water become bright, and the air dark, making the detection of the free surface easy. The flume is completely shielded with drapes, so that no

reflexes from the glass or unwanted external light disturbed the image.

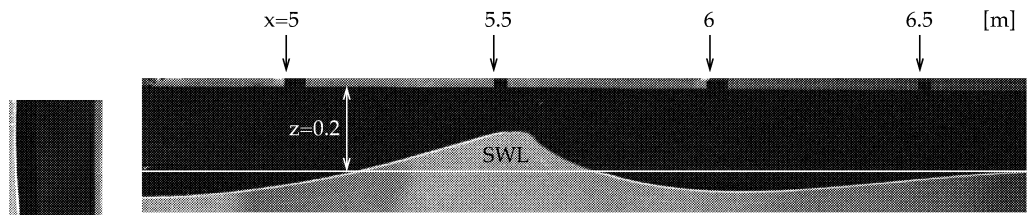


FIGURE 49. Reference marks in the image. The physical coordinates are resolved from the position of known physical points in the image.

Another important detail is that the image contains information of a reference frame, making it possible to convert pixel coordinates in the image to physical coordinates. By introducing at least two reference points in the image where the physical coordinates are known, it is possible to derive the physical position of all other points in the image¹. The points are introduced in the image by placing a bright band with black marks for each half meter on the front of the glass 20cm above SWL. The band is carefully aligned so that it is parallel to the SWL, and it runs continuously through the section where the measurements are taken. Figure 49 shows the band together with the physical coordinates of the marks. The principle of coordinate transformation was described in *Chapter 2.6.4*.

The image acquisition equipment is identical to the one used in the PIV applications (described in *Chapter 2.5*). The image acquisition system consists of camera, lens, film, trigger control and scanner. The sampling interval is also 1/32s, and this is achieved in the same way as for the PIV measurements, i.e., by doing subsequent runs, and shifting the trigger time and camera position for each run. When the film is digitized, the resolution is approximately 2 mm in physical coordinates, i.e., each pixel covered 2x2 mm² of physical scale. Shutter time and aperture are 1/125s and 2.8, respectively.

The camera is positioned 3.5 meters from the tank side, and this allows 2.2m of the flume to be captured on the film. This is as far from the tank as the laboratory environment permits. It is sufficient, but in some cases the whole wave geometry does not fit into one image frame. This is the reason why some parameters have fewer measurement points than others. A wider field of view can be accomplished by using a shorter focal length, or by using two cameras, taking pictures of different parts of the flume. Both these methods have disad-

1. This is only applicable in 2D, and in the case were all physical points studied are located in a plane that is parallel to the image plane (film plane).

vantages. When using a shorter focal length, the distortion of the recorded image increases, introducing systematic errors in the measurements. If two cameras are used, it is important that they are triggered at the same time. With mechanical shutters there is an uncertainty in the triggering time. This could cause problems, as the two images have to be matched to find the whole geometry.

The vertical position of the camera is 30 cm below SWL, and the camera is pointed perpendicular to the flume walls. This is to assure that only the silhouette of the wave is shown in the image, and no 3D effects are visible. The camera is focused on the wet surface of the glass wall closest to the camera, and the measured geometry are actually the contact line between the free surface and the wall. The horizontal camera position are shifted for each exposure, keeping the wave geometry at the same relative position in the image.

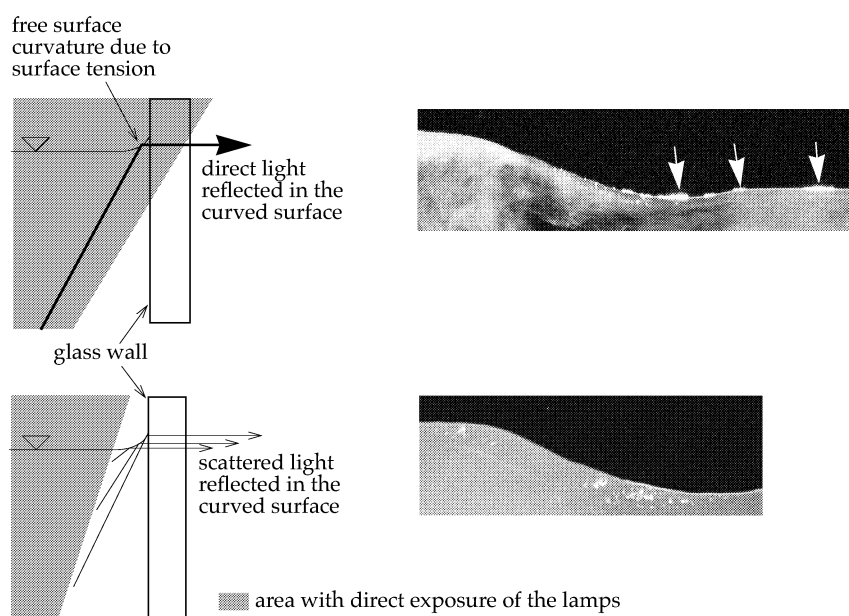


FIGURE 50. Bumps on the free surface due to surface tension effects. The top picture is taken without shielding the light, and the arrows mark the spots where the direct light from the lamps is reflected to the camera due to the curvature of the free surface. The bottom picture is taken after the lights have been shielded, and only scattered light is reflected. The intensity of the scattered light is much less than the direct light, and causes no spots on the free surface.

Due to the surface tension of the water, the surface tends to stick to any surface it interacts with, including the glass walls of the flume. Because of this curvature, the light from the lamps is reflected directly into the camera causing the air-water interface to look extremely bright in several spots on the free surface (Fig. 50, top). Diffraction in

the camera lens causes these spots to appear as bumps on the free surface, and this again causes measurement errors in the surface tracking algorithm. The problem is solved by shielding the light so that the area where the free surface interacts with the walls are not directly exposed by the lamp (Fig. 50, bottom). No direct light, only scattered light is reflected to the camera, and the spots on the free surface are avoided.

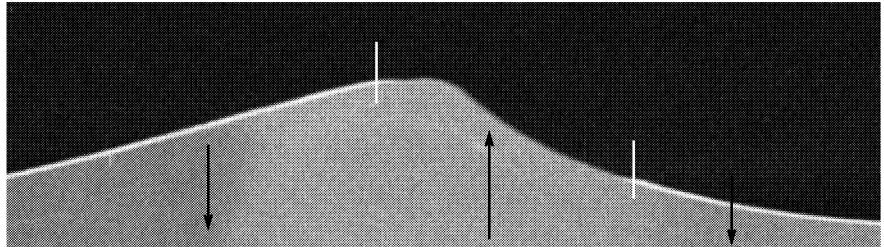


FIGURE 51. Effect of the surface tension on the free surface visualisation. The black arrows indicate the vertical water movement, and the white marks indicate where the movement shifts direction (shifting point). In the area where the water is moving down the surface curves upwards, and this area becomes bright due to the reflection of the scattered light. In the area with upward water movement the surface curves downward, and no light is reflected.

However, the surface curvature causes additional problems. The interface between the water and glass curves downward when the water is moving up, and upward when the water is moving down. The effect of this is illustrated in Figure 51, where the interface between air and water becomes bright where the surface interface curves upward. This introduces a systematic error in the measurements, and limits the accuracy of the measurements of the free surface coordinates to $\pm 1\text{mm}$. It results in the trough points being overestimated by approximately 1mm. It may also lead to uncertainty in the zero-crossing points if the point where the vertical movement shifts direction (shifting point) is located at SWL. The derivative and curvature of the free surface are only influenced at the shifting points, and the shifting point seldom coincides with the inflection points and maximum crest curvature point, where the first and second derivatives are evaluated. As this is a systematic error it is possible to compensate for it in the tracing algorithm. This was not done here. The effects were, however, taken into account when the parameters in the b-spline fit were optimized (see *Chapter 3.3.2*) and therefore partly compensated for.

As stated earlier, it is the contact line between the free surface and the glass which is taken to be the wave geometry, and this is a main disadvantage of the procedure. An improvement would be to

3.1 Space Domain Wave Geometry

use a vertical laser sheet perpendicular to the wave crests similar to the one used in the PIV recordings, and to measure the geometry from the silhouette of the wave in the sheet, as done by Duncan et al. (1999). This would eliminate the errors caused by the surface tension effects. The method was not implemented due to lack of proper equipment. Since the width of the measurement area is significantly larger (approximately 2m) than for the PIV measurements (50cm), the PIV illumination system could not be used.

3.1.2 Digital Image Processing

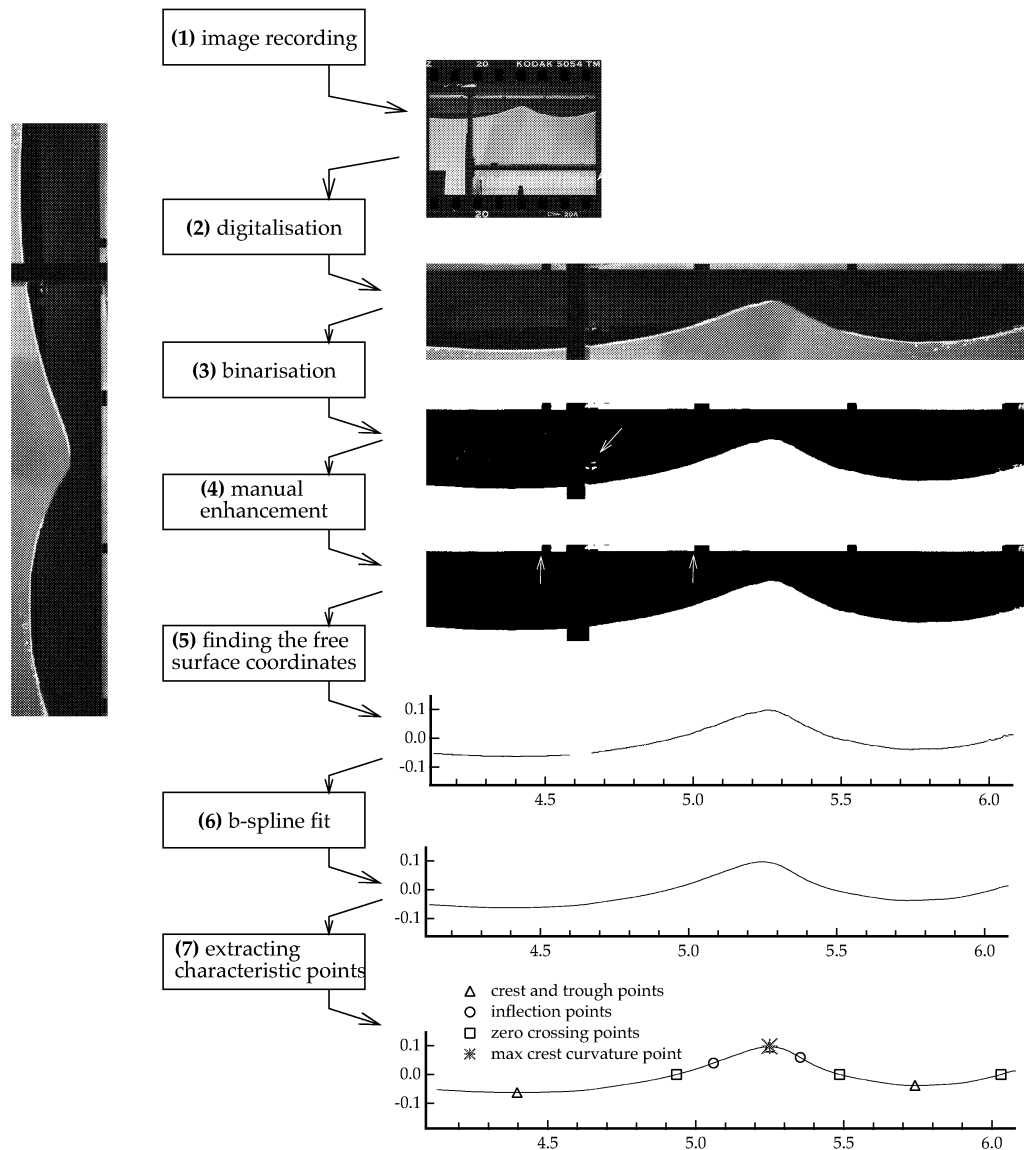


FIGURE 52. The digital image processing and analysis routine.

Once the image is captured on film (1), the digital image processing and analysis are conducted. The steps in the digital image process are shown in Figure 52, and will be described in the following. The first step is to digitize the image (2), preparing it for computer analysis. This is done with a Nikon Coolscan II film scanner. The

resolution of the scanner is 106 pixel/mm, and it has a grayscale resolution of 8 bits (256 levels).

The image is then converted into a binary image (3). This is done because it simplifies the subsequent manual image enhancement, which will be explained later. The binarisation has the disadvantage that information is lost. Accuracy on sub pixel level is impossible in a binary image. This limits the resolution of the measurements to the image resolution. As the image resolution is high this is a minor problem, but if the image resolution was lower an algorithm that uses the gray scale image to find the location of the free surface with sub pixel resolution should be used.

Each pixel in the image has an intensity value from 0 to 1, where 0 is black, and 1 is white. In the gray scale image the intensity value of each pixel has 256 levels between 0 and 1. Water is bright (high intensity), and air is black (low intensity). The free surface can be detected as the position where the intensity makes a jump between low and high values. Due to disturbances in the image, bright spots can appear above the free surface, creating unwanted intensity jumps (the arrow marks such a spot in Fig. 52). These spots make the automatic free surface detection difficult. In the binary image these spots are easily identified, and can be removed manually (4).

The free surface coordinates are then extracted from the binary image (5). This is done in three steps: i) The pixel coordinates¹ of the free surface are detected by searching for spots where the intensity shifts from 0 to 1. ii) The pixel coordinates of the reference points² are detected. The lower left corners of the black marks on the top edge of the image are the reference points (indicated by arrows in Fig. 52). iii) The pixel coordinates are transformed to physical coordinates. This can be done when both the pixel and the physical coordinates of the reference points are known (see *Chapter 2.6.4*).

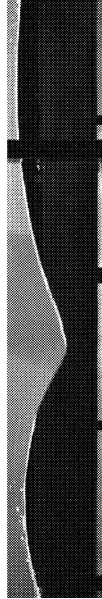
Once the free surface coordinates are found, the next step is to find the characteristic points on the free surface. The first step in this process was to fit a b-spline to the free surface coordinates (6). The b-spline is a semi-analytic function, and its derivatives can easily be found. The derivatives are required for calculating the characteristic points, as well as the wave parameters (see *Chapter 3.4*). The use of b-spline will be described in *Chapter 3.3*.

Once the b-spline and its derivatives are found, the characteristic points and wave parameters are calculated (7). The characteristic

1. The pixel coordinates are the coordinates of the different pixels in the image. The origin is at the upper left corner of the image, and the pixel in this corner has the pixel coordinates (1,1); the pixel to its right has coordinates (1,2); and so on.

2. The reference points are described on page 84.

points (crest point, trough points, inflection points and zero-crossing points) are identified by first computing 50 points evenly distributed over the b-spline curve fit. From these points a first approximation of the points is found. The first and second derivative are used to find the crest, trough and inflection points, respectively. Newton interpolation was used to find the location of the points with high accuracy.



3.2 Time Domain Wave Geometry

The time domain measurements of the geometry is done by using surface piercing wave gauges. The gauges consist of two vertical parallel rods (electrodes), 3mm in diameter, and 12.5mm apart. The electrodes are self-carrying, so no supporting structure is needed. A wave height meter module (amplifier) from Danish Hydraulic Institute based on measurements of the conductivity between the parallel electrodes is used. The signal is logged to a computer with a sampling frequency of 16 Hz.

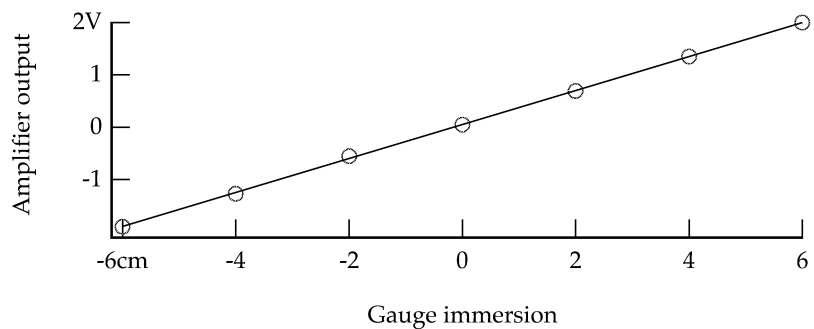


FIGURE 53. Example of calibration curve for the wave gauges used in the time domain wave geometry measurements. The squares are measurement points, and the line is linear. The steepness of the line is the calibration constant [cm/V], which is used to compute the surface elevation from the amplifier output.

One important feature of the wave gauges is the linearity between the signal from the amplifier and the actual surface elevation. The signal from the gauges is assumed to be linear, and the signal (in volts) is multiplied with the calibration constant (in meter/volts) to get the wave elevation (in meter). If the relationship between the signal and the surface elevation is non-linear, this would introduce a systematic error. Figure 53 shows an example of the calibration. A linear curve fit is made, and the calibration constant is the derivative of the linear fit. The linear correlation coefficient is 0.9999,

3.2 Time Domain Wave Geometry

and the wave gauges can be considered linear. The error estimate (standard deviation) for the calibration constant is less than 0.3mm. The wave gauges were re-calibrated each day to assure that drift in the amplifier gain does not disturb the measurements.

The zero level of the amplifiers has a tendency to drift between each run, creating an unwanted offset in the time series. To compensate for this, the mean of each time series is subtracted from the series itself, and thus compensating for the zero level drift.

Another effect that limits the accuracy of the wave gauge measurements is the surface tension effect. The surface tension makes the free surface stick to any hard surface it interacts with. It also sticks to the wave gauges, so that it curves upwards if the water is moving down, and downwards if the water is moving up. This effect causes an uncertainty in the measurements of approximately 1mm. Dirt on the wave gauges can have an influence on the surface tension effect, and the gauges were cleaned each day to assure stable conditions.

Measurements with wave gauges were done at several positions over the flume length. The positions are given in Figure 54.

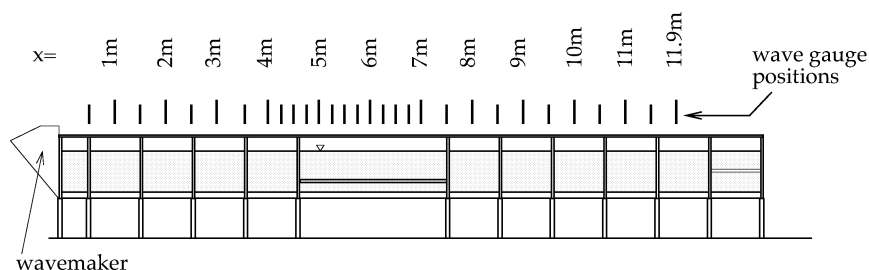


FIGURE 54. Positions of the wave gauges in the flume. Space domain measurements were taken each 50cm from $x=0.5\text{m}$ to $x=11.5\text{m}$. In the area from $x=4\text{m}$ to $x=7\text{m}$ measurements were taken each 25cm as this was the breaking zone.

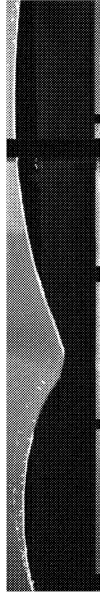
Only two wave gauges/amplifiers were available, and in order to do the measurements at different positions, the wave were repeated several times, taking measurements at different locations in each run.

The measurements are analysed both in the time domain and the frequency domain. In the time domain the wave crest that eventually breaks is identified in the time series measured at each position in the flume, and the wave geometry is analysed using the same routine as for the space domain geometry, i.e., by fitting a b-spline to the measurements and extracting the geometry parameters from the b-spline fit. In the frequency domain the spectral density is found at each position, and the zeroth spectral moment is calculated.

3.3 B-spline Curve Fit

B-spline curves are used in the analysis of the space and time domain free surface geometry and will be described in this section. The b-spline is fitted to the free surface measurements, and characteristic points on the free surface are identified by using the b-spline curve. The main motivation for using the b-spline as a curve fit is that it is easy to find the derivatives of the curve. This feature is particularly useful since the first and second derivatives are used in the free surface analysis. The b-spline has also the advantage that it is a semi-analytic function, and an infinite number of points on the curve can be computed, making it possible to represent the free surface with high resolution.

In this section the theory of b-spline curves is briefly summarised. The theory can be found in Rogers and Adams (1990). Parameters that influence the behaviour of the curve are identified, and the process of choosing optimal values of these parameters are also described.



3.3.1 B-spline Basics

The b-spline curve is a parametric curve of the form

$$\begin{aligned}x &= x(t) \\z &= z(t)\end{aligned}\tag{25}$$

where t is a parameter increasing monotonously along the length of the curve. The functions $x(t)$, $z(t)$ are represented by a sum of weighted polynomials $N_{i,k}$ of order k .

$$\begin{aligned}x(t) &= \sum_{i=1}^{N_{vp}} N_{i,k}(t) X_i \\z(t) &= \sum_{i=1}^{N_{vp}} N_{i,k}(t) Z_i\end{aligned}\tag{26}$$

Here X_i and Z_i are the vertices (or weights), and $N_{i,k}$ is called the basis functions. The basis functions are polynomials of degree $n = k - 1$. N_{vp} is the number of vertices which the b-spline consists of. N_{vp} and k are the two parameters that influence the b-spline fit behaviour relative to the data series. In the next subsection a parameter analysis is presented that shows how these parameters affect the fit, and how the value of these parameters were chosen.

The basis functions are found by using the Cox-deBor recursive formula given in Equation 27.

$$N_{i,1}(t) = \begin{cases} 1 & T_i \leq t < T_{i+1} \\ 0 & \text{else} \end{cases} \quad (27)$$

$$N_{i,k}(t) = \frac{(t-T_i)N_{i,k-1}(t)}{T_{i+k-1}-T_i} + \frac{(T_{i+k}-t)N_{i+1,k-1}(t)}{T_{i+k}-T_{i+1}}$$

Here $N_{i,k}$ is the i 'th basis function of order k , t is the parametric variable and T_i is the knot vector. The elements in the knot vector are in increasing order, i.e., $T_i \leq T_{i+1}$, and the spacing between each point in the knot vector can be chosen freely. From Equation 27 it is obvious that the knot vector spacing has an influence on the b-spline behaviour. The knot vector configuration should therefore be considered carefully on the basis of what kind of data the b-spline is fitted to. For areas in the knot vector with tighter spacing, the b-spline fit will follow the data closer. This could be used to adjust and optimize the fit, so that a minimum of the original information is lost.

When fitting a b-spline curve to a data series, an equation system must be solved to find the vertices X_i and Z_i . Here the analysed data series are coordinates of the free surface given as (x_j, z_j) , $j = 1 \dots N_d$ (N_d is the number of measurement points). The equation system to be solved is given in Equations 28 and 29:

$$\begin{bmatrix} x_1 \\ \vdots \\ x_{N_d} \end{bmatrix} = \begin{bmatrix} N_{1,k}(t_1) & \dots & N_{N_{vp},k}(t_1) \\ \vdots & & \\ N_{1,k}(t_{N_d}) & & N_{N_{vp},k}(t_{N_d}) \end{bmatrix} \begin{bmatrix} X_1 \\ \vdots \\ X_{N_{vp}} \end{bmatrix} \quad (28)$$

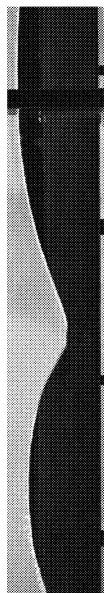
$$\begin{bmatrix} z_1 \\ \vdots \\ z_{N_d} \end{bmatrix} = \begin{bmatrix} N_{1,k}(t_1) & \dots & N_{N_{vp},k}(t_1) \\ \vdots & & \vdots \\ N_{1,k}(t_{N_d}) & \dots & N_{N_{vp},k}(t_{N_d}) \end{bmatrix} \begin{bmatrix} Z_1 \\ \vdots \\ Z_{N_{vp}} \end{bmatrix} \quad (29)$$

Once the vertices X_i and Z_i are found, the b-spline coordinates can be calculated by using Equation 26.

As we see from Equation 26, X_i and Z_i are constants, and thus the derivatives of the curve can be found by differentiating the basis functions. This provides an easy and unique way to find the derivatives of the curve. The first and second derivatives of the basis function are given in Equations 30 and 31, respectively:

$$N'_{i,1} = 0 \text{ for all } t$$

$$N'_{i,k} = \frac{N_{i,k-1}(t) + (t - T_i)N'_{i,k-1}(t)}{T_{i+k-1} - T_i} + \frac{(T_{i+k} - t)N'_{i+1,k-1}(t) - N_{i+1,k-1}(t)}{T_{i+k} - T_{i+1}} \quad (30)$$



$$\left. \begin{aligned} N''_{i,1}(t) &= 0 \\ N''_{i,2}(t) &= 0 \end{aligned} \right\} \text{for all } t$$

$$N''_{i,k}(t) = \frac{2N'_{i,k-1}(t) + (t - T_i)N''_{i,k-1}(t)}{T_{i+k-1} - T_i} + \frac{(T_{i+k} - t)N''_{i+1,k-1}(t) - 2N'_{i+1,k-1}(t)}{T_{i+k} - T_{i+1}} \quad (31)$$

The first and second derivatives of x and z with respect to t are now given by

$$\frac{dx}{dt} = \sum_{i=1}^{N_{vp}} N'_{i,k}(t)X_i \quad (32)$$

$$\frac{dz}{dt} = \sum_{i=1}^{N_{vp}} N'_{i,k}(t)Z_i$$

and

$$\frac{d^2x}{dt^2} = \sum_{i=1}^{N_{vp}} N''_{i,k}(t)X_i \quad (33)$$

$$\frac{d^2z}{dt^2} = \sum_{i=1}^{N_{vp}} N''_{i,k}(t)Z_i$$

The first and second derivatives of z with respect to x can then be found by substitution:

$$\frac{dz}{dx} = \frac{\left(\frac{dz}{dt}\right)}{\left(\frac{dx}{dt}\right)} \quad (34)$$

$$\frac{d^2 z}{dx^2} = \frac{\frac{d^2 z}{dt^2} \frac{dx}{dt} + \frac{dz}{dt} \frac{d^2 x}{dt^2}}{\left(\frac{dx}{dt}\right)^3} \quad (35)$$

3.3.2 B-Spline Parameters

As stated in the previous section, the behaviour of the b-spline fit is influenced by several parameters. It is important that these parameters are chosen carefully to assure that essential information contained in the original data is not lost by the fit. At the same time the b-spline will also serve as a filter removing noise from the measurements, and the choice of parameters influences this filtering.

The parameters influencing the b-spline fit behaviour are the number of vertices N_{vp} , and the order of the basis functions k . In addition the configuration of the knot vector will affect the fit behaviour. The knot vector is chosen to have equal spacing, as this simplifies the process, making all the steps in the geometry analysis easy to describe and to reproduce uniquely.

The influence of the parameters N_{vp} and k on the b-spline fit is illustrated in Figures 55 and 56. In Figure 55 a b-spline is fitted to a data set that consists of 50 points over one wave length of a pure sinusoidal signal. Several different values of N_{vp} and k are used, and the b-spline with first and second derivatives are plotted. From Figure 55 it is clear that an increase in both N_{vp} and k yields better results. An increase in N_{vp} makes the b-spline fit to follow the data points tighter (if $N_{vp} = N_d$ the b-spline is forced to pass through each data point). Increasing the order of the basis function k results in a smoother curve. This conclusion follows from observing the second derivative of the curves with $N_{vp} = 10$. As k increases, the second derivative becomes smoother. This is because an increase in k not only increases the order of the polynomials used in the basis function, but it also increases the number of vertices used to compute each point on the b-spline.

As the data in this case where an ideal signal without any noise, the way to optimize the fit is to increase N_{vp} and k as much as possible. However, a real signal contains noise, and some of the motivation to use a b-spline curve fit is to filter out this noise. Figure 56 shows a b-spline fitted to a sine signal where random noise has been added. The presence of noise has a profound effect on the quality of the fit. The b-spline fit with the highest N_{vp} follows the data points tight, and the noise is transferred from the data to the fit. This results in a

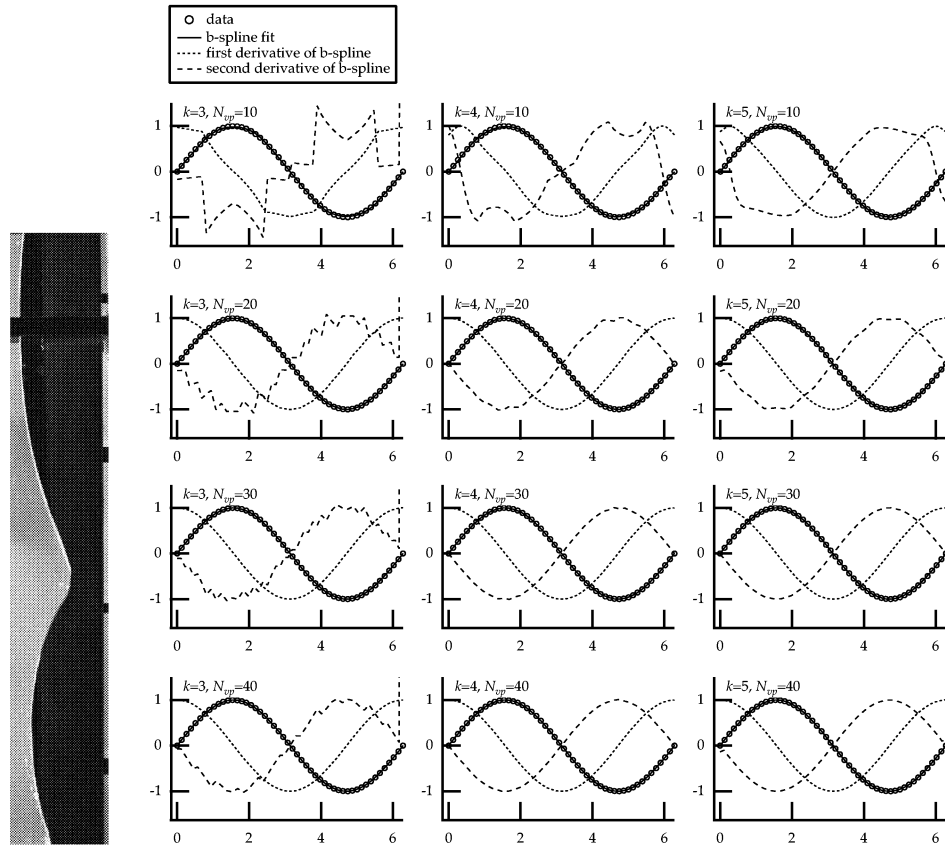


FIGURE 55. B-spline fitted to a sine signal. 50 points over one wave length is used as data points ($N_d = 50$).

second derivative with a high degree of inaccuracy. Increasing N_{vp} results in less noise filtering.

No conclusion can be made based on these two tests to which parameter values to choose. The noiseless signal suggests a large N_{vp} , while the noisy signal suggests a small N_{vp} . As the presence of the noise is important, test cases with representative noise must be used to find the parameters.

The b-spline fit is used both in the analysis of the space and time domain geometry. The measurements of the time domain geometry has approximately thirty data points ($N_d \approx 30$). The number of data points are governed by the sampling frequency (16 Hz). The number of vetices N_{vp} is chosen to be $2/3$ of N_d , and this choice is based on the upper limit for a optimal solution of the equation system. The order of the basis functions is chosen as $k = 4$.

3.3 B-spline Curve Fit

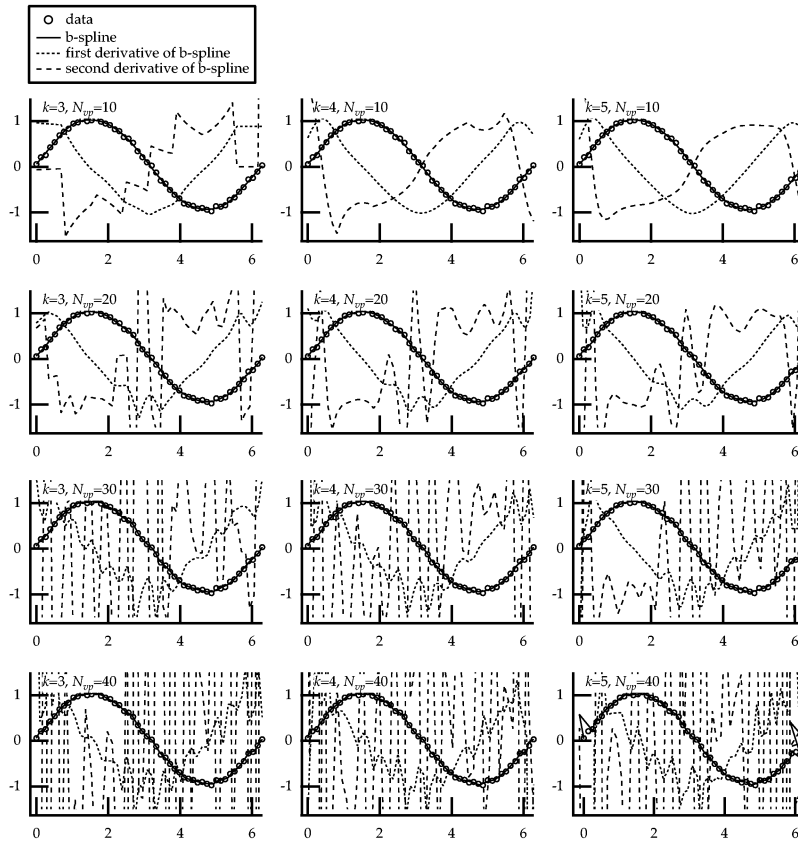


FIGURE 56. B-spline fitted to a sine signal with random noise. 50 points over one wave length is used as data points ($N_d = 50$).

The space domain geometry measurements have approximately 1000 data points, and an analysis is conducted to find the best choice of parameters. A 4th order polynomial is established to resemble a measured free surface profile of an asymmetric wave (Fig. 57). In addition a regular sine wave scaled to have representative wave length and wave height is used as a test case. The analysis is used on surface geometries that start as a regular symmetric wave and evolve to steep asymmetric waves. The sine function and the polynomial are chosen as they represent both these wave geometries; a symmetric and an asymmetric wave, respectively. A digitization of the test cases is simulated to get the same digitized resolution as for the real measurements. Noise that is representative for the measurements is added using a random generator. Care is taken to make sure that the artificial noise is similar to the noise contained in the real measurements. Several different pairs of parameters are tested. Each pair is run ten

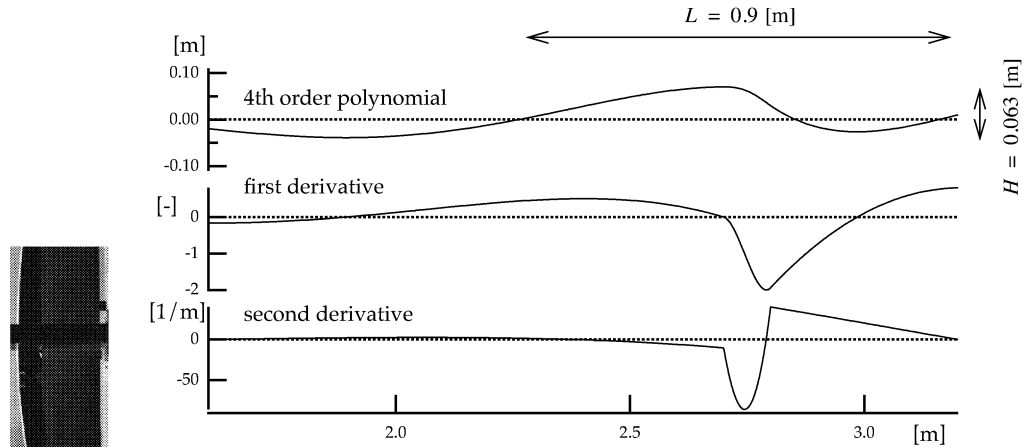


FIGURE 57. Polynomial of 4th order established to resemble the space domain free surface profile of a steep asymmetric wave equal to the real ones studied. The polynomial was used as a test case to find the correct choice of b-spline parameters.

times with different random noise. This is done to test how sensitive the fit is to random noise. The tests are evaluated by finding the significant points on the free surface as described in Figures 59 and 61. The coordinates of the points, the derivatives in the inflection points and the second derivative in the maximum curvature point are found from the curve fit and compared with the correct values. These two tests are made in addition to a third test conducted on a measured profile. No correct answer exists for the real case, so the evaluation is done by manual inspection. The conclusion from these three tests is that the best overall pair of parameters is $k=4$ and $N_{vp}=40$. This pair is used when finding the crest, trough, zero-crossing and inflection points. When finding the maximum crest curvature point, $k=4$ and $N_{vp}=20$ is used instead, since this give better result for the second derivative (se Fig. 56).

3.3.3 Accuracy

The accuracy of the space domain wave parameters calculated from the b-spline fit is assessed by using the same 4th order polynomial as is used to find the b-spline parameters. Random noise comparable to the noise experienced in the measurements is generated and added to the polynomial. In addition the free surface tension effect (see *Chapter 3.1.1*) is simulated.

The characteristic points (as described in Figs. 59 and 61) on the free surface are found using the b-spline analysis, and the result is compared with the known values from the polynomials. Ten such

3.3 B-spline Curve Fit

TABLE 6. Error estimates of the b-spline analysis. The RMS values of the error for the localization of characteristic points on the free surface. The points are described in *Chapter 3.4*.

Point	Property	Error estimate (RMS value) ^a
Crest point	x coordinate	4.1 % of L
	z coordinate	5.8 % of H
Front trough point	x coordinate	2.9 % of L
	z coordinate	6.3 % of H
Rear trough point	x coordinate	2.3 % of L
	z coordinate	7.2 % of H
Front inflection point	x coordinate	1.2 % of L
	z coordinate	10.2 % of H
	steepness	7.7 % of correct value
Rear inflection point	x coordinate	2.0 % of L
	z coordinate	10.5 % of H
	steepness	4.0 % of correct value
Zero-crossing point 1	x coordinate	2.4 % of L
Zero-crossing point 2	x coordinate	1.1 % of L
Zero-crossing point 3	x coordinate	1.9 % of L
Max crest curvature point	x coordinate	1.2 % of L
	z coordinate	6.8 % of H
	curvature	23.9 % of correct value

a. The RMS value is given as percentage of the wave length L for the horizontal (x) coordinate, and of the wave height H for the vertical (z) coordinate. For the steepness and curvature the RMS value are given as percentage of the correct value.

simulations are conducted with different random noise, and the RMS (Root-Mean-Square) of the error is computed.

The results are presented in Table 6. The RMS values are given as percentage of the wave length for the horizontal (x) coordinate, and of the wave height for the vertical (z) coordinate. For the steepness and curvature the RMS values are given as percentage of the correct value.

The position of the crest, trough and zero-crossing points are found with a higher degree of accuracy than the inflection and maximum curvature points, and especially the maximum curvature has

low accuracy. Thus the measurements of the individual maximum curvature and inflection point steepness are not very reliable.

3.4 Wave Geometry Parameters

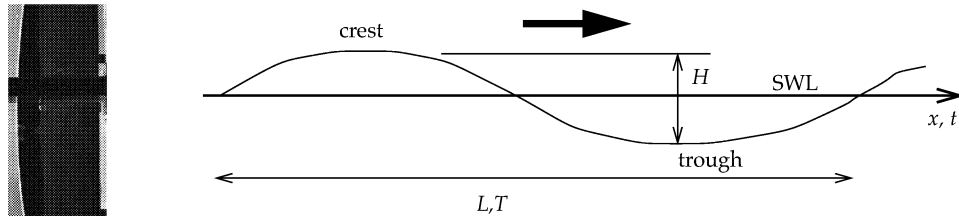


FIGURE 58. Parameters describing the wave geometry in linear wave theory

Figure 58 shows parameters describing a sinusoidal shaped wave. The wave length (L) describes the space domain periodicity of the wave, the wave period (T) describes the time domain periodicity, and the wave height (H) is the vertical distance between the trough, and the following crest. The ratio between the wave height and the wave length is denoted the total wave steepness s , and is given by $s = H/L$. If the wave steepness is small, the wave is described by linear wave theory, and the surface elevation is a sinusoidal function (regular waves), or a sum of sinusoidal functions (irregular waves). For a linear regular wave the geometry is uniquely described by the three parameters T , L and H .

3.4.1 Zero-Downcross Parameters

Zero-downcross analysis is based on defining the wave between two zero-downcross points (time domain geometry). This means the crest, and preceding trough. For waves with higher steepness s the non-linear effects play a more important role. As the steepness increases the free surface deviates more and more from the sinusoidal profile. Waves that approach breaking are usually steep, and their geometry is not sinusoidal. The crest becomes higher and the trough more shallow making the wave horizontally asymmetric. For transient waves the crest is shifted forward relative to the trough point and is closer to the front trough point than to the rear trough point. Hence the geometry of a breaking wave is no longer described by the three parameters T , L and H , and additional parameters are needed to characterize the geometry.

3.4 Wave Geometry Parameters

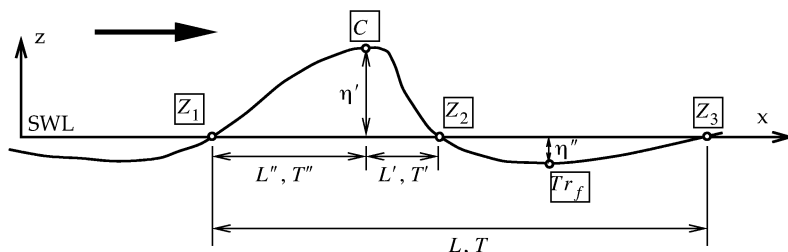
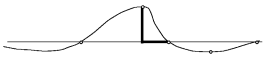
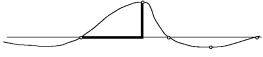
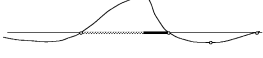



FIGURE 59. Points on the free surface used in the zero-downcross analysis: Zero-crossing points (Z_1 , Z_2 and Z_3), crest point (C) and front trough point (Tr_f).

TABLE 7. Zero-downcross parameters (Kjeldsen and Myrhaug, 1978; Myrhaug and Dahle, 1994).

Parameter	Space domain	Time domain	Linear wave value	
Crest front steepness ε		$\varepsilon = \frac{\eta'}{L'}$	$\varepsilon = \frac{\eta'}{C_w T'}$	$2\frac{H}{L}$
Crest rear steepness δ		$\delta = \frac{\eta'}{L''}$	$\delta = \frac{\eta'}{C_w T''}$	$2\frac{H}{L}$
Vertical asymmetry factor λ		$\lambda = \frac{L''}{L'}$	$\lambda = \frac{T''}{T'}$	1
Horizontal asymmetry factor μ		$\mu = \frac{\eta'}{H}$	$\mu = \frac{\eta'}{H}$	$\frac{1}{2}$

Kjeldsen and Myrhaug (1978) defined parameters based on the zero-downcross analysis to describe the space domain geometry of a two dimensional asymmetric transient wave. These parameters describe the local mean wave steepness at the front and rear of the crest. They also describe the horizontal and vertical asymmetry of the wave. The parameters are derived from the location of five points on the free surface (Fig. 59): Zero-crossing points (Z_1 , Z_2 and Z_3), crest point (C) and front trough point (Tr_f). The parameters are given in Table 7.

The parameters describe the space domain geometry, but they may be estimated from time domain measurements if the phase velocity C_w is known. In this work several wave gauges in the propagating direction are used to record the time domain geometry, and the phase velocity can be found from the measurements. With one wave

gauge, and the phase velocity unknown the linear dispersion relation in deep water, $L = gT^2/2\pi$, can be used.

The time domain representations are only accurate if the wave geometry is constant in time ($\partial\eta'/\partial t = 0$, where η' is the free surface coordinates in a coordinate system moving with the wave). If the wave is highly transient, this will introduce inaccuracies in the estimation of the parameters from the time domain measurements.

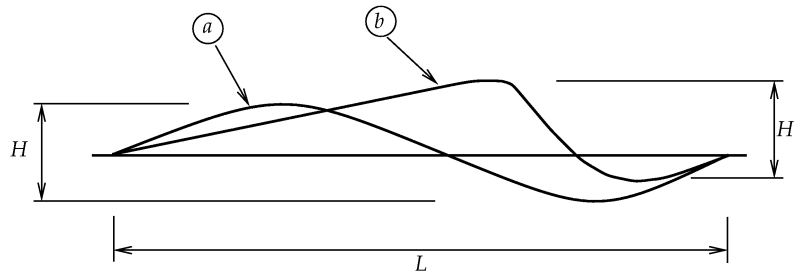
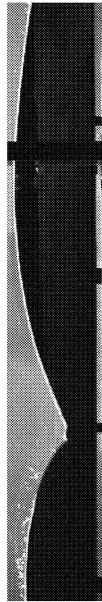


FIGURE 60. Two waves with the same steepness s .

The importance of these additional parameters are illustrated in Figure 60, where two waves with the same length, height and steepness are shown. It is obvious that it is impossible to distinguish between these two waves by using T , L and H . Wave b has both horizontal and vertical asymmetry, and is steeper in the front than in the rear. The zero-downcross parameters discloses these properties.

The parameters have been used in several studies to investigate the evolution of progressive waves up to the onset of, and beyond, breaking (e.g. Kjeldsen and Myrhaug, 1980; Holthuijsen and Herbers, 1986; Myrhaug and Kjeldsen, 1986; Bonmarin, 1989). However, it has not been possible to establish a breaking criterion using these parameters. Due to the physics in the breaking process it is impossible to predict if a wave will break or not based on the development of the geometry of a single wave in a small time interval (less than two wave periods). To predict what happens it may be necessary to consider a wave group over a longer time period. Tulin and Li (1992) concluded that the phenomena underlying the formation of wave groups may control the inception of breaking. Another possibility might be that the parameters do not describe the physical properties of the wave well enough. Therefore it is useful to try to establish parameters that better describe the physics, and correlate with the kinematics in a breaking wave.

3.4.2 Inflection Point Parameters

In the zero-downcross analysis all parameters are derived by the location of the three zero-crossing points, the crest point and the trough point. The geometry between these points are not described, and it could be questioned whether the locations of these points are capable of reflecting all important properties of the wave geometry. When measuring the geometry we are interested in estimating the kinematics from the geometry measurements. Geometry is easy to measure compared to kinematics, which are practically impossible in nature - at sea. It is the knowledge of the wave kinematics that make us capable of estimating the influence a wave will have on its environment. The free surface geometry and the internal kinematics are closely connected, as given from the free surface conditions. A better understanding of the internal kinematics could therefore be established if significant features of the wave geometry are known, and the coupling between the geometry and the kinematics is known. Therefore the parameters used to describe the geometry of a wave should reflect features of the geometry most likely to reveal the internal kinematics.

Which parameters should be considered? Which points on the free surface should be used? In linear wave theory the geometry and internal kinematics is known for a sinusoidal wave. This is used as a guide for choosing the free surface points to base the parameters on. The points are shown in Figure 61.

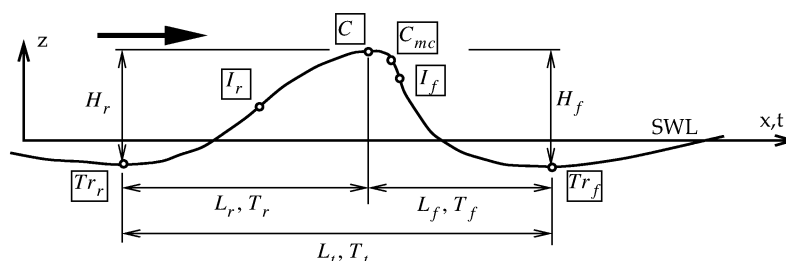


FIGURE 61. Points on the free surface used in the inflection point analysis: Front and rear inflection points (I_f and I_r), front and rear trough points (Tr_f and Tr_r), crest point (C) and maximum crest curvature point (C_{mc}).

Crest point and trough points. These points are obviously important. For a linear wave the horizontal velocity and vertical acceleration have their maxima at these points, and the wave energy can be estimated from the location of these points.

Maximum crest curvature point. In linear wave theory the point on the crest with maximum curvature (the curvature is quanti-

fied by the second spatial derivative) coalesces with the crest point, for which the horizontal velocity and vertical acceleration have its maxima. For a transient and asymmetric wave the crest point is not necessarily the point with the highest curvature. Therefore, in addition to using the crest point, the point on the crest with maximum curvature may be important. In addition, points with high curvature on the free surface could intuitively be the starting points for instabilities that cause foam generation and eventually spilling breakers.

The inflection points. The vertical velocity and the horizontal acceleration in a linear wave have their maxima at the inflection points¹ of the surface, making the inflection points also significant regarding the wave kinematics.

The zero-crossing points, however, may be less important regarding the physics of the wave, as they depend on the zero level used in the analysis. In the laboratory SWL is commonly used as zero level, but in sea measurements there is no SWL. Here the mean water level (MWL) is used. Then the question rises: Should the MWL be taken as the mean over one, or several periods, or the whole ensemble? The parameters based on the zero-crossings may be biased by this choice, and for this reason the zero-crossing points are not used in the additional parameters suggested here. The the new parameters are given in Table 8.

In the zero-downcross analysis only the location of the points was considered, and properties such as the first and second derivatives (steepness and curvature) of the surface in these points were not studied. Steepness parameters were merely estimates of the mean steepness between two points, obtained from the location of the points, e.g. the crest front steepness is calculated from the position of the crest point and the zero-downcross point in front of the wave. In the new parameters the steepness parameters used are the derivative of the surface at the inflection points, i.e., the point with the highest steepness between the troughs and the crest. These parameters are called *front inflection point steepness*, s_{if} , and *rear inflection point steepness*, s_{ir} . Thus s_{if} and s_{ir} yield a quantitative description of the steepest part of the surface.

It is convenient to have parameters that are constants in linear theory, because it gives a reference point for the development of the parameters. In linear theory the front/back inflection point steepness is equal to πs , where s is the steepness. Since s is time dependent for a transient wave, it is difficult to compare this with linear theory. A new parameter is defined by dividing with the *front/back wave steepness*.

1. The inflection point is where the second derivative is zero, i.e., yielding maximum/minimum derivative, or in other words maximum steepness.



3.4 Wave Geometry Parameters


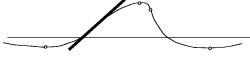

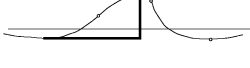




These parameters are called *front/back steepness coefficients* (c_{fs} , c_{rs}), and are equal to $\pi/2$ in linear theory.

The curvature of the free surface has not yet been a subject for investigation, but it should be considered when the surface geometry is analysed, since the curvature is an important property of the free surface. The parameter denoted the *maximum crest curvature* c_{max} is used to quantify and characterize the curvature. c_{max} is the second spatial derivative of the free surface at the maximum crest curvature point, which is the highest second spatial derivative between the two inflection points.

Both the vertical and horizontal asymmetry factors defined by Kjeldsen and Myrhaug (1978) use the zero-crossing points. Three new parameters characterizing the asymmetry of the wave without using the zero-crossing points are suggested here: The *wave steepness asymmetry factor* a_s , the *wave length asymmetry factor* a_l and the *wave height asymmetry factor* a_h . See Table 8 for definitions.

3 Wave Geometry Measurements

TABLE 8. Wave parameters in the inflection point analysis.

Parameter	Space domain	Time domain	Linear wave value	
Front inflection point steepness s_{if}		$s_{if} = \left \frac{\partial \eta}{\partial x} \right _{l_f}$	$s_{if} = \frac{1}{C_w} \left \frac{\partial \eta}{\partial t} \right _{l_f}$	$\pi \frac{H}{L}$
Rear inflection point steepness s_{ir}		$s_{ir} = \left \frac{\partial \eta}{\partial x} \right _{l_r}$	$s_{ir} = \frac{1}{C_w} \left \frac{\partial \eta}{\partial t} \right _{l_r}$	$\pi \frac{H}{L}$
Front wave steepness s_f		$s_f = \frac{H_f}{L_f}$	$s_f = \frac{H_f}{C_w T_f}$	$2 \frac{H}{L}$
Rear wave steepness s_r		$s_r = \frac{H_r}{L_r}$	$s_r = \frac{H_r}{C_w T_r}$	$2 \frac{H}{L}$
Front steepness coefficient c_{fs}		$c_{fs} = \frac{s_{if}}{s_f}$	$c_{fs} = \frac{s_{if}}{s_f}$	$\frac{\pi}{2}$
Rear steepness coefficient c_{rs}		$c_{rs} = \frac{s_{ir}}{s_r}$	$c_{rs} = \frac{s_{ir}}{s_r}$	$\frac{\pi}{2}$
Max crest curvature c_{max}		$c_{max} = \left \frac{\partial^2 \eta}{\partial x^2} \right _{C_{mc}}$	$c_{max} = \frac{1}{C_w^2} \left \frac{\partial^2 \eta}{\partial t^2} \right _{C_{mc}}$	$2\pi^2 \frac{H}{L^2}$
Wave steepness asymmetry factor a_s		$a_s = \frac{s_{if}}{s_{ir}}$		1
Wave length asymmetry factor a_l		$a_l = \frac{L_r}{L_f}$	$a_l = \frac{T_r}{T_f}$	1
Wave height asymmetry factor a_h		$a_h = \frac{H_f}{H_r}$	$a_h = \frac{H_f}{H_r}$	1

3.5 Chapter Summary

The measurements technique used to measure the free surface geometry of the wave was described in this chapter. The space domain geometry was measured using digital image analysis, and the time domain geometry was measured with ordinary wave gauges.

The geometry is analysed using several parameters that describe significant features of the wave, such as local steepness and curvature. In addition to parameters proposed by other authors, a set of new parameters was suggested and described.

As an aid for computing the parameters a b-spline was fitted to the geometry measurements, and the wave geometry parameters were extracted from the b-spline fit. This chapter also contains a summary of basic b-spline theory together with a description of how the b-spline parameters were chosen.



Chapter 4 **Results and Discussion**

In this chapter the results from the measurements of the wave kinematics and geometry of the plunging, intermediate and spilling breaker cases are presented. See *Chapter 1.4.1* for a description of the cases.

The geometry is presented and discussed in the first section, and observations of characteristic geometric features of the wave geometry evolution will be pointed out and discussed. The parameters used in this analysis are described in *Chapter 3.4*. In the second section the wave kinematics measurements are presented and discussed, using the kinematics parameters defined in *Chapter 2.9*.

4.1 Wave Geometry

The geometry measurements presented here are results of experiments conducted with the laboratory setups described in *Chapter 3*. Section 4.1.1 and 4.1.2 contain the basic measurements of the space and time domain geometries. Based on these measurements, several wave geometry parameters (described in *Chapter 3.4*) are calculated, and the findings of this analysis are presented in section 4.1.3.

4.1.1 Space Domain Wave Geometry

Figures 62, 63 and 64 show the time history of the space domain geometry of the three breaking wave cases. As described earlier, the surface profiles are found from analysing images of the wave. The

surface profiles presented in the figures are b-spline functions fitted to the free surface measurements. Because of this, however, it is not possible to identify the foam generation, and the images in Figures 13 to 15 (pages 20-22) should be used in addition to provide a full impression of the post-breaking phase.

Based on Figures 62 to 64 it is possible to obtain an overall qualitative impression of what happens to the geometry as the waves¹ develop into breaking. To start with (at $0.7-0.8T$ before breaking) the wave profiles have an approximate sinusoidal shape. With increasing time the crest above SWL obviously becomes narrower, and the crest develops a horizontal asymmetry with a steeper front than rear. At the breaking point, the wave profiles have a distinctly steeper front than rear. The time it takes for the wave to reach this stage is shorter than the wave period, i.e., in the range $0.7-0.9T$. It is also noticeable that the front trough becomes shallower than the rear trough, adding to the asymmetry of the wave. The difference between the three cases in the pre-breaking phase is not very distinct. The only clear difference is that the horizontal asymmetry is more noticeable for the plunging breaker.



1. When no particular case is mentioned, it applies to all three wave cases. This also applies in the following.

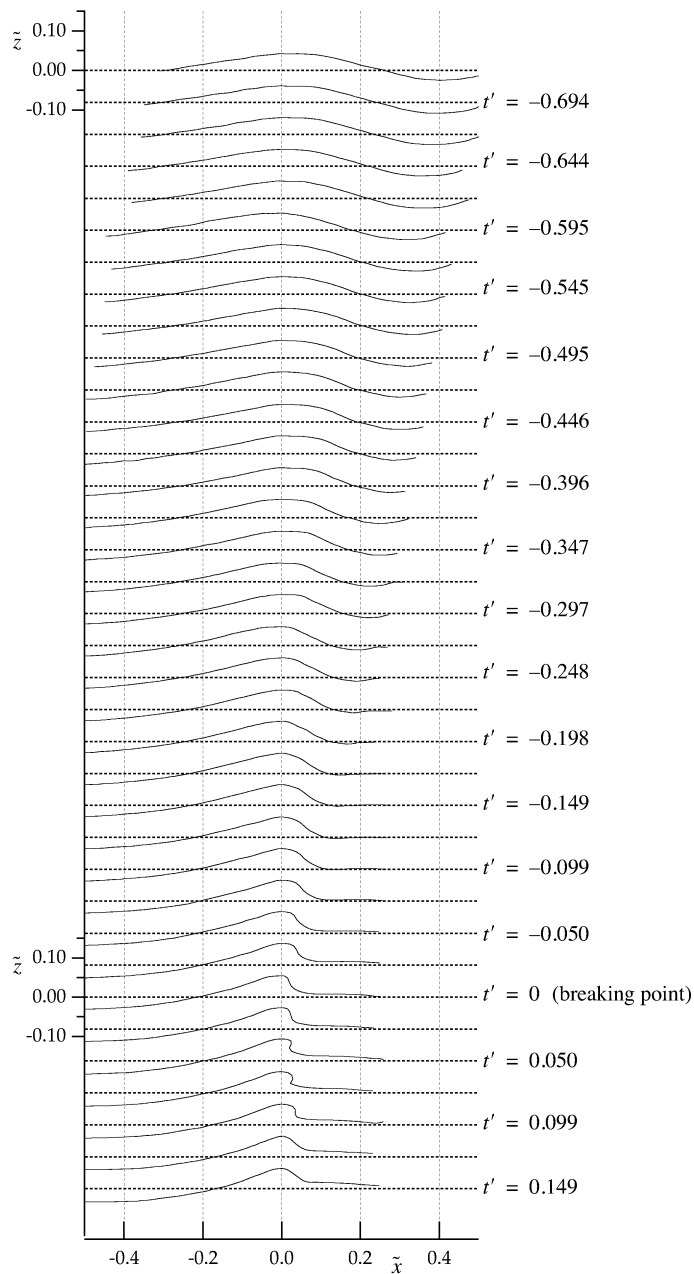


FIGURE 62. Space domain free surface geometry of the plunging breaker (case 1) (see also Fig. 13 on page 20). The frame of reference is wave bound, and origin is always located at the crest point. Horizontal and vertical coordinates are normalized with wave length, and time is normalized with wave period (see *Chapter 2.9.2*).

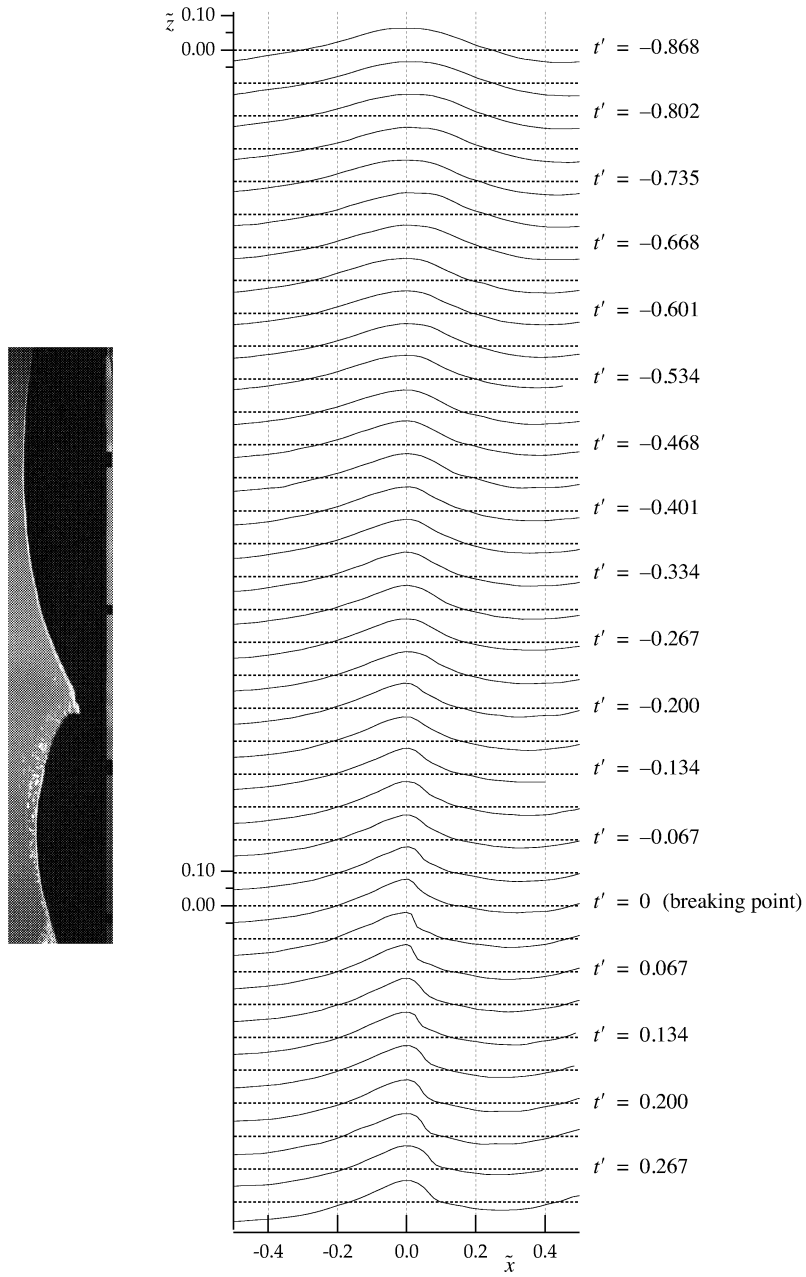


FIGURE 63. Space domain free surface geometry of the intermediate breaker (case 2) (see also Fig. 14 on page 21). Axis as in Figure 62.

4.1 Wave Geometry

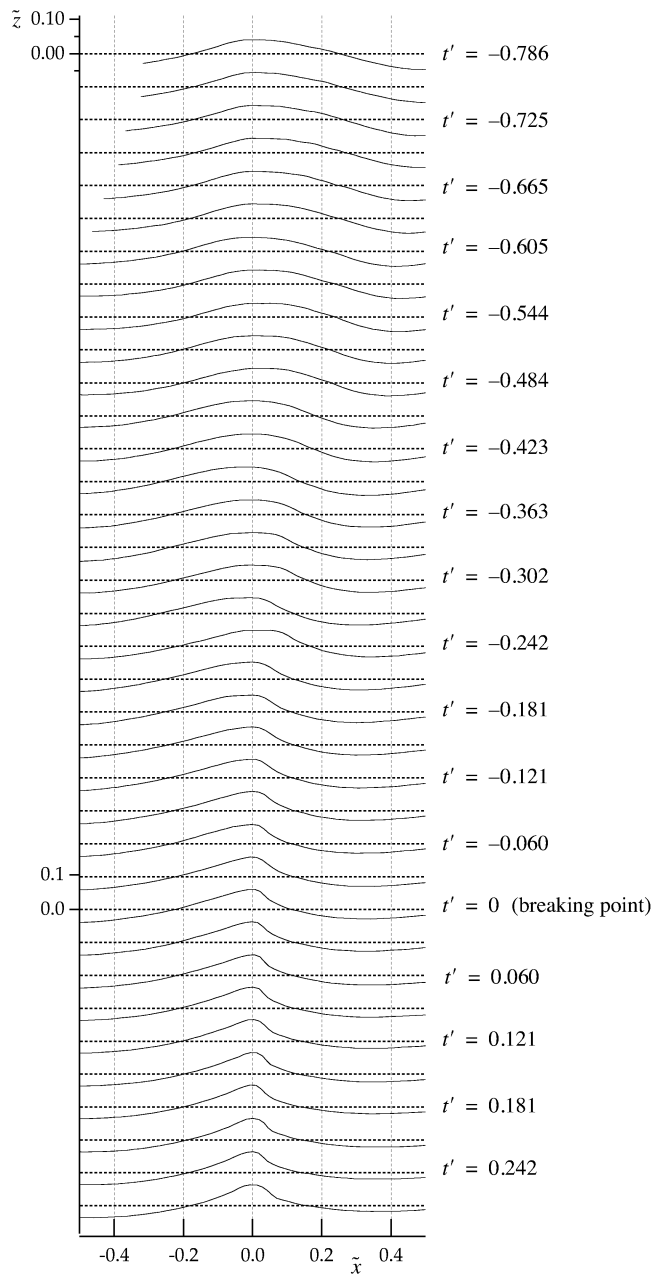


FIGURE 64. Space domain free surface geometry of the spilling breaker (case3) (see also Fig. 15 on page 22). Axis as in Figure 62.

Steepness and Curvature

The steepness and curvature are important properties of the wave geometry, and the first and second spatial derivative of the free surface are the quantitative measures of these features. When observing and discussing the steepness and curvature, it is helpful to use characteristic points on the free surface as reference. Such points have earlier been described in *Chapter 3.4*, and are also shown in Figure 65. In addition to the earlier described points, two additional points are added, helping to characterize the curvature. These are the points of local maximum curvature at the rear (C_{mcr}) and the front (C_{mcf}).

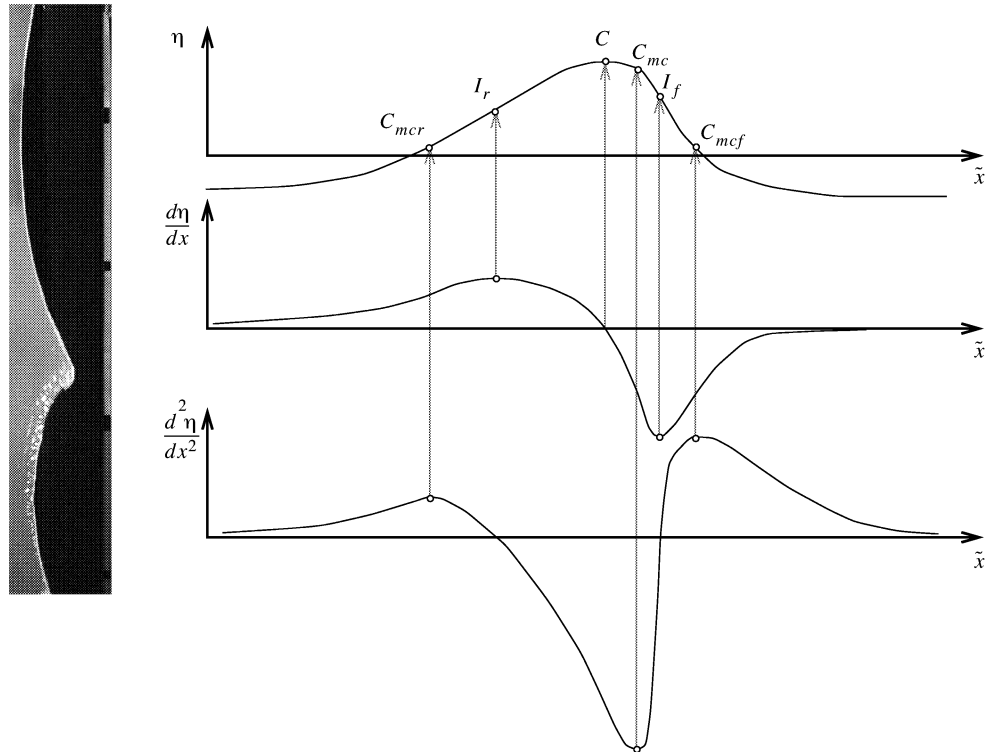


FIGURE 65. Principle description of the free surface geometry with its first and second derivatives. Characteristic points on the free surface used later in the analysis are indicated. These points are the same as described in *Chapter 3.4*, together with the two points of maximum curvature at the rear and the front of the wave (C_{mcr} and C_{mcf}).

Figures 66 to 68 show the free surface spatial derivative of each of the three cases. The derivatives have been calculated from the b-spline function representing the free surface geometry (Figs. 62 to 64) using the method described in *Chapter 3.3*.

Due to noise and inaccuracy the derivative data are not smooth. Especially for the second derivative the noise is noticeable, and the

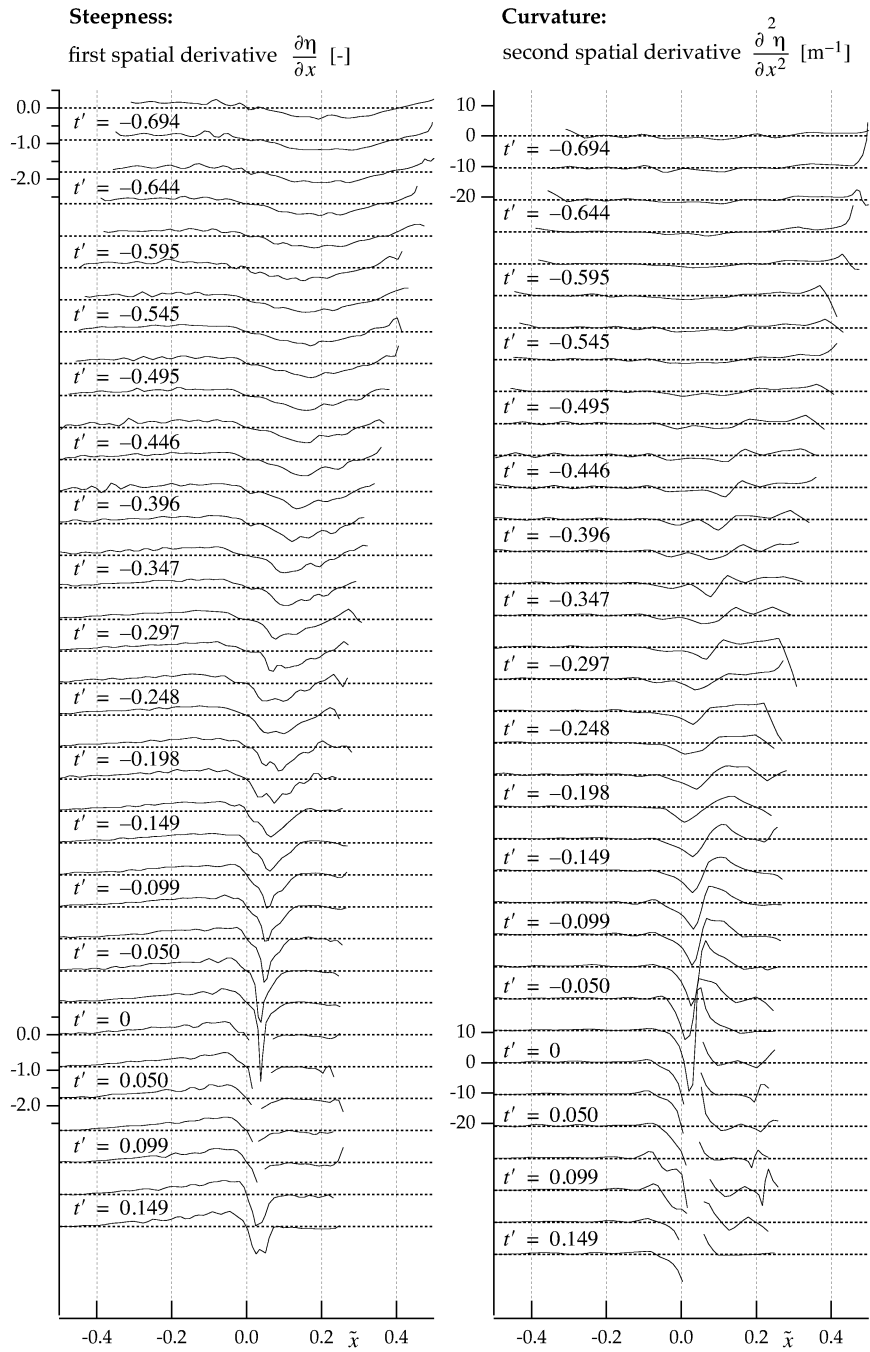


FIGURE 66. Steepness (spatial derivative) and curvature (second spatial derivative) of the free surface for the plunging breaker (case 1). Axis as in Figure 62.

4 Results and Discussion

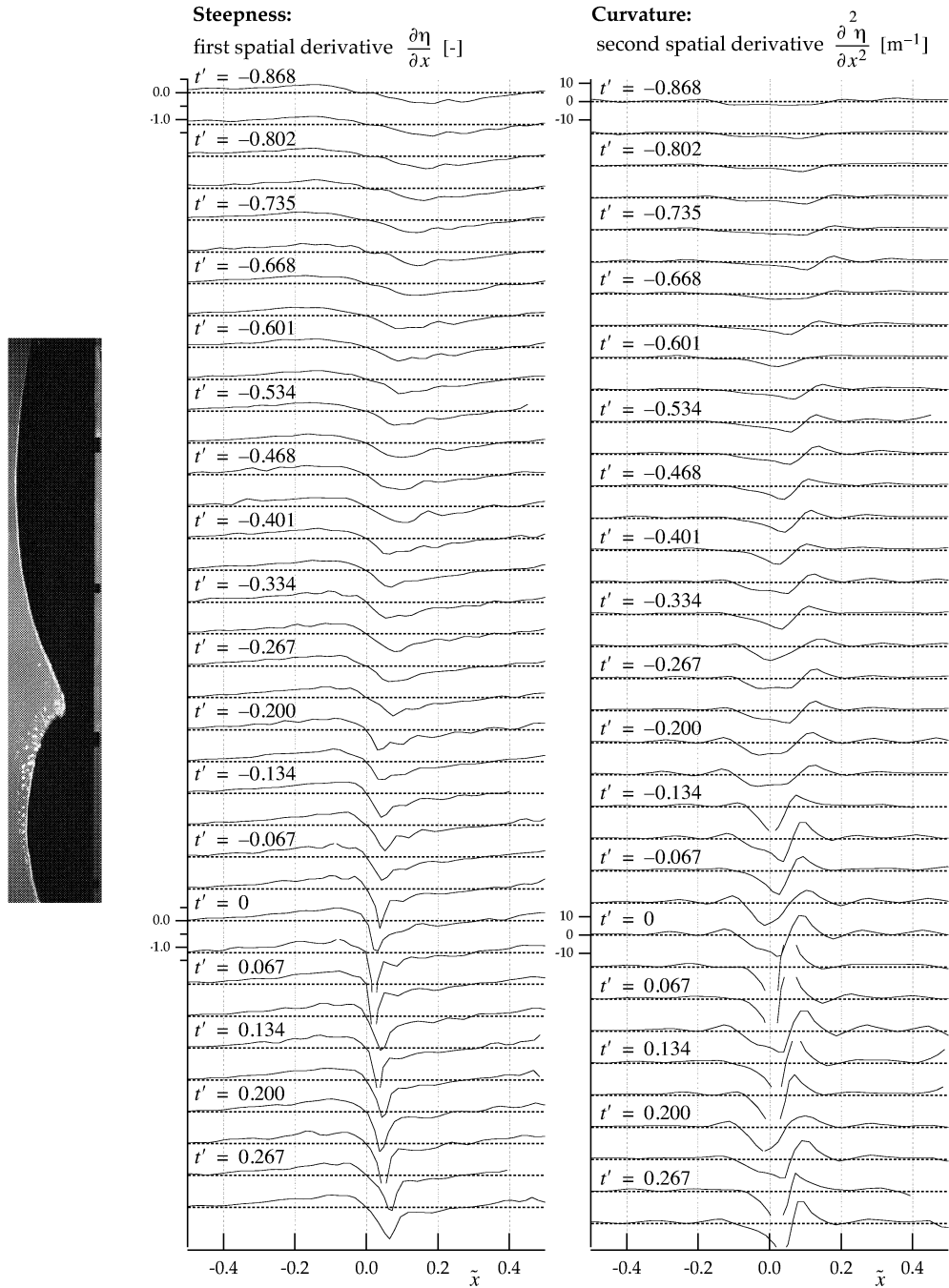


FIGURE 67. Steepness (spatial derivative) and curvature (second spatial derivative) of the free surface for the intermediate breaker (case 2). Axis as in Figure 62.

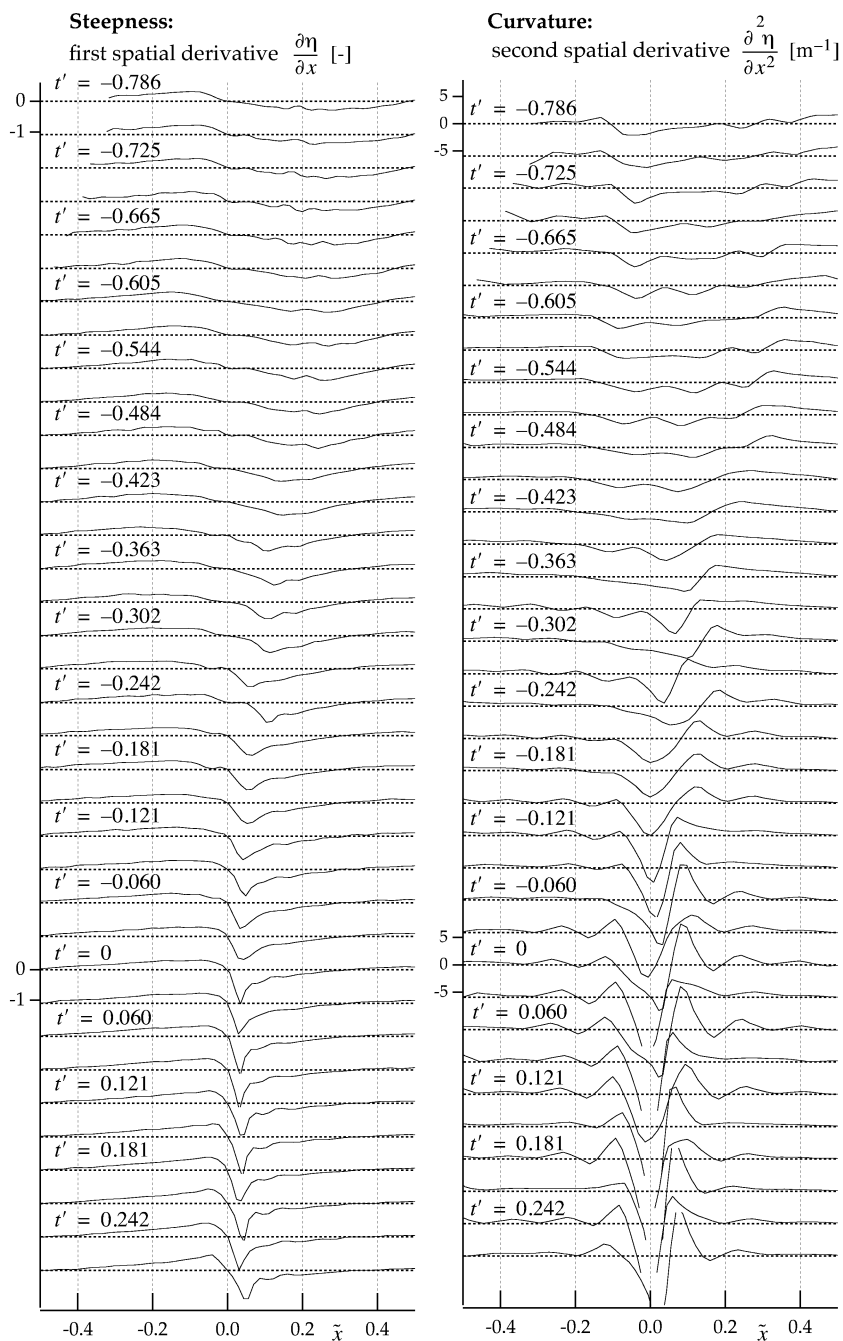
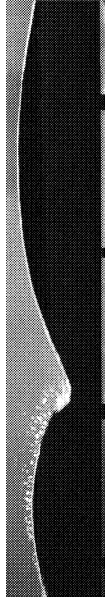


FIGURE 68. Steepness (spatial derivative) and curvature (second spatial derivative) of the free surface for the spilling breaker (case 3).

quality of the curvature data can be questioned. In Table 6 on page 99 error estimates for the b-spline analysis are shown, and it is seen that the curvature has the largest error estimate. It is, however, apparent that even though single measurements of the curvature have large errors, features in the time development and space dependence can be observed from the figures.

The steepness (first derivative) confirms the observations of the free surface development made earlier, e.g. it is clearly observed that the front was steeper than the rear. Based on the derivatives additional observations can be made, which is difficult or impossible to make from the free surface measurements.



The development of the steepness is rather similar for the cases, but the plunging breaker experiences a larger increase in the front face steepness just prior to the breaking point (from $t' \approx -0.15$ to $t' = 0$). This is due to the nature of the plunging breaker: The steepness in the front (at I_f) should theoretically be infinite at breaking, as the front face is vertical at this point.

From the steepness it can also be observed that the point of maximum steepness (I_f) moves closer to the crest point (C) as the waves develop. When the waves are approximately sinusoidal, the maximum steepnesses (I_f and I_r) are located at $x \approx \pm 0.2$ (in linear theory it is 0.25). This applies to both the front and the rear side of the crest. At breaking onset the maximum steepness has moved to approximately $x = -0.08$ and $x = 0.04$, and thus the maximum steepness is closer to the crest point in the front than it is in the rear. This means that both the front and rear face of the waves steepen, and at the same time, the points of maximum steepness (I_f and I_r) move towards each other. Due to this an increased curvature in the crest is inevitable, which is suspected by the increase of the second derivative as the waves evolve. This applies to all the local maximum curvature points (C_{mc} , C_{mcr} and C_{mcf}), but the point with the highest curvature is the point located between the two inflection points I_f and I_r (C_{mc}). The local maximum curvature points C_{mcr} and C_{mcf} on both sides of the crest move towards the crest point, which is also a consequence of the observation made earlier that the crest becomes narrower.

4.1.2 Time Domain Wave Geometry

Measurements of waves in nature are often made by using a wave buoy which measures the time domain development of the surface at a given location. It is seldom that a space domain representation of waves in nature is available. The reason for this is that it is much easier to measure the time domain than the space domain

geometry. Probability models developed to describe the wave environment are therefore usually based on time domain measurements. It is therefore important to consider the time domain geometry versus the space domain geometry.

In this work the measurements of the time domain geometry were done to obtain the connection between the space and time domain geometry, and to find how well the wave geometry parameters could be estimated from the time domain measurements. As the width of the space domain measurements are limited, it is impossible to measure the whole wave group. The time domain measurements, however, give an overview over the whole group, and the development and propagation of the single waves relative to the group is visualized.

The time domain measurements are made by using ordinary wave gauges at several positions in the flume (see *Chapter 3.2* for a description of the laboratory setup). The resulting time series are shown in Figures 69 to 71. The wave crests that eventually break are indicated by rectangular frames.

As the wave group is visualized in the time domain measurements, the methods used to generate the breaking events are clearly illustrated. The plunging and intermediate breakers are generated by focusing a broad-banded wave group, while the spilling breaker is generated by an increase in wave height as the wave crest reaches the front of the monochromatic wave group. A feature of the wave generation method which should be kept in mind, is that the breaking events (at least the spilling and the plunging breakers) take place at the *front* of the group, with little or no wave energy in front of the breaking event. This is different from what usually happens with deep water breaking waves in nature, where the most common case is a breaking event in the middle of a wave group, with wave energy both ahead of and behind the breaking wave.

Another feature that is visible in the time domain measurements is the higher frequency components in the broad-banded wave groups. These components are present prior to breaking, but have vanished after breaking. These waves have been overtaken by the breaking wave.

4 Results and Discussion

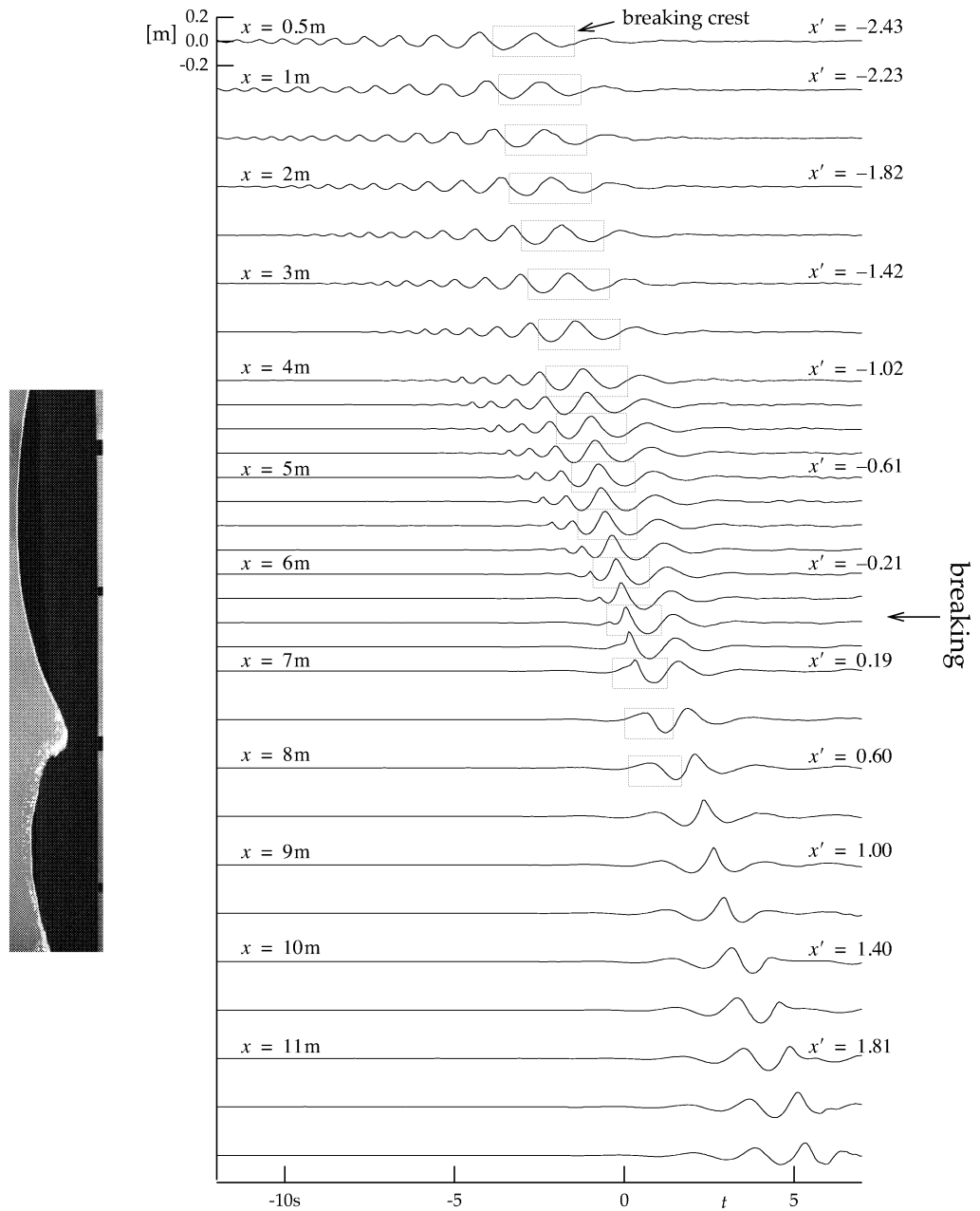


FIGURE 69. Time domain wave geometry of the plunging breaker (case 1). Each time series is measured at different distances from the wave maker, and x is the distance from the wave maker to the wave gauge position. x' is x normalized with the linear wave length, and shifted so that zero is at the position of the breaking point (see *Chapter 2.9.2*). Time t is also shifted so that zero is at the time instance when the wave breaks. The wave crest that eventually breaks is indicated with rectangular frames.

4.1 Wave Geometry

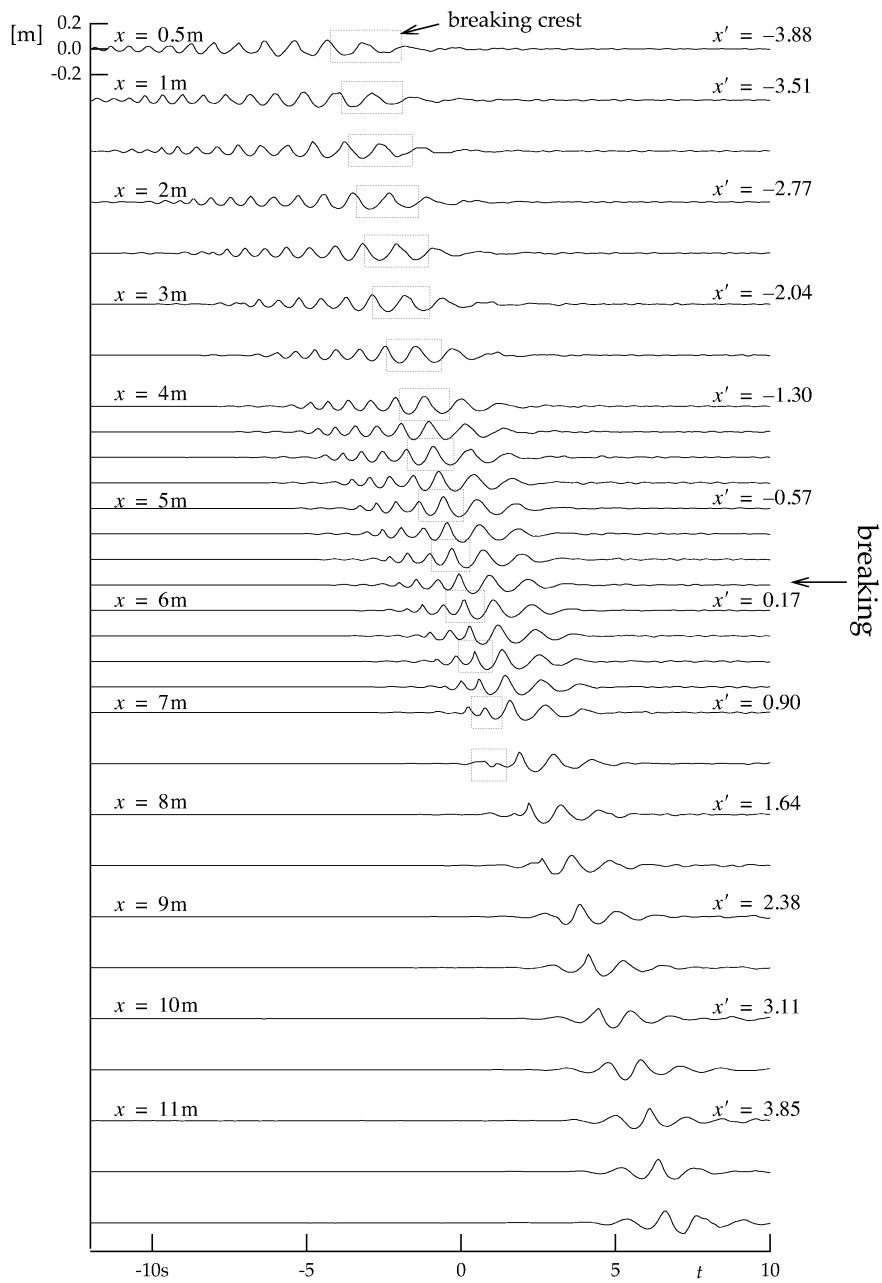


FIGURE 70. Time domain wave geometry of the intermediate breaker (case 2). Axis same as in Figure 69.

4 Results and Discussion

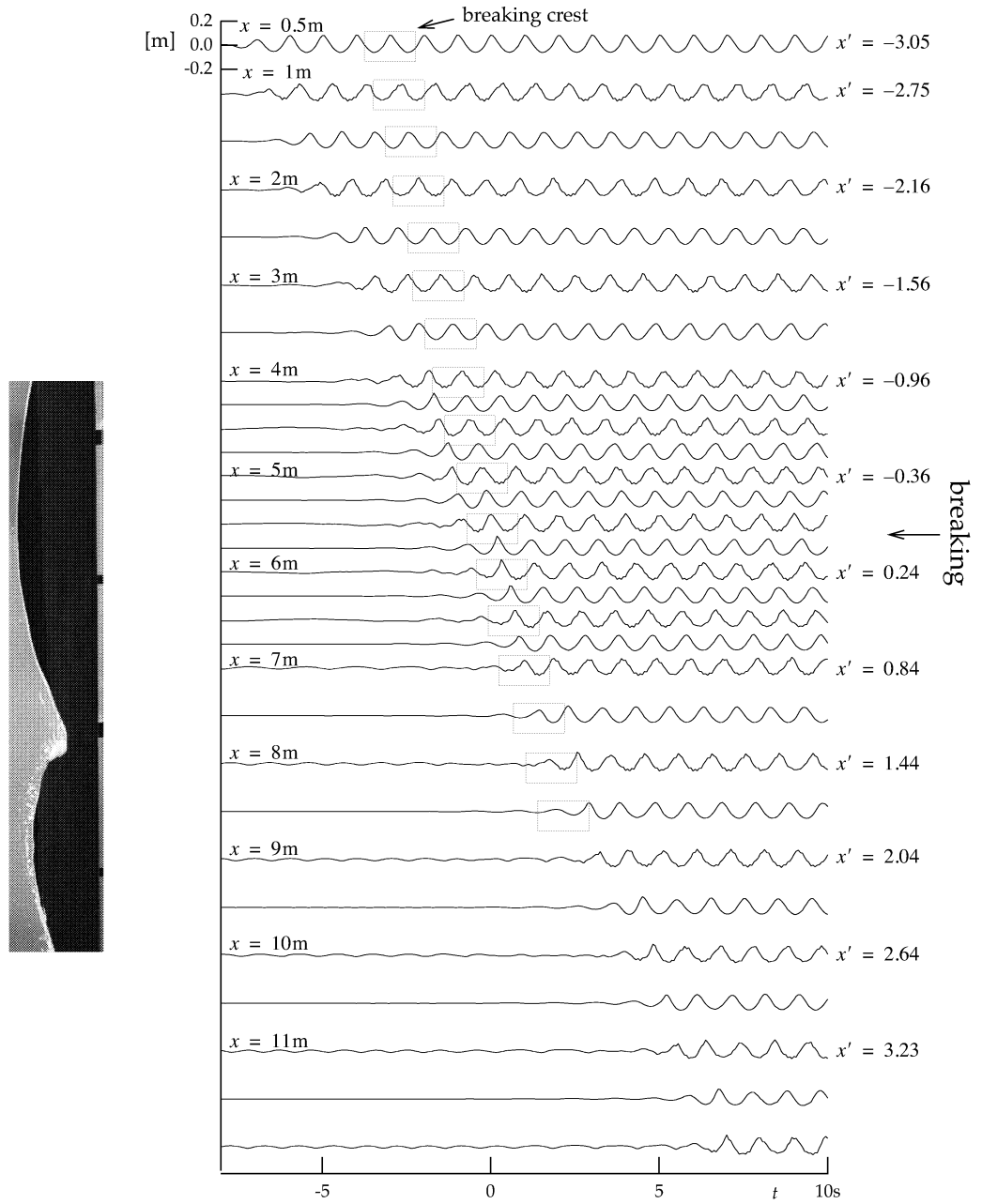


FIGURE 71. Time domain wave geometry of the spilling breaker (case 3). Axis same as in Figure 69.

Frequency Domain Analysis

In a sea state where wave breaking occurs the power spectral density is affected by the breaking, and the breaking will lead to a shift of the peak frequency towards lower frequencies. This phenomenon is called downshifting (Tulin, 1996). The spectral density of the time domain measurements of the broad-band wave cases (the plunging and intermediate breakers) are calculated at each measurement station to study how the spectral density evolves as the wave approaches breaking, breaks and goes through the post-breaking phase. Figures 72 and 73 show the power spectral densities. To better evaluate the time domain changes in the spectrum, the changes relative to the spectral density closest to the wave maker are calculated and shown in the same figures. The zero spectral moment m_0 , representing the total energy in the spectrum is also calculated, and the development of m_0 is shown in Figure 74. The development of the peak frequency is shown in Figure 75.

At frequencies higher than the peak frequency energy is lost for both cases. This was also directly observed from the time series. Apparently this happens gradually, and is not solely connected to the breaking event. This is also supported by the development in the zero spectral moment m_0 (Fig. 74), as m_0 shows a decreasing tendency, which is not uniquely associated with the breaking. For the intermediate breaker m_0 shows a decreasing tendency over the whole measurement range ($x' = -4$ to 0), while for the plunging breaker m_0 is nearly constant up to $x' = -1$ and decreases after. This gradual decrease is probably due to small scale breaking events in the wave groups prior to the main breaking event. Some of this energy is transferred to the lower frequency components. This can partially be caused by a general loss of energy due to viscous damping in the flume.

At frequencies lower than the peak frequency the energy increases. For the plunging breaker this increase seems to originate at the onset of breaking. The peak frequency (Fig. 75) suddenly decreases at the same instant. For the intermediate breaker the low frequency energy increases more gradually, and the peak frequency also shows the same tendency.

The reason for this discrepancy between the two cases can be the difference in the breaking event; the plunging wave occurs suddenly and is more "violent" than the spilling-like intermediate breaker. A spilling breaker has been compared with an avalanche running down the face of the wave, and the energy is released more gradually than for a plunging breaker.

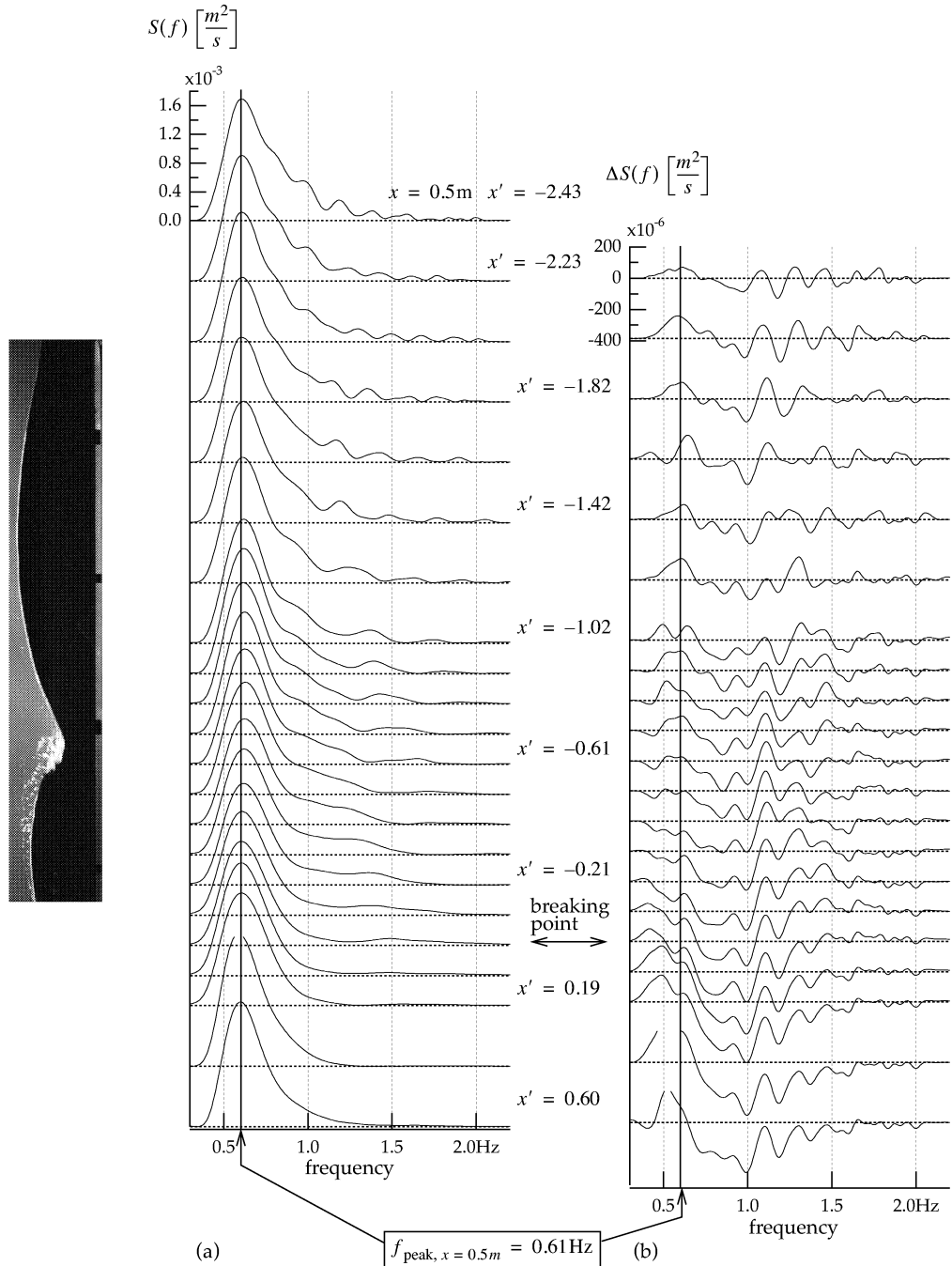


FIGURE 72. (a) Power spectral density $S(f)$ at different x' positions for the plunging breaker (case 1). (b) The change in power spectral density $\Delta S(f)$ relative to the power spectral density at the first position ($x = 0.5m$).

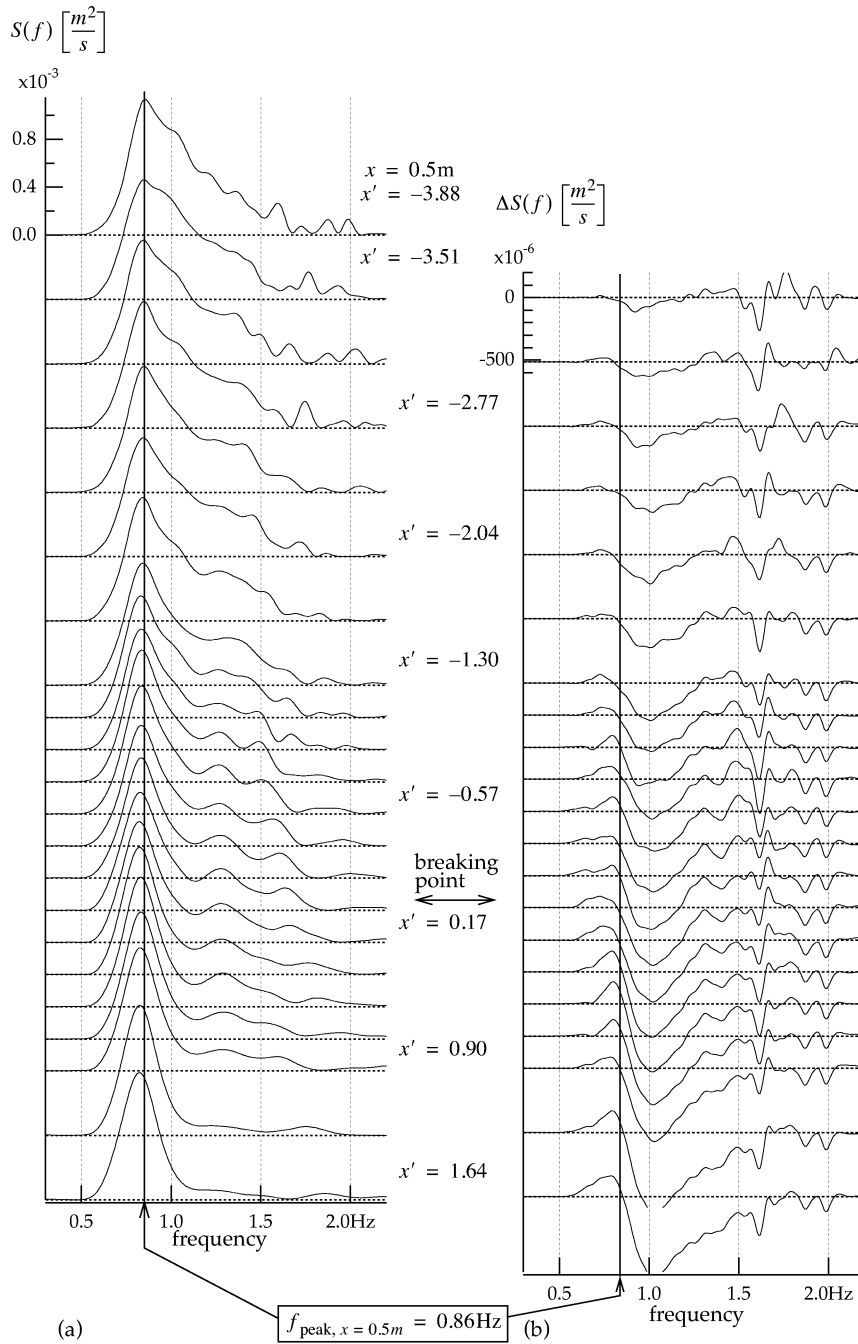


FIGURE 73. (a) Power spectral density $S(f)$ at different x' positions for the intermediate breaker (case 2). (b) The change in power spectral density $\Delta S(f)$ relative to the power spectral density at the first position ($x = 0.5m$).

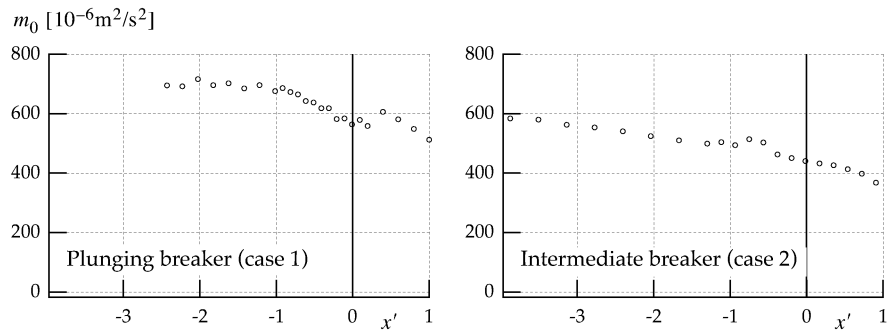


FIGURE 74. Zero spectral moment m_0 as a function of position x' in the wave flume for the plunging and the intermediate breakers. x' is made dimensionless with the mean wave period, and has its origin at the breaking point.

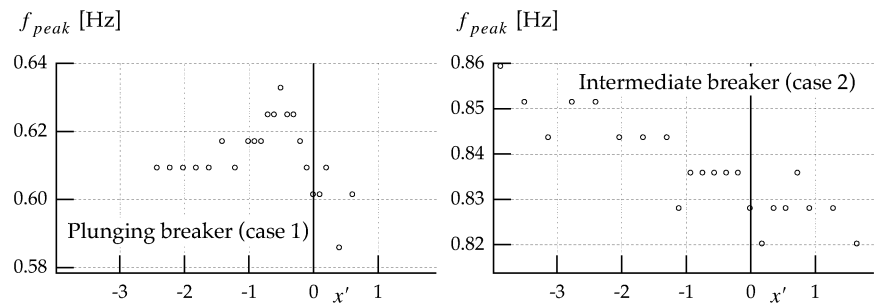
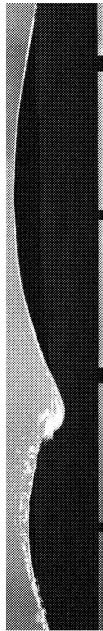


FIGURE 75. The peak frequency f_{peak} of the power spectral density as a function of position x' in the wave flume for the plunging and the intermediate breaker. x' is made dimensionless with the mean wave period, and has its origin at the breaking point.

4.1.3 Geometry Parameters

Based on the measurements of the space and time domain geometry, the wave parameters (described in *Chapter 3.4*) were calculated. These parameters are defined in the space domain, but it is possible to estimate them from the time domain geometry by using the phase velocity of the wave. Both the space and time domain representations of the parameters will be presented here, but if not otherwise specified, it is the space domain representation of the parameters which is considered in the parameter discussion. In the following figures the space domain geometry is to the left, and the time domain geometry is to the right. The abscissa values are t' and x' , which are time t , and horizontal coordinate x normalized with the wave period and the wave length, respectively (see *Chapter 2.9.2*). In addition zero

4.1 Wave Geometry

on the abscissa is located at the breaking point both in space and time. This makes x' and t' analogous coordinates, and the development of the space and time domain parameters should be compared with this in mind. The ordinate is identical for both the space and time domain parameters.

The parameters are divided into three groups: *Basic parameters*, *zero-downcross parameters* and *inflection point parameters*, and will be addressed separately.

Basic Parameters

The basic parameters are *wave length*, *wave height*, *crest height*, *trough depth* and *overall wave steepness*, and are shown in Figures 76 to 83.

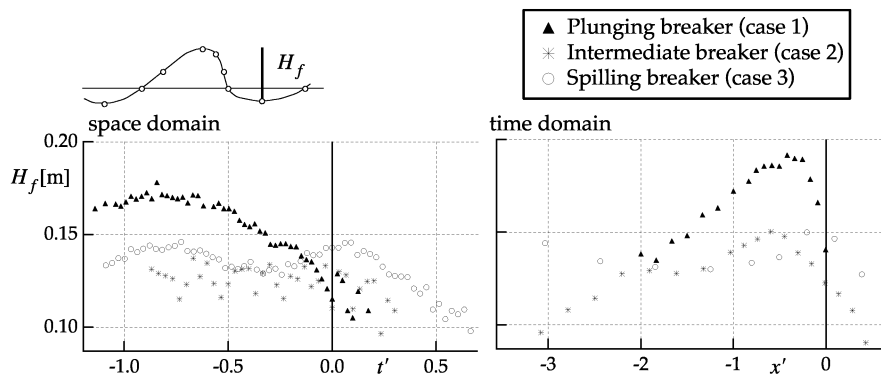


FIGURE 76. Front wave height (H_f). Time t' and horizontal coordinate x' are normalized with wave period and wave length respectively. The origin in both t' and x' are located at the breaking point in both space and time (see *Chapter 2.9.2*).

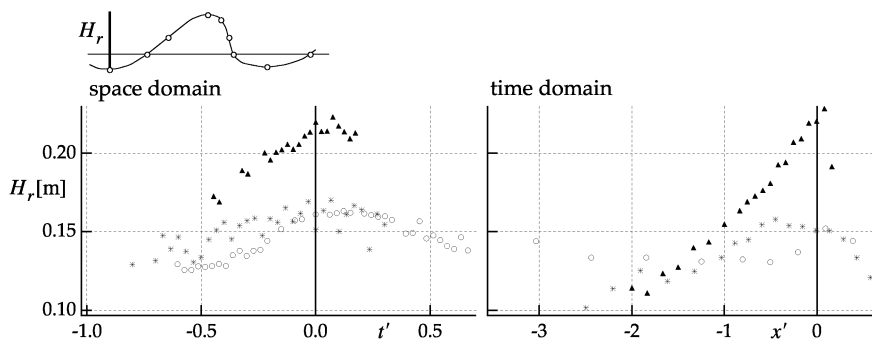


FIGURE 77. Rear wave height (H_r). Legend and axis as in Fig. 76.

4 Results and Discussion

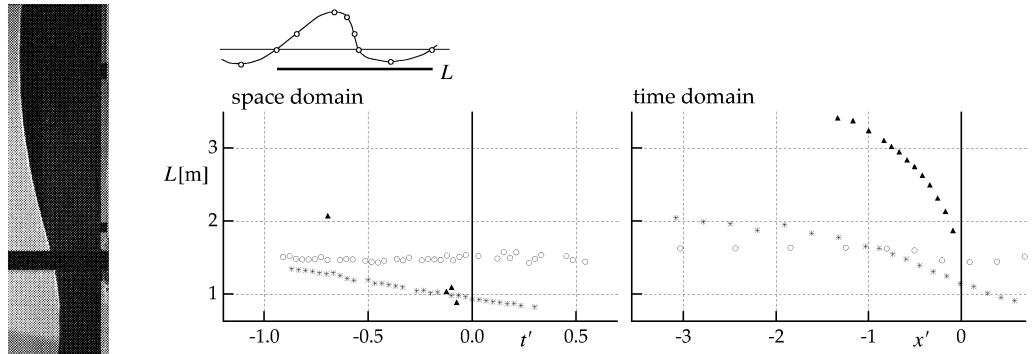


FIGURE 78. Wave length measured between zero down crossings (L). Legend and axis as in Fig. 76 on page 127. (For the plunging breaker the distance between the front zero-crossing point and the rear trough point was too large for both these points to be captured in one frame. The front zero crossing point is therefore absent in most of the frames, and thus only three measurements were made of the time domain wave length for the plunging breaker).

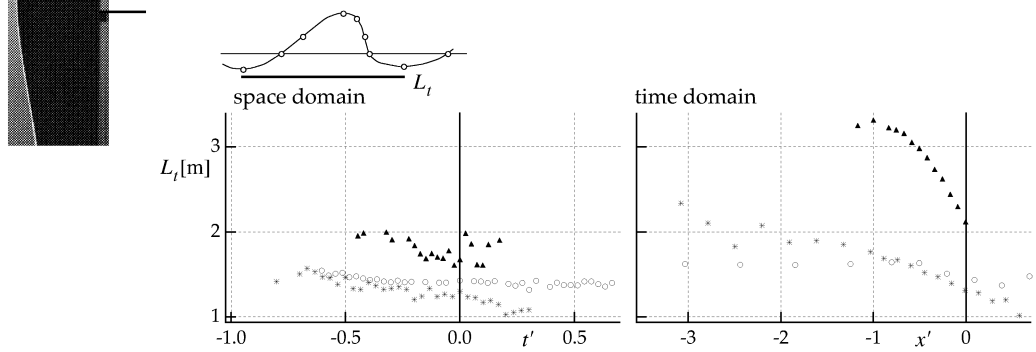


FIGURE 79. Wave length measured between trough points (L_t). Legend and axis as in Figure 76.

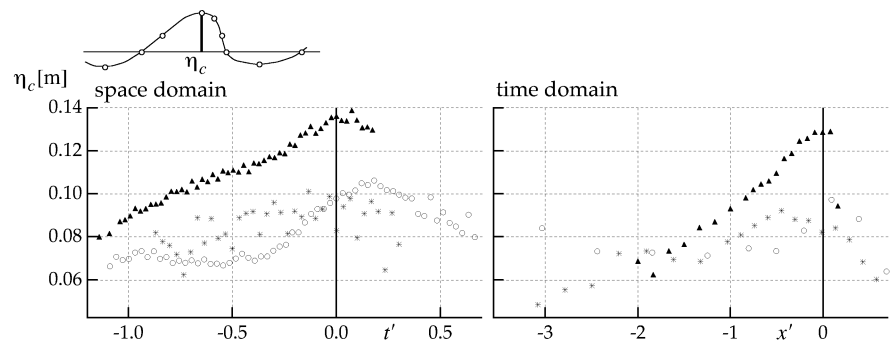


FIGURE 80. Crest height (η_c). Legend and axis as in Figure 76.

4.1 Wave Geometry

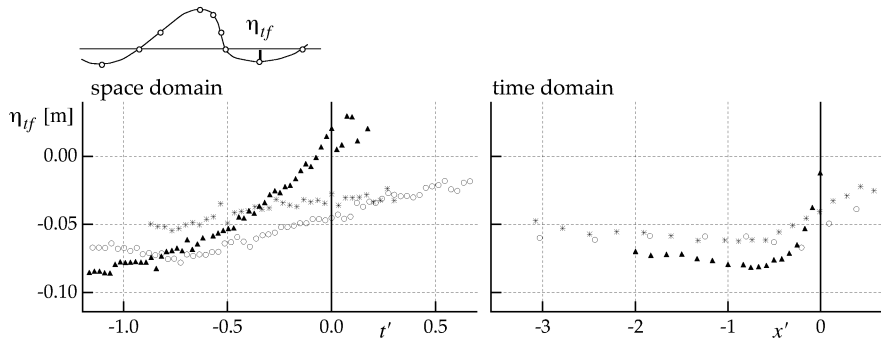


FIGURE 81. Front trough depth (η_{tf}). Legend and axis as in Figure 76.

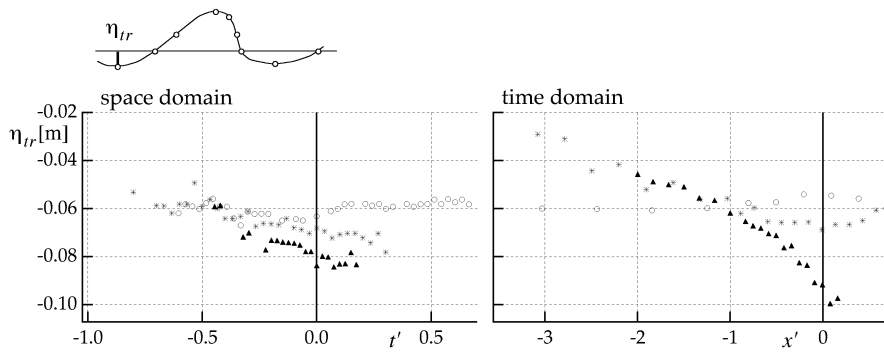


FIGURE 82. Rear trough depth (η_{tr}). Legend and axis as in Figure 76.

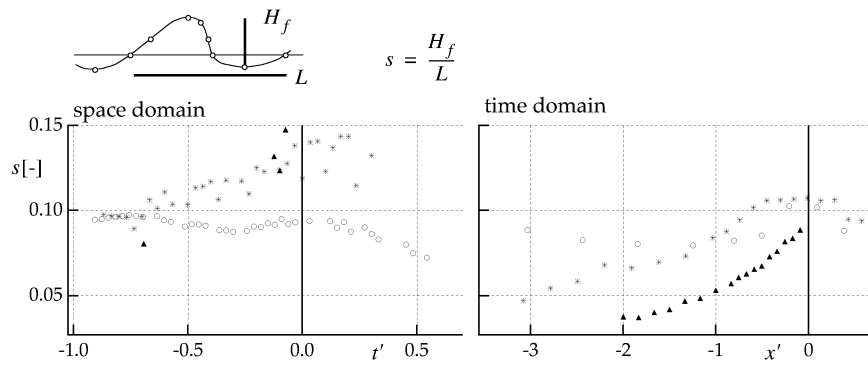
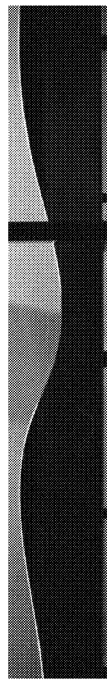


FIGURE 83. Total wave steepness (s). Legend and axis as in Figure 76.



By combining the features of the individual parameters shown in Figures 78 to 83, an impression of the overall qualitative evolution of the wave geometry with time is obtained. This is shown in Figure 84.

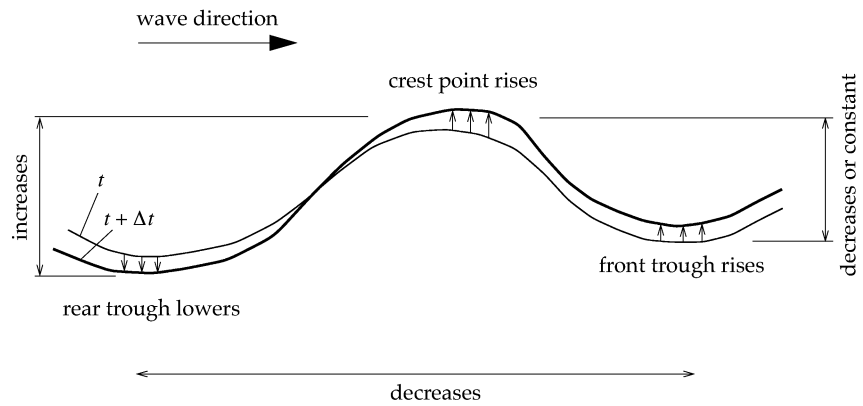


FIGURE 84. Qualitative description of the variation with time of the pre-breaking phase based on the measurements of the basic parameters.

The crest height (Fig. 80) increases, and thereby the crest point of the wave rises. The crest height of the plunging breaker increases with 70% over approximately one wave period, while the crest of the spilling breaker experiences a 55% increase over approximately half a wave period. The intermediate breaker has a more moderate increase of about 40% over one wave period.

The front trough depth (Fig. 81) also increases, and thereby the front trough rises during the pre-breaking phase, while the rear trough (Fig. 82) experiences a lowering. This results in an increase of the wave height measured relatively to the rear trough (Fig. 77), while the wave height relative to the front trough (Fig. 76) decreases (plunging), remains constant (intermediate) or oscillates (spilling).

During this transformation the wave length (Figs. 78 and 79) also decreases (plunging and intermediate breaker) or remains approximately constant (spilling breaker). The resulting total wave steepness (Fig. 83) for the plunging and intermediate breaker increases, while it for the spilling breaker remains almost constant.

Based on these parameters it appears that the plunging breaker experiences larger changes than the other two breakers.

The spilling breaker differs in many ways from the other two cases. It is likely that this is a result of the different methods used to generate the breaking events, i.e., that the spilling breaker is generated from a monochromatic wave group, while the other two cases

are generated from broad-banded wave groups. The oscillation that occurs in several of the parameters (especially pronounced in the front wave height) may also be due to the generation method, as the wave crest has different relative position in the wave group during the transformation, moving towards the front. The change in relative position in the group may cause oscillation of the wave crest. This also suggests that for different types of breaking waves there can be large differences in the way the wave geometry evolves in the pre-breaking phase, and this may be highly affected by the wave generation method.

The agreement between the space and time domain geometry is good for the measurements of wave heights, crest height and trough depths (vertical distances). For the wave lengths (horizontal distances) and for the total wave steepness the agreement is not so good (note the difference in horizontal scale between the time and space domain parameters). The disagreement between the space and time domain representations of the wave length is due to the transient nature of the wave geometry: The time domain measurements of the wave length is made by multiplying the measured period with the phase velocity. For this method to give correct result it must be assumed that the wave geometry does not change during the measurement period. This is not the case here as the waves are highly transient.

Zero-Downcross Parameters

The zero-downcross parameters were defined by Kjeldsen and Myrhaug (1978) for the purpose of better describing the space domain geometry of transient two-dimensional asymmetric waves. The parameters, which have been used by several investigators, have revealed significant features of asymmetry and steepness of the wave geometry. These features do not appear from the basic parameters discussed in the previous subsection. Figures 85 to 88 show the space and time domain measurements of the zero-downcross parameters. Results from previous investigations by other authors are also shown.

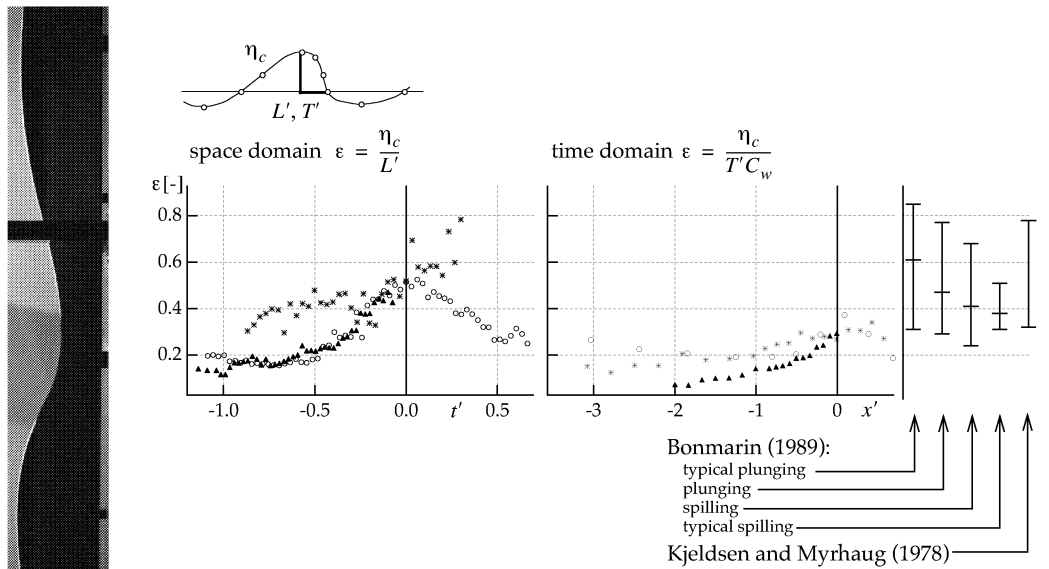


FIGURE 85. Crest front steepness (ϵ). Legend and axis as in Figure 76. C_w is given in Table 3. On the right hand side the values found by Bonmarin (1989)^a (min., mean, max.) and Kjeldsen and Myrhaug (1978)^b (min., max.) are shown. These values are for measurements at breaking point, and should therefore be compared to the values at $t' = 0$ and $x' = 0$.

- a. The measurements conducted by Bonmarin (1989) were made from film of approximately 100 single deep water breaking waves and are space domain measurements. The waves were classified into typical plunging, plunging, spilling and typical spilling, depending on how well the wave resembles a plunging or spilling breaker.
- b. Kjeldsen and Myrhaug (1978) measured the geometry parameters from images and film of deep water breaking waves, and this resulted in space domain measurements.

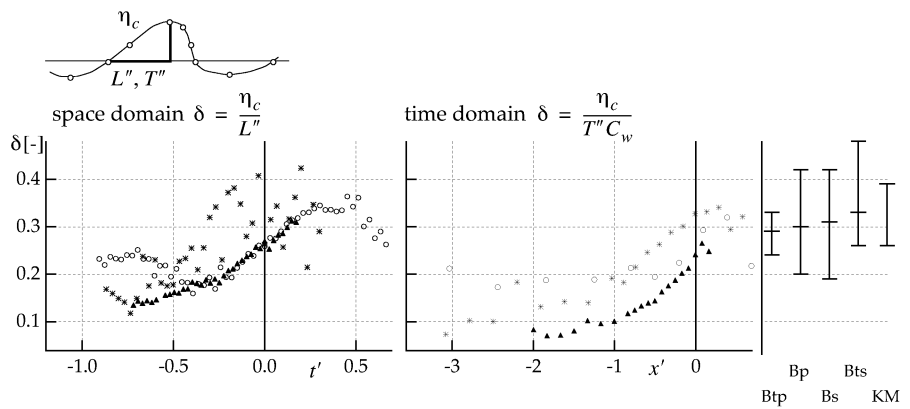


FIGURE 86. Crest rear steepness (δ). Legend and axis as in Figure 76. Intervals on the right are as in Figure 85.

4.1 Wave Geometry

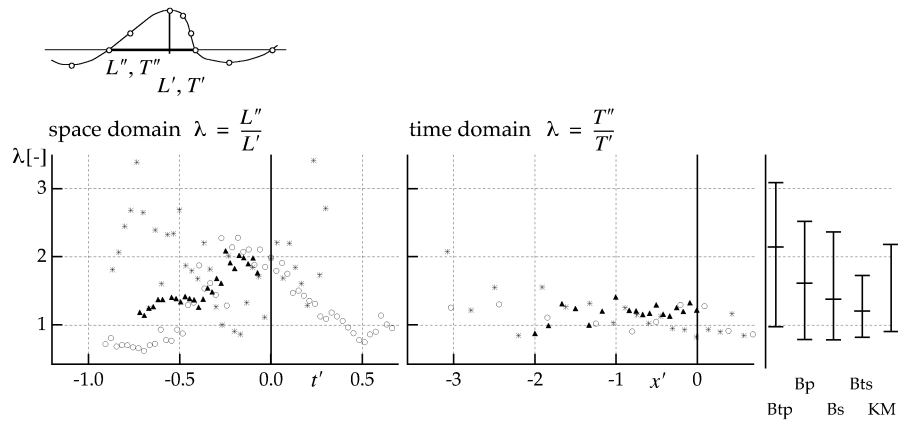


FIGURE 87. Vertical asymmetry factor (λ). Legend and axis as in Figure 76. Intervals on the right are as in Figure 85.

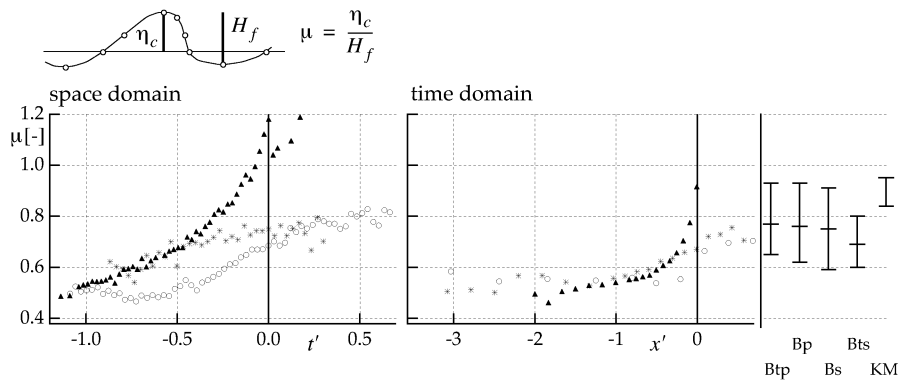


FIGURE 88. Horizontal asymmetry factor (μ). Legend and axis as in Figure 76. Intervals on the right are as in Figure 85.

Quantitatively the zero-downcross parameters describes the steepness and asymmetry of the waves; features especially important in the transient pre-breaking phase.

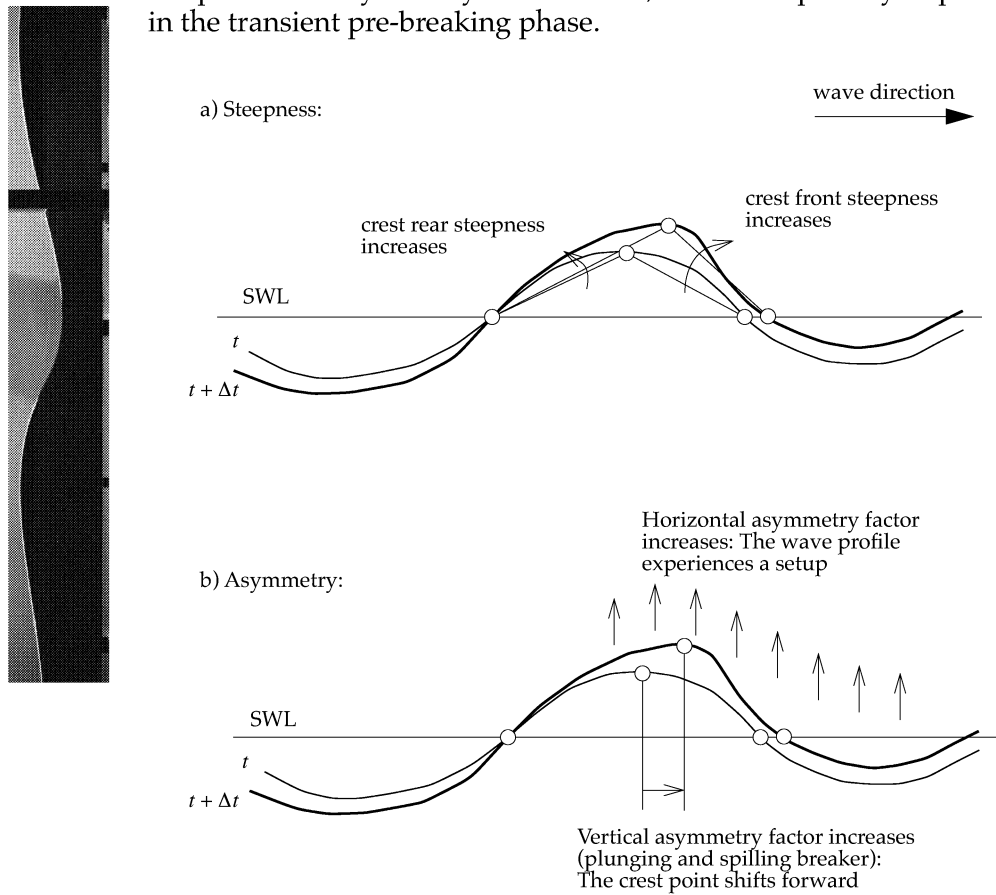


FIGURE 89. Qualitative description of the evolution in the pre-breaking phase based on the measurements of the zero-downcross parameters.

Figure 89 describes qualitatively the development of the wave based on the zero-downcross parameters. The steepness in the crest (Fig. 89a) increases both in the front and in the rear. The increase is, however, more pronounced in the front, and the crest front steepness (Fig. 85) for the plunging and spilling breaker increases rapidly from an initial value of $\epsilon \approx 0.2$ at $t' = -0.5$, to $\epsilon \approx 0.5$ at the breaking point. For the intermediate breaker the crest front steepness also increases prior to breaking, but the initial value of ϵ is larger, and the increase is not as large as for the plunging and spilling breakers. All three cases have approximately the same crest front steepness at the breaking point ($\epsilon \approx 0.55$). This is in good agreement with the measurements done by Bonmarin (1989) and Kjeldsen and Myrhaug (1978).

The crest rear steepness (Fig. 86) increases for the plunging breaker from $\delta \approx 0.15$ at $t' = -0.75$, to $\delta \approx 0.25$ at the breaking point. For the spilling breaker the crest rear steepness is not monotonously increasing, but seems to oscillate prior to breaking. The period for this oscillation is approximately equal to the linear wave period. This oscillation corresponds to the oscillation observed for the front wave height and crest height (Figs. 76 and 80, respectively).

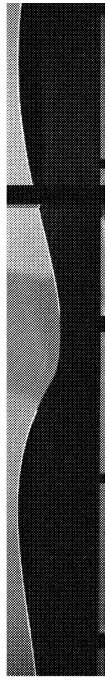
The asymmetry of the crest (Fig. 89b) increases also. During the pre-breaking phase the vertical asymmetry factor λ (Fig. 87) increases for the plunging and the spilling breaker corresponding to a forward shifting of the crest point. For a linear wave the crest point is located half the distance between the two zero-crossing points, with $\lambda = 1$. When λ increases, this means that the crest point moves closer to the front zero-upcrossing point, and away from the rear zero-downcrossing point. The degree of vertical asymmetry also seems to correlate with the transient behaviour of the wave, i.e., a high degree of vertical asymmetry corresponds to a high degree of transient effects. The results for the intermediate breaker indicate a decrease in λ , but the results do not show a clear trend, making any conclusions difficult. At the breaking point, λ is approximately equal for the three cases ($\lambda \approx 2.0$), corresponding to the measurements of Bonmarin (1989) and Kjeldsen and Myrhaug (1978).

The vertical asymmetry factor can also be expressed as the relationship between the crest front steepness and the crest rear steepness: $\lambda = \varepsilon/\delta$, and thus an increase in the vertical asymmetry factor also represents an increase in crest front steepness relative to the crest rear steepness, being consistent with the earlier observations.

The horizontal asymmetry factor μ (Fig. 88) shows an increase for all three cases. μ represents the vertical position of the local wave geometry relative to the still water level (SWL). For a linear wave $\mu = 0.5$, which means that the crest height and trough depth are equal. An increase in μ above 0.5 means that the crest height becomes larger than the trough depth, indicating that the local wave geometry rises relative to SWL. For the plunging breaker the increase of μ above 1 means that the front trough point rises above SWL. At $t' = -1.0$, μ is approximately 0.5 for all the wave cases, while all the cases show an increase in μ at the breaking point ($t' = 0$).

The present results from the measurements of the zero down-cross parameters are in good agreement with the results of Bonmarin (1989) and Kjeldsen and Myrhaug (1978), except for the following differences:

- i) The horizontal asymmetry factor for the plunging breaker is larger in the present measurements than in the two others.



ii) For the crest front steepness and the vertical asymmetry factor Bonmarin reported significantly larger values for the plunging than for the spilling breaker. In the present measurements the crest front steepness and the vertical asymmetry factor are approximately equal for all the three cases.

iii) The horizontal asymmetry factor is not in agreement with the Kjeldsen and Myrhaug (1978) measurements, which is lower for the plunging breaker and higher for the intermediate and spilling breaker. Compared with the measurements of Bonmarin (1989), however, the horizontal asymmetry factor for the intermediate and spilling breaker are in good agreement.

The space and time domain measurements of the crest front steepness, crest rear steepness and vertical asymmetry factor do not agree well. For the horizontal asymmetry factor, however, the correspondence between space and time domain measurements is good. This is because the horizontal asymmetry factor only requires measurements of vertical distances, while the other parameters involve measurements of horizontal distances. Time domain measurements of horizontal distances are biased if the wave geometry is transient. This indicates that measurements of the zero-downcross parameters from time domain representations of the wave geometry (time series from wave gauge/wave buoy measurements) can be biased significantly due to transient wave geometry, and this should be taken into account in analysis of these parameters from time domain measurements.

Inflection Point Parameters

The inflection point parameters were suggested as a supplement and possibly an improvement of the zero-downcross parameters (see *Chapter 3.4.2*)¹. Both the inflection point parameters and the zero-downcross parameters describe the local steepness and asymmetry in the crest, while the inflection point parameters in addition describe the curvature at the crest. Thus the inflection point parameters, representing an alternative approach, mainly describe the same geometric features as the zero-downcross parameters. Since these geometric features have been discussed earlier, the following discussion of the inflection point parameters will mainly focus on the similarity between the two parameter sets.

The inflection point steepness parameters (s_{if} and s_{ir}) are shown in Figures 90 and 91. The corresponding zero-downcross

1. Some of the suggested new parameters were found to give no additional information to that established by other parameters. These parameters are not presented in the main text, but can be found in *Appendix C*.

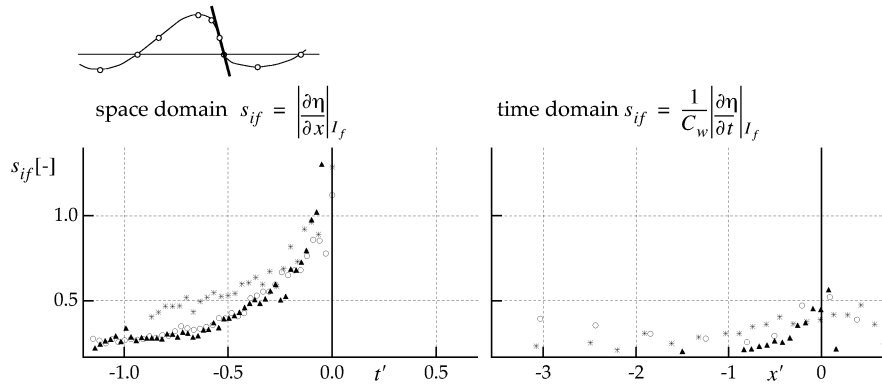


FIGURE 90. Front inflection point steepness (s_{if}). Legend and axis as in Figure 76.

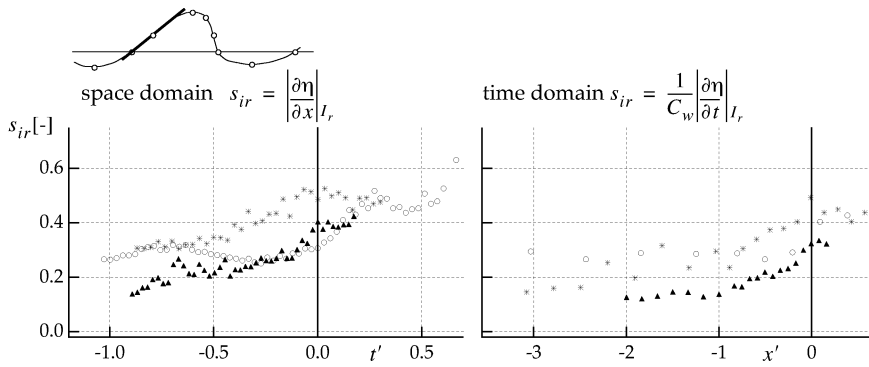


FIGURE 91. Rear inflection point steepness (s_{ir}). Legend and axis as in Figure 76.

parameters are the crest front steepness ϵ (Fig. 85) and crest rear steepness δ (Fig. 86). It can be proven that the inflection point parameters will always have a larger value than (or equal to) the corresponding zero-downcross parameters. ϵ and δ are the mean value of the surface steepness between the crest point and the front/rear zero-crossing points, while s_{if} and s_{ir} are the maximum steepness in the front/rear of the crest (see Fig. 92). Besides this the inflection point steepness parameters show an overall similar behaviour with the zero-downcross parameters. The inflection point parameters show, however, a smoother behaviour than the zero-downcross parameters. This is especially noticeable for the rear steepness of the intermediate breaker (δ compared with s_{ir}). There is also less difference in front steepness between the different breaking wave cases for the inflection point steepness.

For the front inflection point steepness s_{if} there is large discrepancies between the space and time domain representations. The behaviour of the space and time domain representations seems to

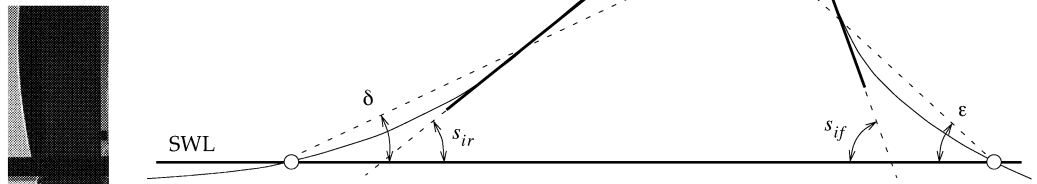


FIGURE 92. The inflection point steepnesses (s_{if} and s_{ir}), the crest front and crest rear steepness (ϵ and δ).

have a certain similarity, i.e., as if the difference is a result of scaling. It might be caused by an error in the measurements of the phase velocity C_w , which also would lead to the same difference in the rear inflection point steepness measurements. For s_{ir} , however, there is good agreement between the space and time domain representations, so the discrepancies in Figure 90 could not be caused by this. A good explanation for this discrepancy is not found, but it is most likely connected to the transient behaviour of the wave, because the front shows a higher degree of transient behaviour than the rear.

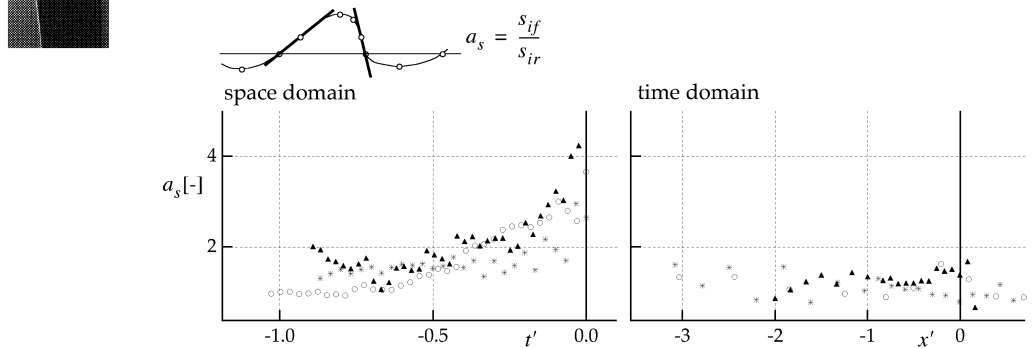


FIGURE 93. Wave steepness asymmetry factor (a_s). Legend and axis as in Figure 76.

The wave steepness asymmetry factor a_s (Fig. 93) describes the vertical asymmetry of the wave crest, and corresponds to the zero-downcross parameter λ (vertical asymmetry factor, see Fig. 87). As for the steepness parameters, the similarity between the zero-downcross parameter λ and the inflection point parameter a_s is apparent, and no new conclusions can be drawn based on a_s .

There are large discrepancies between the space and time domain representations of a_s . This is due to the discrepancy in the space and time domain measurements of s_{if} , which has been discussed earlier.

4.1 Wave Geometry

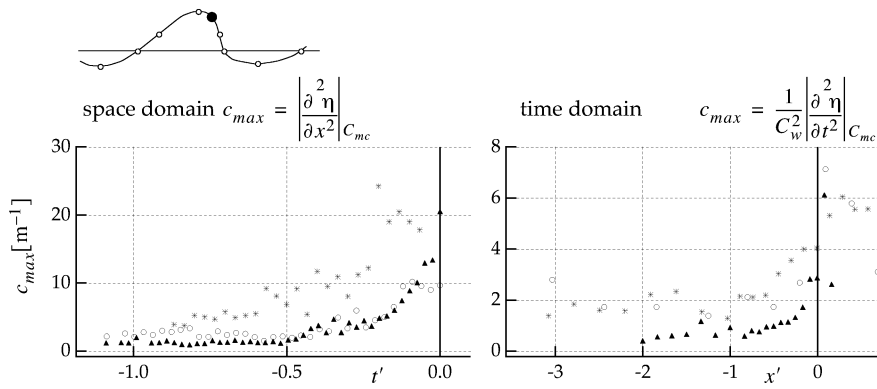


FIGURE 94. Maximum crest curvature (c_{max}). Legend and axis as in Figure 76. Note that the ordinate axis values are not equal for the space and time domain representations.

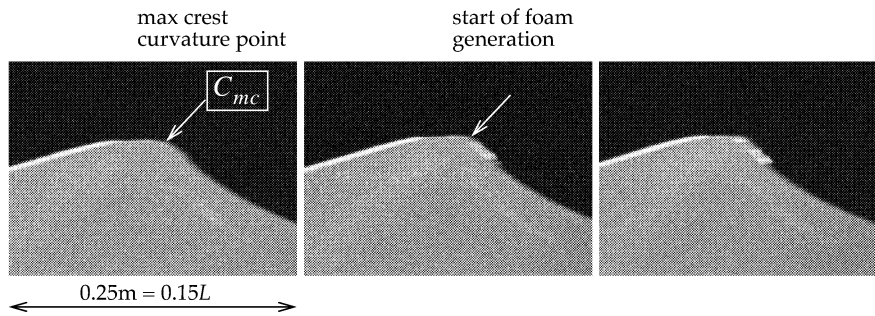
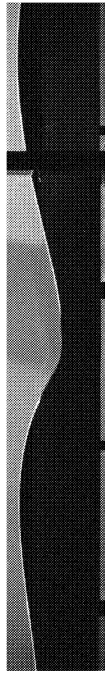


FIGURE 95. Details of the crest at the start of breaking for the spilling breaker. Time between each exposure is $1/32s$.

The point at the crest with the highest second derivative is referred to as the maximum crest curvature point, and the value of the second derivative at this point is denoted max crest curvature (c_{max}). Figure 94 shows the development of c_{max} . It appears that c_{max} increases up to breaking for all three cases. The spilling and plunging breakers have almost the same c_{max} values except close to breaking. However, from about $t' \approx -0.1$ the plunging breaker experiences a larger increase up to breaking where $c_{max} \approx 20m^{-1}$. For the spilling breaker c_{max} is nearly constant with the value $10m^{-1}$ from $t' \approx -0.1$, and up to breaking. The intermediate breaker shows generally higher values. Thus the value of c_{max} is not an indication on whether the wave breaks or not, since for the value for which the spilling breaker produces foam, the plunging and the intermediate breakers remain unbroken.

Analysis of the crest of the spilling breaker indicates that the foam generation starts in the vicinity of the max crest curvature point

(Fig. 95). For a spilling breaker this suggests that the point of max curvature plays an important role in the breaking process.



4.2 Wave Kinematics

In this section the measurements of the wave kinematics will be presented. As described earlier, the kinematics were measured using PIV, which resulted in a series of velocity vector fields (*Appendix A*). Based on these velocity fields, parameters characterising the velocity were computed, upon which the following analysis is based. The four parameters (see *Chapter 2.9.1*) that are computed from the velocity fields are:

- Velocity at the surface $z = \eta$: $U_\eta(x, t)$
- Velocity at $z = 0$: $U_0(x, t)$
- Local wave number: $k(x, t)$
- Mean velocity direction: $\bar{\theta}(x, t)$

These parameters are all functions of x and t as they are calculated at different x positions for each time step. The parameters, coordinates and time are normalized before they are presented (see *Chapter 2.9.2*). The parameters are presented in two different ways; focusing on the space domain dependency, and focusing on the time domain development of the parameters. The space domain dependency of the parameters is presented by plotting the parameters as a function of x at subsequent time steps, while the time domain development is presented by plotting the parameters at five different horizontal positions relative to the crest point as a function of time. The wave kinematics parameters were measured using a sampling frequency of 32 Hz. In this chapter only a selection of time instances of the measurements are shown (in *Appendix B* the set of measurements are shown).

In sections 4.2.1 to 4.2.4 the measurements of these parameters will be presented, and in section 4.2.5 selected measurements will be compared with 5th order Stokes theory as a partly verification of the measurements.

4.2.1 Velocity

The velocity at the surface (U_η) is the particle velocity magnitude at the free surface. U_η is an important parameter for several reasons: 1. The breaking events have their origin at the free surface, 2. The highest velocities in a wave are located at the surface, 3. As the waves grow steeper and the kinematics become non-linear, it is difficult to estimate the velocities at the crest. Thus measurements of the velocities at the free surface could give valuable information of the flow for non-linear waves.

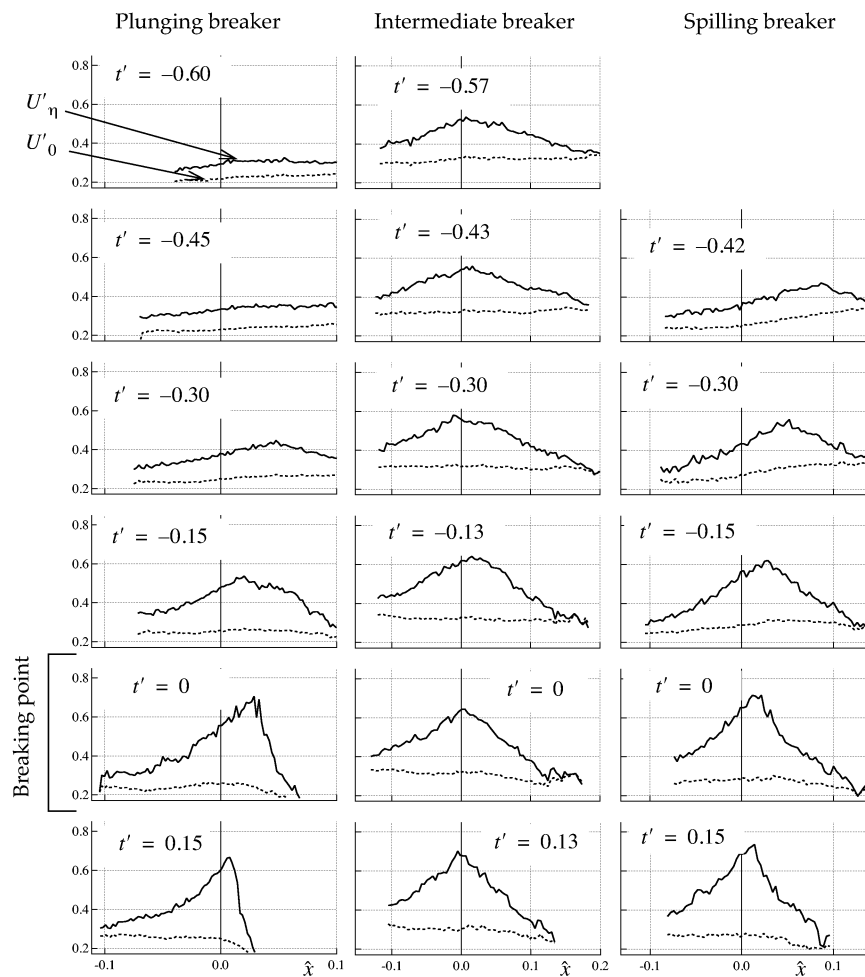
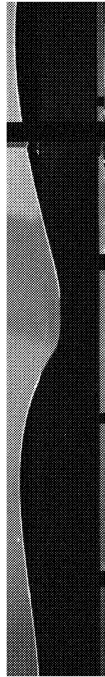


FIGURE 96. The particle velocity calculated at the surface (U'_η , whole line) and at $z = 0$ (U'_0 , dotted line) based on the velocity measurements for the three wave cases at different time steps relative to the breaking point ($t' = 0$). $\hat{x} = 0$ corresponds to the location in the crest where the velocity is horizontal.



It is difficult to measure the velocity close to the free surface using the PIV technique, as particles tend to gather at the surface, making it difficult to resolve each individual particle image. Due to this it is difficult to measure the velocity at the exact position of the free surface, and therefore U'_η is found by extrapolation (see *Chapter 2.9.1*). The velocity at $z = 0$ (U'_0) is found directly from the same extrapolation. U'_0 can also be found directly from the measurements as it is possible to measure the velocity at $z = 0$, and this parameter is denoted \hat{U}'_0 . In *Appendix B* (Figs. 114 to 117) U'_0 and \hat{U}'_0 are compared. As observed from these figures there is reasonable agreement between U'_0 and \hat{U}'_0 , indicating that the curve fitting gives representative results. Due to the nature of curve fitting, U'_0 is smoother than \hat{U}'_0 , and can be interpreted as a filtered representation of \hat{U}'_0 . Therefore U'_0 is used in the following discussion.

U'_η and U'_0 are shown in Figure 96. All three wave cases show an increase in U'_η as the waves approach breaking, and at the breaking point the maximum velocity is between 0.6 and 0.7. The plunging breaker shows a strong velocity increase, as U'_η rises from approximately 0.3 to 0.7 over a period of $0.6T$. The increase is especially strong in the wave front of the wave (at $\hat{x} > 0$, where $\hat{x} = 0$ is the point where the velocity is horizontal), where U'_η has its maximum value. U'_η also shows that the plunging breaker develops into a highly asymmetric wave, with larger velocities in the front than in the rear. This would imply that the kinetic energy shifts towards the front face as the wave evolves. This is consistent with the numerical simulation of a plunging breaker by Vinje and Brevik (1981). They also found that the peak surface velocity is located in front of the point of horizontal velocity.

The intermediate breaker shows a weaker increase than the plunging breaker, as U'_η initially was higher (at $t' = -0.57$). Nor does it show the same asymmetric features as the plunging breaker, and the point of maximum U'_η is located close to $\hat{x} = 0$.

The development of U'_η for the spilling breaker resembles more the development of the plunging breaker, as the increase is relatively strong, and the asymmetry is significant.

For a plunging breaker it should be expected that the velocity at the free surface exceeds the phase velocity at the breaking point. Thus it is worth noticing that U'_η never exceeds 0.8, which means that the velocity at the free surface is well below the phase velocity (since U'_η is normalized with the phase velocity). One explanation is that the velocity only exceeds the phase velocity in a small zone very close to the free surface. As explained earlier, the velocity data in this zone is not measured, but is a result of extrapolation, and the extrapolation may not be capable of resolving the possible large velocities close to

the surface. Accordingly it might be that the velocity very close to the surface does not follow the expected (but not necessarily correct) exponential function with depth. Another explanation is that the phase velocity used to normalize the velocities is higher than the actual velocity of the crest geometry, i.e., that using the velocity of the crest point as an estimate of the phase velocity is not correct. This is plausible since the crest point is shifted forward relative to the rest of the crest geometry as the wave evolves, and this shifting may cause an increase in the crest point velocity.

The velocity at $z = 0$, U'_0 , shows only minor changes during the development into breaking, and remains almost constant with time. U'_0 is also relatively constant with respect to the horizontal coordinate, and thus the asymmetry at the surface for the plunging and spilling breakers is not apparent at $z = 0$.

One interesting feature that should be noted, is the correlation between asymmetry and transient behaviour. This was also noticed for the geometry analysis. The plunging breaker having the most pronounced asymmetry, is the wave that transforms most rapidly, while the intermediate breaker being less asymmetric, does not transform as rapidly. The spilling breaker lies between the other two both with respect to asymmetry and transient behaviour. This suggests that asymmetry implies transformation of the wave, and the degree of asymmetry is correlated with the degree of transformation.

The development in time of the particle velocities is shown in Fig. 97. As pointed out previously, and as observed in Fig. 97, the velocity at the surface increases more, and becomes larger in the front ($\hat{x} > 0$) than in the rear ($\hat{x} < 0$) of the crest for the plunging and spilling breakers. The free surface steepness shows similar behaviour (see Figs. 90 and 91 at page 137): At $t' = -1$ the steepnesses in the front and in the rear are almost equal, but as the wave evolves further, the steepness in the front increases more than in the rear. At the breaking point ($t' = 0$) the wave becomes asymmetric with respect to the free surface steepness. The development of the velocity and the free surface steepnesses is thus correlated for the plunging and spilling breakers. For the intermediate breaker, however, there seems to be less correlation, since the steepness shows asymmetric behaviour, while the velocity at the surface does not show it clearly.

4 Results and Discussion

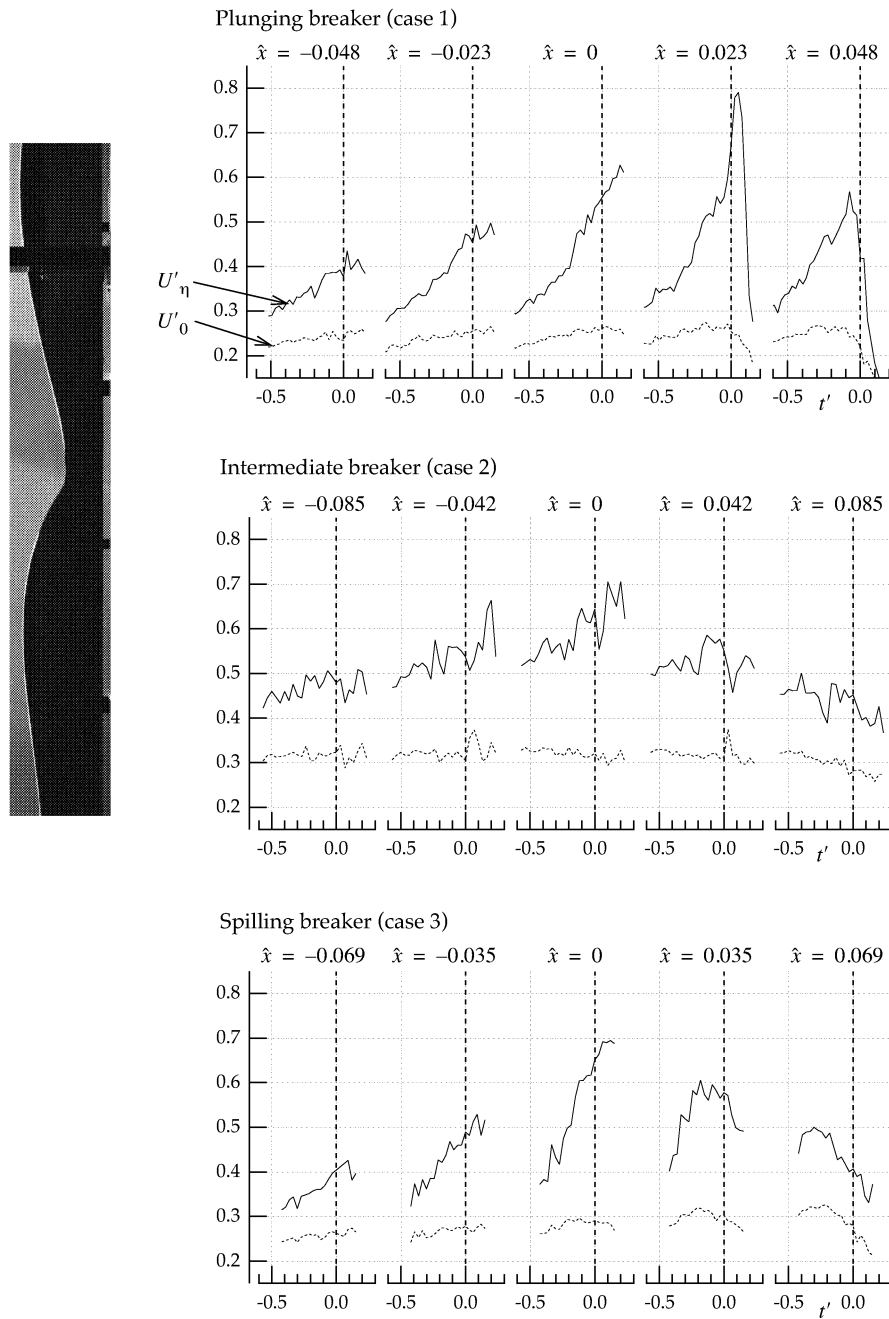


FIGURE 97. Time history of the surface velocity (U'_η) and velocity at $z = 0$ (U'_o) at five different \hat{x} positions in the crest. $\hat{x} = 0$ corresponds to the location in the crest where the velocity is horizontal, and $t' = 0$ is the time of breaking.

4.2.2 Local Wave Number

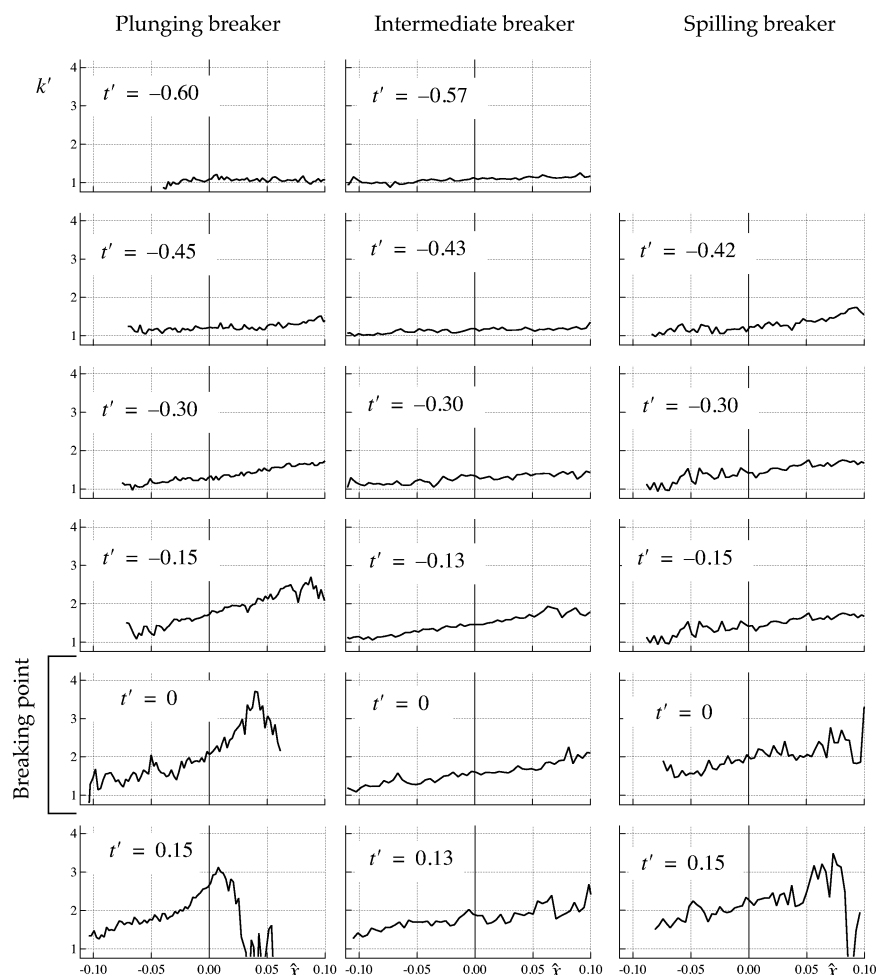


FIGURE 98. The local wave number (k') for the three wave cases at different time steps relative to the breaking point ($t' = 0$). $\hat{x} = 0$ corresponds to the location in the crest where the velocity is horizontal. The wave number is normalized with the wave length: $k' = kL/(2\pi)$. This means that $k' = 1$ corresponds to a linear wave.

Figures 98 and 99 show the development of the local wave number k' . As described earlier (*Chapter 2.9.1*), the local wave number is k in the exponential function fitted to each vertical vector row. In this context k' should be interpreted as a parameter describing the decay of the particle velocities with depth. Larger k' values indicate faster decay than smaller k' values. At about half a wave period prior to breaking ($t' = -0.5$), it is observed that k' is close to 1, and thus the velocity decay corresponds to that of a linear wave with

4 Results and Discussion

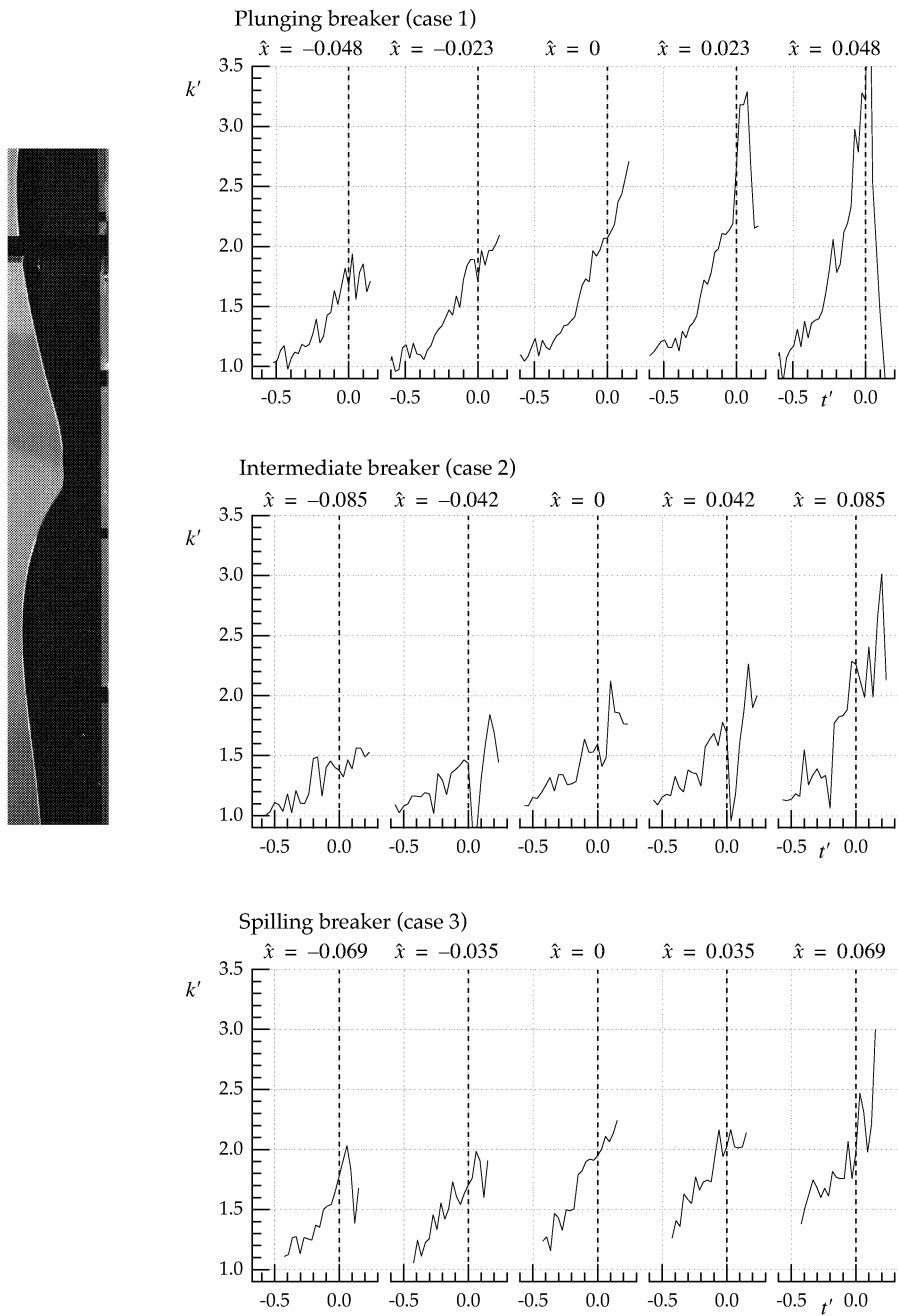


FIGURE 99. Time history of the wave number k' at five different \hat{x} positions in the crest. $\hat{x} = 0$ corresponds to the location in the crest where the velocity is horizontal, and $t' = 0$ is the time of breaking.

the same phase velocity. However, as the wave evolves towards breaking, k' increases. Similar to the development of U'_{η} , the increase of k' is larger in the front ($\hat{x} > 0$) than in the rear ($\hat{x} < 0$) of the crest, showing that k' varies over the crest close to breaking. For wave models based on harmonic components the depth decay is constant over the crest. This suggests that wave models describing steep and asymmetric waves should contain a space domain dependent wave number, rather than being based on harmonic components.

4.2.3 Mean Velocity Direction

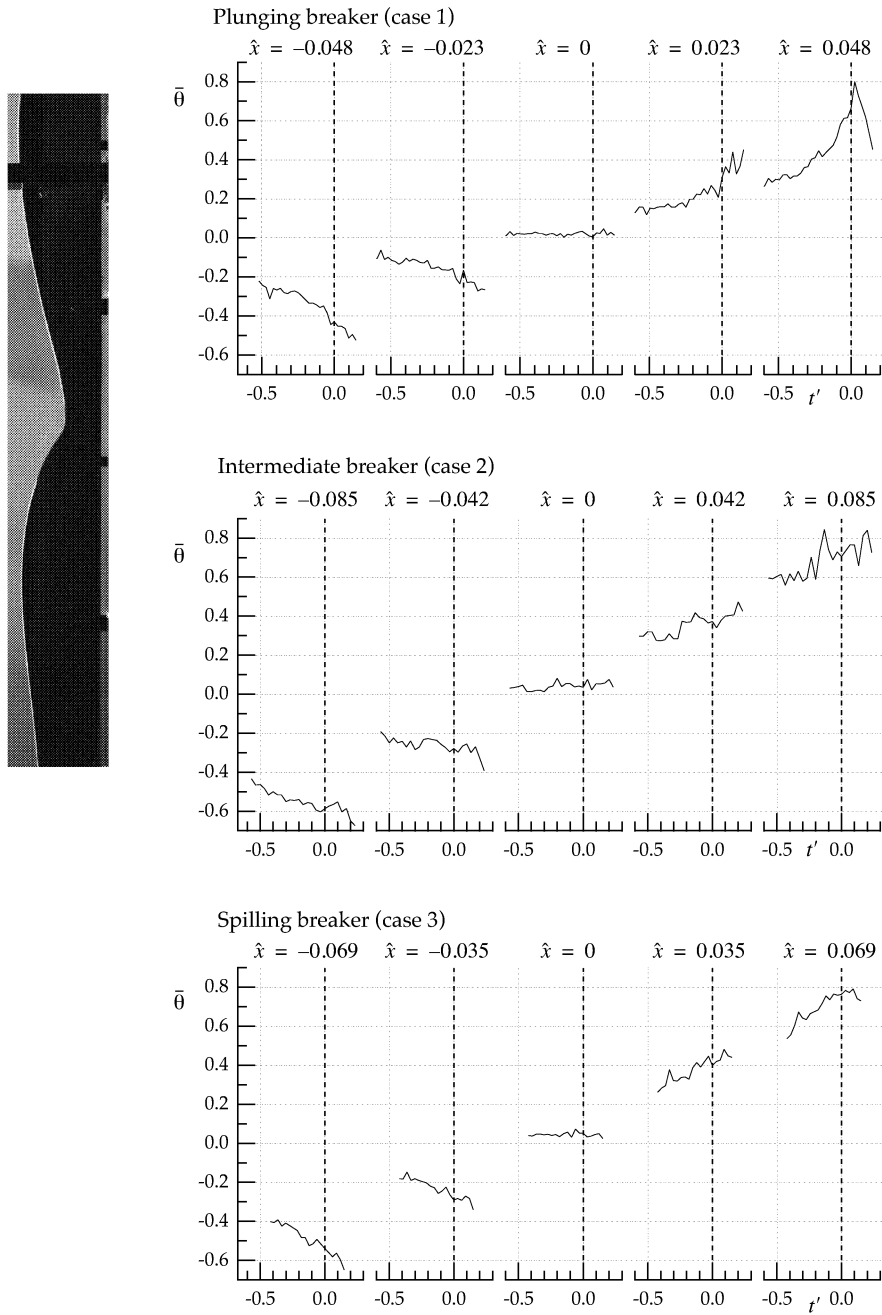


FIGURE 100. Time history of the mean velocity direction $\bar{\theta}$ at five different \hat{x} positions in the crest. $\hat{x} = 0$ corresponds to the location in the crest where the velocity is horizontal, and $t' = 0$ is the time of breaking.

The development in time of the mean velocity direction $\bar{\theta}$ is shown in Fig. 100. All the three breaking wave cases show the same behaviour: the direction shifts downwards in the rear, and upwards in the front. This is similar to what a linear wave would experience if its wave length decreases, and which is the behaviour found earlier in Figure 78 and 79 on page 128: All three cases show a decrease in wave length as the waves approach breaking.

4.2.4 Principal Development of the Kinematics

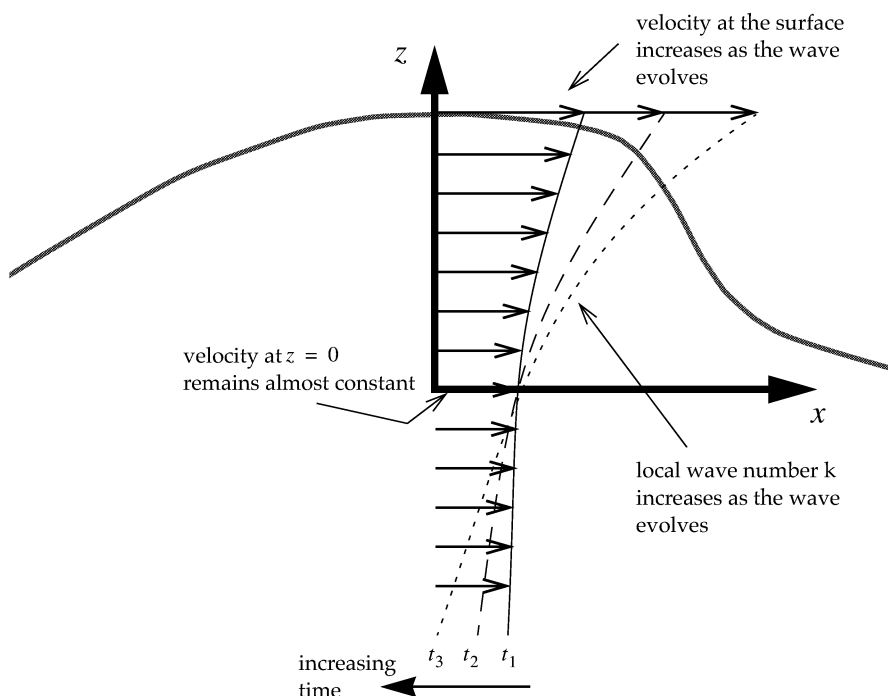
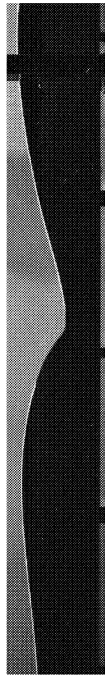


FIGURE 101. Principal development of the kinematics in the crest of a breaking wave. The velocity profile is sketched at three different time instants.

In order to get a more complete picture of what happens in the wave crest as the wave evolves towards breaking, the development of U'_{η} , U'_0 and k' should be considered jointly. Both U'_{η} and k' increase towards breaking, while U'_0 remains almost constant. This leads to the development illustrated in Figure 101, where the velocity profiles at three subsequent time instances are shown. Since U'_{η} and k' increase, the velocity profiles pivot around $z = 0$ where the velocity remains almost constant. Consequently the kinetic energy

increases above $z = 0$, while it decreases below $z = 0$, suggesting a transfer of energy upwards in the wave.

4.2.5 Comparison with Stokes 5th Order Theory



As a check of the validity of the measurements a comparison with Stokes 5th order theory (Fenton, 1985) is made. According to Stokes 5th order theory the wave is vertically symmetric, and thus the comparison should be made with measurements of such waves. On the other hand, it can be assumed that the largest discrepancies between theory and measurements appear for the steepest waves. Therefore the best test for validity would be to compare the theory with the measurements taken of the wave when it was as steep as possible, but before it becomes vertically asymmetric. For each case a time instant was chosen when the wave geometry was close to fulfil this condition. The measurements taken at these time instants were then used for comparison with the theory. The chosen time instants (t'), with the corresponding wave length (L) and wave height (H) are given in Table 9. The input parameters to the Stokes 5th order theory are wave height (H), wave length (L) and with a water depth (d) of 1m.

TABLE 9. Data for the cases used in comparison with Stokes 5th order theory

Breaker Case	Time t' [-]	Wave length L [m]	Wave height H [m]	Total wave steepness s [-]
Plunging	-0.495	1.955	0.163	1/12.0=0.083
Intermediate	-0.501	1.325	0.131	1/10.1=0.099
Spilling	-0.423	1.406	0.131	1/10.8=0.093

The results are shown in Figures 102 to 104. The same parameters as in the kinematic analysis are used in the comparison.

Overall the agreement is good for the plunging breaker, while there appears to be differences between the measurements and predictions for the intermediate and spilling breakers. However, the differences in the kinematics clearly originates from the differences in the free surface elevation. This is especially noticeable for the spilling breaker (Fig. 104) where the measured free surface elevation is vertically asymmetric. This asymmetry is inherited in the surface velocity U'_{η} , and gives differences in U'_{η} at the front face of the wave.

4.2 Wave Kinematics

Based on the comparison it can be concluded that the measurements of the kinematics show reasonable agreement with Stokes 5th order theory, supporting the overall validity of the measurements.

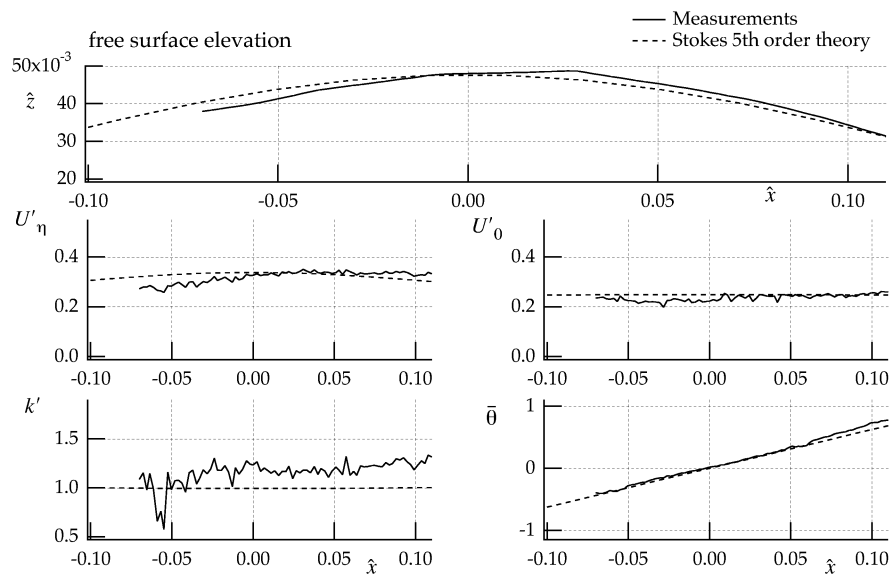


FIGURE 102. Comparison between measurements and Stokes 5th order theory at $t' = -0.495$ for the plunging breaker.

4 Results and Discussion

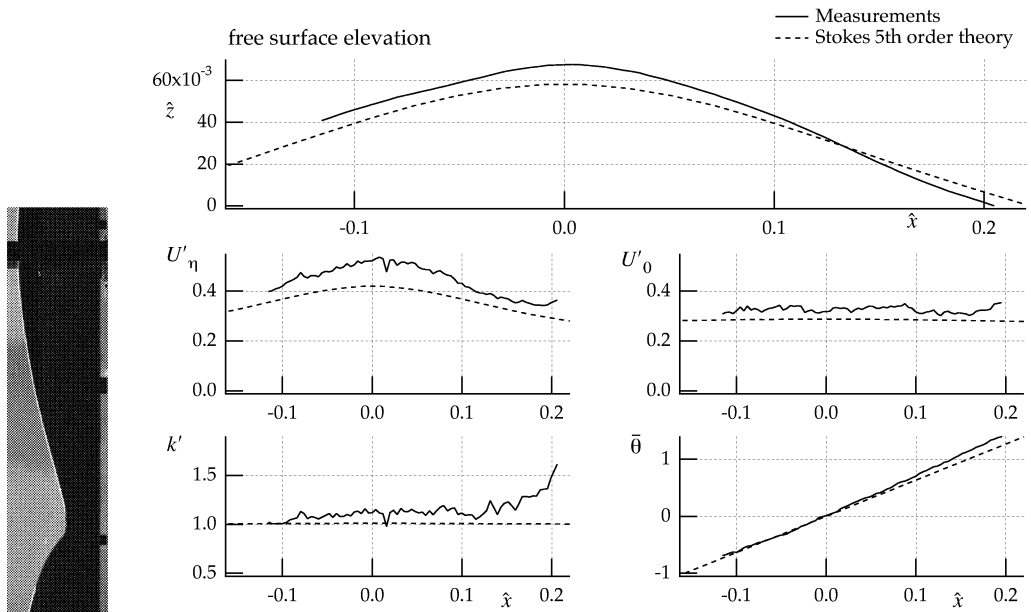


FIGURE 103. Comparison between measurements and Stokes 5th order theory at $t' = -0.501$ for the intermediate breaker.

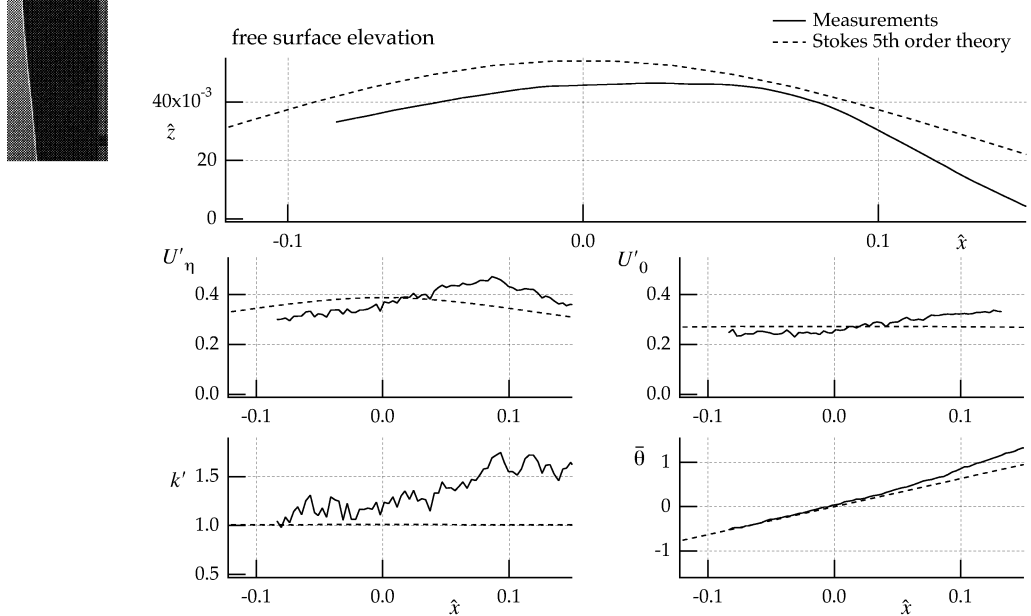


FIGURE 104. Comparison between measurements and Stokes 5th order theory at $t' = -0.423$ for the spilling breaker.

4.3 Chapter Summary

In this chapter the results from measurements of the geometry and kinematics of the three breaking wave cases have been presented. The main findings are summarized in the following.

Geometry

The geometry is analysed using the zero-downcross parameters, as well as a new set of parameters suggested for the first time here. The parameters are calculated both from the time and the space domain representations of the free surface geometry.

- A principal description of the development of the wave profile geometry is extracted from measurements of the free surface: The crest and the front trough rises, while the rear trough lowers. The steepness and curvature in the crest increase, with the front always steeper than the rear, resulting in an asymmetric wave.
- Both the space and time domain representations of the wave geometry have been presented, and the wave geometry parameters have been calculated using both representations. Parameters involving horizontal distances show large differences between the space and time domain representations, while parameters involving only vertical distances show good agreement between the two representations.
- Quantitative estimates of the steepness (first derivative) and the curvature (second derivative) of the free surface are also presented. These measurements provide detailed information of the development of the free surface geometry.
- The zero-downcross parameters provide a good description of the changes in geometry of a transient wave. The new parameters suggested in this thesis supports the information given by the zero-downcross parameters.
- For the spilling breaker it was observed that the foam generation starts in the vicinity of the point with the maximum curvature, suggesting a connection between curvature and foam initiation.

Kinematics

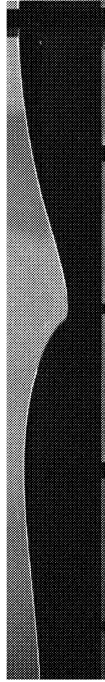
The analysis of the kinematics is done using a set of parameters:

- Velocity at the surface $z = \eta$: $U_\eta(x, t)$
- Velocity at $z = 0$: $U_0(x, t)$
- Mean velocity direction: $\bar{\theta}(x, t)$

• Local wave number: $k(x, t)$

These parameters reveal new features of the development in time and space of the wave kinematics.

- There appears to be a correlation between the steepness of the free surface and the particle velocity at the free surface; high steepness corresponds to high particle velocities.
- The kinetic energy above $z = 0$ increases, while it decreases below $z = 0$, and this suggests that energy is shifted upwards in the wave during the transformation towards breaking.
- The measurements of the kinematics show correlation between asymmetry and transient behaviour, i.e., transient effects increase with increasing asymmetry.
- The local wave number, describing the variation of velocity with depth, is not constant over the crest. This suggests that harmonic components should not be used in wave models describing steep asymmetric and transient waves.



5.1 Summary and Conclusions

The objective of this thesis is to experimentally study different breaking wave cases, and to measure in detail the free surface geometry and the internal kinematics of the waves as they approach breaking. The three principal wave cases chosen are: A plunging breaker, a spilling breaker, and an intermediate breaker.

A wave laboratory is designed, planed, constructed and built as a part of this work. The laboratory contains a wave flume which is 13.5m long, 1m deep and 0.6m wide. The flume has walls and bottom made of glass, enabling optical measurements techniques.

For the measurements of the kinematics the Particle Image Velocimetry (PIV) method is used. An estimate of the error involved in the PIV measurements was found by a Monte Carlo simulation of the PIV image analysis algorithm. From this analysis the RMS value of the error was found to be 3.9 percent of the velocity magnitude, and 1.7 degrees of the velocity direction. In addition to this analysis error, which is a software error, errors in the hardware also occurred. The accumulated errors from the hardware were approximately 2-3 percent, and this gives an estimate of the total error of approximately 6 percent.

Both the space and time domain representations of the free surface geometry were measured. The space domain geometry is measured using digital image analysis, while the time domain geometry is measured with standard wave gauges.

Both the kinematics and the geometry are described and analysed using several parameters. The kinematics are described by a set of four parameters:

- Velocity at the surface $z = \eta$: $U_\eta(x, t)$
- Velocity at $z = 0$: $U_0(x, t)$
- Local wave number: $k(x, t)$
- Mean velocity direction: $\bar{\theta}(x, t)$

The purpose of the parameters is to give a better understanding of the space and time domain development of the kinematics, and they appear to be a reasonable compromise between simplicity and accuracy.

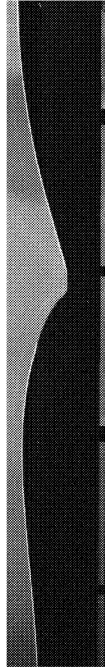
The geometry is analysed using several parameters that describe significant features of the wave, such as local steepness and curvature. In addition to parameters proposed by other authors, a set of new parameters is suggested and described.

The results presented here represent a thorough and detailed mapping of the breaking process. Much data are gathered and analysed, and throughout the thesis it is sought to present the data in the most intuitive way, so that other investigators may benefit from it.

The main findings are summarized in the following.

Geometry

- A principal description of the development of the wave profile geometry is extracted from measurements of the free surface: The crest and the front trough rises, while the rear trough lowers. The steepness and curvature in the crest increase, with the front always steeper than the rear, resulting in an asymmetric wave.
- Both the space and time domain representations of the wave geometry have been presented, and the wave geometry parameters have been calculated using both representations. Parameters involving horizontal distances show large differences between the space and time domain representations, while parameters involving only vertical distances show good agreement between the two representations.
- Quantitative estimates of the steepness (first derivative) and the curvature (second derivative) of the free surface are also presented. These measurements provide detailed information of the development of the free surface geometry.
- The zero-downcross parameters provide a good description of the changes in geometry of a transient wave. The new parameters suggested in this thesis supports the information given by the zero-downcross parameters.



5.2 Suggestions for Further Work

- For the spilling breaker it was observed that the foam generation starts in the vicinity of the point with the maximum curvature, suggesting a connection between curvature and foam initiation.

Kinematics

- There appears to be a correlation between the steepness of the free surface and the particle velocity at the free surface; high steepness corresponds to high particle velocities.
- The kinetic energy above $z = 0$ increases, while it decreases below $z = 0$, and this suggests that energy is shifted upwards in the wave during the transformation towards breaking.
- The measurements of the kinematics show correlation between asymmetry and transient behaviour, i.e., transient effects increases with increasing asymmetry.
- The local wave number, describing the variation of velocity with depth, is not constant over the crest. This suggests that harmonic components should not be used in wave models describing steep asymmetric and transient waves.

5.2 Suggestions for Further Work

Numerical wave model using non-harmonic components

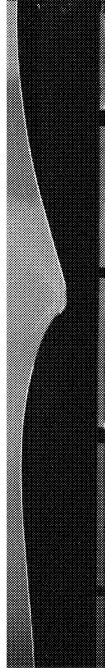
The measurements of the local wave number k showed that k is not constant over the crest, and that it also varies with time. This may suggest that analytical models used to describe steep and asymmetric waves should not use harmonic components. Establishing a wave model based on a space dependent $k(x)$ could give a better analytical or numerical description of steep, asymmetric wave kinematics.

Breaking waves in a larger wave field

The breaking waves studied here took place at the front of wave groups, and this had an influence on the measurements. The lack of wave energy in front of the breaking event is not representative of deep water breaking waves. Similar measurements should be conducted on breaking waves within a larger wave group, so that wave energy is present both in front of and behind the breaking wave.

Simultaneous measurements of kinematics and geometry

The laboratory facilities demanded that the kinematics and the geometry had to be measured at different runs. In addition the geometry were measured close to the flume walls, while the kinematics were measured in the middle of the flume. Because of this it was difficult to directly compare details in the kinematics and the geometry. A laboratory setup that measure the kinematics and geometry simultaneously at the same location, will give measurements where comparison between details in the wave is easier.



Asymmetric, steep and transient non-breaking waves

By comparing measurements of asymmetric, steep and transient waves that do not break with similar waves that break, features of the waves deciding whether the waves break or not could be revealed. Therefore it would have been useful to try to generate waves which goes through a transformation similar to the pre-breaking phase discussed in this thesis, but which eventually do not break.

More detailed observation of the crest curvature

Observations of the curvature indicates a connection between the point of maximum curvature and the initiation of foam generation in a spilling breaker. This should be investigated further in more detail. Duncan et al. (1999) investigated the crest profile evolution of a spilling breaker and discovered that the breaking process began with the formation of a bulge¹ near the crest on the forward face of the wave. Capillary waves were in turn formed upstream of the leading edge of the bulge. It is possible that the formation of this bulge is connected to the curvature of the free surface, and further investigations regarding this could give interesting results.

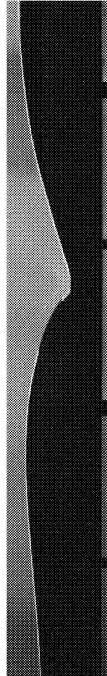
Acceleration field measurements

The acceleration field is also an important feature of the wave kinematics. Several investigators have suggested breaking criteria based on the acceleration in the crest (Ochi, 1998), and the mapping of the whole acceleration field of a breaking wave could lead to better understanding of the breaking process. Dewhirst et al. (1996) described a method for measuring acceleration fields using digital particle image velocimetry (DPIV), which can be used to measure the acceleration field in breaking waves.

1. a rounded swelling, an outward curve.

Wind and current

The possibilities to incorporate wind and current were considered when the flume was designed, and future installations of such facilities are planned. The motivation for this is, among other things, that breaking waves at sea are often influenced by wind and current. If one hopes to be able to accurately forecast breaking waves, these effects must be fully understood, and taken into account. A step towards such an understanding would be a thorough experimental study, similar to the one presented here, but with the influence of wind and current incorporated.



References

-
- Adrian, R. J. (1991). "Particle-Imagin Techniques for Experimental Fluid Mechanics." *Annual Review of Fluid Mechanics*, 23, pp. 261-304.
- Banner, M. L. and Peregrine, D. H. (1993). "Wave breaking in deep water." *Annual Review of Fluid Mechanics*, 25, pp. 373-397.
- Banner, M. L. and Phillips, O. M. (1974). "On the Incipient Breaking of Small Scale Waves." *Journal of Fluid Mechanics*, 65(4), pp. 647-656.
- Bonmarin, P. (1989). "Geometric properties of deep-water breaking waves." *Journal of Fluid Mechanics*, 209, pp. 405-433.
- Brücker, C. (1996). "3-D Scanning-Particle-Image-Velocimetry (3-D SPIV)." *Lecture Series 1996-03*, von Karman Institute for Fluid Dynamics, Brussels.
- Cokelet, E. D. (1978). "Breaking Waves - the Plunging Jet and Interior Flow-Field." *Wave-induced Forces on Cylinders*, September 2-6, The University of Bristol.
- Dahle, E. A. and Kjærland, O. (1980). "The Capsizing of M/S HEL- LAND-HANSEN." *Transactions of The Royal Institution of Naval Architects*, 122, pp. 51-70.
- Dahle, E. A. and Myrhaug, D. (1996). "Capsize Risk of Fishing Vessels." *Ship Technology Research*, 43, pp. 164-171.
- Dewhirst, T. P., Jakobsen, M. L. and Greated, C. A. (1996). "Multiple CCD Camera DPIV for Force and Acceleration Measurements in
-

References

High-speed Flows." *IMEchE Symposium on Optical Methods and Data Processing in Heat and Fluid Flow*, C516/046, pp. 251-257.

Dold, J. and Peregrine, D. H. (1986). "An Efficient Boundary-integral Method for Steep Undsteady Water Waves.", *Numerical Methods for Fluid Dynamics II*, K. W. Morton and M. J. Baines, eds., Oxford University Press.

Duncan, J. H. et al. (1994). "The Formation of Spilling Breaking Water Waves." *Physics of Fluids*, 6(8), pp. 2558-2560.

Duncan, J. H. et al. (1999). "Gentle Spilling Breakers: Crest Profile Evolution." *Journal of Fluid Mechanics*, 379, pp. 191-222.

Fenton, J. D. (1985). "A Fifth-Order Stokes Theory for Steady Waves." *Journal of Waterway, Port, Coastal and Ocean Engineering*, 111(2), pp. 216-233.

Garrison, T. (1993). *Oceanography: an invitation to marin science*, Wadsworth Publishing Company, Belmont, California.

Gray, C. et al. (1991). "An Analysis of the Scanning Beam PIV Illumination System." *Journal of Measurement Science and Technology*, 2.

Greated, C. A. et al. (1992). "Particel Image Velocimetry (PIV) in the Coastal Engineering Laboratory." *Coastal engineering 1992 : proceedings of the twenty-third international conference*, pp. 212-225.

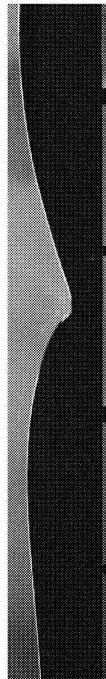
Holman, J. P. (1994). *Experimental Methods for Engineers*, McGraw-Hill. Inc.

Holthuijsen, L. H. and Herbers, T. H. C. (1986). "Statistics of Breaking Waves Observed as Whitecaps in the Open Sea." *Journal of Physical Oceanography*, 16, pp. 290-297.

Kjeldsen, S. P. and Myrhaug, D. (1978). "Kinematics and Dynamics of Breaking Waves." Report *STF 60 A 78100*, River and Harbour Laboratory (NHL) at The Norwegian Institute of Technology.

Kjeldsen, S. P. and Myrhaug, D. (1979). "Breaking Waves in Deep Water and Resulting Wave Forces." *Offshore Tecchnology Conference*, April 30-May 3, Houston.

Kjeldsen, S. P. and Myrhaug, D. (1980). "Wave-Wave interactions, Current-Wave Interactions and Resulting Extreme Waves and



References

- Breaking Waves." *Proc. 17th Conf. on Coastal Engineering*, 23-29 March, Sydney, Australia, Vol III, pp. 2277-2302.
- Klein, M. V. and Furtak, T. E. (1986). *Optics*, Wiley, New York.
- Lamb, H. (1932). *Hydrodynamics*, Cambridge University Press.
- Longuet-Higgins, M. S. (1969). "On Wave Breaking and the Equilibrium Spectrum of Wind Generated Waves." *Proceedings of the Royal Society of London. A, Mathematical and physical sciences*, 310, pp. 151-159.
- Longuet-Higgins, M. S. (1974). "Breaking Waves - in Deep or Shallow Water." *10th Symposium on Naval Hydrodynamics*, June 24-28, Cambridge, Mass., pp. 597-605.
- Longuet-Higgins, M. S. (1978a). "The Instabilities of Gravity Waves of Finite Amplitude in Deep Water, I. Superharmonics." *Proceedings of the Royal Society of London. A, Mathematical and physical sciences*, 360, pp. 471-488.
- Longuet-Higgins, M. S. (1978b). "The Instabilities of Gravity Waves of Finite Amplitude in Deep Water, II. Subharmonics." *Proceedings of the Royal Society of London. A, Mathematical and physical sciences*, 360, pp. 489-505.
- Longuet-Higgins, M. S. (1980). "The Unsolved Problem of Breaking Waves." *Proc. 17th Conf. Coastal Engineering*, 23-29 March, Sydney, Australia, pp. 1-29.
- Longuet-Higgins, M. S. (1985). "Accelerations in Steep Gravity Waves." *Journal of Physical Oceanography*, 15, pp. 1570-79.
- Longuet-Higgins, M. S. (1994). "The Initiation of Spilling Breakers." *International Symposium: Waves - Physical and Numerical Modelling*, The University of British Columbia, Vancouver, Canada, pp. 24-37.
- Longuet-Higgins, M. S. and Cleaver, R. P. (1994). "Crest instabilities of gravity waves. Part 1. The almost-highest wave." *Journal of Fluid Mechanics*, 258, pp. 115-129.
- Longuet-Higgins, M. S. et al. (1994). "Crest instabilities of gravity waves. Part 2. Matching and asymptotic analysis." *Journal of Fluid Mechanics*, 259, pp. 333-344.
-

References

- Longuet-Higgins, M. S. and Cokelet, E. D. (1976). "The deformation of steep surface waves on water - I. A numerical method of computation." *Proceedings of the Royal Society London A*, 350, pp. 1-26.
- Lourenco, L. M. (1996). "Particle Image Velocimetry." *Lecture Series 1996-03*, von Karman Institute for Fluid Dynamics, Brussels.
- Mei, C. C. (1989). *The Applied Dynamics of Ocean Surface Waves*, World Scientific, Singapore.
- Memery, L. and Merlivat, L. (1984). "The Contribution of Bubbles to Gas Transfer Across an Air-Water Interface." *Oceanic Whitecaps and Their Role in Air-Sea Exchange Processes*, E. C. Monahan and G. Mac Niocaill, eds., D. Reidel Publishing Company, Dordrecht, Holland, pp. 95-100.
- Mitchell, J. H. (1893). "The Highest Waves in Water." *Phil Mag.*, 36, pp. 430-437.
- Mooney, M. J. (1993). "A Tsunami is Coming." *Mariners Weather Log*, Fall 1993, pp. 29-32.
- Myrhaug, D. and Dahle, E. A. (1994). "Ship capsizing in breaking waves." *Fluid Structures Interaction in Offshore Engineering*, S. K. Chakrabarti, ed., Computational Mechanics Publications, pp. 43-84.
- Myrhaug, D. and Kjeldsen, S. P. (1984). "Parametric modeling of joint probability density distributions for steepness and asymmetry in deep water waves." *Applied Ocean Research*, 6(4), pp. 207-220.
- Myrhaug, D. and Kjeldsen, S. P. (1986). "Steepness and Asymmetry of Extreme Waves and the Highest Waves in Deep Water." *Ocean Engineering*, 13(6), pp. 549-568.
- Myrhaug, D. and Kjeldsen, S. P. (1987). "Prediction of Occurrences of Steep and High Waves in Deep Water." *Journal of Waterway, Port, Coastal and Ocean Engineering*, 113/2, pp. 122-138.
- New, A. L. et al. (1985). "Computation of Overturning Waves." *Journal of Fluid Mechanics*, 150, pp. 233-251.
- Newland, D. E. (1993). *An Introduction to Random Vibrations, Spectral & Wavelet Analysis*, Longman Scientific & Technical, New York.



References

- Phillips, O. M. (1966). *The Dynamics of the Upper Ocean*, Cambridge University Press, Cambridge.
- Phillips, O. M. (1985). "Spectral Characteristics of Breaking Waves." *The Ocean Surface*, pp. 111-123.
- Ochi, M. K. and Tsai, C.-H. (1983). "Predictions of Occurrence of Breaking Waves in Deep Water." *Journal of Physical Oceanography* 13, pp. 2009-2019.
- Ochi, M. K. (1998). *Ocean Waves - The Stochastic Approach*, Cambridge University Press, Cambridge.
- Qiao, H. and J. H. Duncan (2001). "Gentle spilling breakers: crest flow-field evolution." *Journal of Fluid Mechanics*, 439, pp. 57-85.
- Quinn, P. A. (1995). "Breaking Waves on Beaches," PhD Thesis, The University of Edinburgh.
- Quinn, P. A. et al. (1994). "A Critical Analysis of the Particle Image Velocimetry technique as applied to Water Waves." *Flow Visualization and Image Analysis*, F. T. M. Nieuwstadt, ed., Kluwer Academic Publishers, Dordrecht.
- Raffel, M. and Kopenhans, J. (1996). "Theoretical and Experimental Aspects of PIV Recording Utilizing Photographic Film and Mechanical Image Shifting." *Lecture Series 1996-03*, von Karman Institute for Fluid Dynamics, Brussels.
- Ramberg, S. E. and Griffin, M. E. (1987). "A Laboratory Study of Steep and Breaking Deep Water Waves." *Journal of Waterway, Port, Coastal and Ocean Engineering*, 113, pp. 493-406.
- Resch, F. (1986). "Oceanic Air Bubbles as Generators of Marine Aerosol." *Oceanic Whitecaps and Their Role in Air-Sea Exchange Processes*, E. C. Monahan and G. Mac Niocaill, eds., D. Reidel Publishing Company, Dordrecht, Holland, pp. 101-112.
- Rogers, D. F. and Adams, J. A. (1990). *Mathematical Elements for Computer Graphics*, McGraw-Hill.
- Royer, H. and Stanislas, M. (1996). "Stereoscopic and Holographic Approaches to get the Third Velocity Component in PIV." *Lecture Series 1996-03*, von Karman Institute for Fluid Dynamics, Brussels.

References

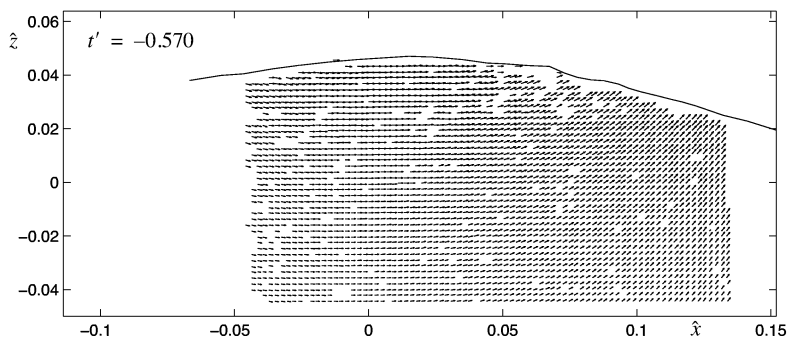
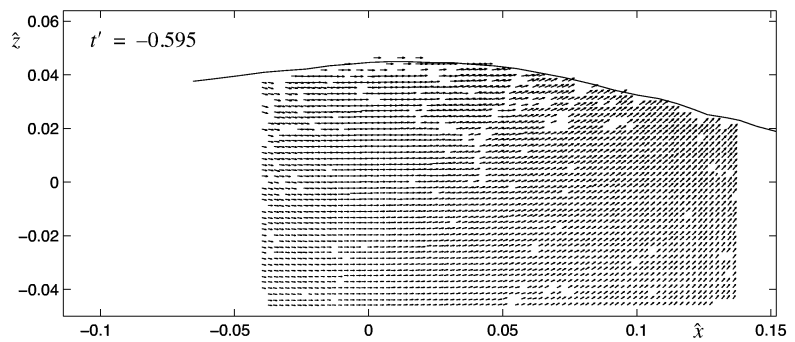
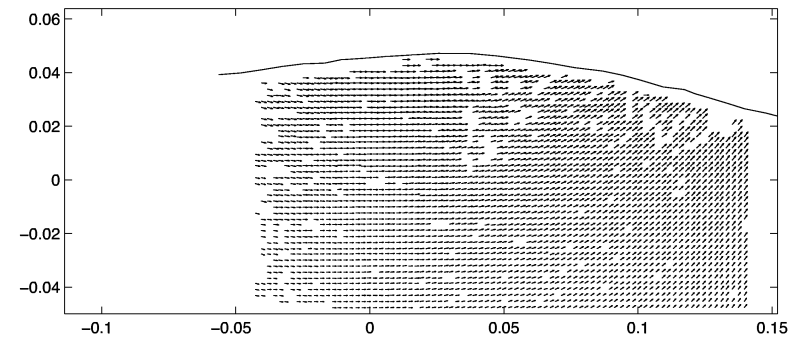
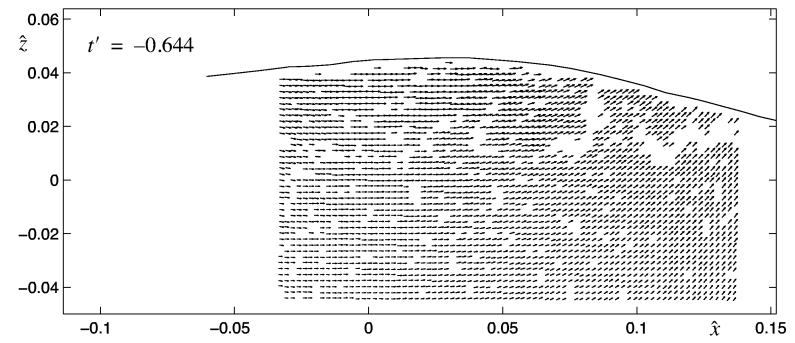
- Skyner, D. J. (1992). "The Mechanics of Extreme Water Waves", PhD Thesis, The University of Edinburgh.
- Smith, F. G. W. (1973). *The Seas in Motion*, Thomas Y. Crowell Company, New York.
- Stokes, G. G. (1849). "On the Theory of Oscillatory Waves", *Transactions of the Cambridge Philosophical Society*, 8, pp. 441-455.
- Thorpe, S. A. and Humphries, P. N. (1980). "Bubbles and Breaking Waves." *Nature*, 283, pp. 463-465.
- TSI. (1994). "Particle Image Velocimetry: TSI Seminar on Fluid Flow Instrumentation", TSI.
- Tulin, M. P. and M. Landrini (2000). "Breaking Waves in the Ocean and around Ships", 23rd Symposium on Naval Hydrodynamics, Val De Reuil, France, September 17-22, 2000, pp. 1-32.
- Tulin, M. P. (1996). "Breaking of Ocean Waves and Downshifting." *Waves and Nonlinear Processes in Hydrodynamics*, J. Grue, B. Gjevik, and J. E. Weber, eds., Kluwer Academic Publishers, Oslo, Norway, pp. 177-190.
- Tulin, M. P. and Cointe, R. (1986). "A Theory of Spilling Breakers." *Sixteenth Symposium on Naval Hydrodynamics*, Berkeley, Calif., pp. 93-105.
- Tulin, M. P. and Li, J. J. (1992). "On the Breaking of Energetic Waves." *International Journal of Offshore and Polar Engineering*, 2(1), pp. 46-53.
- Van Dorn, W. G. and Pazan, S. E. (1975). "Laboratory Investigation of Wave Breaking." *AD A013 336*, Scripps Institution of Oceanography.
- Vinje, T. and Brevig, P. (1980). "Breaking Waves on Finite Water Depths. A Numerical Study." , The Norwegian Institute of Technology - Division of Marine Hydrodynamics and Norwegian Hydrodynamic Laboratories - Division Ship and Ocean Laboratory.
- Vinje, T. and Brevig, P. (1981). "Numerical Simulation of Breaking Waves." *Advances in Water Resources*, 4 (June), pp. 77-81.



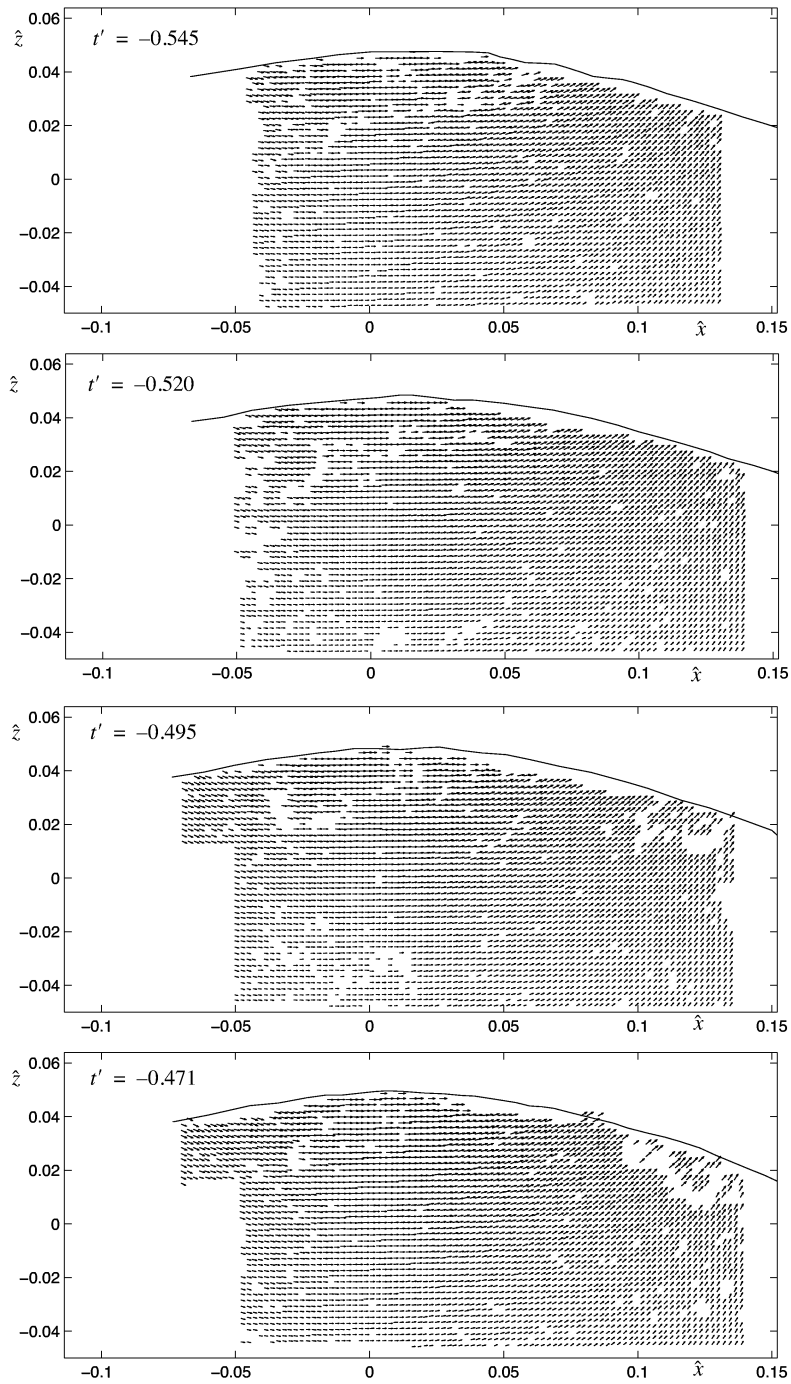
Appendix A **Vector Field Plots of the Wave Kinematics Measurements**

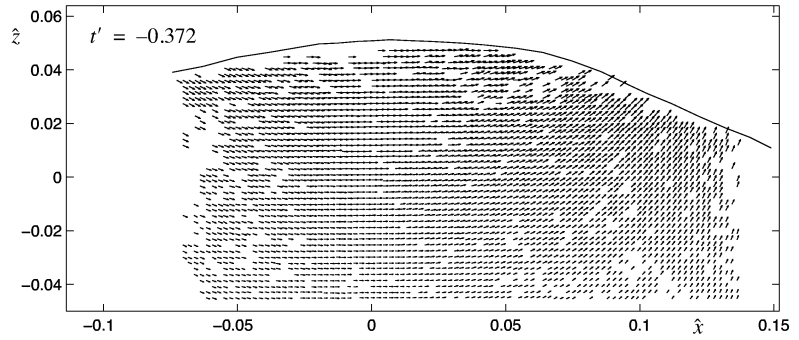
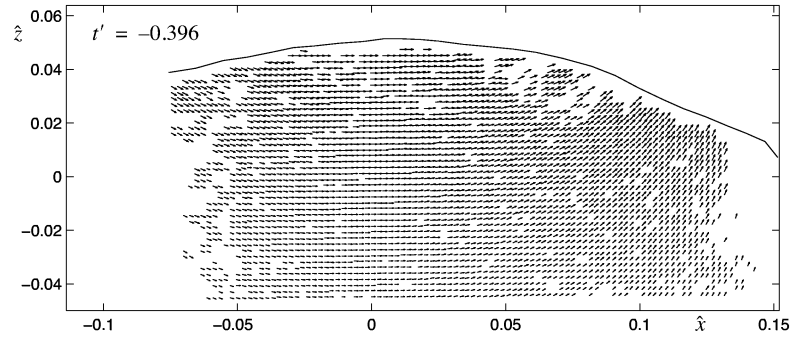
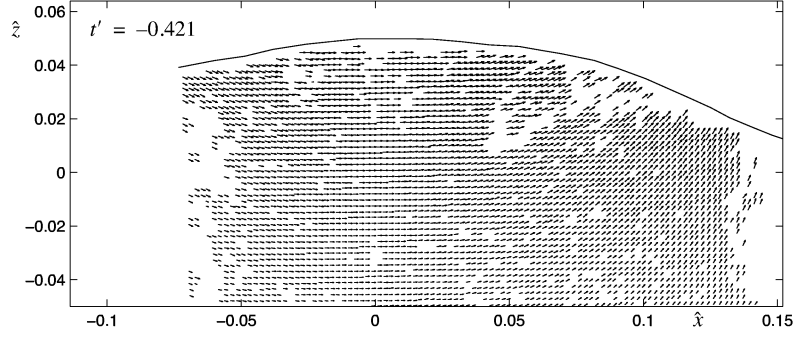
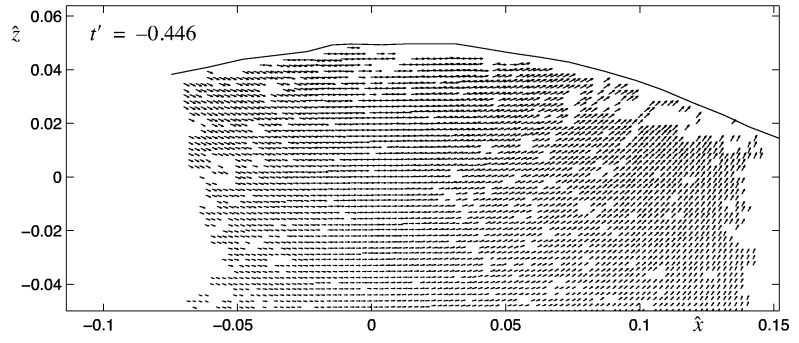
In this appendix the complete velocity fields from the PIV measurements are presented. They were the basis for calculating the parameters used in the kinematic analysis. Axis values and time are normalized as described in *Chapter 2.9.2*.

A.1 Plunging Breaker (case 1)

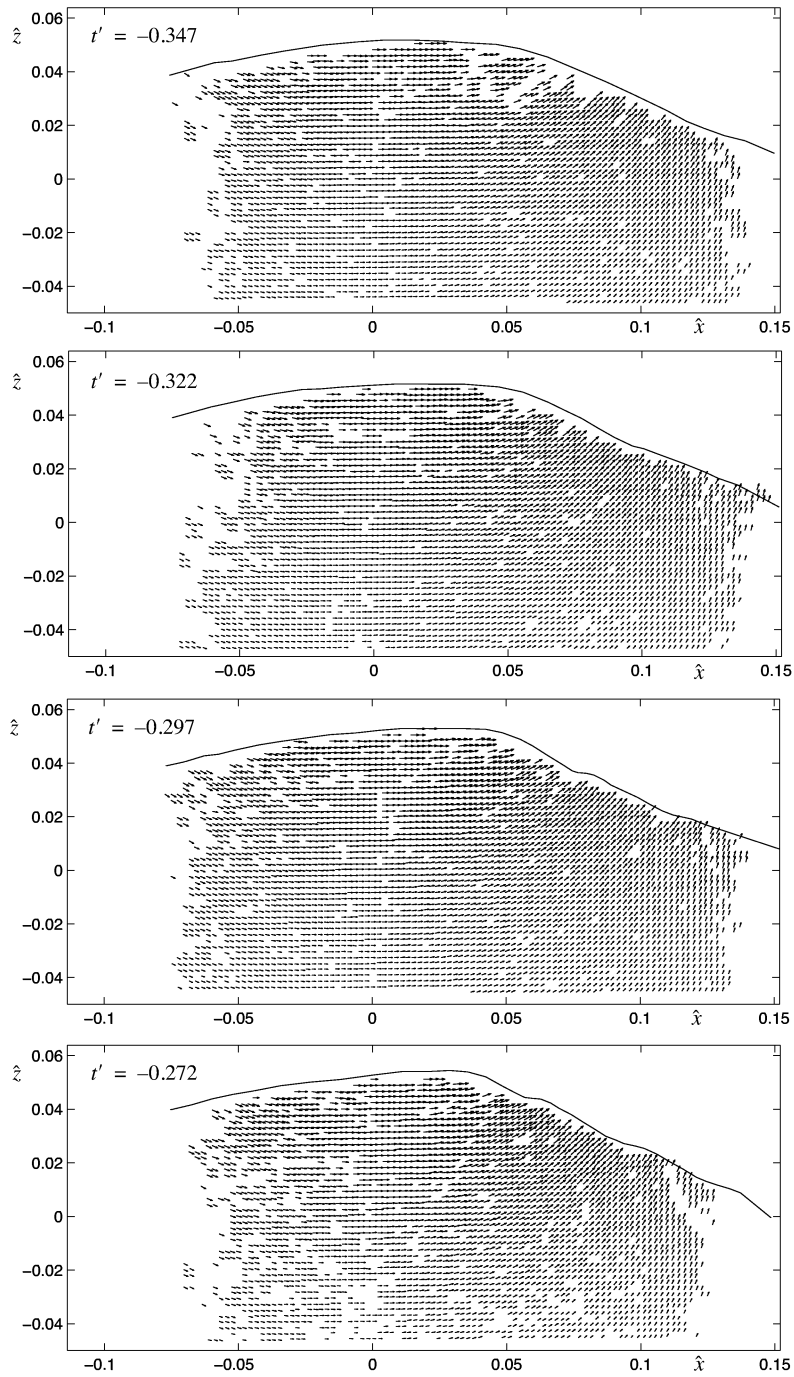


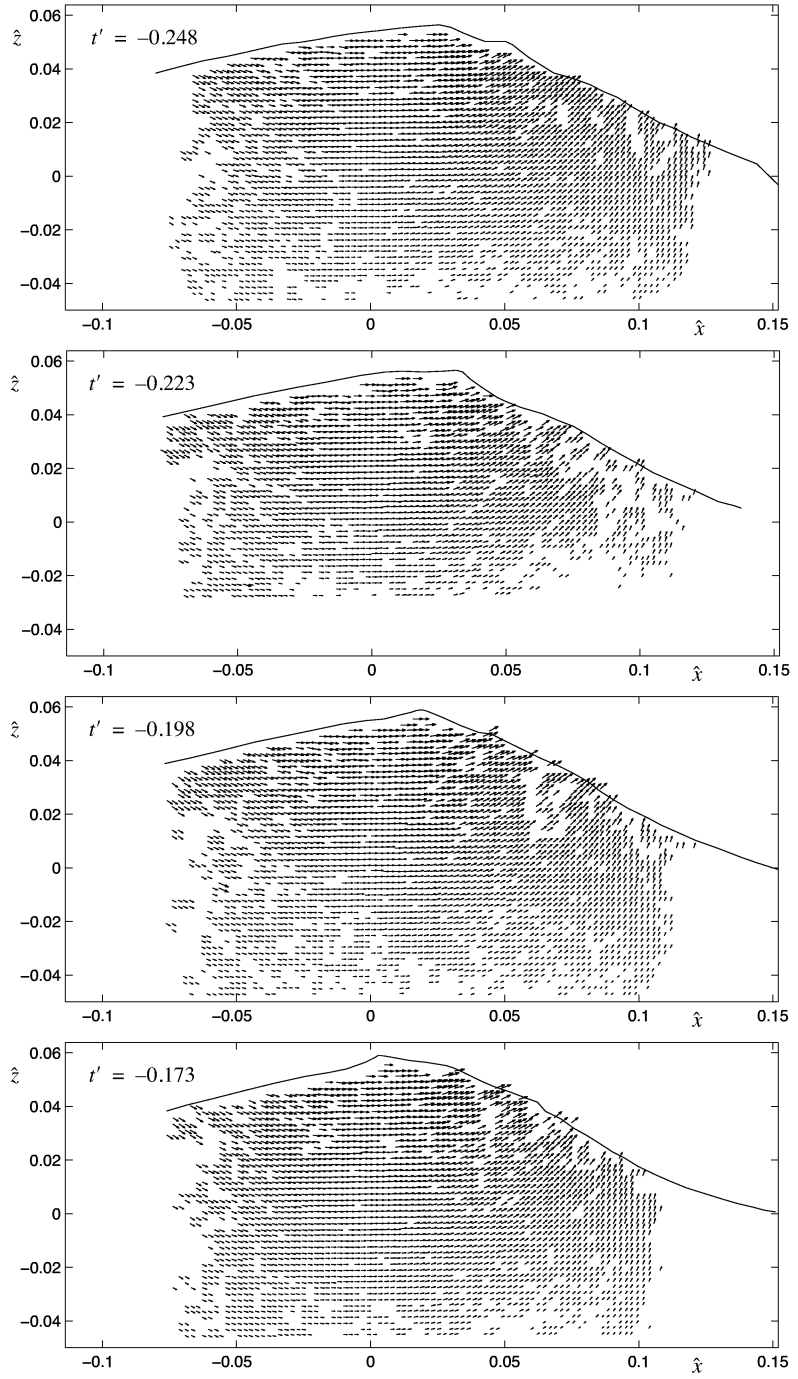
A.1 Plunging Breaker (case 1)



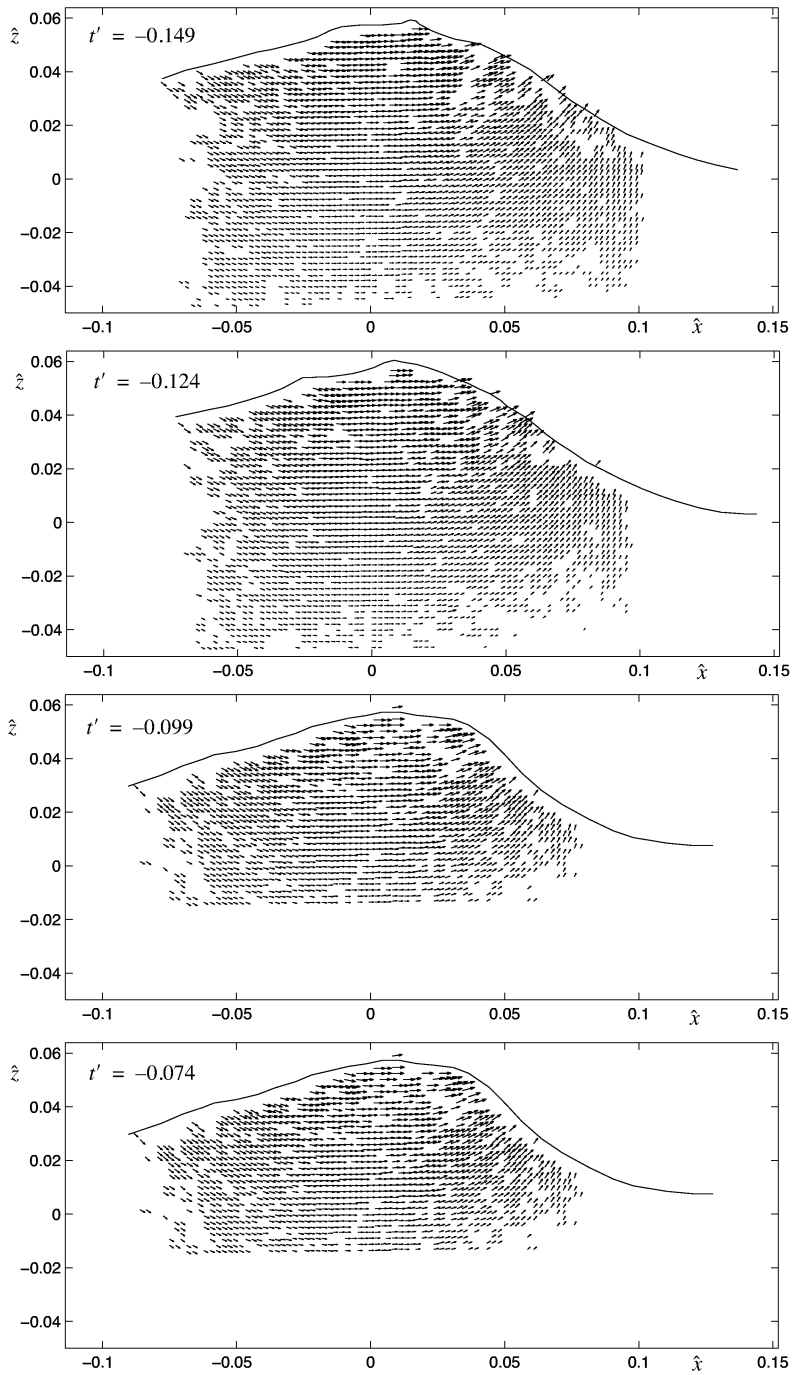


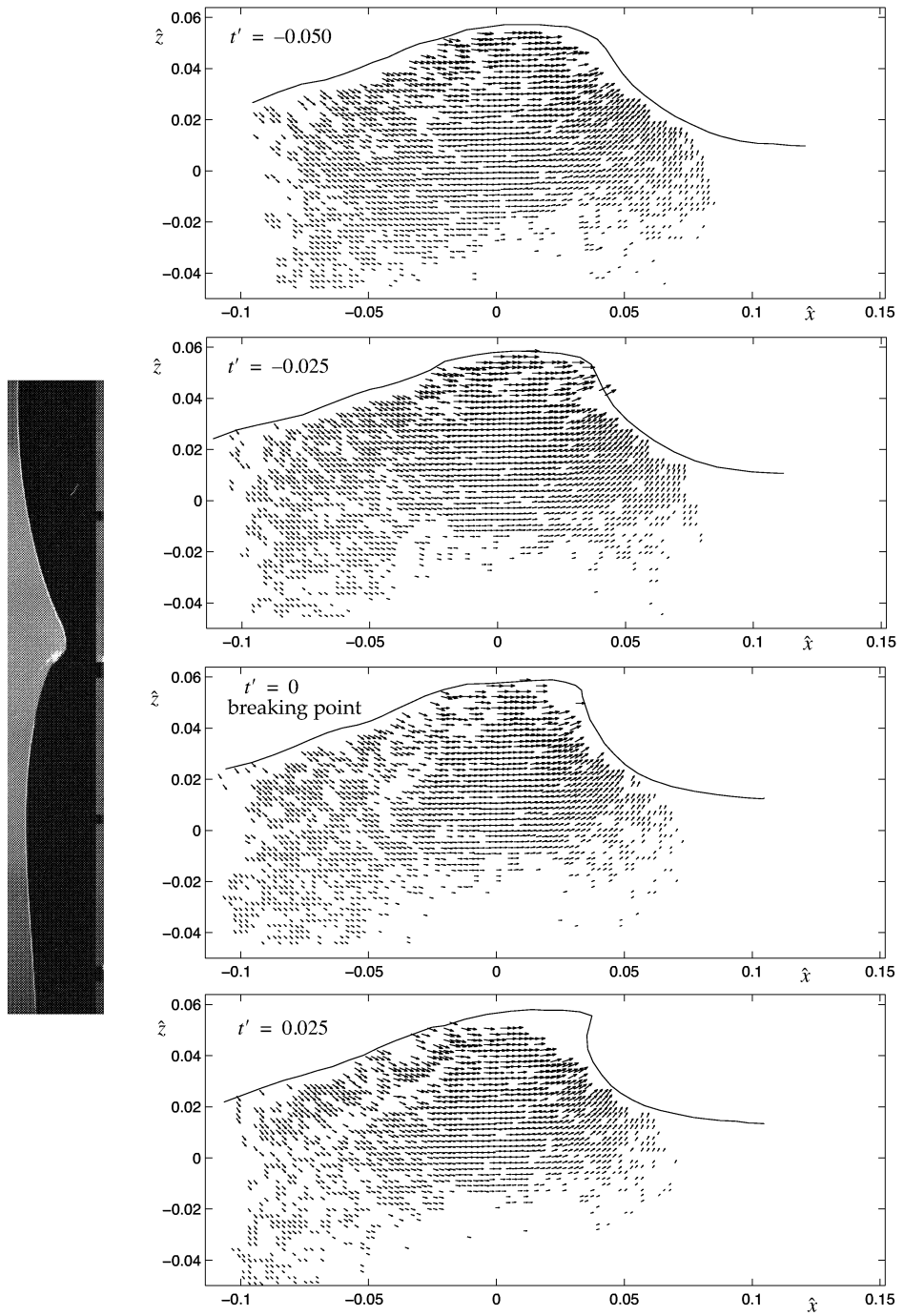
A.1 Plunging Breaker (case 1)



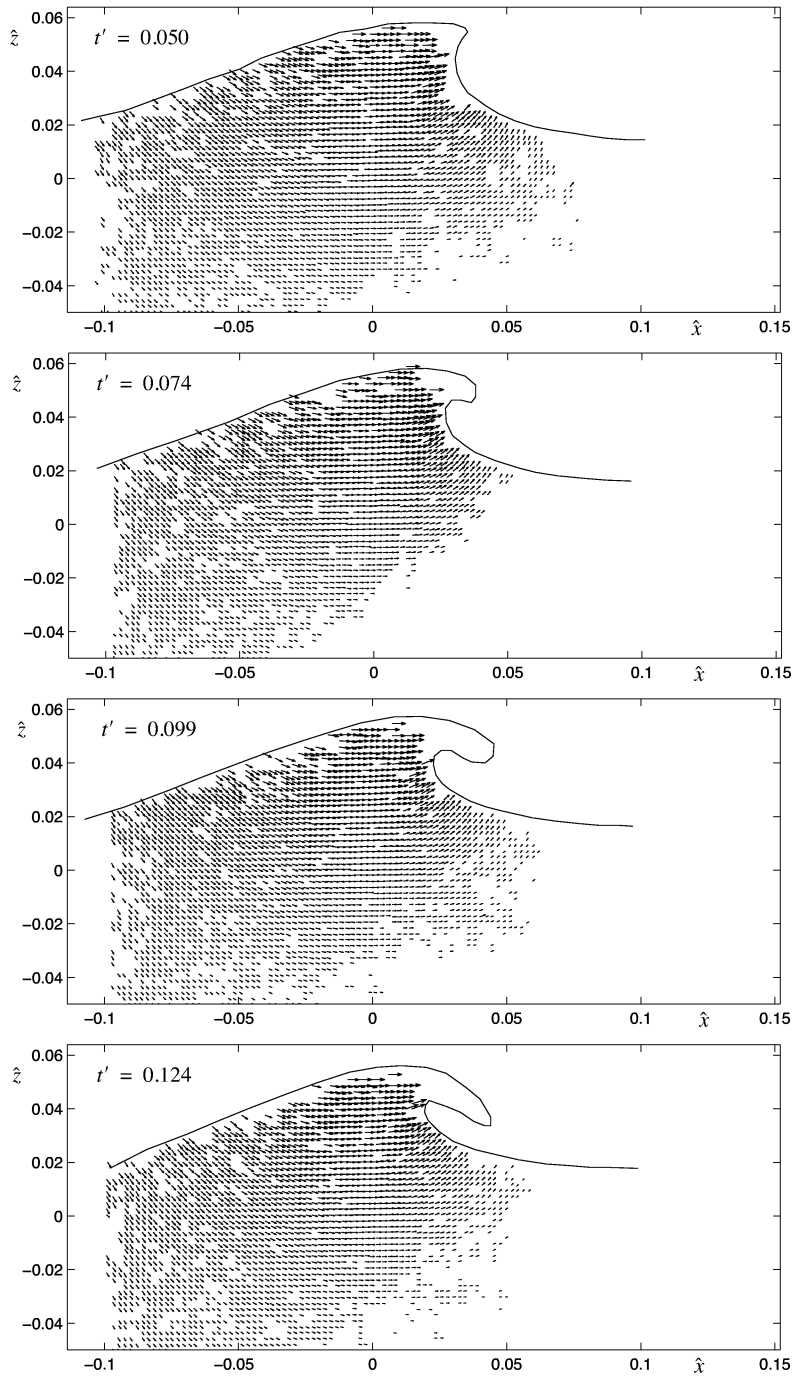


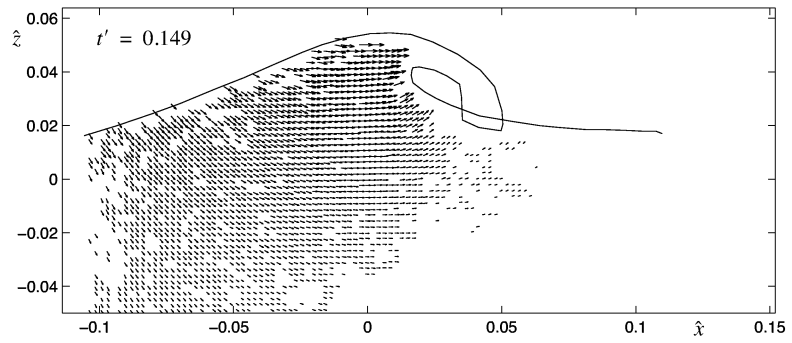
A.1 Plunging Breaker (case 1)



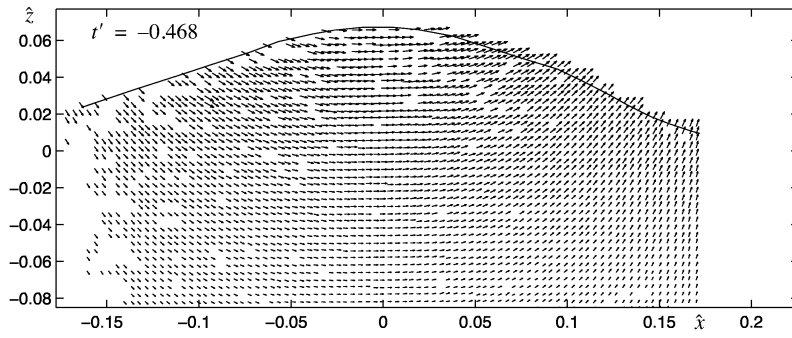
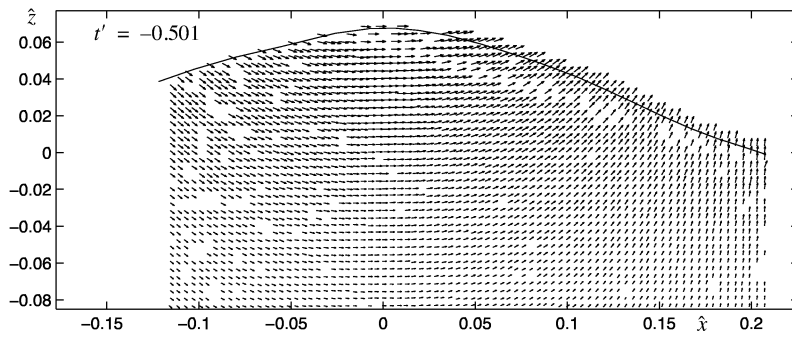
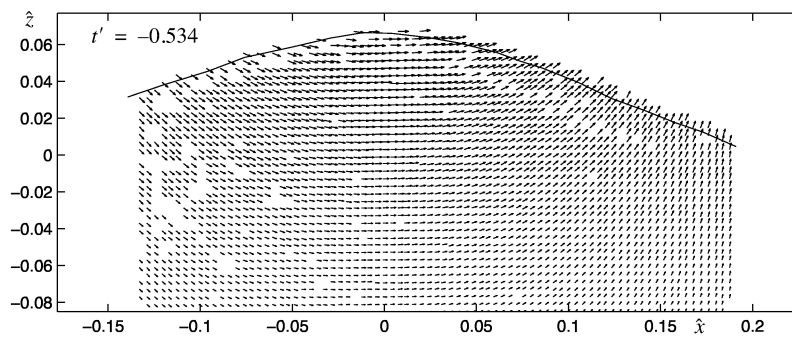
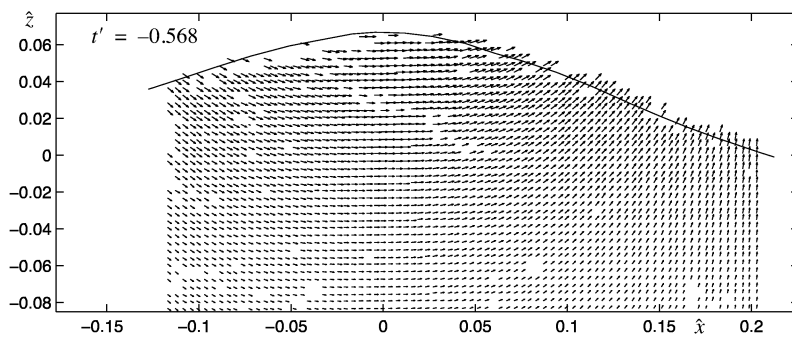


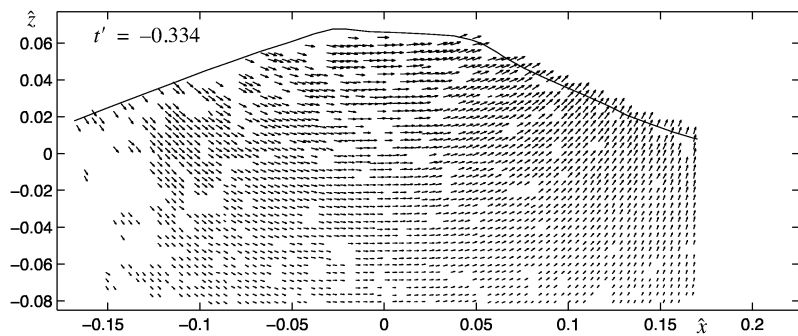
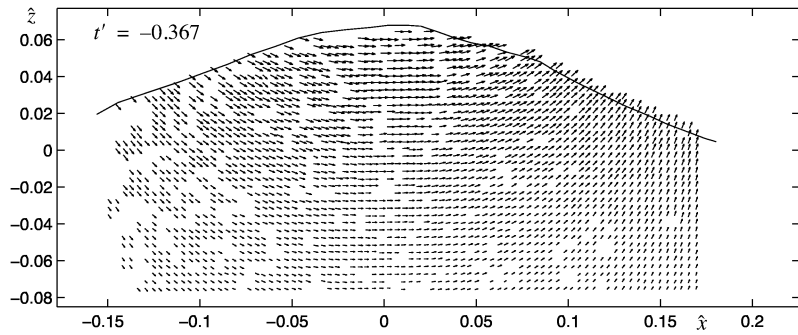
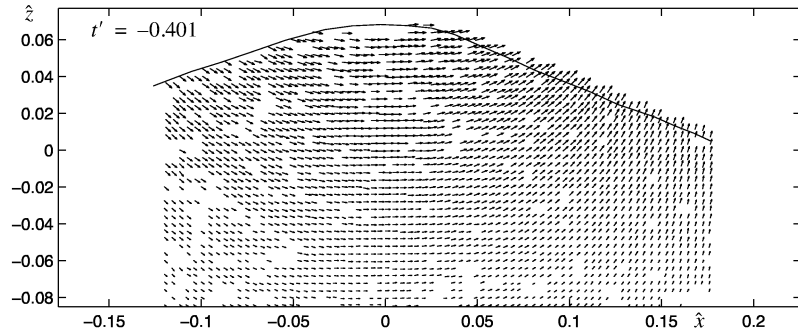
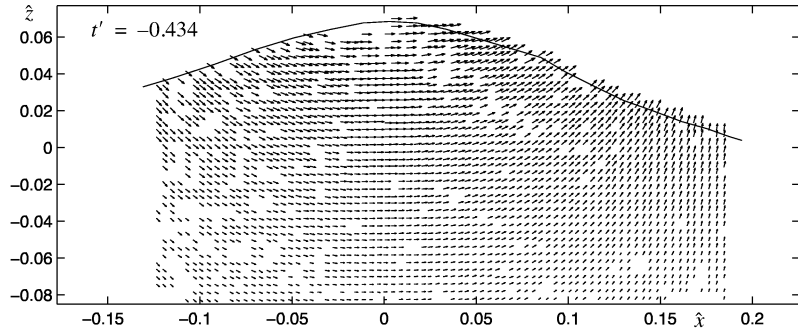
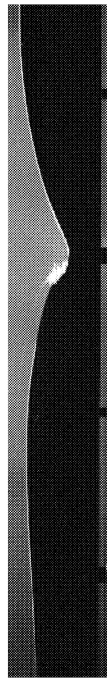
A.1 Plunging Breaker (case 1)



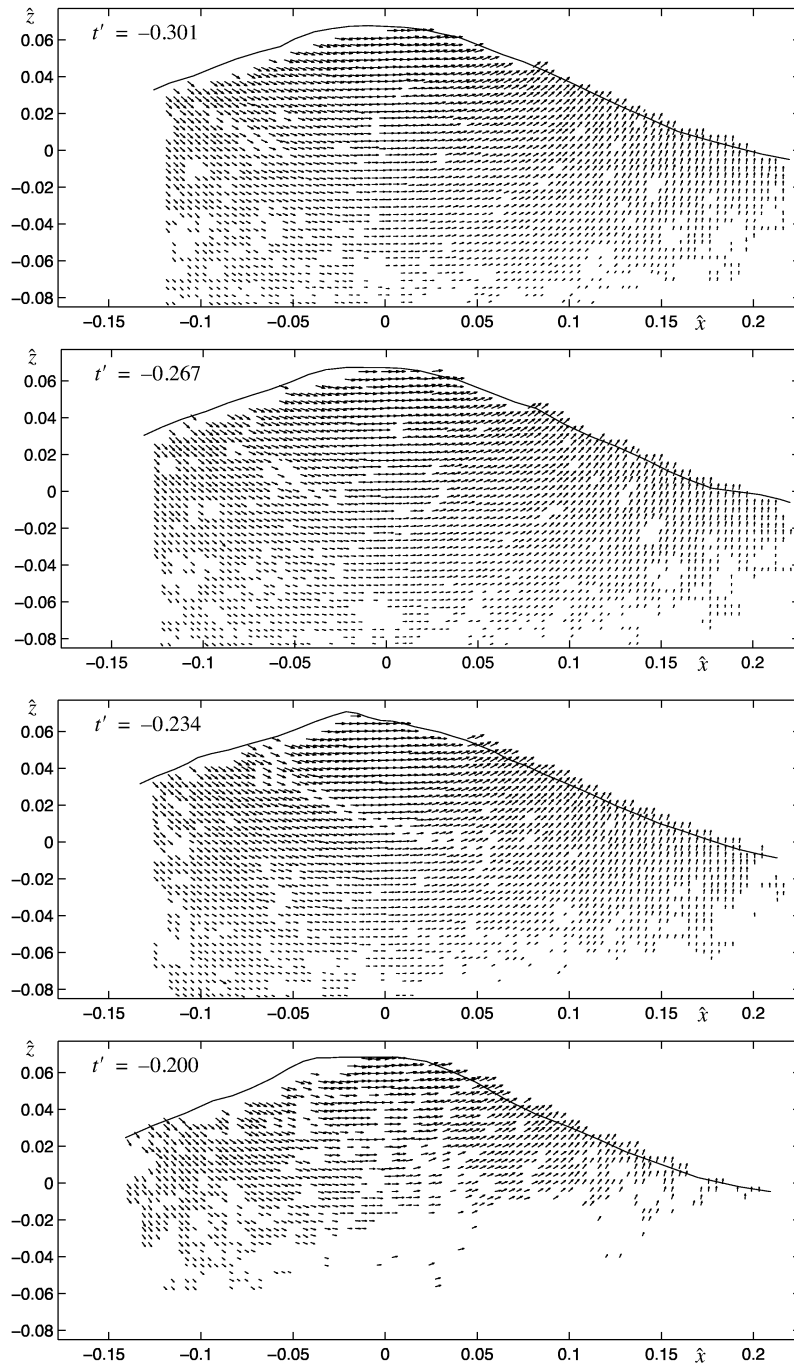


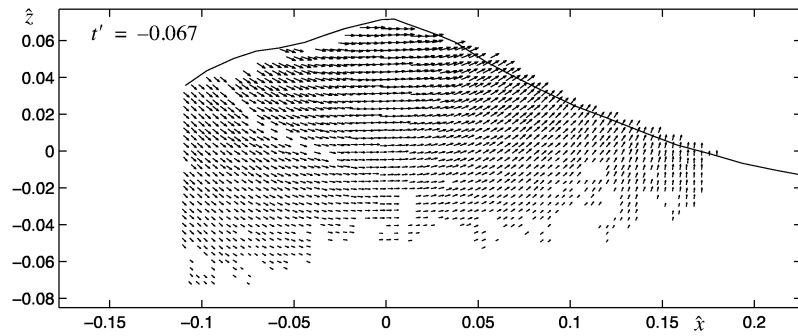
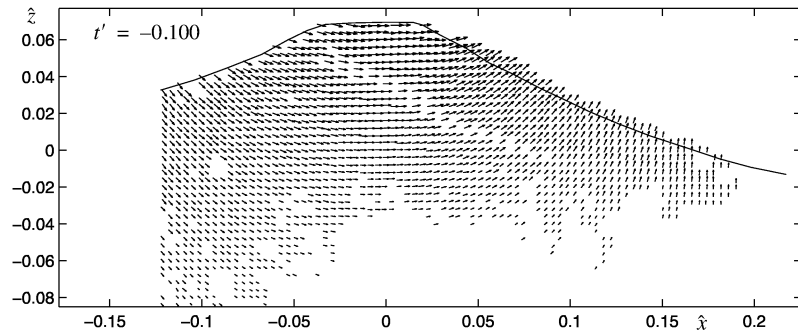
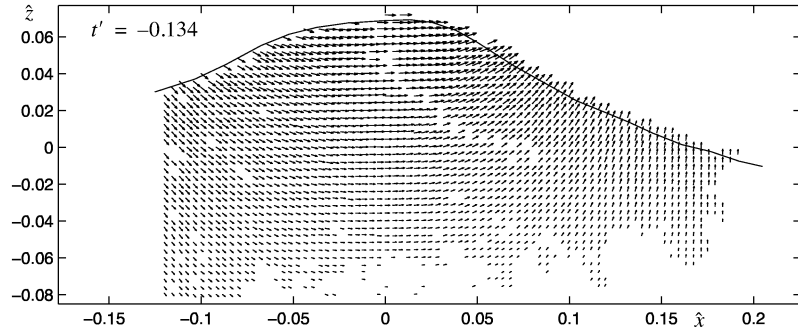
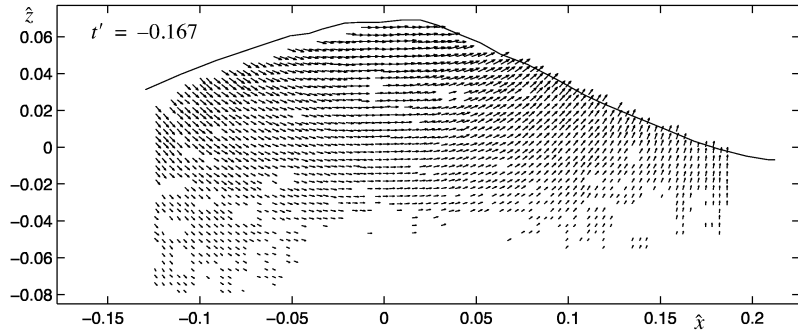
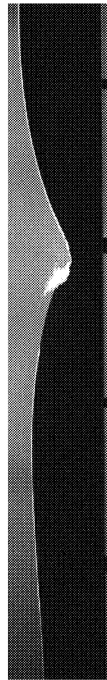
A.2 Intermediate Breaker (case 2)



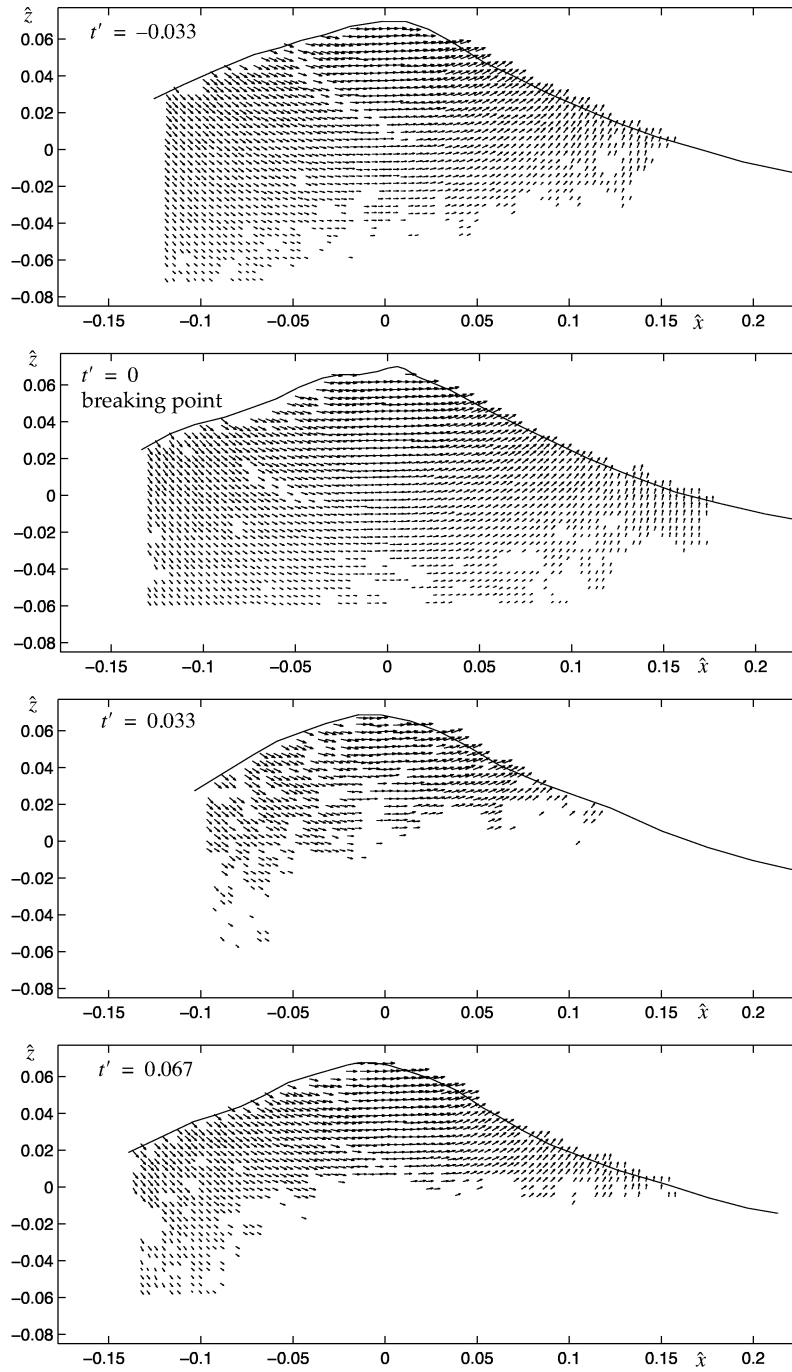


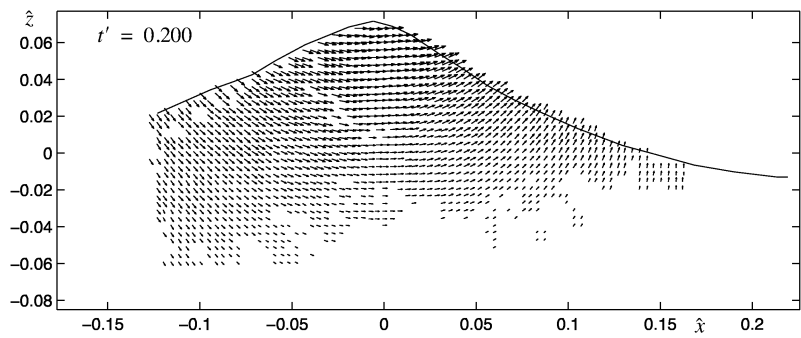
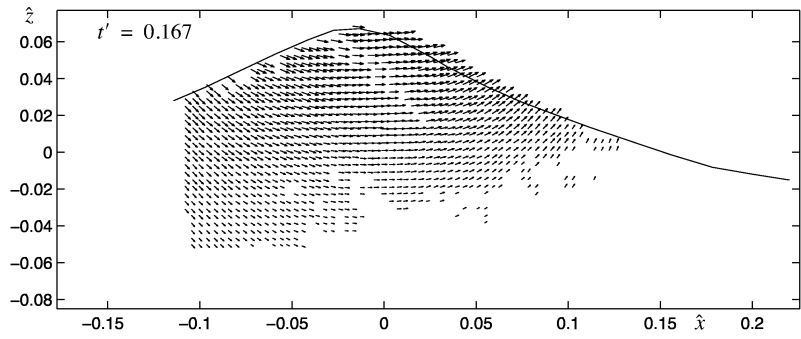
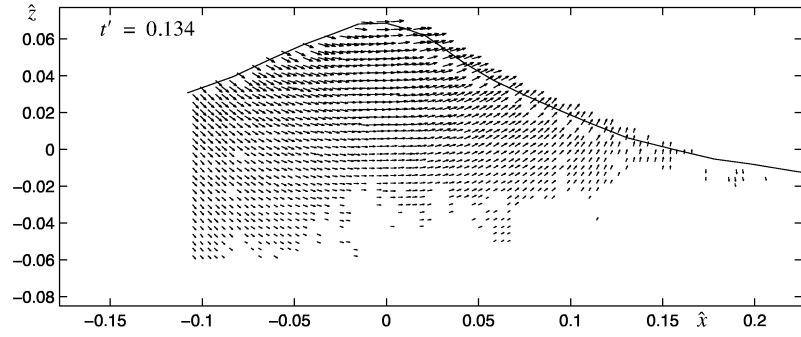
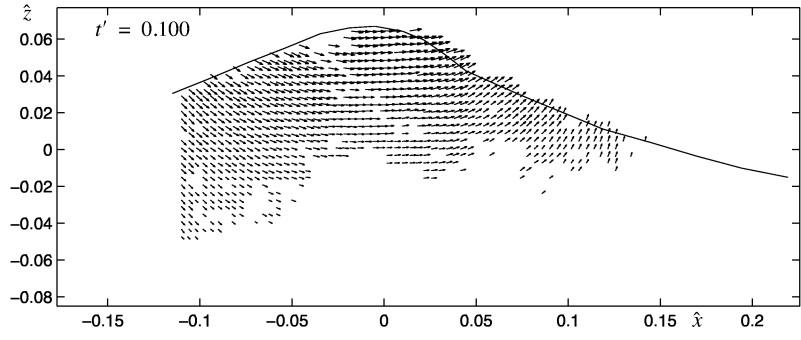
A.2 Intermediate Breaker (case 2)



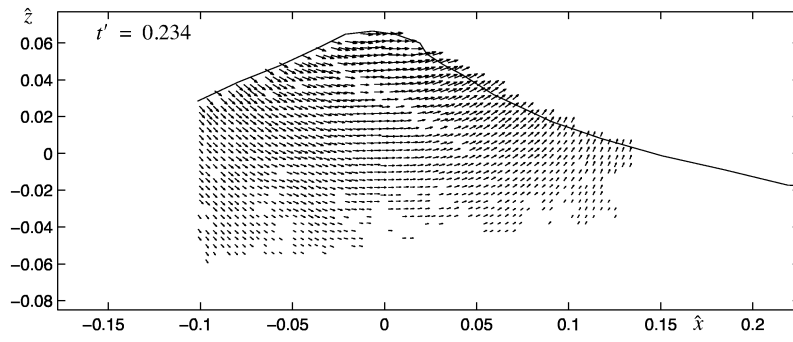


A.2 Intermediate Breaker (case 2)

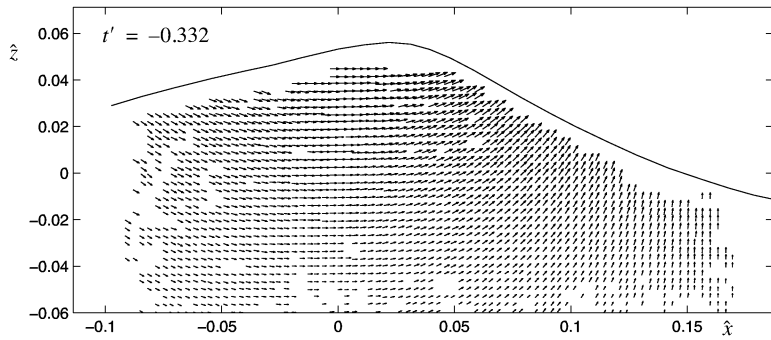
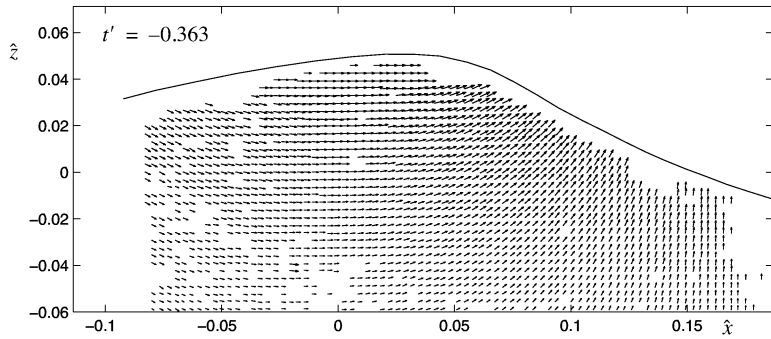
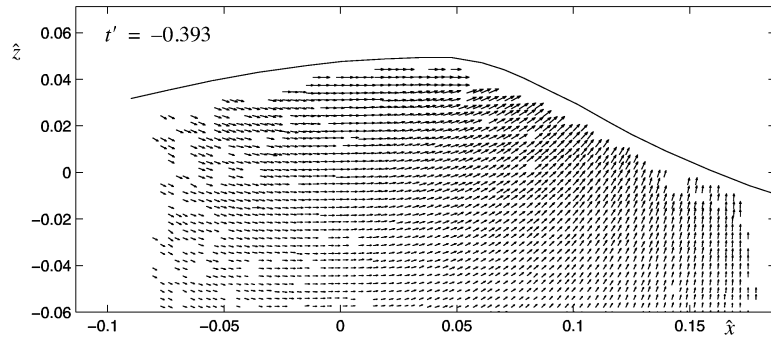
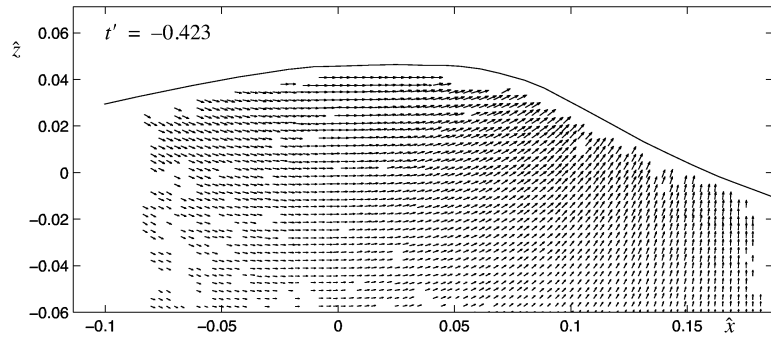




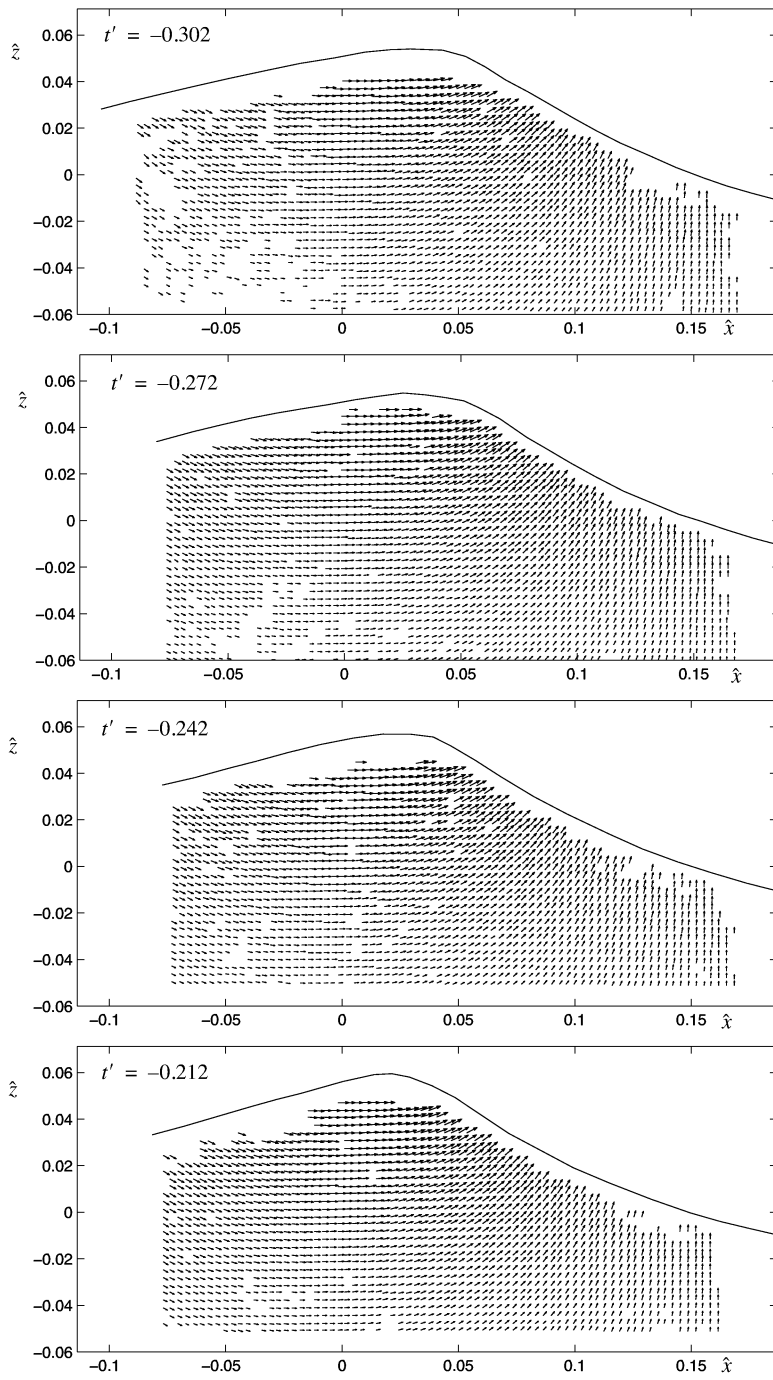
A.2 Intermediate Breaker (case 2)

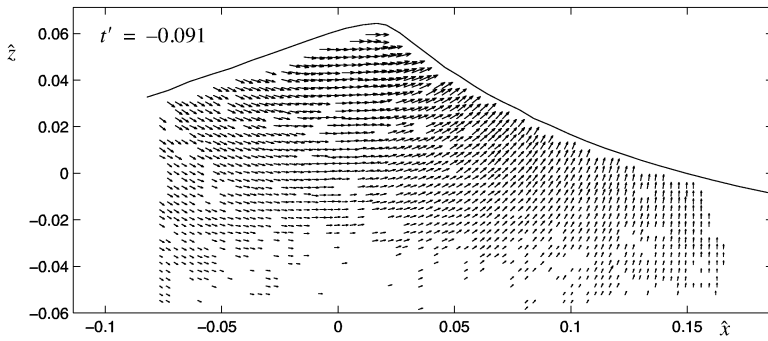
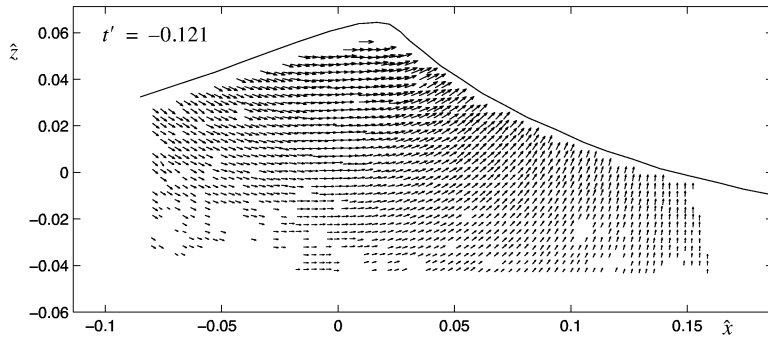
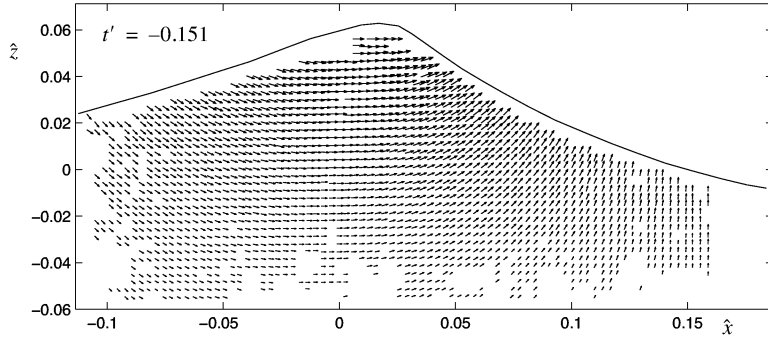
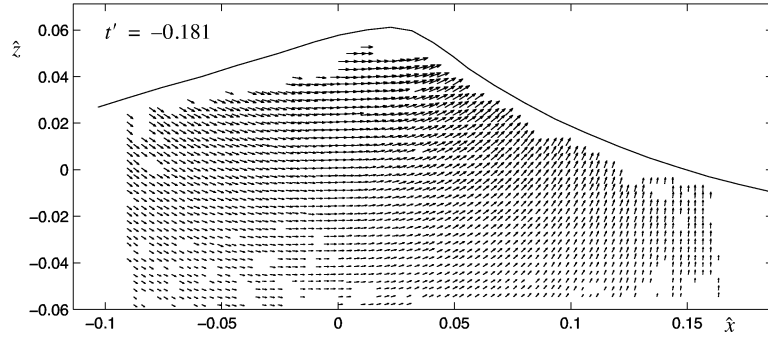


A.3 Spilling Breaker (case 3)

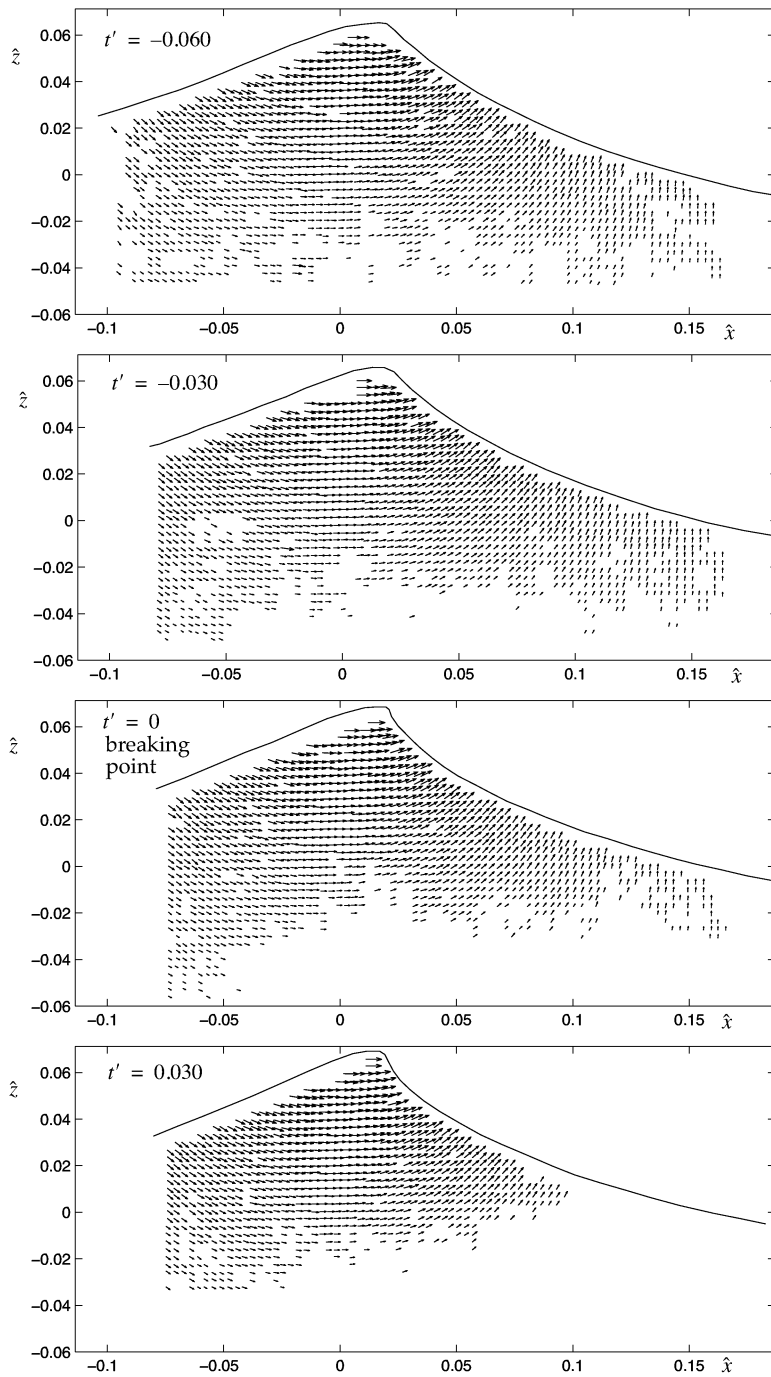


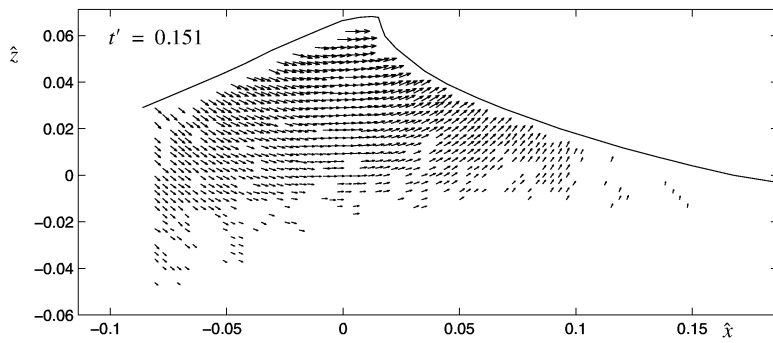
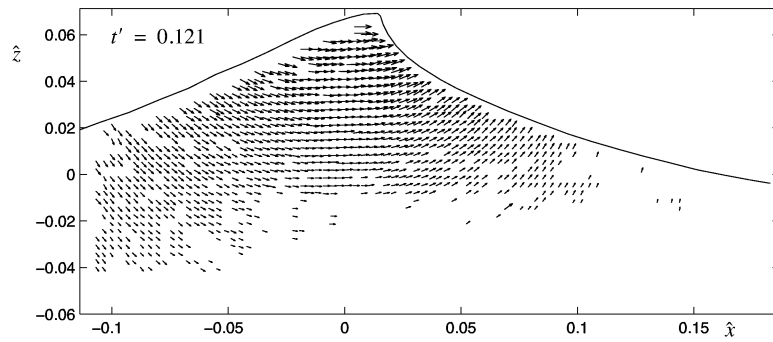
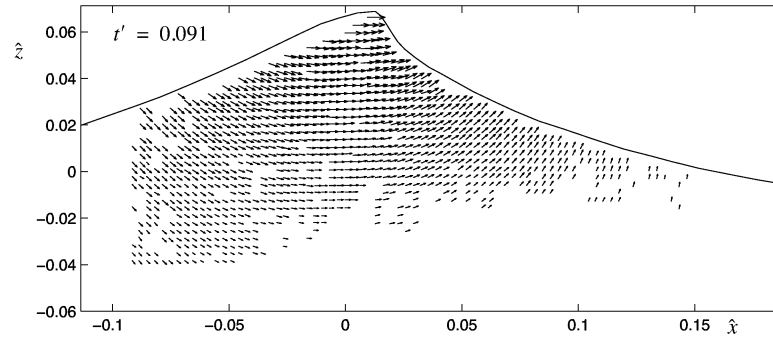
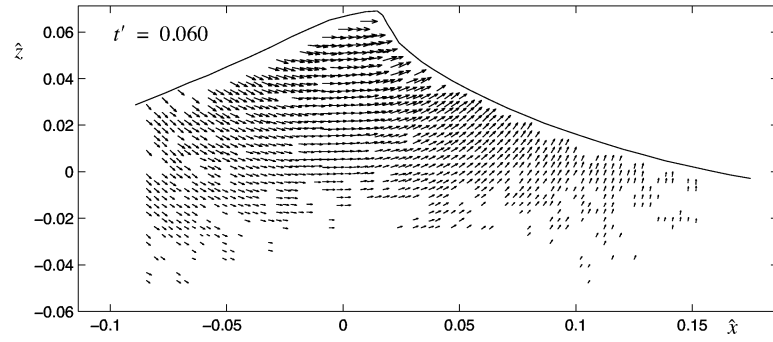
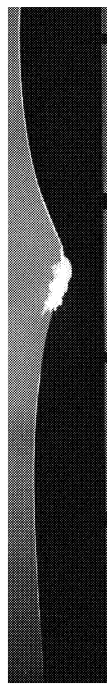
A.3 Spilling Breaker (case 3)





A.3 Spilling Breaker (case 3)





Appendix B **Additional Wave Kinematic Parameter Measurements**

In this appendix the wave kinematic parameters are shown with full temporal sampling frequency (32Hz). The appendix also includes a comparison between the velocity at $z = 0$; extrapolated (U'_0) and measured (\hat{U}'_0), see Figures 114 to 117.

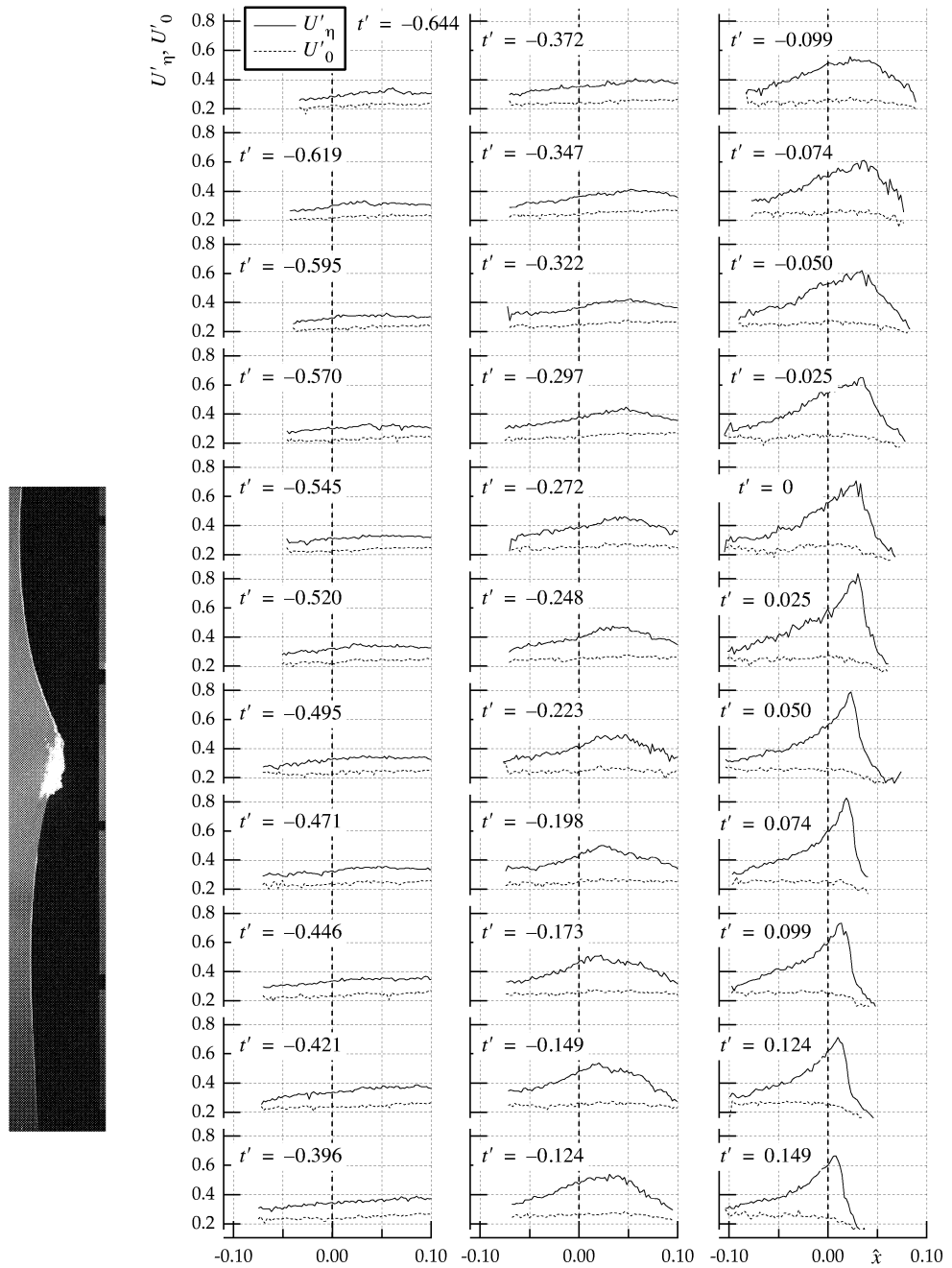


FIGURE 105. The plunging breaker (case 1): Surface velocity (U'_η) and velocity at $z = 0$ (U'_o) as a function of \hat{x} for sequent time steps. $\hat{x} = 0$ is the point in the crest where the velocity is horizontal, while $t' = 0$ corresponds to the breaking point.

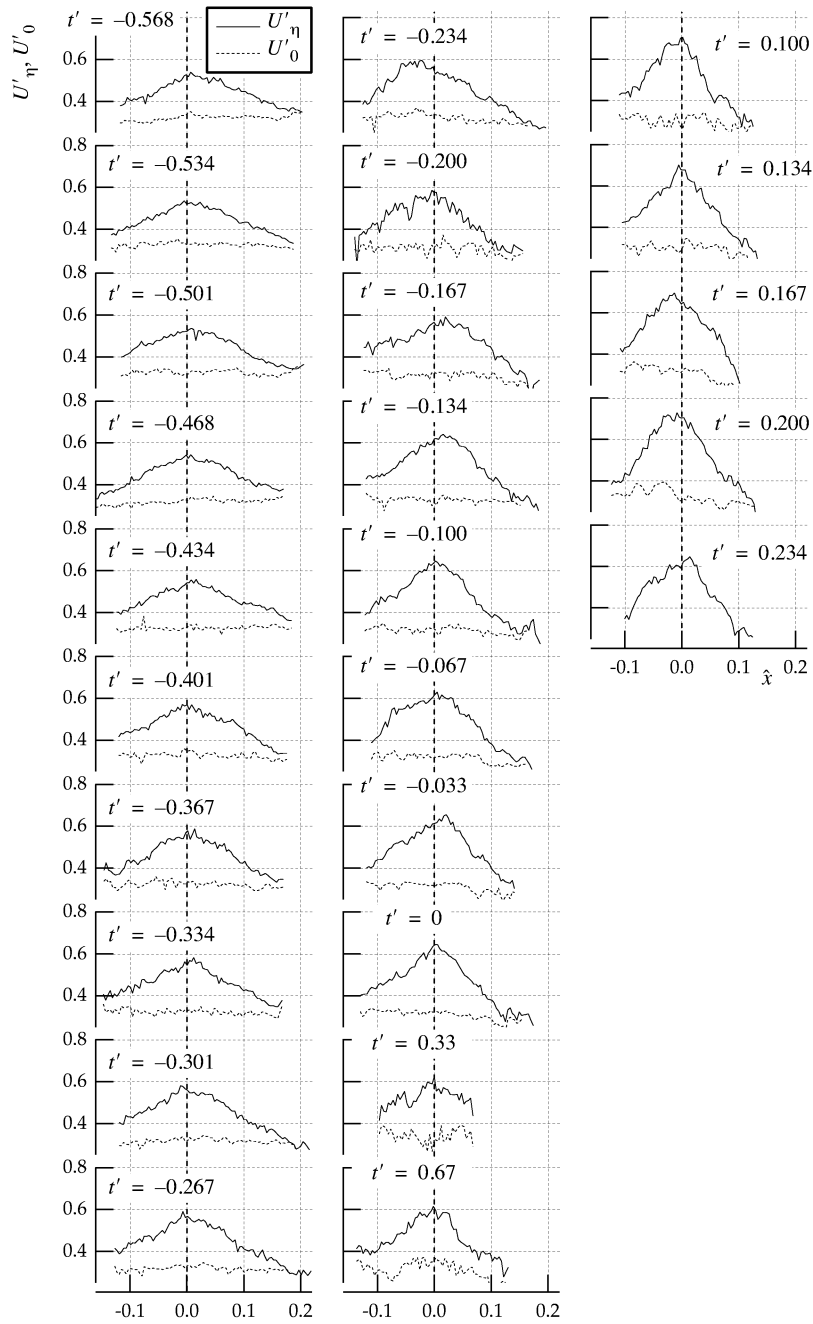


FIGURE 106. The intermediate breaker (case 2): Surface velocity (U'_η) and velocity at $z = 0$ (U'_o) as a function of \hat{x} for sequent time steps. $\hat{x} = 0$ is the point in the crest where the velocity is horizontal, while $t' = 0$ corresponds to the breaking point.

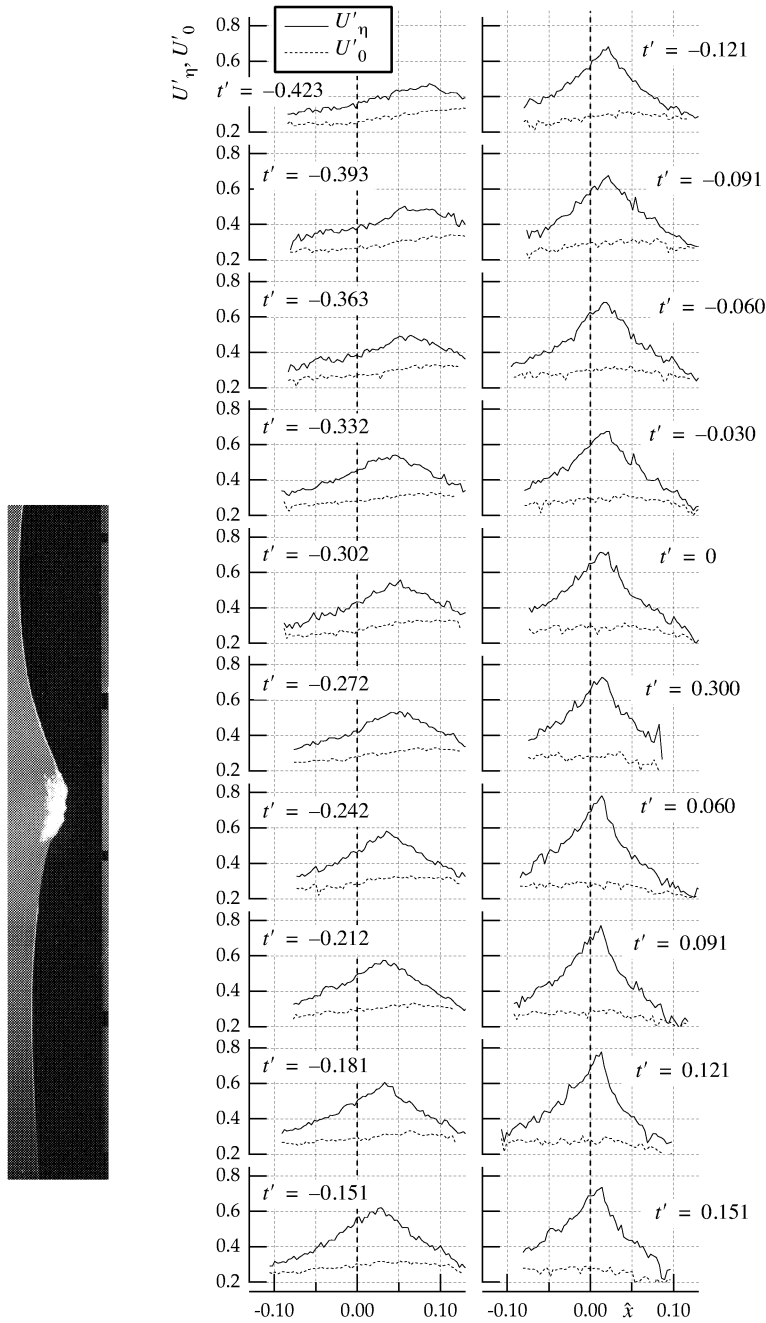


FIGURE 107. The spilling breaker (case 3): Surface velocity (U'_{η}) and velocity at $z = 0$ (U'_0) as a function of \hat{x} for sequent time steps. $\hat{x} = 0$ is the point in the crest where the velocity is horizontal, while $t' = 0$ corresponds to the breaking point.

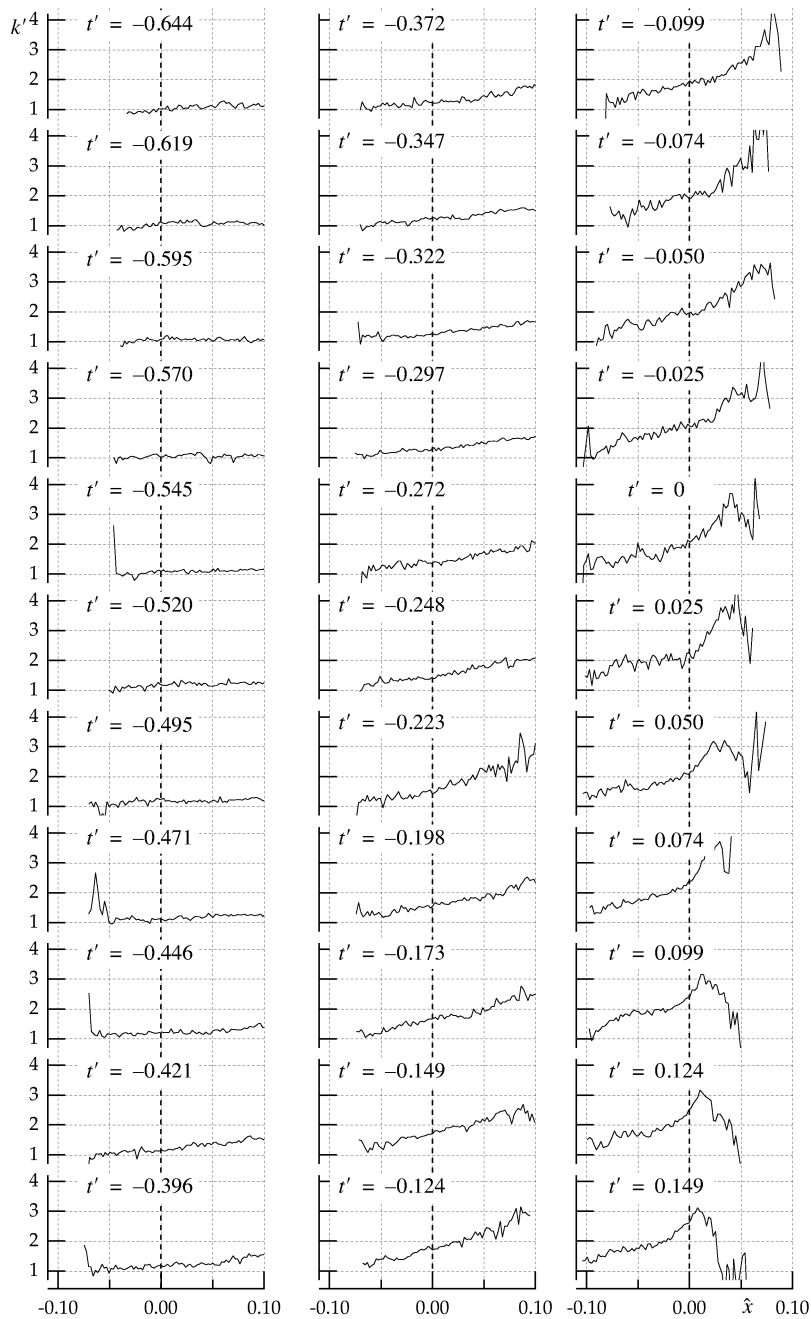


FIGURE 108. The plunging breaker (case 1): Wave number k' as a function of \hat{x} for sequent time steps. $\hat{x} = 0$ is the point in the crest where the velocity is horizontal, while $t' = 0$ corresponds to the breaking point.

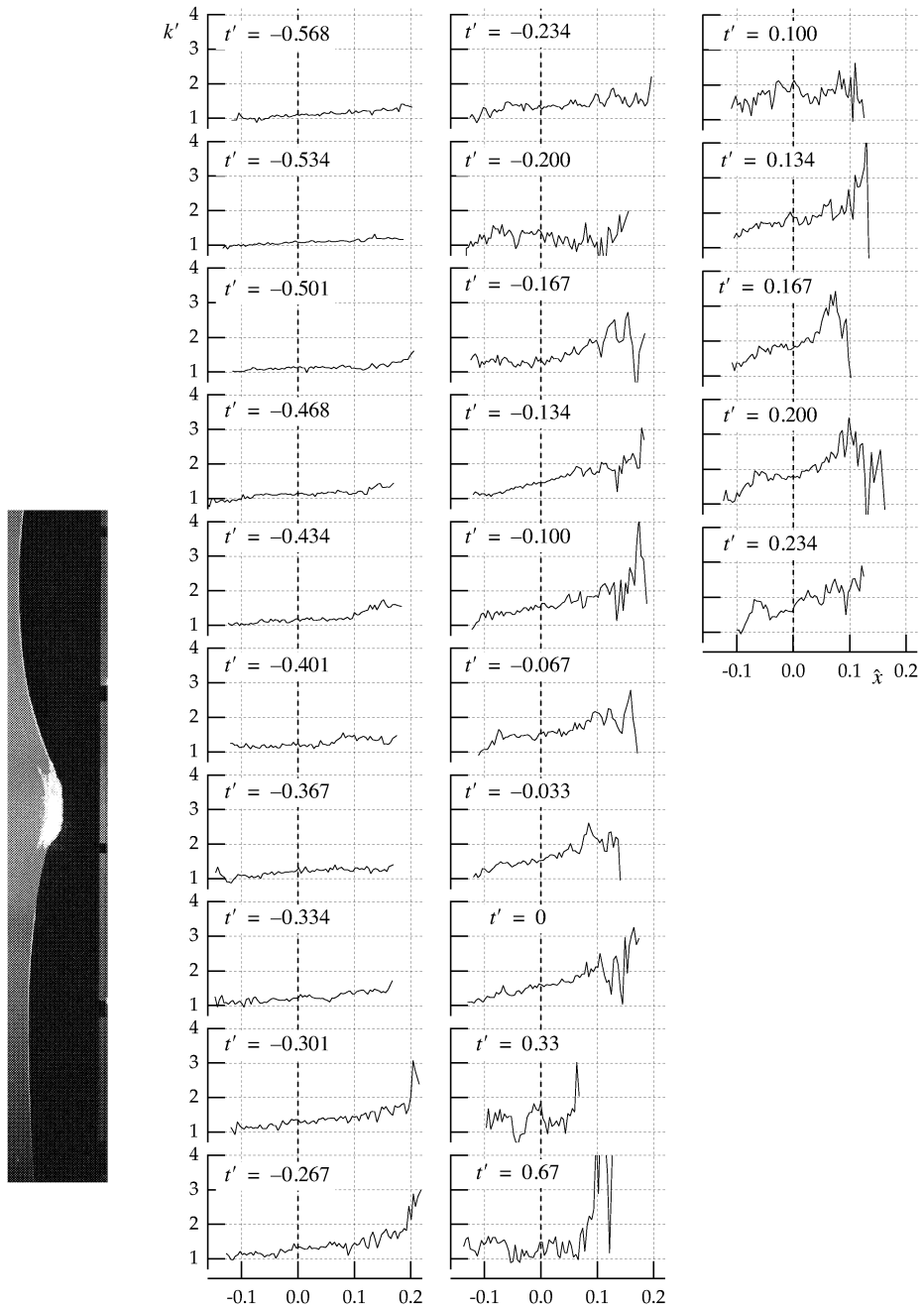


FIGURE 109. The intermediate breaker (case 2): Wave number k' as a function of \hat{x} for sequent time steps. $\hat{x} = 0$ is the point in the crest where the velocity is horizontal, while $t' = 0$ corresponds to the breaking point.

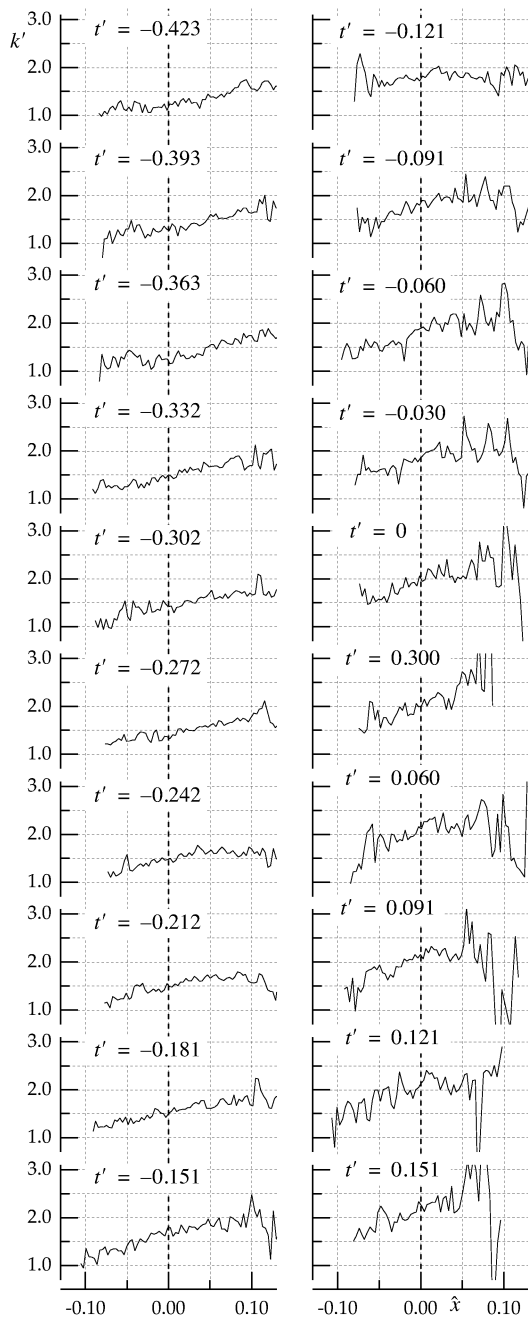


FIGURE 110. The spilling breaker (case 3): Wave number k' as a function of \hat{x} for sequent time steps. $\hat{x} = 0$ is the point in the crest where the velocity is horizontal, while $t' = 0$ corresponds to the breaking point.

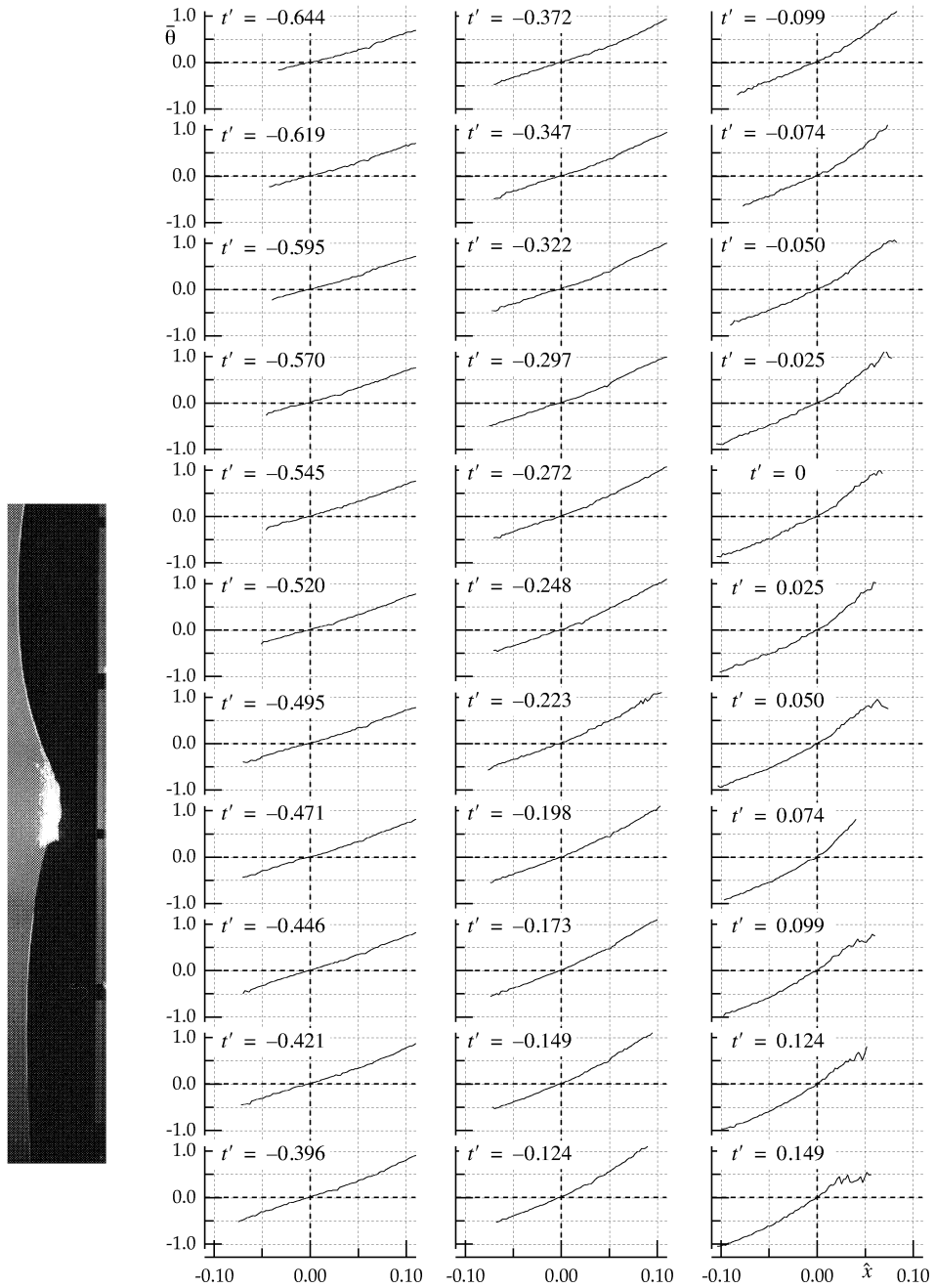


FIGURE 111. The plunging breaker (case 1): Mean velocity direction $\bar{\theta}$ as a function of \hat{x} for sequent time steps. $\hat{x} = 0$ is the point in the crest where the velocity is horizontal, while $t' = 0$ corresponds to the breaking point.

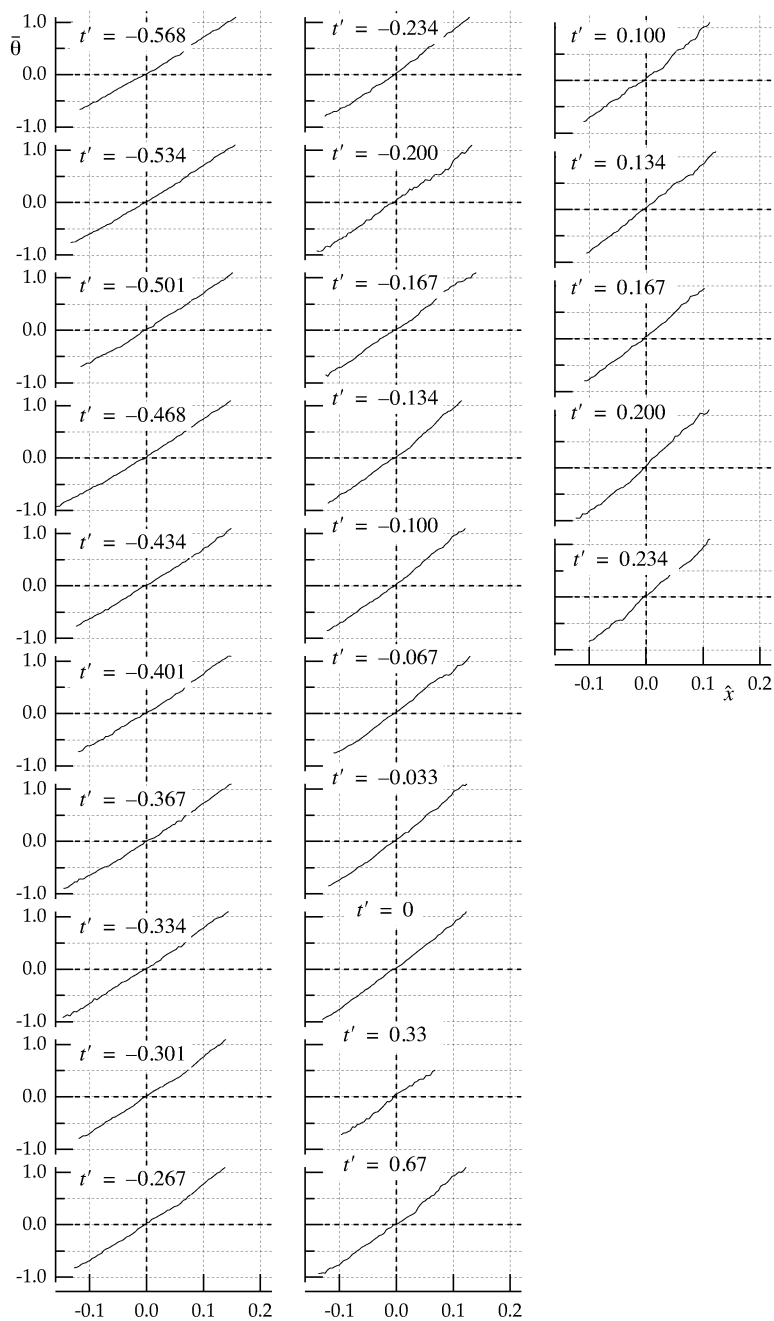


FIGURE 112. The intermediate breaker (case 2): Mean velocity direction $\bar{\theta}$ as a function of \hat{x} for sequent time steps. $\hat{x} = 0$ is the point in the crest where the velocity is horizontal, while $t' = 0$ corresponds to the breaking point.

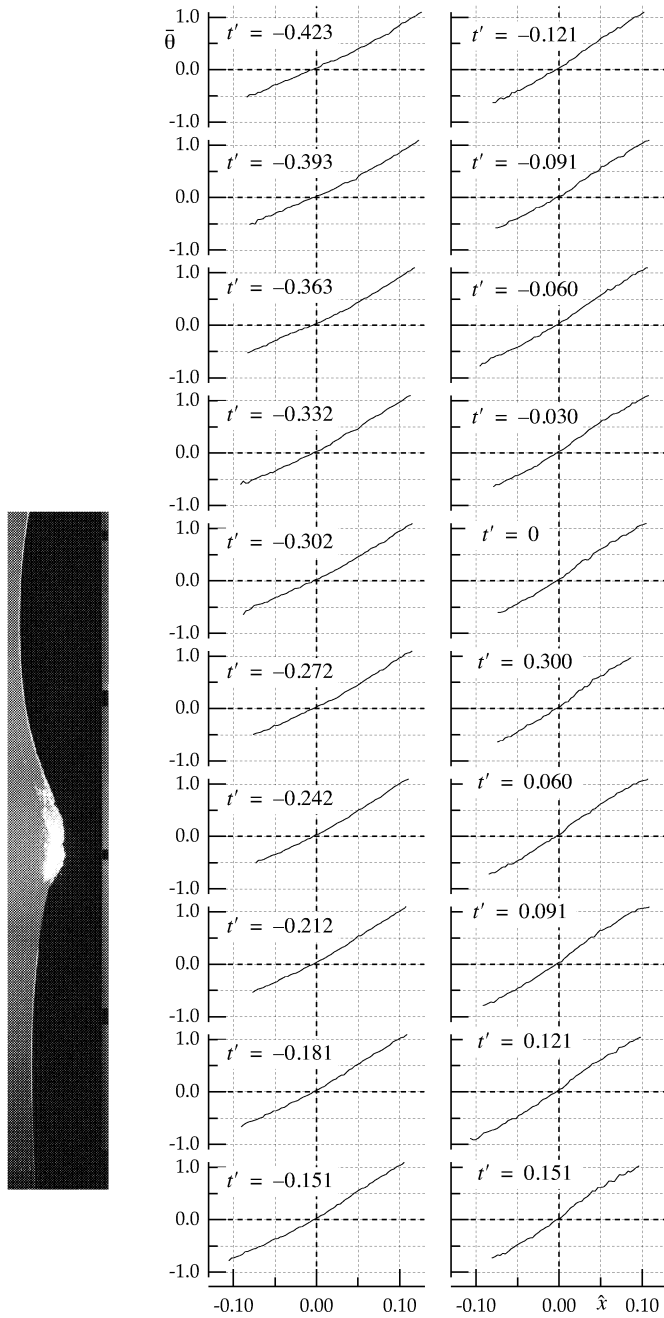


FIGURE 113. The spilling breaker (case 3): Mean velocity direction $\bar{\theta}$ as a function of \hat{x} for sequent time steps. $\hat{x} = 0$ is the point in the crest where the velocity is horizontal, while $t' = 0$ corresponds to the breaking point.

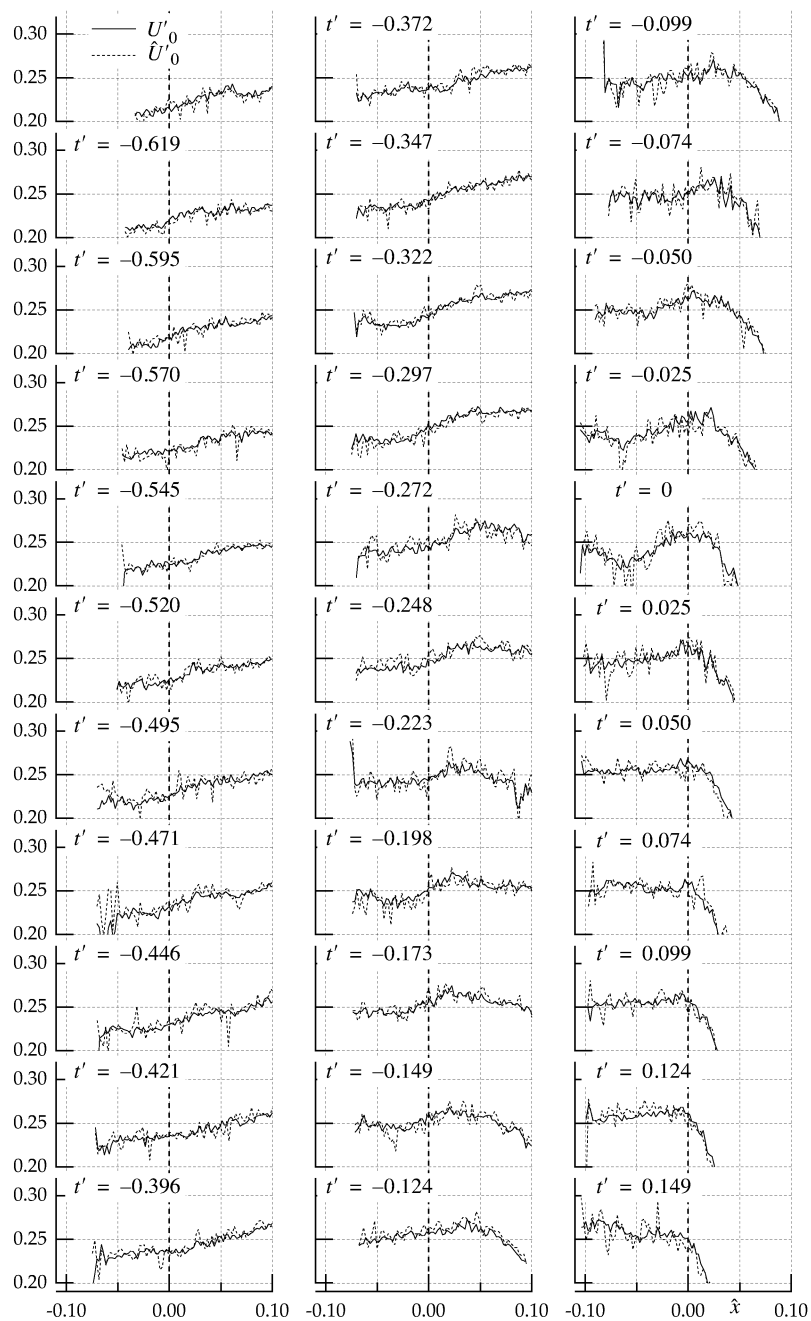


FIGURE 114. The plunging breaker (case 1): Extrapolated (U'_0) and measured (\hat{U}'_0) velocity at $z=0$ as a function of \hat{x} and t' . $\hat{x} = 0$ is the point in the crest where the velocity is horizontal, while $t' = 0$ corresponds to the breaking point.

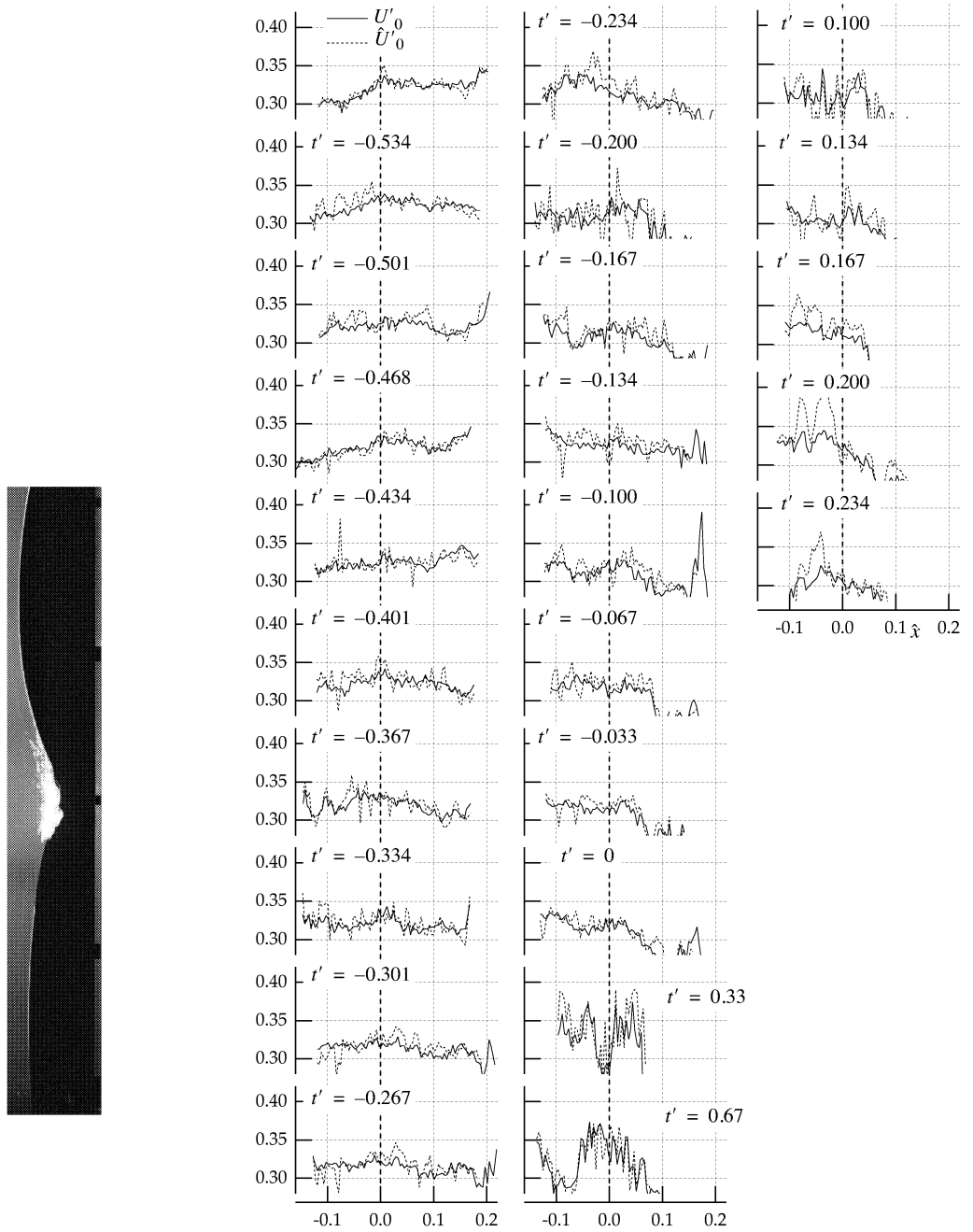


FIGURE 115. The intermediate breaker (case 2): Extrapolated (U'_0) and measured (\hat{U}'_0) velocity at $z=0$ as a function of \hat{x} and t' . $\hat{x} = 0$ is the point in the crest where the velocity is horizontal, while $t' = 0$ corresponds to the breaking point.

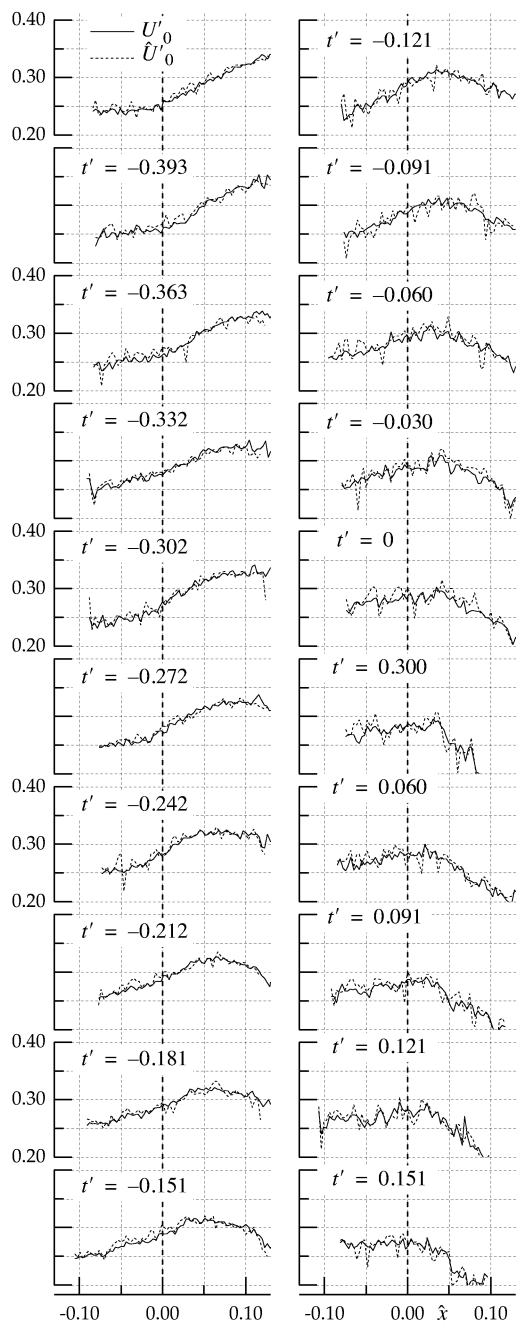


FIGURE 116. The spilling breaker (case 3): Extrapolated (U'_0) and measured (\hat{U}'_0) velocity at $z=0$ as a function of \hat{x} and t' . $\hat{x} = 0$ is the point in the crest where the velocity is horizontal, while $t' = 0$ corresponds to the breaking point.

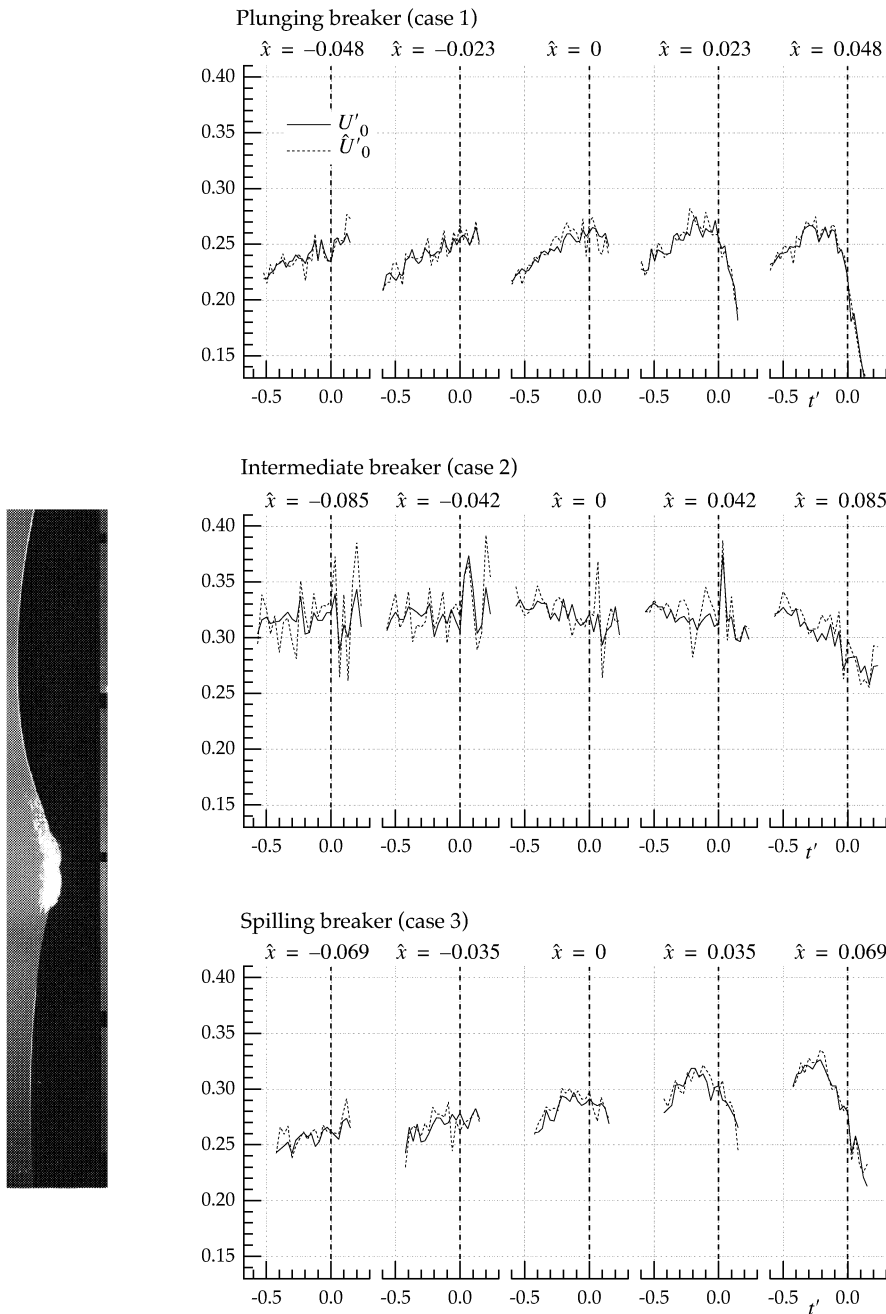


FIGURE 117. Time history of the extrapolated (U'_0) and measured (\hat{U}'_0) velocity at $z=0$ at five different \hat{x} positions in the crest. $\hat{x} = 0$ is the point in the crest where the velocity is horizontal, while $t' = 0$ corresponds to the breaking point.

Appendix C **Additional Wave Geometry Parameter Measurements**

Some of the parameters defined in *Chapter 3.4* are not presented and discussed in the main text. They are omitted because they add little new information about the wave geometry development, but supports the other parameters used. These parameters are shown in this appendix.

The additional parameters are:

- Front wave steepness s_f
- Rear wave steepness s_r
- Front steepness coefficient c_{fs}
- Rear steepness coefficient c_{rs}
- Wave length asymmetry factor a_l
- Wave height asymmetry factor a_h

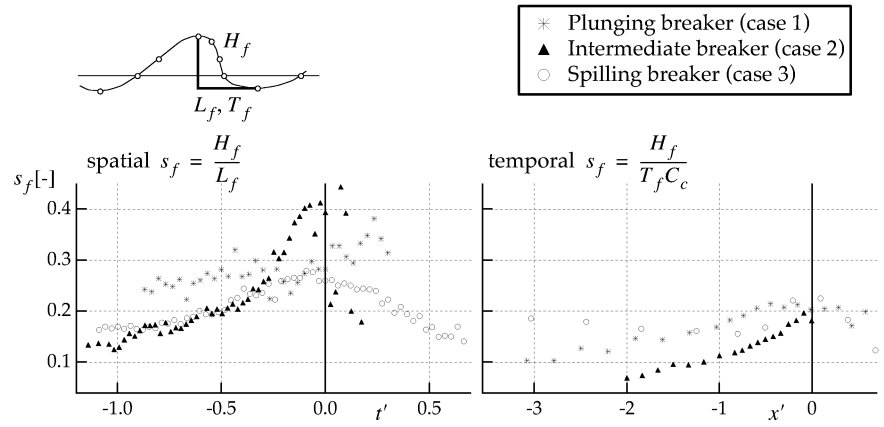


FIGURE 118. Front wave steepness (s_f). Time t' and horizontal coordinate x' are normalized with wave period and wave length, respectively. The origin in both t' and x' are located at the breaking point in both space and time (see Chapter 2.9.2).

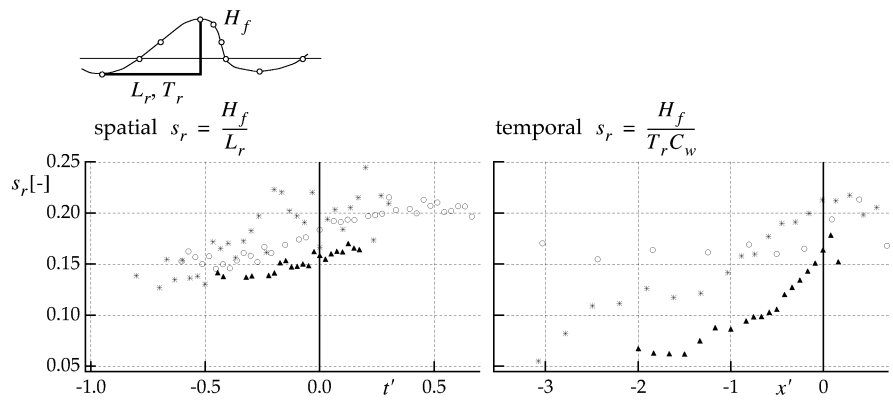


FIGURE 119. Rear wave steepness (s_r). Legend and axis as in Fig. 118.

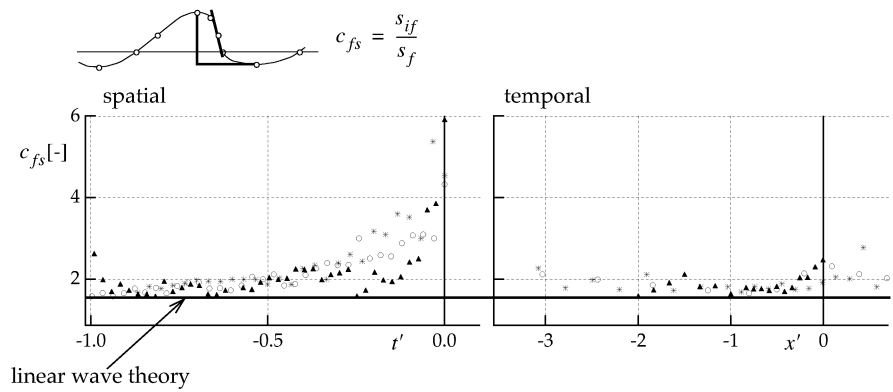


FIGURE 120. Front steepness coefficient (c_{fs}). Legend and axis as in Fig. 118.

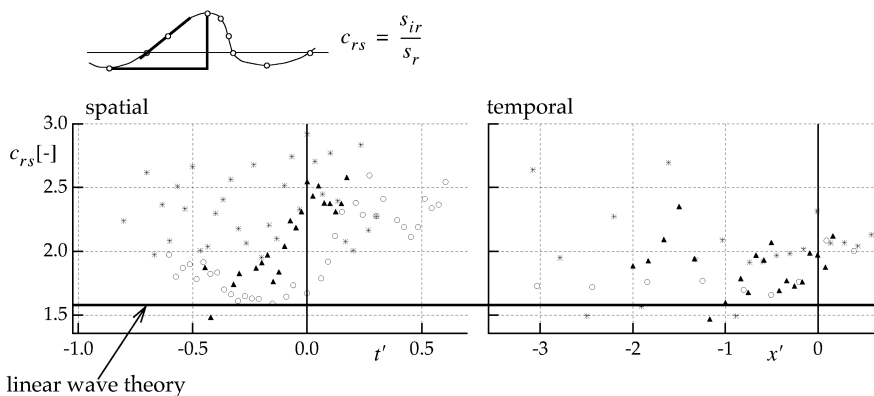


FIGURE 121. Rear steepness coefficient (c_{rs}). Legend and axis as in Fig. 118.

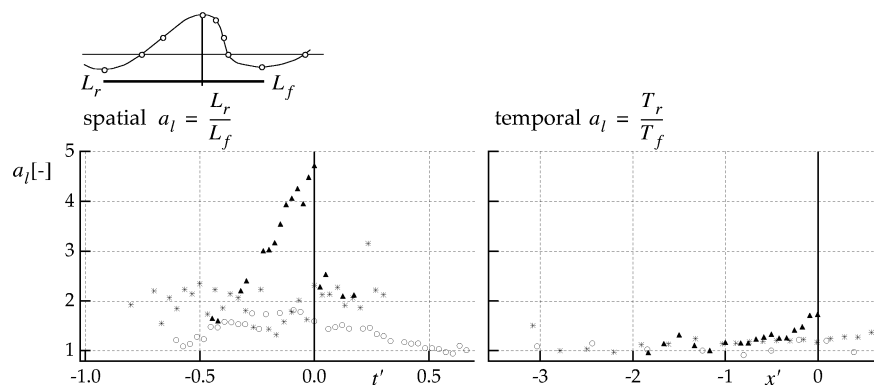


FIGURE 122. Wave length asymmetry factor (a_l). Legend and axis as in Fig. 118.

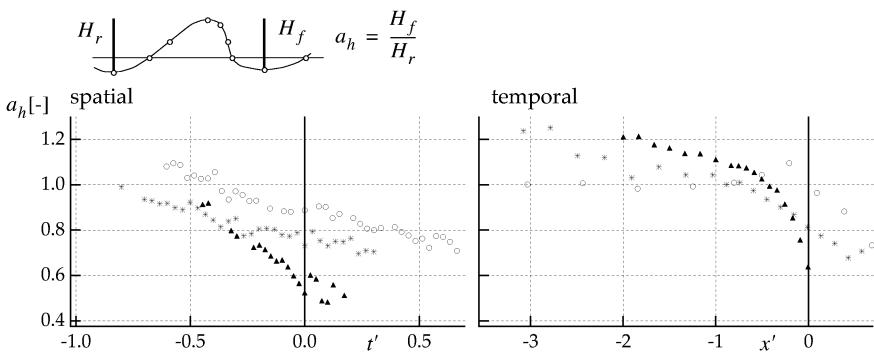


FIGURE 123. Wave height asymmetry factor (a_h). Legend and axis as in Fig. 118.

PREVIOUS DR.ING. THESES

Department of Marine Hydrodynamics

- Løtveit, Magne : A Study of Pressure- and Velocity Relations in the Slip-Stream of Propellers of Single Screw Ships to clarify the Propeller Action behind the Hull. 1963. (in Norwegian)
- Dahle, Emil Aall : A Study of the Coefficients in the Differential Equations for the Rolling Motion of a Vessel. 1971. (in Norwegian)
- Langfeldt, Jan N. : A Theoretical and Experimental Study of the Feasibility of Two-Phase (Gas-Water) Jet Propulsion of Craft. 1972.
- Berg, Tor Einar : Manoeuvring of Vessels. 1978. (in Norwegian)
- Skjördal, Svein O. : Wave Induced Oscillations of Ship Hulls. 1978.
- Nielsen, Finn G. : Hydrodynamic Relations of Oil Booms. 1980.
- Liapis, Nicolas : Hydrodynamic Analysis of the Ship-Buoy System. 1980.
- Pettersen, Bjørnar : Calculation of Potential Flow about Ship Hulls in Shallow Water with Particular Application to Manoeuvring. 1980.
- Rye, Henrik : Ocean Wave Groups. 1981.
- Utnes, Torbjørn H. : Forward-Speed Effects on the Hydrodynamic Motion Coefficients of a Surface-Piercing Body. 1982
- Børresen, Rolf : The unified theory of ship motions in water of finite depth. 1984.
- Aarsnes, Jan Vidar : Current Forces on Ships. 1984.
- Skomedal, Nere : Application of a Vortex Tracking Method to Three-Dimensional Flow Past Lifting Surfaces and Blunt Bodies. 1985.
- Løken, Arne Edvin : Three-dimensional second order hydrodynamic effects on ocean structures in waves. 1986.
- Aanesland, Vidar : A Theoretical and Numerical Study of Ship Wave Resistance. 1986.
- Sortland, Bjørn : Force Measurements in Oscillating Flow on Ship Sections and Circular Cylinders in a U-Tube Water Tank. 1986.
- Falch, Sigurd : A numerical study of slamming of two-dimensional bodies. 1986.
- Lian, Walter : A numerical study of two-dimensional separated flow past bluff bodies at moderate KC-numbers. 1986.
- Braathen, Arne : Application of a vortex tracking method to the prediction of roll damping of a two-dimensional floating body. 1987.
- Gang Miao : Hydrodynamic Forces and Dynamic Responses of Circular Cylinders in Wave Zones. 1989.

- Greenhow, Martin : Linear and Non-Linear Studies of Waves and Floating Bodies. Part I and Part II. 1989.
- Chang Li : Force Coefficients of Spheres and Cubes in Oscillatory Flow with and without Current. 1989.
- Jæger, Arild : Seakeeping, Dynamic Stability and Performance of a Wedge Shaped Planing Hull. 1989.
- Hoff, Jan Roger : Three-dimensional Green function of a vessel with forward speed in waves. 1990.
- Rong Zhao : Slow-Drift of a Moored Two-Dimensional Body in Irregular Waves. 1990.
- Løland, Geir : Current Forces and Flow through Fish Farms. 1991.
- Krokstad, Jørgen R. : Second-order Loads in Multidirectional Seas. 1991.
- Mørch, Hans J. B. : Aspects of Hydrofoil Design; with Emphasis on Hydrofoil Interaction in Calm Water. 1992.
- Steen, Sverre : Cobblestone Effect on SES. 1993.
- Kvålsvold, Jan : Hydroelastic Modelling of Wetdeck Slamming on Multihull Vessels. 1994.
- Ulstein, Tore : Nonlinear Effects of a Flexible Stern Seal Bag on Cobblestone Oscillations of an SES. 1995.
- Solaas, Frøydis : Analytical and Numerical Studies of Sloshing in Tanks. 1995.
- Bratland, Anne K. : Wave-Current Interaction Effects on Large-Volume Bodies in Water of Finite Depth. 1995.
- Herfjord, Kjell : A Study of Two-dimensional Separated Flow by a Combination of the Finite Element Method and Navier-Stokes Equations. 1995.
- Pedersen, Egil : A Nautical Study of Towed Marine Seismic Streamer Cable Configurations. 1996.
- Hansen, Edmond H. : A Discrete Element Model to Study Marginal Ice Zone Dynamics and the Behaviour of Vessels Moored in Broken Ice. 1998.
- Haugen, Elin Marita : Hydroelastic Analysis of Slamming on Stiffened Plates with Application to Catamaran Wetdecks. 1999.
- Tønnessen, Rune : A Finite Element Method Applied to Unsteady Viscous Flow Around 2D Blunt Bodies with Sharp Corners. 1999.
- Haslum, Herbjørn Alf : Simplified Methods Applied to Nonlinear Motion of Spar Platforms. 2000.
- Baarholm, Rolf Jarle : Theoretical and experimental studies of wave impact underneath decks of offshore platforms. 2001.
- Greco, Marilena : A Two-Dimensional Study of Green-Water Loading. 2001.
- Holmedal, Lars Erik : Wave-current interactions in the vicinity of the sea bed. 2002.